UNIVERSTIY OF CALIFORNIA SAN DIEGO

Thermal Transport in Granular and Hydrogel Materials for Solar-thermal Energy Harnessing and Management

A dissertation submitted in partial satisfaction of the requirements for the degree Doctor of Philosophy

in

Engineering Sciences (Mechanical Engineering)

by

Jian Zeng

Committee in charge:

Professor Renkun Chen, Chair
Professor Shengqiang Cai
Professor Javier E. Garay
Professor Jian Luo
Professor Ping Liu

2022

The Dissertation of Jian Zeng is approved, and it is acceptable in quality and form for publication on microfilm and electronically.

University of California San Diego

2022

DEDICATION

Dedicated to my loving parents who always support me

through every single adventure

especially this one

TABLE OF CONTENTS

LIST OF FIGURES

LIST OF TABLES

ACKNOWLEDGEMENTS

As I approach this significant milestone in my life, I would like to sincerely acknowledge and thank those who have helped me achieve this goal. First and foremost, I would like to express my appreciation and gratitude to my advisor, Prof. Renkun Chen for his great support and guidance. The philosophy of research I learn from him will be great asset for my entire life. His innovative thoughts, rigorous thinking and eagerness for thorough understanding always inspire me through every step towards this thesis. I would like to thank him for his invaluable advice on how to become a careful researcher, deep thinker, and helpful teacher.

I appreciate my committee members for their guidance and collaborations in my Ph.D. research. I thank Prof. Ping Liu for his great collaboration on polyelectrolyte hydrogel for solar desalination. I thank Prof. Javier E Garay for his collaboration on high temperature measurement of molten salt and kindly sharing the data. I thank Prof. Shengqiang Cai for his insightful suggestion on the synthesis of hydrogel materials. I thank Prof. Jian Luo for sharing the spinel oxide materials as benchmark sample for our MPR measurement.

I would like to thank my great lab mates in TEMP lab. I could not have achieved the exciting results without their supports and assistance. I would like to express special appreciation to Ka Man Chung for his continuous collaboration in the past four years on the Gen3 project. I thank Xintong Zhang for his substantial contribution to DEM modeling. I thank Tianshi Feng, Sarath Reddy Adapa, Yu Pei, Dr. Wonjae Jeon, Haowen Zhang and Tobias Hang for their assistance and helpful discussion. I thank our alumni Prof. Shuang Cui, Prof. Qingyang Wang and Dr. Yang Shi for their supports in the

hydrogel projects. I thank Prof. Sunmi Shin, Dr. Sahngki Hong, Dr. Lizzie Rubin, Dr. Jeongmin Kim and Dr. Jianlin Zheng for helpful discussions in the lab.

I would like to thank all my friends in San Diego, especially Shuai Wu and Haotian Mao for their great support. I would like to thank Dr. Qiguang He, Dr. Rui Kou and Prof. Ying Zhong for their collaborations. I would like to thank Dr. Peng Chen, Dr. Yun Zhou, Yangting Sun, Saina Shawulieti and Yizhi Li for the friendship. I could not name everyone who has shared the happiness and supported me through the difficulties in my Ph.D. study, but your supports are highly appreciated.

I have received immense support from our collaborators, including Dr. Cliff Ho and Dr. Kevin Albrecht in Sandia National Laboratories, Dr. Zhiwen Ma and Dr. Youyang Zhao in National Renewable Energy Laboratories, Dr. Kevin Robb in Oak Ridge National Laboratories, Prof. Peiwen Li, Dr. Xiaoxin Wang and Ye Zhang in University of Arizona, Prof. Peter Loutzenhiser and Malavika Bagepalli in Georgia Institute of Technology, Dr. Megan Watkins in Brayton Energy, Dr. Chiranjeev Kalra and Myles Bean in Heliogen. This material is based upon work supported by the U.S. Department of Energy's Office of Energy Efficiency and Renewable Energy (EERE) under Solar Energy Technologies Office (SETO) Agreement Number DE-EE0008379. The views expressed herein do not necessarily represent the views of the U.S. Department of Energy or the United States Government. I would like to thank the guidance from our program manager, Dr. Matthew Bauer.

Last but not least, I would like to express my deepest and most sincere gratitude to my loving parents and families. They always give me unconditional supports for every adventure I take, especially this one.

Chapter 2, in full, is a reprint of the materials as it appears in ‘Measurement of High-temperature Thermophysical Properties of Bulk and Coatings Using Modulated Photothermal Radiometry’ *International Journal of Heat and Mass Transfer,* (170) 2021, 120989 by Jian Zeng, Ka Man Chung, Qingyang Wang, Xiaoxin Wang, Yu Pei, Peiwen Li and Renkun Chen. The dissertation author was the primary investigator and first author of this paper.

Chapter 3, in full, is a reprint of the materials as it appears in ‘*In-situ* Thermal Transport Measurement of Flowing Fluid Using Modulated Photothermal Radiometry’, *International Journal of Heat and Mass Transfer*, 180 (2021), 121767 by Jian Zeng, Ka Man Chung, Sarath Reddy Adapa, Tianshi Feng and Renkun Chen. The dissertation author was the primary investigator and first author of this paper.

Chapter 4, in full, is a reprint of the materials as it appears in ‘Measurement and Analysis of Thermal Conductivity of Ceramic Particle Beds for Solar Thermal Energy Storage’, *Solar Energy Materials and Solar Cells*. (230) 2021, 111271 by Ka Man Chung, Jian Zeng, Sarath Reddy Adapa, Tianshi Feng, Malavika V. Bagepalli, Peter G. Loutzenhiser, Kevin J. Albrecht, Clifford K. Ho and Renkun Chen. The dissertation author was the primary investigator and co-first author of this paper. It is also a reprint of the materials as it appears in ‘Thermal Conductivity Modeling of Monodispersed Microspheres using Discrete Element Method’ *Journal of Applied Physics,* (130) 2021, 165104 by Jian Zeng, Ka Man Chung, Xintong Zhang, Sarath Reddy Adapa, Tianshi Feng, Yu Pei and Renkun Chen. The dissertation author was the primary investigator and first author of this paper.

Chapter 5, in full, is being prepared for publication by Jian Zeng, Xintong Zhang,

Ka Man Chung, Sarath Reddy Adapa, Tianshi Feng and Renkun Chen. The dissertation author was the primary investigator and first author of this paper.

Chapter 6, in full, is a reprint of the materials as it appears in 'Multi-layer temperature-responsive hydrogel for forward-osmosis desalination with high permeable flux and fast water release' *Desalination*, 459 (2019), 105-113 by Jian Zeng, Shuang Cui, Qingyang Wang and Renkun Chen. The dissertation author was the primary investigator and first author of this paper.

Chapter 7, in full, is a reprint of the materials as it appears in 'Osmotic pumping and salt rejection by polyelectrolyte hydrogel for continuous solar desalination' *Advanced Energy Materials*, 9(38), 2019 1900552 by Jian Zeng, Qingyang Wang, Yang Shi, Ping Liu and Renkun. . The dissertation author was the primary investigator and first author of this paper.

Chapter 8, in full, is being prepared for publication by Jian Zeng, Xintong Zhang, Ka Man Chung, Ravi Prasher and Renkun Chen. The dissertation author was the primary investigator and first author of this paper.

VITA

2015	Bachelor of Engineering, South China University of Technology
2017	Master of Engineering, South China University of Technology
2022	Doctor of Philosophy, University of California San Diego

PUBLICATIONS

*These authors contributed equally to this work.

1. **J. Zeng*,** K.M. Chung*, X. Zhang*, S.R. Adapa, T. Feng, Y. Pei and R. Chen, "Thermal Conductivity Modeling of Monodispersed Microspheres using Discrete Element Method," *Journal of Applied Physics*, 130, 165104, 2021.
2. K.M. Chung***, J. Zeng***, S. R. Adapa, T. Feng, M. V. Bagepalli, P. G. Loutzenhiser, K. J. Albrecht, C.K.Ho, R. Chen "Measurement and Analysis of Thermal Conductivity of Ceramic Particle Beds for Solar Thermal Energy Storage", *Solar Energy Materials and Solar Cells*. 230, 111271, 2021.
3. **J. Zeng*,** K.M. Chung*, S. R. Adapa, T. Feng, R. Chen "In-situ Thermal Transport Measurement of Flowing Fluid using Modulated Photothermal Radiometry", *International Journal of Heat and Mass Transfer*, 180, 121767, 2021.
4. **J. Zeng*,** K.M. Chung*, Q. Wang, X. Wang, Y. Pei, P. Li and R. Chen, "Measurement of High-temperature Thermophysical Properties of Bulk and Coatings Using Modulated Photothermal Radiometry," *International Journal of Heat and Mass Transfer*, 170, 120989, 2021.
5. **J. Zeng,** Q. Wang, Y. Shi, P. Liu and R. Chen, "Osmotic pumping and salt rejection by polyelectrolyte hydrogel for continuous solar desalination," *Advanced Energy Materials*, 9(38), 1900552, 2019.
6. **J. Zeng**, S. Cui, Q. Wang and R. Chen, **"**Multi-layer temperature-responsive hydrogel for forward-osmosis desalination with high permeable flux and fast water release,**"** *Desalination*, 459, 105-113, 2019.
7. K.M. Chung*, **J. Zeng***, S. R. Adapa, T. Feng, A.Z. Zhao, J.E. Garay and R. Chen, "Thermal Conductivity Measurement of Molten Salt Using Modulated Photothermal Radiometry," ***in prep***.
8. **J. Zeng**, X. Zhang, K.M. Chung, R.S. Prasher and R. Chen, "Scalable Moisture Thermal Battery for Sustainable Thermal Management of Unsteady Heat Loads," ***in prep***.

9. K.M. Chung*, Y. Zhang*, **J. Zeng***, X. Wang, F. Haddad, P. Li and R. Chen, "*In-situ* Thermal Transport Characterization of Flowing Molten Salt for Concentrating Solar Power," ***in prep***.
10. **J. Zeng***, X. Zhang*, K.M. Chung, S.R. Adapa, T. Feng and R. Chen, "Mechanistic Origin of Near-wall Thermal Resistance in Moving Granular Media Induced by Granular Diffusion," ***in Prep***.
11. R. Kou, Y. Zhong, Q. Wang, J. Kim, **J. Zeng**, R. Chen and Y. Qiao, "Hollow-structured Bilayer System for Windowpane Insulation," *Journal of Energy Engineering*, 147(4), 06021001, 2021.
12. Y. Shi, Q. Wang, **J. Zeng**, Y. Yao and R. Chen, "Boiling with Ultralow Superheat Using Confined Liquid Film," *Applied Thermal Engineering*, 184, 116356, 2021.
13. Q. He, Z. Wang, Y. Wang, Z. Wang, C. Li, R. Annapooranan, **J. Zeng**, R. Chen and S. Cai, "Electrospun Liquid Crystal Elastomer Microfiber Actuator," *Science Robotics*, 6(57), eabi9704, 2021.

ABSTRACT OF THE DISSERTATION

Thermal Transport in Granular and Hydrogel Materials for Solar-thermal Energy Harnessing and Management

by

Jian Zeng

Doctor of Philosophy in Engineering Sciences (Mechanical Engineering)

University of California San Diego, 2022

Professor Renkun Chen, Chair

Nowadays, 80% of the developed world's energy comes from fossil fuels. With the aim to peak the carbon emission by 2030 and neutralize it by 2050, sustainable energy sources are being actively explored. It is estimated that 90% of the current energy budget is in the form of thermal energy, implying the significance of efficient harnessing and management of thermal energy towards an energy-efficient world.

Concentrating solar power (CSP) coupled to thermal energy storage have gained extensive attention in recent years due to their capability to store high-grade thermal energy at low cost for on-demand electricity generation. However, current R&D effort in

CSP has been hindered by the limited knowledge in heat transfer of high-temperature components in CSP, such as solar-absorbing coatings, alloy containments, granular flow and molten salt, etc. One of the challenges stems from the lack of suitable *in-situ* measurement tool for these materials due to their high temperature and corrosive natures. To tackle this difficulty, a non-contact laser-based modulated photothermal radiometry (MPR) thermal measurement system was developed. The MPR uses the thermal emission from the specimen surface as the thermometry probe, which is suitable for high-temperature measurement under harsh environment. The system was first characterized by bulk materials and solar-absorbing coating. The MPR system was modified for the measurement of the intrinsic thermal conductivity and convection heat transfer coefficient of flowing fluid in a channel. Afterwards, the MPR system was applied for the measurement of moving particle bed for CSP. The effective thermal conductivity of moving particle with variation in the flowing velocity, temperature, particle size, and particle morphology was obtained. We disseminated the near-wall thermal resistance from the bulk thermal resistance. The discrete element modelling (DEM) indicated that the near-wall thermal resistance was induced by the diffusive motion of particles away from the wall in a moving particle bed.

Low-grade thermal energy is a universal form of energy with easy access and low cost. The low-grade heat was utilized for desalination and water harvesting using hydrogel materials. We developed a new class of thermo-responsive hydrogels for forward-osmosis desalination where the hydrogel draws water molecules across the membrane from seawater due to its high ionic strength. This new class of draw agent processed the unique LCST phase transition to

release water in liquid phase at 35 ℃ to avoid the latent heat penalty in conventional FO desalination. Subsequently, we applied polyelectrolyte hydrogels for continuous solar-driven evaporative desalination, where solar energy was directly converted to heat to evaporate the seawater. Due to the unique osmotic pumping mechanism within the hydrogel, the salt crystallization problem was avoided as opposed to conventional capillary wicks. Lastly, we demonstrated that the hydrogel materials could also be applied for water harvesting from moisture in the air by the adsorption-desorption process. The generic idea was to coat a thin hydrogel layer on a metallic scaffold with 100-1000-fold enhanced effective surface for fast heat and mass transfer kinetics. We achieved a daily water yield an order-of-magnitude higher than the state-of-the-art techniques. Due to the evaporative latent heat in the desorption process, we found that the water harvesting device also manifested itself a superior heat sink for power electronic thermal management. Based on the similar geometric design, we developed a moisture thermal battery (MTB) and demonstrated its capability of passive thermal management of 5G device and CPU.

1. Chapter 1: Introduction

Nowadays, 80% of the developed world's energy comes from fossil fuels. With the aim to peak the carbon emission by 2030 and neutralize carbon emission by 2050, sustainable energy sources are being actively explored. While nuclear fission energy has made major contribution to electricity generation, its attractiveness is severely undermined due to the safety and environmental concern, especially after Fukushima nuclear disaster in Japan in 2011. Other sustainable energy sources, such as wind power, tidal power and photovoltaic suffer from their intermittent nature and thus fail to meet the civil demand so far. It is estimated that 90% of the current energy budget is in the form of thermal energy according to LLNL energy flow chart[1]. Efficient harnessing and management of thermal energy becomes increasingly important under the context of water-energy nexus. To alleviate the water-energy nexus, efforts must be paid not only in the front of thermal energy harnessing from sustainable sources, but also effective management to improve the thermal efficiency in energy-intensive processes.

Concentrating solar power (CSP) coupled to thermal energy storage have gained extensive attention in the recent years due to their capability to convert solar energy to high-grade thermal energy and to store it at low cost for on-demand electricity generation[2,3]. One of the main objectives of the R&D efforts in CSP is to increase the efficiency by elevating the operating temperatures to above 700^{o}C from the current limit of ~ 550^{o}C[2,3]. A key component of the next-generation CSP system is the heat transfer medium. Conventional heat transfer media such as oil and molten nitrate salts have stable temperature limits of less than 400^{o}C[4] and 600^{o}C[5]

respectively. Ceramic-based particle can push the temperature up to ~800^{o}C and are considered a candidate heat transfer medium for the next-generation CSP. However, the understanding of heat transfer mechanism in moving particle bed is still limited, especially at high temperature and high moving velocity, hindering the optimal design of the heat transfer component in CSP. One of the major challenges stems from the lack of proper *in-situ* measurement technique to characterize the thermal conductivity of moving particle bed, which determines the heat transfer kinetics of the particle heat exchanger. Therefore, it is imperative to the develop an *in-situ* measurement system capable of probing the heat transfer mechanism of moving particle bed under extreme operational conditions.

While CSP is a promising renewable energy source with stable power output, the large infrastructure construction and capital investment undermine its attractiveness in the remote area. Efficient harnessing and management of the low-grade thermal energy using distributed low-cost infrastructure is estimated to reduce the current annual electricity consumption by ~ 30% and equivalent annual carbon emission by 500 million ton$_{CO2}$[5-9]. Low-grade thermal energy has been widely used for desalination[10-13] and atmospheric moisture harvesting[14-18] from air to mitigate the water scarcity in the less-developed region due to their easy-access and low-cost. However, current water harvesting techniques still suffer from the low thermal efficiency and slow kinetics. To solve this bottleneck, a new class of materials should be developed and a protocol of structural engineering for fast heat and mass transfer kinetics should be proposed. Low-grade thermal energy is universal from the industrial waste-heat ready to be utilized, which otherwise

consumes 8-21% of the annual electricity consumption for active cooling[5-7]. Therefore, it is of significance to demonstrate passive thermal management of low-grade heat source and the effective recovery of low-grade thermal energy for water harvesting.

1.1. Overview of concentrating solar power

Figure 1-1 shows the schematics of the concentrating solar power plant (CSP) [19]. There are arrays of mirrors on the field to focus the sunlight on to the top of the solar tower receiver with the magnification of ~ 1000 suns (i.e., heat flux of ~ 1000 kW m^{-1}). The heat transfer fluid (HTF) flows on top of the solar tower to absorb the concentrated sunlight and heats up to above 700°C. There are candidates of HTF for the next-generation CSP as shown in Figure 1-1a, including the ceramic particles and chloride-based molten salt. For the falling particle receiver, since the ceramic particles are intrinsically black[20], they directly absorb the sunlight as it falls driven by gravity. On the contrary, the molten salts flow inside an alloy tube for containment. To absorb the sunlight, the tube surface is coated with a black coating of tens of micron thick, e.g., Pyromark 2500[21,22] or other spinel-oxide based black coatings[23]. Solar energy is then converted into thermal energy and is transferred to the flowing molten salt by conduction heat transfer through the coating and steel containment and convective heat transfer between the molten salt and wall. The conductive heat transfer rate depends on the thermal conductivity of the coating and containment materials. However, there is a lack of database of high temperature thermal conductivity of the containment materials, usually Inconel and Nickle based alloys, such as Incone 625 and

Hastelloy, etc. While there are several techniques for high temperature thermal conductivity measurement, such as the laser flash analysis (LFA) [24,25], transient hot-wire (THW) [26], hot-disk transient plane-source (TPS) [27,28], 3ω method [29-31], as well as the pump-probe time or frequency domain thermoreflectance (TDTR/FDTR) techniques [32-35], they suffered from the intrinsic limitation of low sensitivity of thin coating and strict requirement of smooth surface. Therefore, they failed to measure the thermal conductivity of solar-absorbing coating. As such, engineers had to design the receiver based on the estimated thermal conductivity, putting the tens of million USD constructions under huge uncertainty in thermal performance. Therefore, it is imperative to develop a thermal conductivity measurement technique capable of measuring coating, containment materials and HTF under extreme conditions.

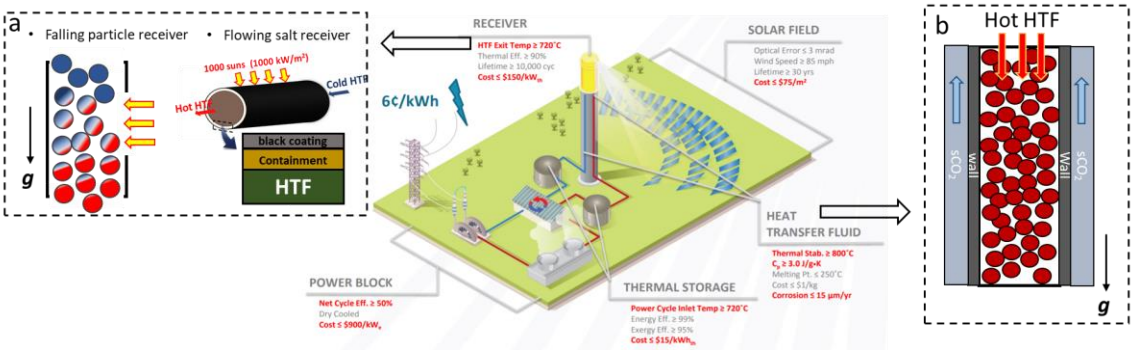

Figure 1-1. Schematics of concentrating solar power plant. (a) Details of the solar receiver. The heat transfer medium is heated by the concentrated sunlight to high temperature after flowing through the receiver. For ceramic particles, sunlight is directly absorbed. For molten salt, sunlight is absorbed by the black coating on the surface of the tube and the flowing molten salt is heated up by heat transfer at the wall. (b) Details of the heat exchanger. The supercritical carbon dioxide (sCO_2) is heated up by the hot heat transfer fluid flowing at the counter direction. The heat transfer coefficient is mainly determined by the thermal properties of the heat transfer fluid.

The hot heat transfer fluid from the receiver is transferred to the heat exchanger as shown in Figure 1-1b. To achieve higher thermal efficiency, Brayton

cycle based on supercritical carbon dioxide (sCO_2) is employed as opposed to the steam-based Rankine cycle at lower temperature before. The sCO_2 is heated up by the hot fluids (either particles or molten salt) flowing in the opposite direction. The effective heat transfer coefficient (HTC) from HTF to sCO_2 is estimated by[36]:

$$U = \left(\frac{1}{h_{sw}} + \frac{\delta_w}{k_w} + \frac{1}{h_{CO_2 w}} \right)^{-1} \tag{1-1}$$

where h_{sw} is the heat transfer coefficient between HTF and wall, δ_w is the thickness of wall, k_w is the solid thermal conductivity of wall materials (which is usually high-temperature alloy), and $h_{CO_2 w}$ is the heat transfer coefficient between the CO_2 flow and wall. Due to small thickness of wall and high velocity of CO_2 flow, the major thermal resistance lies in the HTF-wall heat transfer. The h_{sw} depends on both the intrinsic bulk thermal conductivity of HTF and the fluid flow. Due to the high-temperature and corrosive nature, it has been challenging to measure the properties of molten salt using contact method. Besides, in most global measurement methods, only the effective heat transfer coefficient can be obtained while the details of the heat transfer mechanism are lost, limiting our ability to improve the thermal performance. For example, due to the discrete nature of particle flow, it has been well-known that there is near-wall thermal resistance close to the wall which worsen the h_{sw}. Nevertheless, the near-wall thermal resistance of particle flow has not been quantified so far due to the lack of in-situ measurement capability.

In the first part of this thesis, I developed a laser-based non-contact and non-destructive thermal characterization fool capable of measuring bulk materials, coating, flowing fluid and moving particle bed up to 700°C. In the modulated

photothermal radiometry (MPR), the sample is heated by an intensity-modulated laser to probe into different depths of the sample [37,38]. The MPR uses the thermal emission from the specimen surface as the thermometry probe. In chapter 2, the instrumentation development of the MPR tool was described in detail. The capability, sensitivity and measurement uncertainty were rigorously analysed. I demonstrated the accurate MPR measurement on bulk materials and solar-absorbing coatings. In chapter 3, the MPR tool was extended to measure flowing fluid in a tube. The intrinsic thermal conductivity of flowing fluid could be obtained without contact, manifesting the wide application scope of MPR from materials characterization to *in-operando* diagnostic of working agent in the CSP system, which is of significance for the safe operation of CSP plant. In chapter 4 and 5, the MPR was used to measure the thermal conductivity of moving particle bed. For the first time, the near-wall thermal resistance was differentiated from the bulk thermal resistance of a moving particle bed. We proved that the diffusion-driven granular motion was the micromechanical origin of near-wall thermal resistance of particle flow. The finding in these results provide helpful guidance for the thermal design of particle-based processes including CSP, thermochemical reactor and nuclear reactor, etc.

1.2. Overview of hydrogels for water harvesting and thermal management

Figure 1-2a shows the distribution of water resource on earth. It is seen that about 96.5% of total water resource is in the seawater. Therefore, desalination of seawater has always been an attractive topic in face of the water scarcity. There are several prevailing desalination techniques being actively investigated, including reverse-osmosis,

membrane desalination, forward-osmosis, and evaporative desalination. Among them, forward-osmosis (FO) and evaporative desalination show the potential of using low-grade thermal heat for energy efficiency desalination and thus received extensive attention in the recent years. Forward-osmosis technology utilizes the osmotic pressure across the membrane to separate the salt and water molecules, and thus the FO flux is highly dependent on ionic strength of the draw agent. Conventionally, inorganic salts are used which yield a high FO flux of ~ 20 liter per m^2 per hour (LMH). However, they suffered from the high energy consumption in the regeneration process to release the water from the draw agent, e.g., by ultrafiltration, membrane distillation or evaporation. to justify the sustainability of FO desalination, it is imperative to develop a new class of draw agents with lower regenerative energy consumption, especially from more abundant and low-cost energy sources, such as thermal energy from the waste heat and sunlight. In chapter 6, a thermo-responsive hydrogel-based draw agent was developed to achieve energy-efficient forward-osmosis desalination. The new draw agent possessed unique lower critical solution temperature (LCST) phase transition at 35℃, above which the drawn water was released from the draw agent in the liquid phase to avoid the latent heat penalty. High FO flux was achieved by the multi-layer design to facilitate the heat and mass transfer kinetics.

Solar-driven evaporative desalination directly converted solar energy to heat to evaporate the seawater. Recent progress in the interfacial heating by confining heat in a shallow layer of water in the solar evaporator[39] significantly improve the thermal efficiency of solar evaporation to avoid conductive heat loss to the environment. However, most solar evaporators utilized the capillary pressure

in microporous matrix. Although the capillary pumping is able to provide high liquid flux, they suffered from two inherent challenges. Firstly, the liquid flux is limited by the tradeoff between the capillary pumping pressure and flow resistance, as the former scales inversely with the pore size (i.e., 1/d) and the latter as d^2 for the same flow rate. Second, the micropores are easily blocked by the salt crystal during evaporation. Therefore, to enable the long-term stable operation of solar-driven evaporation, a new liquid supply mechanism rid of micropores should be developed. In chapter 7, a new liquid pumping mechanism, i.e., osmotic pumping, was proposed for simultaneous high liquid flux and salt rejection. We demonstrated high thermal efficiency, high liquid flux, and long operation time using the osmotic pumping method.

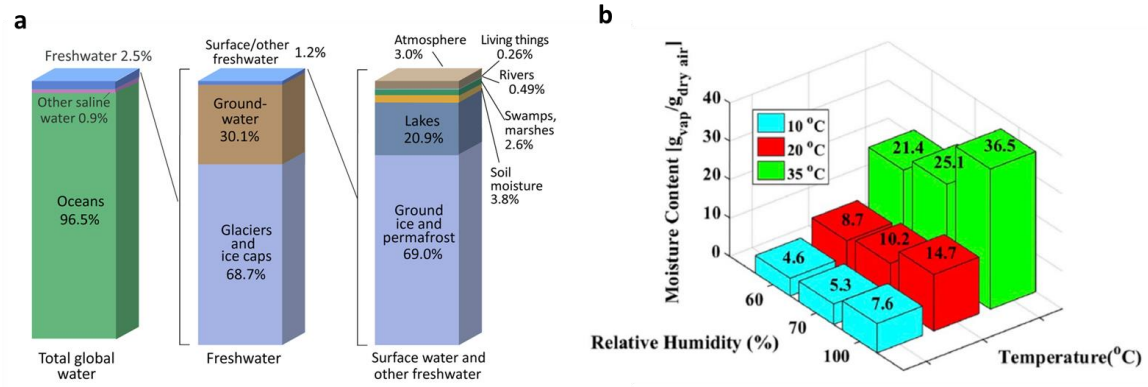

Figure 1-2. Water resources on earth. (a) Water resource distribution on earth. (b) Water concentration in the atmospheric air.

Although thermally driven desalination techniques are promising to solve the water-energy nexus in the coastal area, they are beyond reach in the inland area. As shown in Figure 1-2a, about 3% of the accessible fresh resources is trapped in air, which is about 6 times more than the total volume of fresh water preserved in river[40]. However, this resource has been less explored compared to

counterparts in river and lake. Figure 1-2b shows the water content in air as a function of temperature and relative humidity (RH) [41]. For example, for at T_a = 20 °C and RH = 60%, the moisture content is about 15 g_{water} m^{-3}, indicating that only 200 m^3 is needed to produce 3 L of water (daily water need for adult). Recent advance on hygroscopic materials opens the possibility to explore the water moisture in air by adsorption-desorption process. However, the high latent heat of water during the desorption process hinders the energy efficiency of the cycle. To solve this, we utilized the thermoresponsive hydrogel as sorbent to avoid the latent heat penalty. To improve the water yield, we significantly enlarge the effective surface area by coating thin hydrogel layer on a porous metal scaffold which improved heat and mass transfer kinetics. On the contrary, when a non-thermoreponsive hydrogel coating was used, due to the high latent heat during the desorption process, a significant amount of heat was carried away by the vapor, and thus, this design can also be used for passive thermal management of high-power electronics. Based on the hydrogel-based adsorption-desorption process, we can demonstrate both water harvesting from air and thermal management of electronics on the same devices, with minor modification of the hydrogel coating.

1.3. Thesis structure

As shown in Figure 1-3, this thesis centres around thermal energy harnessing and management for water-energy nexus. This thesis is separated into two parts:

Part I: Thermal transport in high-temperature media for concentrating solar power.

Chapter 2 introduces the instrumentation development of the high temperature measurement MPR tool in detail. The capability, sensitivity and measurement uncertainty were rigorously analysed. Thermal conductivity bulk materials and solar-absorbing coatings were measured up to 700°C.

Chapter 3 describes the modified MPR system for flowing fluid in a tube. The intrinsic thermal conductivity of flowing fluid could be obtained without contact when the critical criteria was met. The modified MPR system provided an *in-operando* diagnostic tool of working agent in the CSP system, which is of significance for the safe operation of CSP plant.

Chapter 4 describes the modified MPR for thermal conductivity measurement of stationary particle bed. Discrete element modelling of stationary particle bed was conducted to obtain the realistic packing structure of particle bed. Modelled thermal conductivity based on the realistic packing structure was compared to the experiment.

Chapter 5 describes the modified MPR for thermal conductivity measurement of moving particle bed. The near-wall thermal resistance of moving particle bed was differentiated from the bulk thermal resistance. Discrete element modelling was conducted to explain the micromechanical origin of the near-wall thermal resistance.

Part II: Hydrogel materials for water harvesting and thermal management.

Chapter 6 describes thermoresponsive hydrogel draw agent for for-ward osmosis. A multi-layer structure was introduced to improve the FO flux while maintaining the unique LCST phase transition of thermoresponsive hydrogel.

Chapter 7 describes solar-driven evaporative desalination using polyelectrolyte hydrogel. Osmotic pumping effect was used instead of capillary pressure to achieved simultaneously high evaporative flux and salt-rejection ability. Long-term stable operation of the system was demonstrated.

Chapter 8 describes adsorption-desorption based water harvesting and thermal management using hydrogel. A thin hydrogel layer was coated on a metallic scaffold with 100-1000-fold enhanced effective surface area. When coating the scaffold with thermoresponsvie hydrogel, we realized water harvesting from air. When coating the scaffold with non-thermoresponsive hydrogel, we developed a moisture thermal battery for passive thermal management of power electronics.

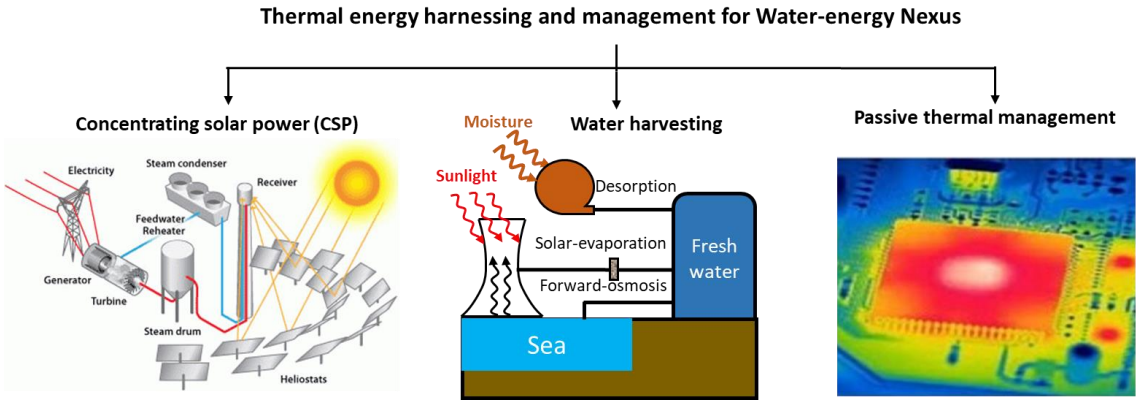

Figure 1-3. Thesis structure centered around granular media and hydrogel materials for concentrating solar power, water harvesting and thermal management.

Part I: Thermal transport in high-temperature media for concentrating solar power

2. Chapter 2: Instrumentation development of modulated photothermal radiometry

2.1. Introduction

Thermal transport at high temperatures is a significant process for many applications [42], such as concentrated solar power (CSP) plants [43,44], thermal energy storage [45], and thermal barrier coatings for gas-turbine engines [46]. There are several established techniques for high temperature thermal conductivity measurement, such as the laser flash analysis (LFA) [24,25], transient hot-wire (THW) [26], hot-disk transient plane-source (TPS) [27,28], 3ω method [29-31], as well as the pump-probe time or frequency domain thermoreflectance (TDTR/FDTR) techniques [32-35], etc. However, there are still limitations of these techniques under certain circumstances, for example, on samples with rough surfaces and at high temperature. In a typical LFA measurement, the thermal diffusivity could be obtained from the time delay of temperature rise at the backside of the sample upon pulsed heating. Although LFA is capable of measuring bulk materials with high throughput, it is insensitive to thin films [47,48] and the typical commercial LFA instrument can only measure samples with a thickness of ~ 100 μm or above [49,50]. The 3ω method [29] is another popular technique that is capable of measuring bulk materials and coatings with the thickness from 10 μm [51] down to 10-100 nm [52]. However, the 3ω technique needs a thin metallic strip serving both as a heater and a thermometer, and thus it requires time-consuming microfabrication process that is sometimes not feasible for rough

surfaces [53]. Besides, it is challenging to preserve the functionalities of the 3ω heater at high temperature in air. TDTR/FDTR are noncontact optical heating and sensing techniques to measure the thermal properties of both bulk and thin films. Thin films can be accurately measured with a short thermal penetration depth via either short time delay or high modulation frequency [33,34,54]. However, the techniques also need a thin and optically smooth transducer layer (e.g., Au or Al) [55] for pump laser absorption and probe laser reflectance, which poses challenges at high temperature and for rough surfaces. The THW and TPS methods work well for rough surfaces, e.g., particles [56] and liquids [26], however, they rely on the electric resistance of heater/sensor wires (e.g., Pt wire for THW) in intimate contact with the sample, thus possessing a similar challenge in thermal stability as other contact methods.

Photothermal radiometry (PTR) using either modulated (continuous wave) and pulsed laser is a well-known non-destructive and non-contact thermal characterization tool for bulk materials [37,57], thin film specimens [58-60] and superlattices [61], and interfacial thermal resistance [62], etc. In the modulated photothermal radiometry (MPR), the sample is heated by an intensity-modulated laser to probe into different depths of the sample [37,38]. The MPR uses the thermal emission from the specimen surface as the thermometry probe. While this thermometry approach does not have the high spatial resolution offered by the thermoreflectance method, it is not affected by the stability issue of thermal transducers and surface roughness as in the 3ω method and the thermoreflectance techniques. Therefore, MPR can serve as an attractive and convenient alternative for measuring thermal conductivity of rough or porous samples at high temperature. While MPR has been previously established, most of the previous studies only focus on the

measurement at room temperature [37,57,63] despite a few reports on the pulsed photothermal radiometry at the elevated temperature [64]. Due to the intrinsically non-linear relationship between the infrared (IR) emissive power (E_a) and temperature, i.e., $E_a \sim T_o^3$ for surface temperature oscillating around the baseline sample temperature of T_o, the emission signal increases substantially at higher temperatures for MPR, leading to a greater measurement sensitivity at higher temperature, which is advantageous over many other techniques. In the meantime, there are also perceived challenges associated with high-temperature MPR measurement, including a suitable sample holder with good temperature uniformity within the measurement spatial window and a suitable black laser absorption and IR emission coating suitable at high temperature in air.

In this chapter, we demonstrate the MPR measurement of bulk materials and coatings up to 973 K. The MPR setup is carefully designed for high temperature measurement with consideration of heat loss and temperature uniformity. We first calibrate the MPR system by measuring common bulk solids, including borosilicate glass [29,65,66], Pyroceram 9606 [67,68], 8 mol% Y_2O_3 stabilized ZrO_2 (8YSZ) [69] and stainless steel 304 (SS304) [70], to confirm the acceptable measurement error from MPR (< 10%). Subsequently, we measure several solar-absorbing coatings, including Pyromark 1200, Pyromark 2500, and black spinel oxide ($Cu_{0.5}Cr_{1.1}Mn_{1.4}O_4$) coatings synthesized before by the authors [23], with variation in the substrate materials and coating thickness. We find that the thermal conductivities for these coatings are in the range of 0.4 - 0.8 W m^{-1} K^{-1} from room temperature to 700 ^oC, depending on the compositions and temperature, indicating a possibly considerable temperature drop within the coatings for high-temperature CSPs. The MPR technique reported here can provide a facile thermal

conductivity diagnostic tool for high temperature materials with broad applications, such as CSP, nuclear reactors, and thermal barrier coating for turbines, etc. It sets the foundation for the measurement of flowing fluid, stationary particle bed, and moving particle bed in the later chapters.

2.2. Instrumentation development and configuration

2.2.1. Principle of MPR Measurement

Figure 2-1 shows the principle of the MPR measurement on a two-layer sample. The sample is heated up by the intensity-modulated laser q_s, leading to the oscillation of the surface temperature rise θ_s of the sample at the same frequency (f) of the heating laser. Thermal emission from the sample surface is collected by and IR-detector which will be used to calculate the θ_s. For a two-layer sample with thicknesses of L_1 and L_2 for the top layer and the substrate respectively, the laser flux is assumed to be absorbed at the surface of the first layer. The light absorbing coatings (10-50 μm) on the sample surfaces are based on Pyromark 1200, Pyromark 2500, and a black spinel oxide ($Cu_{0.5}Cr_{1.1}Mn_{1.4}O_4$) [23]. The coating has small skin depth (< 5 μm [21,22]) at the laser wavelength. Therefore, the assumption of the surface heat flux is valid. To simplify the problem to one-dimensional (1D) heat transfer, one has to make sure that the thermal penetration depth, $L_p = \sqrt{2\alpha/\omega}$, where α is the thermal diffusivity and ω is the angular frequency, is much smaller than the laser spot size, which is around 6 mm in this experiment. The thermal penetration depth can be adjusted by changing the modulation frequency of the incident laser. For example, at low frequency where $l_1 \ll L_p < l_1 + l_2$, the thermal response is mainly determined by the property of the second layer (i.e., substrate). We also control L_p to be smaller than the total thickness of sample to avoid the

backside effect (i.e., utilizing the adiabatic boundary condition on the backside). At high frequency where $L_p < l_1$, the thermal response is only sensitive to the first layer (i.e., coating). By modulating the thermal penetration depth, we can probe into different layers of the sample.

The 1D heat transfer model for a multi-layer sample with the adiabatic boundary condition on the back side and heating on the front side is [50,71]:

$$\theta_s = -\frac{d}{c} q_s \tag{2-1}$$

where θ_s is the surface temperature oscillation defined as $\theta_s = T_s - T_o$; T_s is the transient surface temperature and T_o is the baseline surface temperature by the cartridge heaters and DC component of the laser heating; q_s is the AC component of the laser heat flux; d and c are elements in the following transfer matrix:

$$M = \begin{pmatrix} a & b \\ c & d \end{pmatrix} = M_n M_{n-1} \cdots M_i \cdots M_1 \tag{2-2}$$

where M_i is the transfer matrix for the i^{th} layer with the subscript 1 for the top layer and n for the bottom layer. For the two-layer sample shown in Figure 2-1b, the first layer is the coating and the second layer is the substrate. The transfer matrix M_i is expressed as follows:

$$M_i = \begin{pmatrix} \cosh\left(D_i\sqrt{j\omega}\right) & -\frac{\sinh\left(D_i\sqrt{j\omega}\right)}{e_i\sqrt{i\omega}} \\ -e_i\sqrt{j\omega}\sinh\left(D_i\sqrt{j\omega}\right) & \cosh\left(D_i\sqrt{j\omega}\right) \end{pmatrix} \tag{2-3}$$

where $D_i = \frac{l_i}{\sqrt{\alpha_i}}$, l_i and α_i are the thickness and thermal diffusivity of the i^{th} layer. j is the imaginary. e_i is the thermal effusivity of the i^{th} layer.

In the MPR measurement of solar-absorbing coatings on a substrate, the coating absorbs the laser flux and emits thermal radiation. Therefore, the multi-layer model is

reduced to the two-layer model assuming that the substrate is a semi-infinite medium (adiabatic boundary condition on the back side):

$$\theta_s = \frac{q_s}{e_f\sqrt{i\omega}}\left[\frac{e_f \cosh\left(D_f\sqrt{j\omega}\right)+e_s \sinh\left(D_f\sqrt{j\omega}\right)}{e_f \sinh\left(D_f\sqrt{j\omega}\right)+e_s \cosh\left(D_f\sqrt{j\omega}\right)}\right] \quad (2\text{-}4)$$

where e_f and e_s are thermal effusivities of the coating and the substrate, respectively; q_s is laser heat flux; $D_f = \frac{l_f}{\sqrt{\alpha_f}}$, where α_f is the thermal diffusivity of the coating; $a_f = k_f/(\rho_f c_f)$, where ρ_f, c_f and k_f are the density, specific heat, and thermal conductivity of the coating, respectively. Notably, The measurement for bulk material is conducted at the low frequency range (1 Hz < f < 20 Hz) with $L_p \gg l_f$, where l_f is the thickness of the coating. Under this condition, Equation 2-4 is reduced to Equation 2-5 at the low frequency limit with $L_p \gg l_f$.

$$\theta_s = \frac{q_s \exp\left(-\frac{\pi}{4}i\right)}{e_s\sqrt{\omega}} + \frac{q_s l_f}{k_f} \quad (2\text{-}5)$$

where the first term on the right-hand side depends on the thermal effusivity of the substrate ($e_s = \sqrt{\rho_s c_s k_s}$) and is proportional to $\omega^{-1/2}$ while the second term depends on the properties of the coating and is frequency independent. To obtain the thermal properties of the coating ($e_f$and a_f), the thickness of the coating and the laser flux were measured separately, which contributes to the measurement uncertainty, as we shall discuss in the Section 2.3.3. k_f and $\rho_f c_f$ can be determined from the measured e_f and a_f.

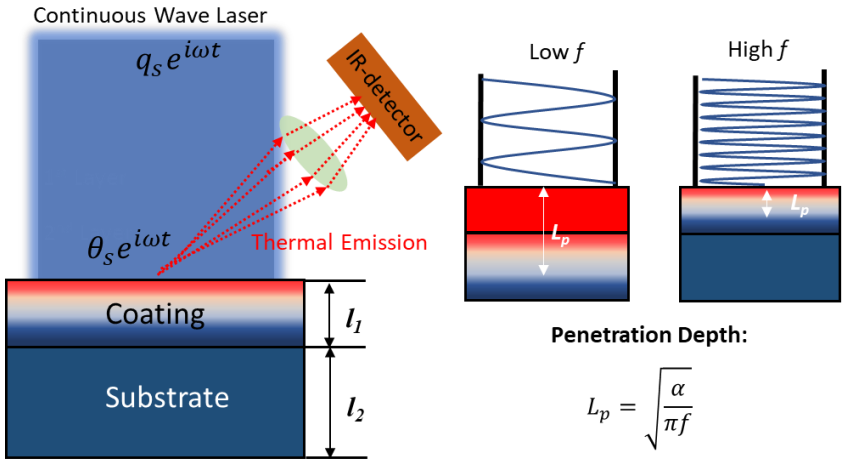

Figure 2-1. Principle of MPR measurement on a two-layer sample.

2.2.2. Details of MPR System

Figure 2-2 shows the schematics of the MPR system and the principle of the measurement. As shown in Figure 2-2a, a continuous wave (CW) diode laser (Naku Technology Co., Ltd, CivilLaser, 445 nm, 6 W, frequency range: 0-30 kHz ,blue fiber-coupled laser) is driven by a waveform-generator (Agilent 33120A), providing a sinusoidal wave with intensity modulation at the frequency of f. Before heating the sample surface, the laser beam is homogenized to a top-hat profile using a homogenizer (EKSMA Optics, GTH-3.6-1.75FA). The laser spot size is controlled to be around 6 mm in diameter. The sample is heated up by the modulated laser flux, leading to the oscillation of the surface temperature rise θ_s of the sample at the same frequency (f) of the heating laser. Thermal emittance from the sample surface is collected with a pair of parabolic mirrors (Thorlab Inc., MPD169-G01, focal length of 3 inches) and focused to a high-speed HgCdTe (MCT) detector (Kolmar Technologies, Inc., KMPV11-0.25-J1/DC70). The IR detection spot size on the sample is estimated to be ~0.5 mm in diameter. The samples are coated with a thin black absorbing coating (10-50 μm) serving

as a transducer layer with high visible absorptance at the laser wavelength (> 97%) and infrared thermal emittance (>90%) [23], as shown in Figure 2-2a. The coating is also stable up to 800 °C in air [23] for high-temperature operation. A germanium (Ge) filter (Thorlab Inc., WG91050-G) is placed in front of the MCT detector to filter short-wavelength light, such as the small reflection of the incident laser from the sample surface and the ambient light. The surface temperature rise θ_s is obtained from measuring the emitted power from the surface. The relationship between the measured voltage signal from the MCT detector and the surface temperature is calibrated using a pyrometer (Lumasense Technologies IGA 320/23-LO) that can also measure the temperature of the central area of 1 mm^2 within the laser spot. Thermal response signal (in voltage) from the MCT detector is recorded using a lock-in amplifier (Stanford Research System SR830) with the sinusoidal signal from the waveform-generator serving as the reference signal. The photograph of MPR system is shown in Figure 2-3.

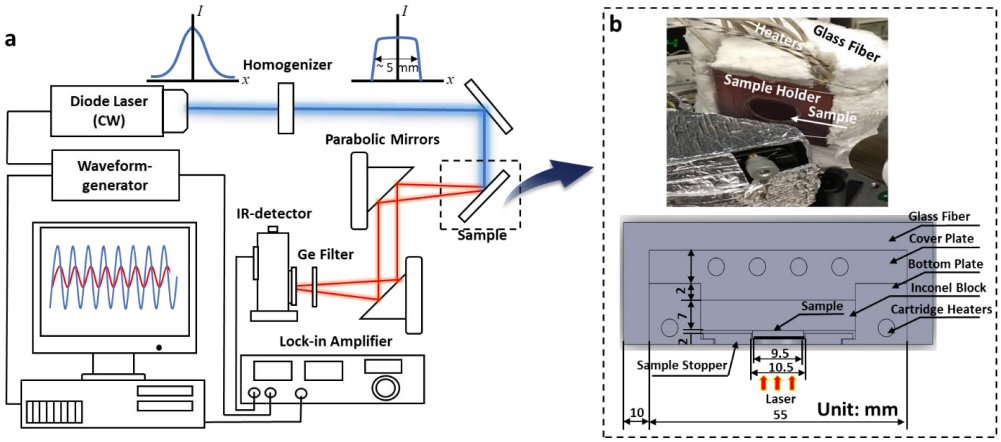

Figure 2-2. Details of MPR system. (a) Configuration of MPR system. (b) Photograph (top) and schematic (bottom) of the high-temperature sample holder for the MPR measurement. Samples are placed at the center of the holder made of Inconel 625 alloy.

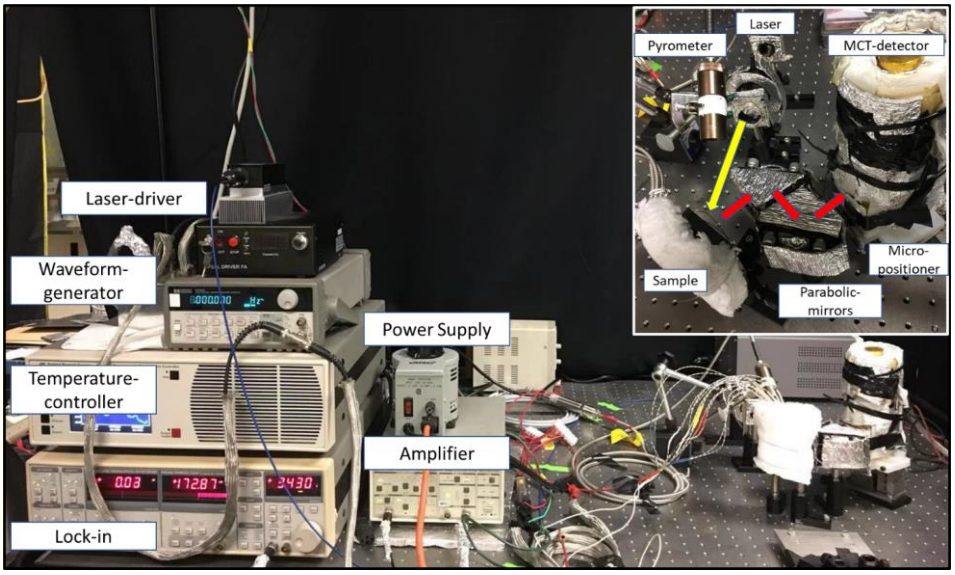

Figure 2-3. Photograph of the MPR setup. Inset: MCT infrared detector and a pair of parabolic mirrors.

A sample holder is designed for high temperature measurement up to 973 K in air. Figure 2-2b shows the photograph of the sample holder (top) and the cross-section view of the holder (bottom). The sample is made of a cover plate, a bottom plate, a block, and a sample stopper, all made of Inconel 625 alloy due to its high temperature stability in air. The cover plate and the bottom plate create a cavity to house the block and the disk-shaped sample of 10 mm in diameter. The sample is pressed by the sample stopper to make good contact with the underlying block. The sample stopper has a circular opening slightly smaller than the sample diameter for optical access. The entire setup is assembled using screws that tighten the cover plate and the bottom plate. The two plates are embedded with seven cartridge heaters of 6 mm in diameter providing a total power up to 420 W. The back and sides of the sample holder are wrapped by 10 mm thick glass fiber to reduce heat loss. The front surface of the sample is exposed for optical access.

The sample holder is designed to ensure the temperature uniformity in the sample. The temperature uniformity of the sample holder is verified by finite element modeling

using COMSOL. It is important to validate the temperature uniformity because it represents the characteristic temperature of the sample, which strongly influence the thermal properties of the materials. Figure 2-4 shows more details of the sample holder with the mounting posts. We simulate the temperature distribution in the sample using the parameters listed in Table 2-1 using COMSOL Multiphysics, with the *heat transfer in solid* module. The heat transfer coefficient for the sample surface is 120.6 $W \cdot m^{-2} \cdot K^{-1}$, including both the radiation and convection heat transfer coefficient for heat loss. All the other surfaces are assumed to be convection heat transfer only (h_{conv} =47.6 $W \cdot m^{-2} \cdot K^{-1}$), because of the radiation effect due to the low thermal emissivity of Inconel alloy surface. The radiation heat transfer coefficient is calculated by:

$$h_r = \varepsilon\sigma(T_0^2 + T_{air}^2)(T_o + T_{air}) \tag{2-6}$$

and the natural convection heat transfer coefficient is calculated by:

$$h_{conv} = 1.43 \left(\frac{\Delta T}{L}\right)^{\frac{1}{4}} \tag{2-7}$$

where T_o is the sample surface baseline temperature (~1000 K) without the leaser heating and T_{air} is the ambient air temperature (300 K). ΔT is the difference between T_o and T_{air}. L is the characteristic length of sample holder. The heater power is set to be 170 W and the DC components of the laser power varied from 2 W to 7 W to heat up the sample to above 1000 K.

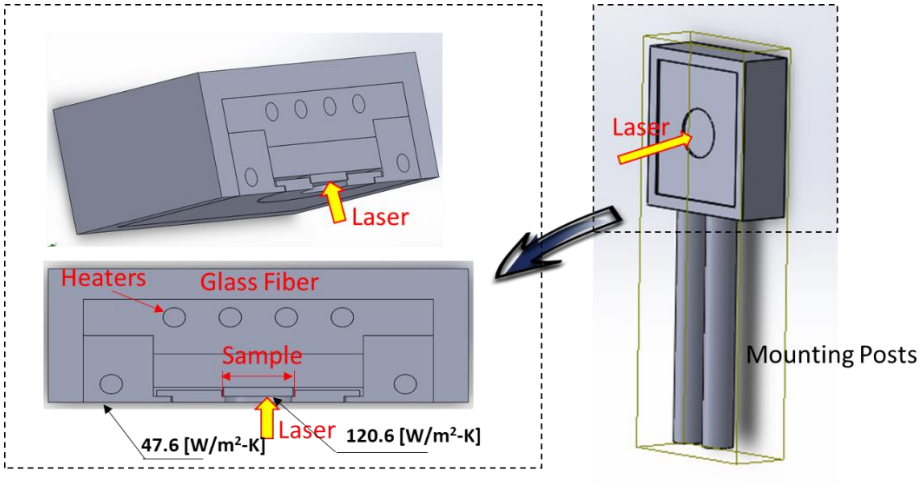

Figure 2-4. Details of the sample holder for the high temperature measurement. The sample surface has both radiation and convection heat transfer conditions (h =120.6 W·m^{-2}·K^{-1}) and all the other surfaces are assumed to be convection heat transfer only (h_{conv} = 47.6 W·m^{-2}·K^{-1}), because of the radiation effect due to the low thermal emissivity of Inconel alloy surface.

Table 2-1. COMSOL simulation parameters for sample holder at high temperature.

Operational Conditions	
Parameter	**Value**
Heater Power	170 [W]
Laser Power	2 – 7 [W]
Convective Heat Transfer Coefficient (h_{conv})	47.6 [W·m^{-2}·K^{-1}]
Radiative Heat Transfer Coefficient (h_r, $at\ T_s = 1000\ K$)	73 [W·m^{-2}·K^{-1}]
Heat Transfer Coefficient on Sample Surface (h)	120.6 [W·m^{-2}·K^{-1}]
Ambient Temperature	293.15 [K]
Materials	
Sample	Borosilicate Glass
Sample Holder	Inconel 625
Insulation	Glass Fiber
Heater	Copper

Figure 2-5a shows the COMSOL simulation results for the temperature distribution inside the sample holder when the heater power is 170 W and the DC laser power is 2 W, which results in sample surface temperature T_a of around 1050-1100 K. It is noted that the DC laser power, set at 2 W in this work, was inevitable to avoid the truncation of the AC component of laser power in our measurement. The laser spot size is set to be 6 mm in diameter. Both the convective and radiative heat losses from the surface are considered. Figure 2-5b and 2-5c show the simulated temperature distribution within the sample (SiO_2) with diameter of 10 mm and thickness of 1.5 mm. Figure 2-5b shows the temperature distribution along the thickness direction at the center of the sample. Due to the heat loss from the sample surface and the fact that the heating power is applied from the sides and the back of the sample, there is a temperature gradient along the thickness direction. In our measurement, the sample surface was coated with a black light absorbing coatings for laser absorption and thermal emission [23], which led to a considerable radiative heat loss. Temperature gradient within the Inconel block is smaller than that within the sample due to the higher thermal conductivity of Inconel. Since some of the heat loss is compensated by the DC component of the laser heating (2 W), the maximum temperature difference within the sample is about 10 K. In actual measurements, we only consider the temperature uniformity within the thermal penetration depth, which is generally less than 0.5 mm at 1 Hz, the lowest frequency used in our measurements (e.g., for glass with thermal diffusivity of ~ 0.6 $mm^2\ s^{-1}$, the penetration depth is ~ 0.3 mm at 1 Hz). Within this penetration depth, the temperature difference is less than 5 K, indicating negligible temperature non-uniformity along the thickness direction. Figure 2-5c shows the temperature distribution on the surface of the

sample along the lateral direction. In general, the temperature decreases from the center to the edge due to the laser heating effect until it is 4 mm away from the center where the sample is mainly heated up by the cartridge heaters. The maximum temperature difference along the lateral direction is ~ 45 K. In the actual measurement, the MPR detector focuses on the center of the sample with the detection spot of about 0.5 mm in diameter. Within the IR detection spot, the temperature difference is less than 5 K, indicating negligible temperature difference along the lateral direction. Overall, the above analysis indicates that the temperature difference is less than 5 K, along both the lateral and normal directions, within the sample up to 973 K in the frequency range of interest (i.e., > 1 Hz).

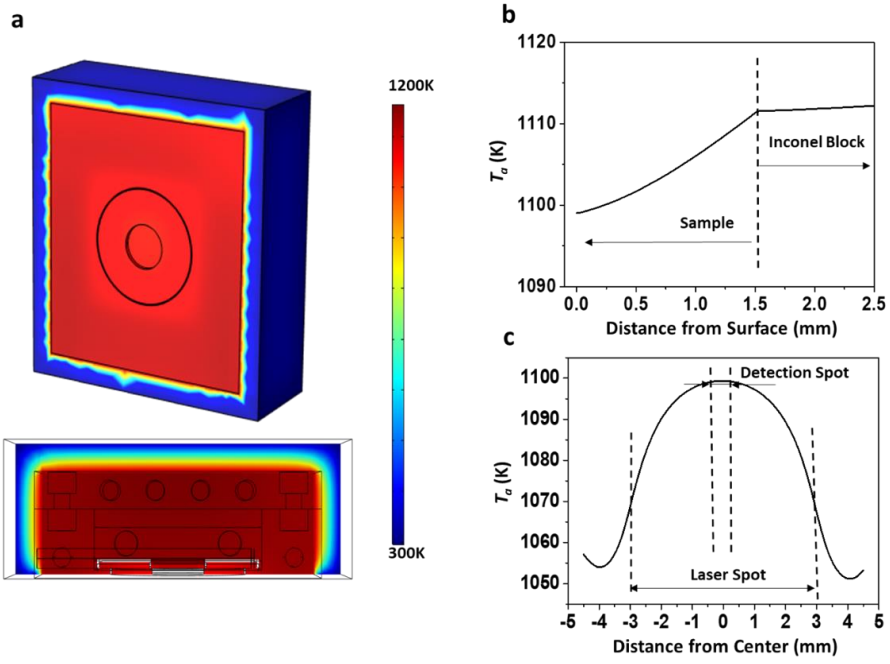

Figure 2-5. Finite-element simulation using COMSOL for the temperature distribution in the high-temperature sample holder. (a) Temperature profile of the sample holder with the heater power of 170 W and the DC component of laser power of 2 W. The upper row shows the external surface while the lower row shows the cross-section of the holder. (b) Temperature distribution within the sample along the thickness direction. (c) Temperature distribution along the radial direction on the sample surface.

While the DC component of the laser power is set to be 2 W throughout our measurement, the temperature non-uniformity can be further reduced with higher DC laser power to compensate the heat loss as shown in the Figure 2-6. Figure 2-6a and 2-6b show the temperature distribution within the sample using different DC components of laser power from 2 W to 7 W, along the sample thickness direction and radial direction, respectively. It is noted that the minimum DC component of laser power is 2 W because the AC component of laser power in our measurement is ~ 2 W. We already showed in the manuscript that the temperature non-uniformity is acceptable using DC laser power of 2 W. As shown in Figure 2-6a, the temperature difference in the thickness direction can be further reduced from ~ 15 K to 5 K with the DC laser power increasing from 2 W to 4 W. At the DC laser power of 7 W, the surface temperature is even higher than that within the sample because the laser power is higher than the heat loss. As shown in Figure 2-6b, the maximum temperature difference along the lateral direction on the sample surface increases with increasing DC laser power because the lases spot is smaller than the sample size. However, temperature difference within the IR detection spot is negligible for all the DC laser power. Overall, we conclude that it is suitable to apply the DC laser power of 2 W based on our current configuration. The grid independence test has been conducted by changing the mesh sizes until the simulation results converged.

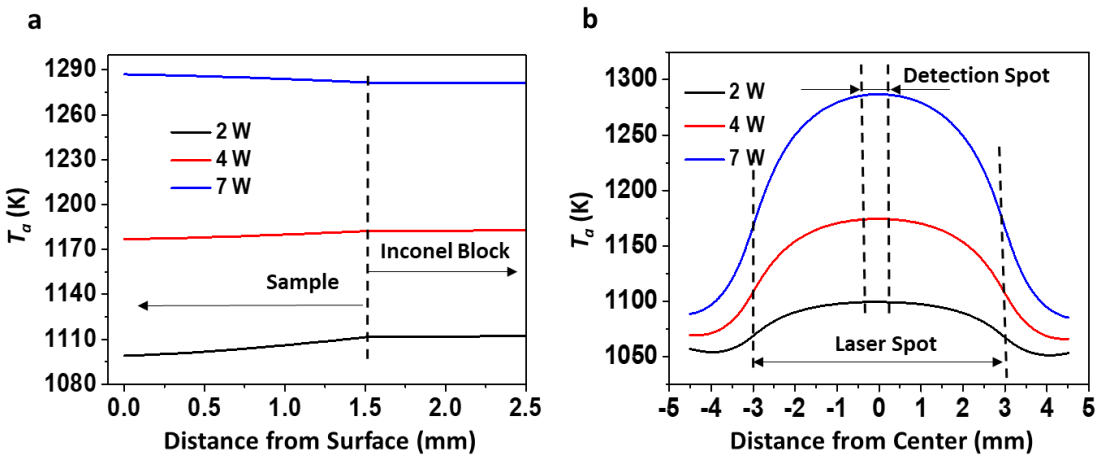

Figure 2-6. Temperature distribution in the sample with different laser power from 2 W to 7 W. (a) Temperature distribution within the sample in the thickness direction. (b) Temperature distribution along the radial direction on the sample surface.

2.2.3. Data reduction and sensitivity analysis

(a) Measurement of bulk materials

According to the Equation 2-5, we can obtain e_s from the slope (m_s) of the $|\theta_s|$ *vs* $\omega^{-\frac{1}{2}}$ plot, i.e.:

$$m_s = \frac{d|\theta_s|}{d\omega^{-1/2}} \tag{2-8}$$

Since m_s is only proportional to e_s^{-1} for the same q_s, we can obtain the thermal effusivity of an unknown sample by comparing it to a known reference sample without measuring the heat flux and calibrating the surface temperature. This reduces the measurement uncertainty if the reference sample is well-known [33], because there is no need to measure the laser power and spot size separately. In this case, the thermal effusivity of the unknown sample could be obtained by:

$$e_s = \frac{m_{ref}}{m_s} e_{ref} \tag{2-9}$$

where e_s and e_{ref} are denoted as the thermal effusivities of the unknown sample and the reference sample respectively; m_s and m_{ref} are the slope of $|\theta_s|$ *vs* $\omega^{-1/2}$

curves for the unknown sample and the reference sample, respectively. We also separately measured the thermal diffusivities α_{ref} of Pyroceram 9606 from 297K to 973K using a laser flash analyzer (NETSCH LFA 467) as shown in Figure 2-7a, which showed very close results compared to Refs. [67,68]. We used the specific heat data c from Refs. [67,68]. The thermal effusivity of Pyroceram 9606 can be obtained by $e_{ref} = \sqrt{\alpha_{ref}(\rho c)^2}$ as shown in Figure 2-7b. The measured e_{ref} will be used as the reference value for other samples.

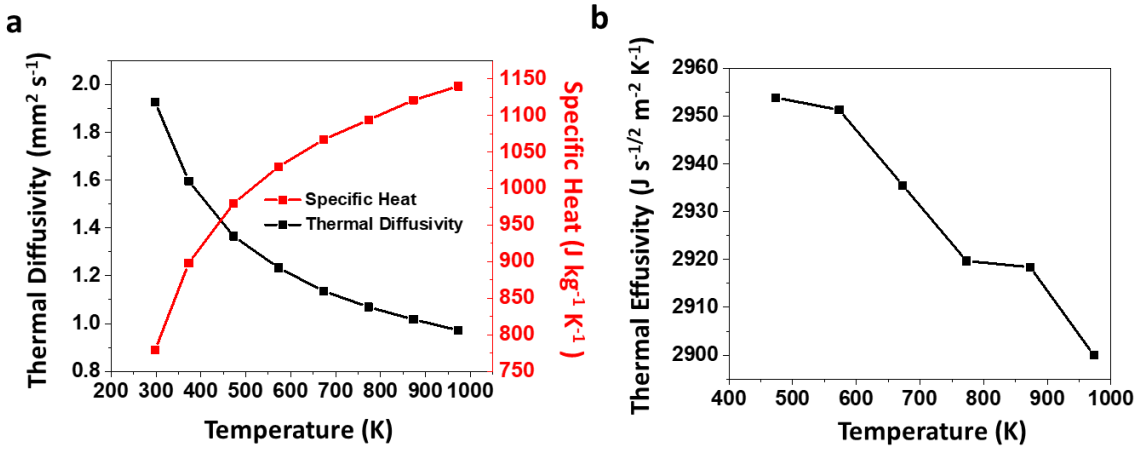

Figure 2-7. Thermophysical properties of Pyroceram 9606. (a) Thermal effusivity measured using LFA and specific heat quoted from Ref. [72]. (b) Thermal effusivity of Pyroceram 9606 calculated from the thermal diffusivities and specific heats.

(b) Measurement of soar-absorbing coatings

We demonstrate the high temperature MPR measurement of coatings by measuring the solar-absorbing coatings, including Pyromark 1200, Pyromark 2500, and black spinel oxide ($Cu_{0.5}Cr_{1.1}Mn_{1.4}O_4$), all of which are suitable for high temperature CSP. Both the Pyromark 1200 and Pyromark 2500 (Tempil Co., USA) are state-of-the art solar-absorbing coatings for commercial CSP solar towers. They are silicone-based paints with high solar absorptance and good stability at high temperature in air. The $Cu_{0.5}Cr_{1.1}Mn_{1.4}O_4$ coating is made from black spinel oxide nanopowder, as reported by

the authors previously[23]. We prepared Pyromark and black spinel oxide coatings following the same procedures reported in Refs.[23,73]. Briefly, the Pyromark/black spinel oxide paints were dissolved in a mixture of organic solvents (xylene, toluene and isobutanol) and a resin (SILIKOPHEN), and were then spray-coated onto different substrates with controlled thickness. Subsequently, all the samples were annealed in a furnace up to 600 ℃ for curing. All the chemicals are procured from commercial providers, as reported in Ref. [23]. Different from the bulk material measurements, we sweep the modulation frequency from 1 to > 1000 Hz and fit the thermal response curve with Equation 2-4 to directly obtain both e_f and D_f. Since D_f is related to the thermal diffusivity by $D_f = \frac{l_f}{\sqrt{\alpha_f}}$, α_f can be obtained with the knowledge of the coating thickness l_f. Subsequently, the e_f and α_f will be used to calculate the thermal conductivity and volumetric heat capacity of the coatings. It is noted that in this measurement, the absolute value of the surface temperature oscillation $|\theta_s|$ is used, which requires addition calibration using a high-temperature pyrometer since the output of the MCT detector is voltage. Figure 2-8a shows the signal of the MCT detector for a 53 μm thick Pyromark 1200 coating on an 8YSZ at a baseline sample surface temperature of 200 ºC, within the frequency range from 1 Hz to 300 Hz. However, we only measure the surface temperature oscillation up to 20 Hz using the pyrometer because the signal measured by the pyrometer is distorted at higher frequency. The emittance of the coating is set at 0.9 for the pyrometer based on the measurement results on the optical properties of the coatings reported by us before[74,75]. We chose the frequency range from 1 to 12 Hz to calibrate the MCT as shown in Figure 2-8b the V_{IR} and $|\theta_s|$ at the same frequency are

plotted at the same dot. The calibration equation is thus obtained as follows with the R^2 for the linear fitting greater than 0.995:

$$|\theta_s| = 13.099 V_{IR} + 2.1179 \tag{2-10}$$

where V_{IR} is in the unit of mV.

We then extrapolate the calibration curve from 12 Hz to 300 Hz for the signal of the MCT detector using the calibration equation above and obtain the $|\theta_s|$ from 1 to 300 Hz as shown in Figure 2-8c.

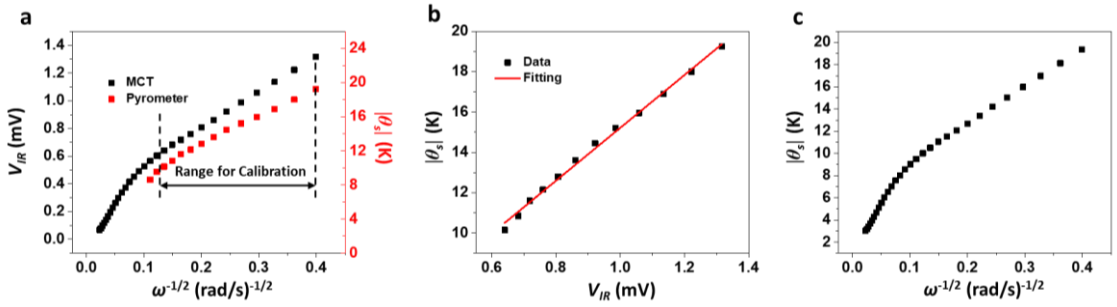

Figure 2-8. Calibration of the MCT detector using a pyrometer for 53 μm thick Pyromark 1200 on an 8YSZ substrate at 200 oC. (a) Signals from the MCT and pyrometer. The output from the MCT is voltage (shown on the left *y* axis) while that for the pyrometer is temperature (shown on the right *y* axis). The MCT detector sweeps the frequency from 1 Hz to 300 Hz while the pyrometer only scans up to 12 Hz due the limited of the response time. (b) Calibration curve shown as V_{IR} vs $|\theta_s|$. (c) $|\theta_s|$ from 1 to 300 Hz by calibrating the signal from the MCT detector using the calibration equation (**Equation 2-10**).

To further confirm the accuracy of our measurement, we also validate the fitting results for thermal conductivity using the intercept in the low frequency limit (Equation 2-5) as to be discussed in chapter 2.3.3. In addition, in frequency-domain measurement, the phase signal was widely used to extract the thermal properties because the calibration process was waived. However, in our measurements, we measure both the bulk and coating materials. In bulk materials under the 1-D planar heat source heat transfer assumption, the phase lag is always 45° and thus we cannot extract the thermal properties

of the bulk materials. In the coating measurements, we can also extract the thermal properties of the coatings using the phase signal, using Equation 2-4, i.e., $\frac{Im(\theta_s)}{Re(\theta_s)}$ instead of $|\theta_s|$. While this is not applicable to bulk materials, we compared the thermal conductivities of coatings measured by the phase and amplitude signals to confirm the accuracy our measurement based on the amplitude of thermal response as to be discussed in chapter 2.3.3.

(c) Sensitivity analysis

Figure 2-9 shows the sensitivity analysis, simulated for the MPR measurement on a 40 μm thick Pyromark 1200 coating on a SS304 substrate, with the following simulation parameters: e_f = 900 J $s^{-1/2}$ m^{-2} K^{-1}, a_f = 0.3 mm^2 s^{-1}, and e_s = 8703 J $s^{-1/2}$ m^{-2} K^{-1}. As shown in Figure 2-9a, the thermal response can be delineated into three regions, i.e., i) the substrate-dominated region in the low frequency range with $L_p > 100$ μm, where the thermal response is dominated by the properties of the substrate, indicated by the small slope; ii) the transitional region in the intermedium frequency range with 40 μm $< L_p <$ 100 μm, where the thermal response is sensitive to both the substrate and the coating its slope changes rapidly; and iii) the coating-dominated region in the high frequency limit with $L_p <$ 40 μm, where the thermal response is dominated by the properties of the coating, as indicated by the large slope. The phase of the thermal response as shown in Figure 2-9b deviates from 45° at the low frequency due to the existence of the coating but converges to 45° at high frequency, where the penetration depth is much smaller than the coating thickness and the heat transfer model is reduced to that in a homogeneous material (i.e., the coating). Figure 2-9c displays the sensitivity of

the amplitude of thermal response to e_f, α_f and e_s, respectively. The sensitivity of $|\theta_s|$ is defined as:

$$S_\theta = \frac{\Delta|\theta_s| / |\theta_s|}{\Delta\gamma/\gamma} \tag{2-11}$$

where $|\theta_s|$ is the amplitude of surface temperature oscillation, γ is the thermal property, which can be e_f, α_f or e_s. For example, the sensitivity on e_f of 1 means that 1% change in e_f leads to 1% change in $|\theta_s|$. Figure 2-9d shows the sensitivity of the slope m of the $|\theta_s|$ *vs* $\omega^{-\frac{1}{2}}$ curve to e_f, α_f and e_s, respectively. The sensitivity of m is defined as:

$$S_m = \frac{\Delta m/\mathrm{m}}{\Delta\gamma/\gamma} \tag{2-12}$$

As expected, Figures 2-9c and 2-9d show that both the $|\theta_s|$ and m are sensitive to e_s in the low frequency limit (long thermal penetration depth) and to e_f in the high frequency limit (short thermal penetration depth), while they are most sensitive to α_f within the transitional frequency range, because α_f directly dictates the thermal penetration depth.

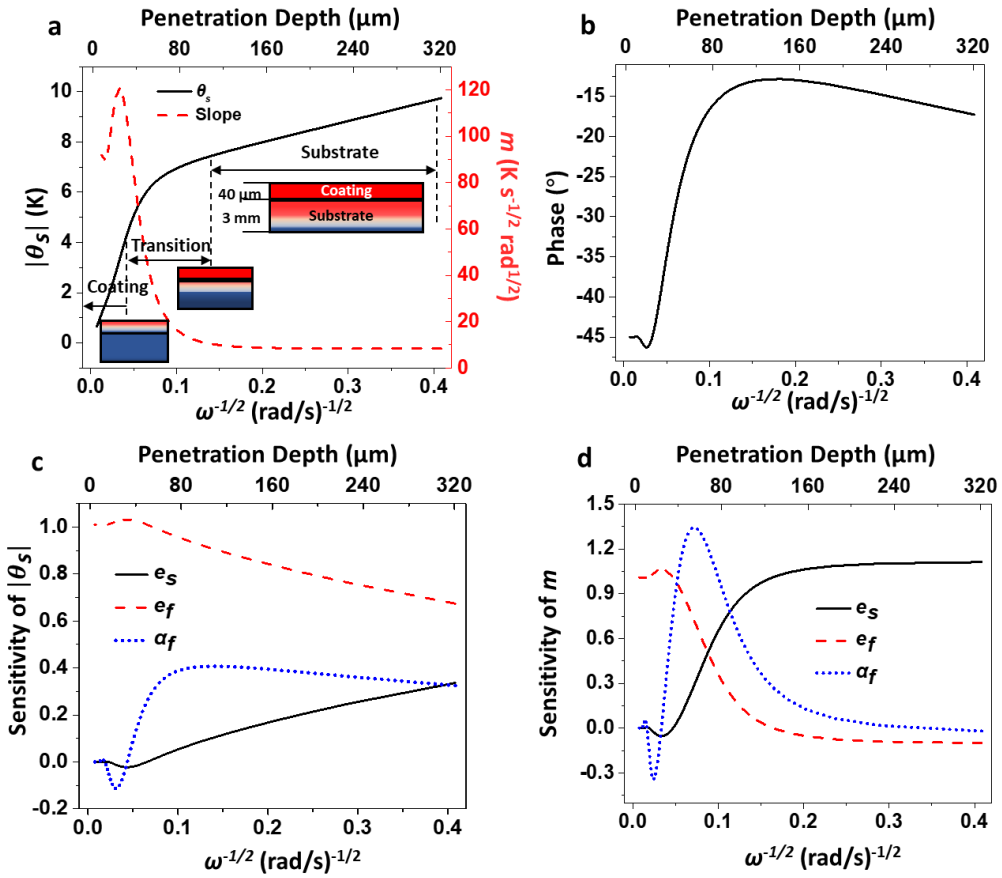

Figure 2-9. Simulation of the thermal response and the sensitivity analysis for a 40 μm Pyromark 1200 coating on a SS304 semi-infinite substrate. (a) $|\theta_s|$ (left y-axis) and slope m of the $|\theta_s|$ *vs* $\omega^{-1/2}$ curve (right y-axis) as a function of $\omega^{-1/2}$ (bottom *x*-axis), and the corresponding thermal penetration depth in the coating ($L_p = \sqrt{2\alpha_f/\omega}$, top *x*-axis)). (b) Phase of thermal response. (c) Sensitivity of $|\theta_s|$ on e_f, α_f and e_s. (d) Sensitivity of m on e_f, α_f and e_s.

2.3. Results and Discussions

2.3.1. Systematic error of MPR measurements

This section presents the analysis of systematic error of the MPR measurement. Typical measurement uncertainty of MPR is found to be ~ 10%, validating that the MPR technique is a feasible alternative for high temperature measurement and for samples with rough surface. The measurement uncertainty

including both the systematic and random error which is the standard deviation of repeated tests to be discussed in section.

(a) Systematic error of measurement of bulk materials

Thermal effusivity of bulk materials are measured by comparing the slope m of thermal response curve $|\theta_s|$ *vs* $\omega^{-1/2}$ to a reference sample as shown in Equation 2-9. In this study, we used Pyroceram 9606 as the reference sample because its thermal properties were well-known with a small scattering in literature values of < 3% [67,68]. Although the emissive power from the sample surface is intrinsically non-linear to $|\theta_s|$, it can be assumed linear within a narrow range of $|\theta_s|$, i.e., amplitude of the surface temperature rise due to the AC laser heating. Since the output voltage V_{IR} of the IR detector is proportional to the received emissive power, it can be expressed as:

$$V_{IR} \propto 4\varepsilon\sigma T_o^3 |\theta_s| \tag{2-13}$$

where ε is the thermal emittance of sample surface, σ is the Stefan-Boltzmann constant. Therefore, instead of comparing the slopes of the $|\theta_s|$ *vs* $\omega^{-1/2}$ curves, we can directly compare the slopes of the V_{IR} *vs* $\omega^{-1/2}$ curves without doing the calibration for the IR detector, namely,

$$e_s = \frac{\tilde{m}_{ref}}{\tilde{m}_s} e_{ref} \tag{2-14}$$

where $\tilde{m}$ is the slope of V_{IR} *vs* $\omega^{-\frac{1}{2}}$ curve (as opposed to m, the slope of $|\theta_s|$ *vs* $\omega^{-\frac{1}{2}}$ in Equation 2-8). By comparing the $\tilde{m}$ between the unknown sample and the reference sample, we can obtain e_s without calibrating the IR detector or knowing $|\theta_s|$. The systematic measurement error therefore depends on the measurement accuracy of MCT (~ 3% due to the fluctuation of the ambient temperature and instrumentation noise) and the accuracy of the e_{ref} for the reference Pyroceram 9606 sample (~ 3%) [67,68]. Since both

the $\widetilde{m}_{ref}$ and $\widetilde{m}_s$ are linear to the MCT signal, their uncertainties are also estimated to be ~ 3%. The systematic measurement error of bulk materials using MPR is calculated to be ~ 5.8% by the error propagation shown in Equation 2-15. To obtain the overall measurement uncertainty, the random error also needs to be considered, which will be discussed in chapter 2.3.2.

$$\frac{\Delta e_s}{e_s} = \sqrt{2\left(\frac{\Delta \widetilde{m}}{\widetilde{m}}\right)^2 + \left(\frac{\Delta e_{ref}}{e_{ref}}\right)^2} \tag{2-15}$$

(b) Systematic error of measurement of coatings

The thermal effusivity and thermal diffusivity of coating are obtained by fitting the thermal response curve $|\theta_s|$ *vs* $\omega^{-\frac{1}{2}}$ from 1 Hz to 2 kHz using the least mean square method where the coefficient of determination, or R^2, was maximized. Different from the measurements of bulk materials, both the absolute value of the temperature and the laser heat flux are used for the data fitting. Therefore, the MCT detector was calibrated using a pyrometer in advance. The pyrometer could respond to the temperature oscillation below 20 Hz without waveform distortion; while at higher frequency (e.g., > 100 Hz), the signal would be distorted due to the long response time of the pyrometer. Therefore, $\theta_{s,exp}$ at high frequency was obtained by extrapolating the calibration curve obtained from 1 – 12 Hz. The calibration procedure is shown in detail in the Figure 2-8.

At the low frequency limit, the thermal conductivity of the coating can also be obtained from Equation 2-5 using the intercept, where the measurement uncertainty is given by:

$$\frac{\Delta k_f}{k_f} = \sqrt{\left(\frac{\Delta q_s}{q_s}\right)^2 + \left(\frac{\Delta l_f}{l_f}\right)^2 + \left(\frac{\Delta b}{b}\right)^2} \tag{2-16}$$

where $b = \frac{q_s l_f}{k_f}$ is the *y*-intercept of the $\theta_s \; vs. \omega^{-1/2}$ plot according to Equation 2-5. To obtain the thermal properties of the coating (e_f and α_f), the thickness of coating and the laser flux were measured separately, which contributed to the measurement uncertainty. Although the laser power could be accurately measured with an integrating sphere, it is much more difficult to measure the exact laser spot size accurately, leading to a large uncertainty in the laser heat flux [33]. Since the laser flux is proportional to the thermal effusivity of the reference sample, the uncertainty of laser heat flux is also 3%, the same as the measurement for bulk materials. The uncertainty of the coating thickness is 4.4% due to the porous and non-uniform nature of the coating introduced from the spray-coating process. The uncertainty of *b* is related to the error of θ_s introduced by the linear regression as follows:

$$\Delta b^2 = \frac{S_{\theta_s}^2}{N} \frac{1}{1 - \frac{1(\sum x_i)^2}{N \sum x_i^2}} \tag{2-17}$$

where *N* is the number of frequency points in a single measurement and $x_i = \sqrt{\frac{1}{\omega_i}}$.

The uncertainty of $b = \frac{q_s l_f}{k_f}$ is estimated from three specific measurements: (a) 39 μm Pyromark 1200 on Pyroceram at 473 K (b) 39 μm Pyromark 1200 on Pyroceram at 973 K and (c) 37 μm Spinel oxide on SS304 at 473 K as shown in Figure 2-10 below (only the linear regions at the low frequency are shown). The raw data in the linear range are shown in Table 2-2. There are 12 data points for each measurement (i.e., *N* = 12). The S_{θ_s} is the uncertainty of the linear regression for θ_s calculated as follows:

$$\Delta\theta_s = \sqrt{\frac{\sum\left(\theta_{s,i} - \widehat{\theta_{s,i}}\right)^2}{n-2}} \tag{2-18}$$

where $\theta_{s,i}$ the measured magnitude of temperature at a certain frequency and $\widehat{\theta_{s,i}}$ the expected magnitude of temperature at a certain frequency by the linear regression. The linear regression for the three measurements in Table 2-2 are:

$$\theta_{s,\#1} = \frac{28.615}{\sqrt{\omega}} + 6.4009 \tag{2-19}$$

$$\theta_{s,\#2} = \frac{28.935}{\sqrt{\omega}} + 6.8557$$

$$\theta_{s,\#3} = \frac{7.0016}{\sqrt{\omega}} + 5.002$$

The calculated S_{θ_s} are shown in Table 2-2. The uncertainties of b are then calculated to be ≤ 1% for all the three measurements due to the high linearity. Therefore, the uncertainty of b is estimated to be 1% for all the other measurements. The systematic error of the thermal conductivity measurement for the coating is calculated to be 5.4% from Equation 2-16. At the high frequency limit where the penetration depth is much smaller than the coating thickness, the thermal response is the same as that for a bulk material with the coating properties, and the systematic error of thermal effusivity measurement of coating is 5.8%.

Table 2-2. Raw data for the estimation of uncertainty of thermal conductivity of coatings

#3 37 μm Spinel oxide on SS304 at 473 K			#2 39 μm Pyromark 1200 on Pyroceram at 973 K			#1 39 μm Pyromark 1200 on Pyroceram at 473K			
$\widehat{\theta_{s,i}}(K)$	$\theta_{s,i}\ (K)$	$x_i = \frac{1}{\sqrt{\omega_i}}\ (rad\ s^{-1})^{-\frac{1}{2}}$	$\widehat{\theta_{s,i}}(K)$	$\theta_{s,i}\ (K)$	$x_i = \frac{1}{\sqrt{\omega_i}}\ (rad\ s^{-1})^{-\frac{1}{2}}$	$\widehat{\theta_{s,i}}(K)$	$\theta_{s,i}\ (K)$	$x_i = \frac{1}{\sqrt{\omega_i}}\ (rad\ s^{-1})^{-\frac{1}{2}}$	
7.795234268	7.779371	0.398942	18.39909	18.28066	0.398942	17.71663	17.68084	0.398942	1
7.499829573	7.490331	0.356751	17.31794	17.28606	0.361577	16.64743	16.61581	0.361577	2
7.235666053	7.241398	0.319022	16.33804	16.35552	0.327712	15.67837	15.6727	0.327712	3
6.999439735	7.010121	0.285283	15.44992	15.50165	0.297018	14.80008	14.82328	0.297018	4
6.788196058	6.799106	0.255113	14.64499	14.71857	0.269199	14.00404	14.04619	0.269199	5
6.599292925	6.602703	0.228133	13.91544	13.98693	0.243986	13.28256	13.30263	0.243986	6
6.43036766	6.447827	0.204006	13.25422	13.32235	0.221134	12.62866	12.66992	0.221134	7
6.279307468	6.28369	0.182431	12.65493	12.70253	0.200423	12.036	12.07276	0.200423	8
6.144222974	6.14538	0.163137	12.11178	12.13894	0.181651	11.49885	11.50613	0.181651	9
6.023424649	6.03029	0.145884	11.61949	11.61339	0.164638	11.01201	11.01528	0.164638	10
5.915401612	5.901027	0.130456	11.17331	11.10694	0.149218	10.57076	10.53987	0.149218	11
5.818802798	5.797596	0.116659	10.76892	10.63478	0.135242	10.17085	10.09968	0.135242	12
		0.012839			0.076571			0.03764	(K)
		0.000109			0.00483			0.001167	(K)
		5.002			6.8559			6.3009	Intercept (K)
		0.20%			1.00%			0.54%	x100%

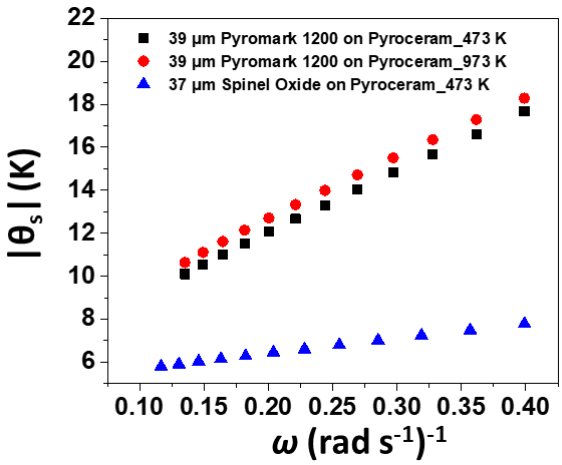

Figure 2-10. Samples for the estimation of uncertainty of thermal conductivity of coatings.

2.3.2. Measurement of bulk materials

In this section, we validate the MPR measurement on bulk materials using different known materials with a wide range of thermal conductivities (e.g., borosilicate glass with k of 1 ~ 2 W m^{-1} K^{-1} and SS304 with k of 17 ~ 30 W m^{-1} K^{-1}.) We used the Pyroceram 9606 as the reference sample to measure the thermal effusivities of other samples because of the consistent results reported in the literature [67,68]. It is noted that all the bulk materials are coated with a black coating, however, only data at the low frequency (i.e., at long thermal penetration depth) are shown. Figure 2-11a shows the thermal response of Pyroceram 9606 at 473 K. According to Equation 2-5, the laser flux q_S can be directly obtained from the slope of the curve with the knowledge of the thermal effusivity for Pyroceram 9606, e_s = 2953.9 J s$^{-1/2}$ m^{-2} K^{-1} at 473 K, which is 82800 W m^{-2}. Figure 2-11b shows the repeatability of MPR measurement on Pyroceram 9606 for five tests. We spray-coated the Pyroceram 9606 with a 39 μm thick Pyromark 1200 for the first four measurements and an 18 μm thick black spinel oxide coating in the fifth measurement. Both coatings have similar absorptance at the laser wavelength and in the

IR spectral range [23]. The same sample is unloaded and then loaded again between consecutive measurements, and thus the random error includes the possible minor changes in the position of the sample, position of the laser spot, and the view factor from the heated sample surface to the IR detector. For substrates with different coatings, the subsequent coating was made on the same substrate after removing the previous one. It demonstrates that the slopes for all the five measurements are consistent at the same temperature, indicating the same thermal diffusivity of the Pyroceram 9606 substrates (Equation 2-5). On the other hand, the intercepts at the *y* axis for the first four measurements are higher than that for the fifth measurement at the same temperature because of the larger coating thickness and the associated thermal resistance. Table 2-3 shows that the random error of the MPR measurement for bulk materials, determined from the standard deviation of multiple measurements as shown in Figure 2-12, is less than 3% at representative temperatures of 473 K, 673 K, and 973 K.

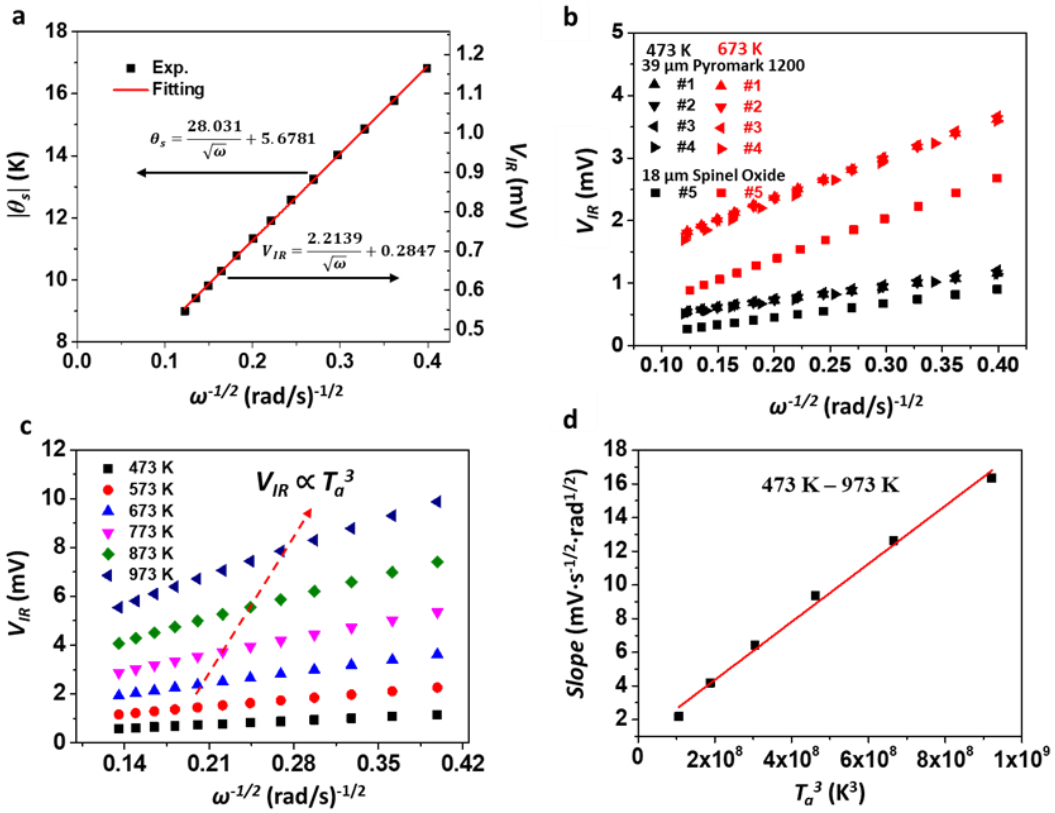

Figure 2-11. Validation of MPR measurement of bulk materials. (a) Measurement of laser heat flux using Pyroceram 9606 at 473 K as a reference sample. (b) Repeatability of MPR measurement and effect of coating materials. All the measurements were done on Pyroceram 9606 substrates. (c) IR detection signal of MPR measurement on a Pyroceram 9606 sample for sample surface baseline temperature (T_o) ranging from 473 K to 973 K. (d) Slope $\tilde{m}$ of V_{IR} vs $\omega^{-1/2}$ as a function of T_o^3, following Equation 2-13.

Table.2-3. MPR Random error of Pyroceram 9606 with different coatings

T_O (K)	Slope $\tilde{m}$ (mV rad$^{1/2}$ s$^{-1/2}$)						Avg.	Std.	Random Error (%)
	39 μm Pyromark 1200				18 μm Black Spinel Oxide				
	#1	#2	#3	#4	#5	#6			
473	2.17	2.21	2.32	2.29	2.28	-	2.26	0.0622	2.76
673	6.41	6.52	6.69	6.55	6.54	-	6.54	0.0997	1.52
973	16.35	-	-	-	16.21	15.48	16.01	0.4645	2.90

To estimate the measurement uncertainty, both the random (< 3%) and systematic errors (5.8% for thermal effusivity of bulk materials and 7.9% for thermal conductivity of

coating) should be considered. The total measurement uncertainty of thermal effusivity of bulk materials is thus 6.5% and that of thermal conductivity of coatings is 8.5%. The error bars shown in the figures in following sections represent the measurement uncertainty including both the systematic and random errors.

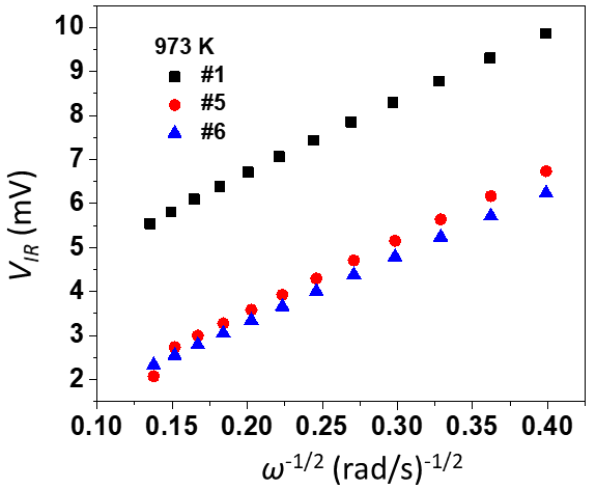

Figure 2-12. Repeatability of MPR Measurement on Pyroceram 9606 at 973 K.

Another fact worth noting in Figure 2-11b is that the slope at T_o = 673 K is higher than that at 473 K because of the increasing emissive power at higher temperature. As shown in Figure 2-11c, the signal increases monotonically with increasing sample temperature from 473 K to 973 K as T_o increases from 473 K to 973 K. This is an intrinsic advantage of the photothermal radiometry where IR detection signal increases with T_o^3 (Equation 2-13), as shown in Figure 2-11d. Raw data for other bulk materials measured in this work are shown in Figure 2-13 which also shows an increasing signal with increasing sample temperature. Figure 2-13 displays the thermal responses for the 8YSZ, SS304, spinel oxide ($(Co_{0.6}Cr_{0.6}Fe_{0.6}Mn_{0.6}Ni_{0.6})O_4$) and borosilicate glass, whose thermal physical properties are well-known. We measured borosilicate up to 773 K, which is limited by the phase change temperature of the glass.

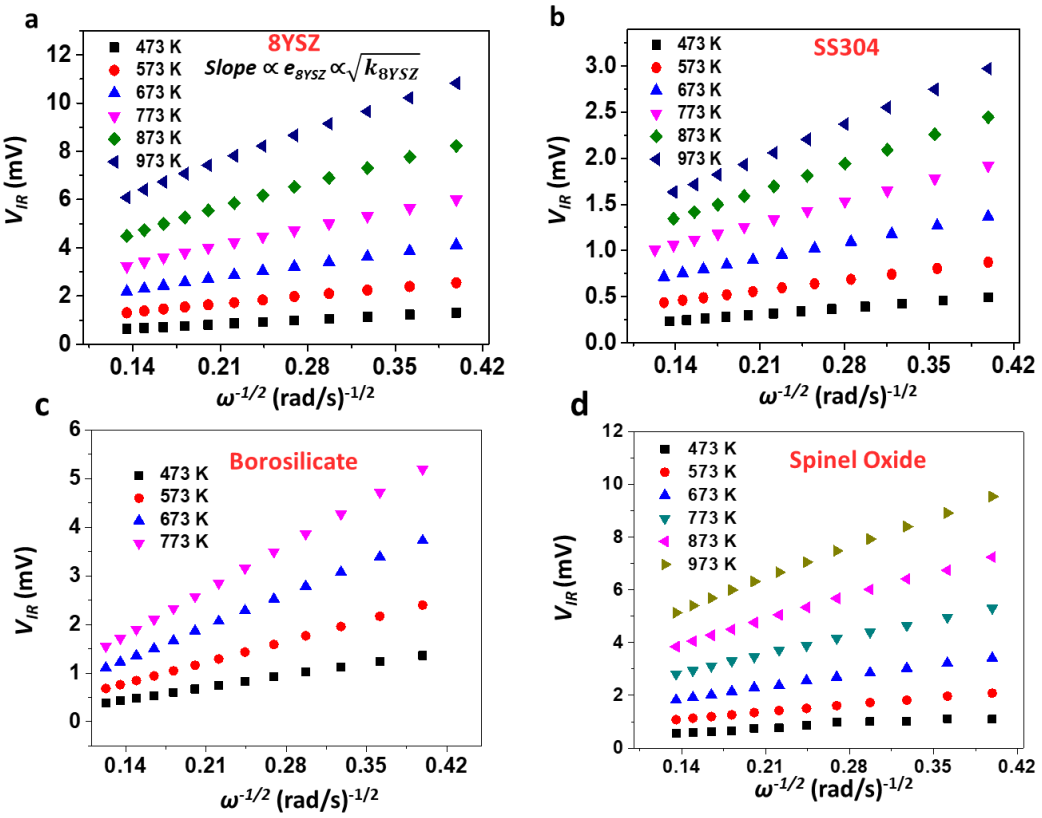

Figure 2-13. Thermal responses of bulk materials. (a) 8YSZ. (b) Stainless steel 304. (c) Borosilicate glass and (d) Spinel oxide $(Co_{0.6}Cr_{0.6}Fe_{0.6}Mn_{0.6}Ni_{0.6})O_4$.

The spinel oxide was made by us and its thermal conductivity was measured using a laser flash analyzer (Netzsch LFA 467) as benchmark as shown in Figure 2-14. We calculate the specific heat of $(Co_{0.6}Cr_{0.6}Fe_{0.6}Mn_{0.6}Ni_{0.6})O_4$ based on the weight-averaged specific heats of its constituents (i.e., simple metal oxides such as MnO_2) . The measured diffusivity and calculated specific heat are shown in Figure 2-14a and the effusivity and thermal conductivity related to the diffusivity and specific heat is shown in Figure 2-14b.

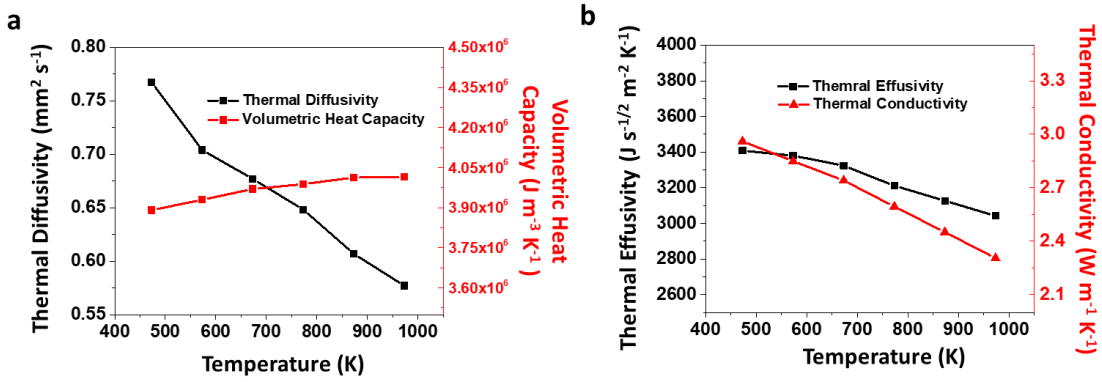

Figure 2-14. Thermophysical properties of spinel oxide (Co0.6Cr0.6Fe0.6Mn0.6Ni0.6) O4. (a) Measured thermal diffusivity using LFA and calculated volumetric heat capacity based on the composition. (b) Calculated thermal effusivity and thermal conductivity according to the thermal diffusivity and heat capacity.

Table 2-4 shows the slope and the measured thermal effusivity for all the materials. It is noted that the heat flux for the measurement of borosilicate glass is reduced by half (i.e., ½ q_s) to avoid the larger temperature oscillation $|\theta_s|$. If the $|\theta_s|$ is too large, the thermal emission signal received by the IR-detector may not be linear to the $|\theta_s|$ due to the non-linear nature of radiation. we only change the heat flux for the borosilicate glass sample while keeping the same q_s for other materials. Figure 2-15 compares the MPR measurement results of bulk materials to the reference values. We measured materials with well-established literature values: borosilicate glass [65,66], Pyroceram 9606 [67,68], 8YSZ [69], and SS304 [70]. The measured materials cover a wide range of thermal effusivity (1800 to 11000 J $s^{-1/2}$ m^{-2} K^{-1}) and thermal conductivity (1.3 to 25 W m^{-1} K^{-1}). We also measured a spinel oxide bulk pellet ($Co_{0.6}Cr_{0.6}Fe_{0.6}Mn_{0.6}Ni_{0.6})O_4$. The spinel oxide powders were prepared by hydrothermal nanoparticle synthesis used by the authors previously [73] and then hot-pressed into a bulk pellet with over 95% relative density. Figure 2-15a compares the measured thermal effusivities to the literature or known values. The thermal effusivity is converted to thermal conductivity using the known

specific heat and density values obtained from the literature [65-70] for glass, SS304, 8YSZ as shown in Figure 2-15b. For the spinel oxide, the reference thermal effusivity and thermal conductivity were obtained from thermal diffusivity measurement using the laser flash analyzer and the theoretically estimated specific heat as shown in Figure 2-14. Figure 2-15c and 2-15d show that the experimental results for both the thermal effusivity and thermal conductivity of the bulk materials are within 10% deviation from the reference values, which confirms the validity of the MPR technique for high temperature measurement.

Table 2-4. Summary of MPR measurement results for bulk materials

T_a (K)	Slope ($mV \cdot rad^{1/2} \cdot s^{-1/2}$)					Thermal Effusivity ($J \cdot s^{-1/2} \cdot m^{-2} \cdot K^{-1}$)				
	Pyroceram	8YSZ	SS304	Spinel	Borosilicate	Pyroceram	8YSZ	SS304	Spinel	Borosilicate
473	2.17	2.56	0.62	2.27	1.39	2953.9	2503.0	8703.3	3088.3	1887.9
573	4.18	4.76	1.13	4.52	2.79	2951.3	2591.8	9607.8	3191.3	1971.1
673	6.41	7.30	1.60	6.79	4.40	2935.5	2578.7	10318	3109.3	2014.4
773	9.37	10.44	2.37	9.29	6.65	2919.7	2620.9	10342	2895.1	2072.4
873	12.62	14.12	3.00	12.40	-	2918.4	2610.3	10974	2869.1	-
973	16.35	17.84	3.87	16.10	-	2900.0	2657.8	11221	2856.2	-

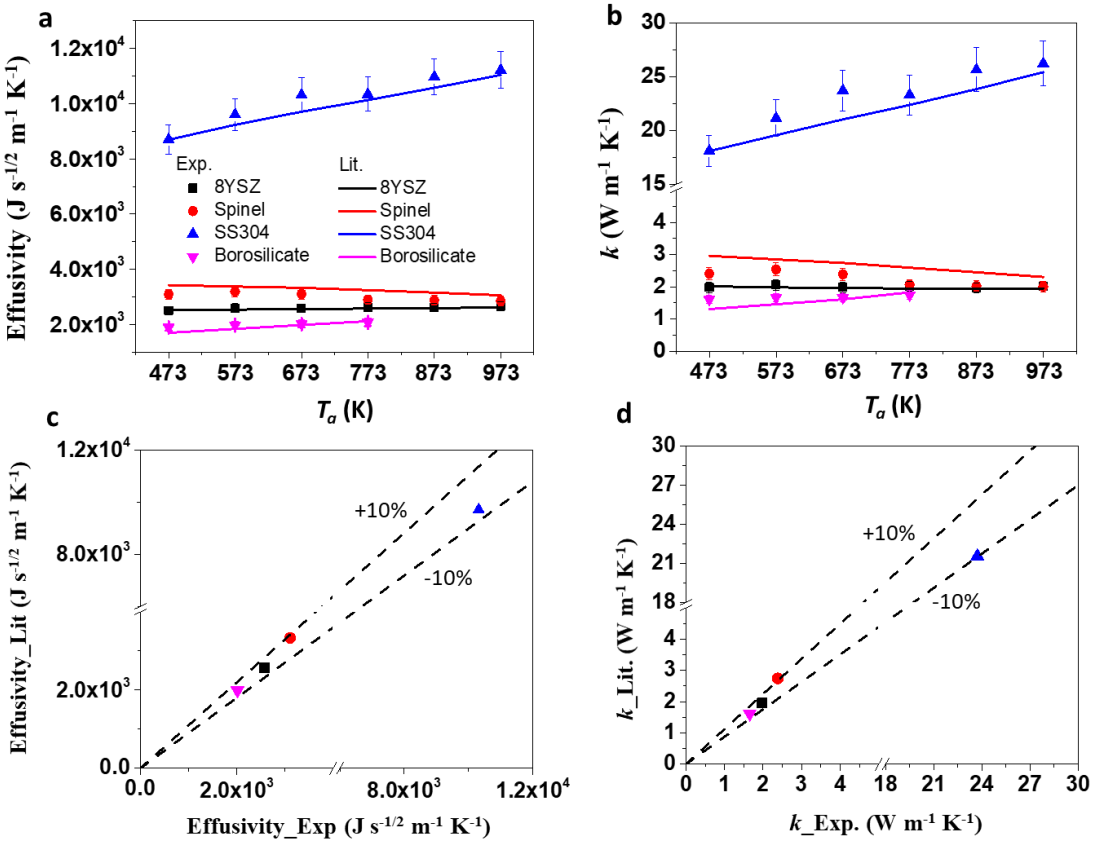

Figure 2-15. Validation of high temperature MPR measurement of bulk materials. (a) Measured thermal effusivity of different bulk materials up to 973 K. (b) Extracted thermal conductivity of different bulk materials up to 973 K by relating to the thermal effusivity using the ρc values. (c) Comparison of the measured thermal effusivity to that from literatures or known values at $T_0 = 673\ K$. (d) Comparison of the measured thermal conductivity to that from literatures or known values at $T_0 = 673\ K$.

2.3.3. Measurement of solar-absorbing coatings

Figure 2-16 shows the MPR measurement on a 53 μm thick Pyromark 1200 coating sprayed on an 8YSZ substrate. Figure 2-16a displays the surface profile of the Pyromark 1200 coating measured using a DektakXT stylus profilometer. The thickness of the coatings was also measured using the profilometer. The surface roughness of the coating is measured to be ~ 3 μm due to the porous nature and the build-up of the paint at the edge of coating during the spray-coating process. However, during the MPR

measurement, the laser spot (~ 6 mm diameter) is focused at the center of the sample and thus the uncertainty of the coating thickness is less than 3 μm. Figure 2-16b depicts the thermal response of the coating on the 8YSZ substrate at different temperatures. Notably, the slope of the curve is smaller in the low frequency range where the signal is dominated by the thermal properties of the 8YSZ substrate. We can extract the thermal properties of the substrate using this range of frequency as shown in chapter 2.3.2. In the high frequency range where the penetration depth is much smaller than the coating thickness, the thermal response is dominated by the properties of the Pyromark 1200 coating. The slope is larger in this range of frequency, indicating a lower thermal effusivity of Pyromark 1200 compared to that of 8YSZ. The transitional penetration depth, where the slope changes rapidly, is about ~ 60 μm, which is close to the thickness of the coating. The transitional frequency is therefore dependent on the thermal diffusivity of the coating. Therefore, we can also obtain the thermal effusivity and diffusivity of the coating by fitting the entire $|\theta_s|$ vs $\omega^{-1/2}$ curves according to Equation 2-4 using the least mean square algorithm, with the information of the surface heat flux (q_s = 82800 W m^{-2}) and the thermal effusivity of the substrates obtained from Section 2.3.2.

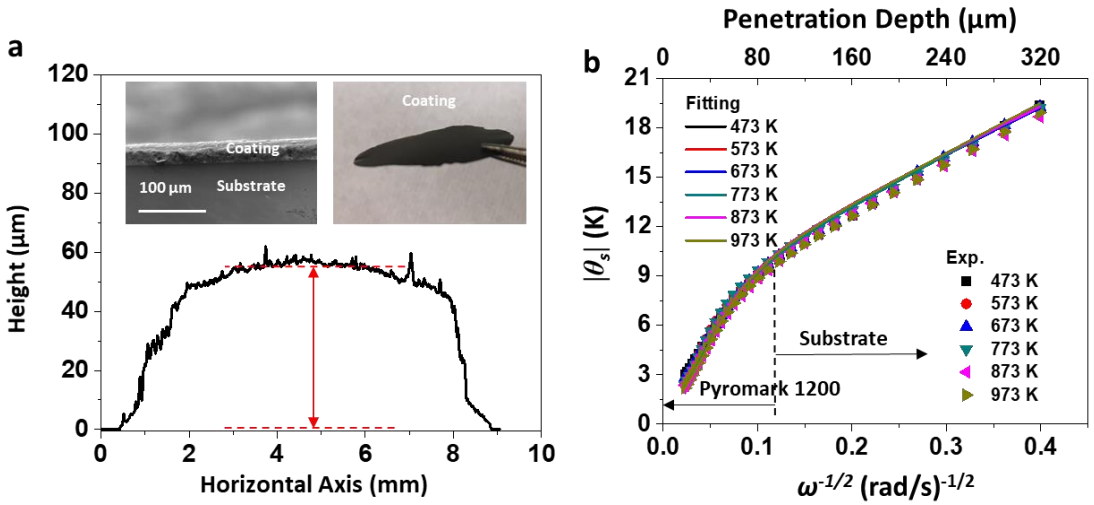

Figure 2-16. MPR measurement of Pyromark 1200 coating on an 8YSZ substrate. (a) Typical surface profile of Pyromark 1200 coating with a surface roughness of ~ 3 μm. The left inset shows the cross-sectional SEM image of the coating and the right inset shows a photograph of the coating after peeled off from the substrate. (b) Thermal response of 53 μm Pyromark 1200 thin-film coating on an 8YSZ substrate from 473 K to 973 K. The penetration depth in the top x -axis is estimated based on the typical thermal diffusivity value of the coating ($\alpha_f = 0.3\ mm^2 s^{-1}$).

Table 2-5 shows the obtained thermal effusivity e_f and thermal diffusivity α_f of the Pyromark 1200 coating. The R^2 values of fitting the experimental thermal response to Equation 2-4 are greater than 0.99 for all the temperatures. The thermal conductivity k_f and the volumetric heat capacity $\rho_f c_f$ of the Pyromark 1200 can be calculated by from the e_f and α_f. The extracted thermal conductivity of Pyromark 1200 and black spinel oxide coating is relatively low, 0.4 ~ 0.6 W m^{-1} K^{-1} at 300 K, which can be attributed to the high porosity of the coating. The coatings are mainly composed of silica-resin and spinel oxide, whose thermal conductivities are both in the range of 1 ~ 3 W m^{-1} K^{-1} (Figure 2-14 and Figure 2-15b). Therefore, the coating is believed to be porous.

Table 2-5. Summary of measurement results for 53 μm Pyromark 1200 on 8YSZ substrate.

T_o (K)	e_f (J s$^{-1/2}$ m^{-2} K^{-1})	D_f (s$^{1/2}$)	α_f (mm^2 s^{-1})	R^2	k_f (W m^{-1} K^{-1})	$\rho_f c_f$ (kJ m^{-3} K^{-1})
473	785.1	0.0787	0.453	0.9980	0.528	1166.5
573	797.6	0.0858	0.381	0.9987	0.492	1292.2
673	865.5	0.0909	0.340	0.9996	0.505	1484.3
773	862.2	0.0995	0.284	0.9999	0.459	1617.9
873	861.5	0.0991	0.287	0.9999	0.462	1608.1
973	872.0	0.1041	0.259	0.9995	0.444	1713.4

To prove the porous nature of the coating, we measured the density of Pyromark 1200 coatings by two methods:

- In the first method (measurement #1), we sprayed the Pyromark 1200 onto a Si substrate and measure the weight gain of the substrate by a balance and thickness of coating using Dektak surface profiler. The area of coating is measured using a ruler. The density can thus be calculated.
- In the second method (measurement #2 and #3), we sprayed the Pyromark 1200 onto a CaF_2 coating. Due to the large difference in the coefficient of thermal expansion (CTE), the Pyromark 1200 detached from the CaF_2 substrate after curing as shown in Figure 2-17a and 2-17b. The thickness of coating was measured using a micrometer. The mass of coating was measured using a balance.

As shown in Table 2-6, from both methods, The density of Pyromark 1200 is as low as ~ 1000 kg·m^{-3}, which is much lower than that of it major composition elements, e.g., silica-resin ~ 2300 kg·m^{-3} and spinel materials 5000 ~ 7000 kg·m^{-3}. This indicates that Pyromark 1200 coating is porous. This is also evidenced from the SEM images reported in Ref.[74], also shown in Figure 2-17c and 2-17d. It is noted that we followed the same process as in Ref. [74] to prepare the coatings.

Table 2-6. Density of Pyromark 1200 Coating

Test	Mass [g]	Thickness [μm]	Area [mm^2]	Density [$kg \cdot m^{-3}$]
#1	0.103	43	1967	1218
#2	0.012	24	456	1096
#3	0.0051	13	340	1154

The measured density of Pyromark 1200 coating is less than 1250 kg m^{-3}, which is considerably lower than that of silica resin (~2300 kg m^{-3}) and spinel oxide (5000 ~ 7000 kg m^{-3}). Besides, the volumetric heat capacity of Pyromark 1200 is measured to be ranging from 1166 to 1713 kJ m^{-3} K^{-1}, which is lower than the common values for most fully dense solids (~ 3000 kJ m^{-3} K^{-1}), further confirming that the coating is highly porous. The porosity nature of the coatings is also consistent with earlier microstructure characterizations on similar coatings made by the authors [23,73]. The volumetric heat capacity for the Pyromark 1200 increases as temperature increases from 473 K to 973 K, which agrees with the trend for glass [65,76] and spinel oxide.

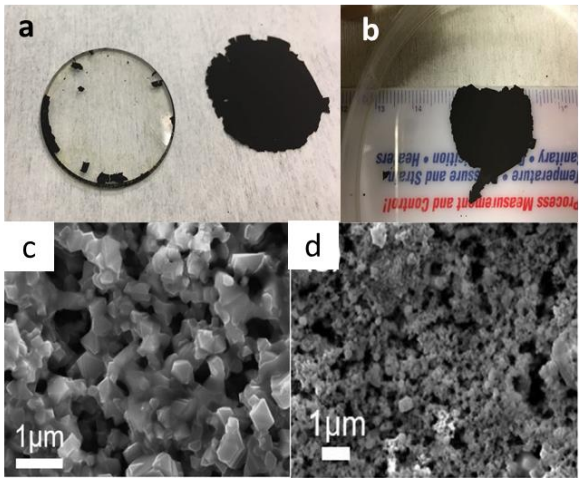

Figure 2-17. Photo and SEM images of Pyromark coating. (a) Photograph of Pyromark coating detached from a CaF_2 substrate. (b) SEM images of Pyromark coating, taken from Ref. [74].

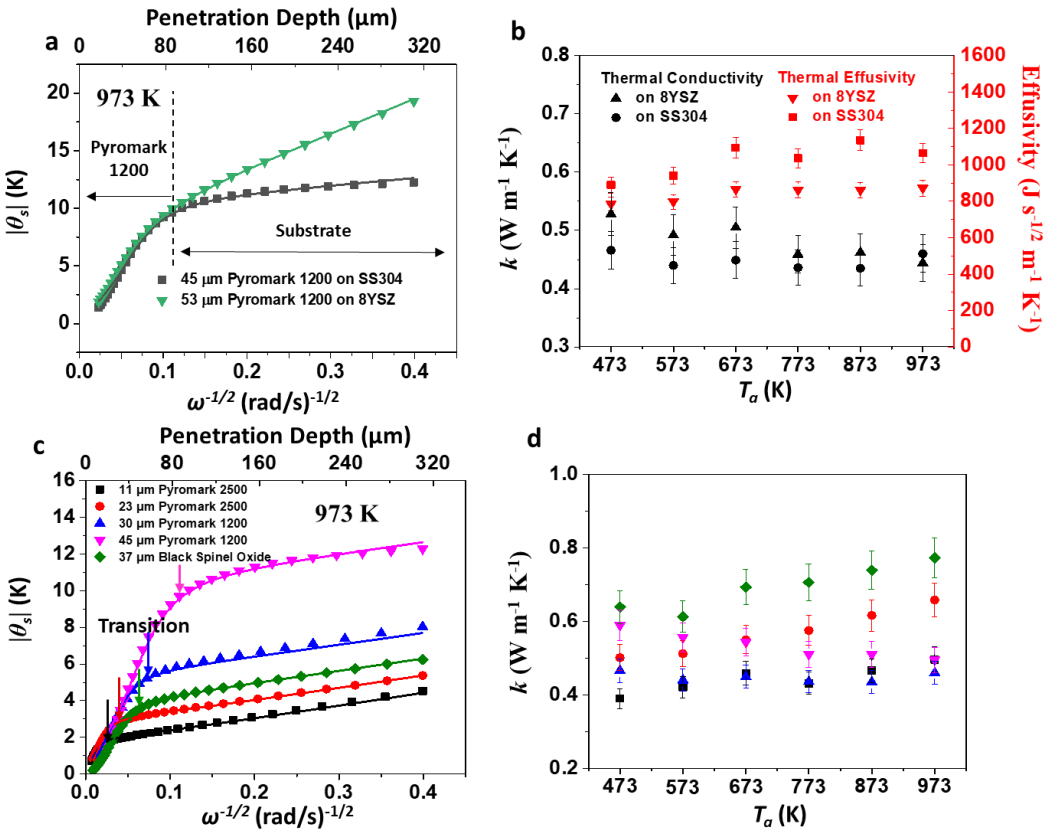

Figure 2-18. Measurement of different solar-absorbing coatings with various coating materials, thicknesses and substrate materials. (a) Effect of substrate materials on the thermal response of the coating measured at T_o = 973 K. (b) Extracted thermal conductivity (left *y*-axis) and thermal effusivity (right *y*-axis) of Pyromark 1200 coated on 8YSZ and SS304 substrates from 473 K to 973 K. (c) Thermal responses of different solar-absorbing coatings with variable thickness spray-coated on SS304 substrates measured at $T_o = 973$ K. (d) Thermal conductivity of different solar-absorbing coatings spray coated on SS304 substrates, measured from 473 K to 973 K.

Figure 2-18 shows the MPR measurements of different solar-absorbing coatings, with variation in the coating materials, substrate materials and coating thickness. Figure 2-18a compares the thermal responses of Pyromark 1200 with similar coating thickness but on different substrates at 973 K, i.e., 53 μm thick coating sprayed on 8YSZ and 45 μm thick coating sprayed on SS304. The thermal response curves for other temperatures (from 473 K to 973 K) can be found in Figure 2-19 below. It is apparent that the transitional region is more distinguishable when using SS304 as the substrate due to the

larger contrast in the thermal effusivities between the coating and the substrate, leading to a higher sensitivity to thermal diffusivity of the coating. Figure 2-18b shows the extracted thermal conductivity and thermal diffusivity of Pyromark 1200 from 473 K to 973 K, by fitting the experimental data using Equation 2-4. Thermal conductivities of Pyromark 1200 measured from the two different substrates (SS304 and 8YSZ) are close, ranging from 0.4 to 0.6 W m^{-1} K^{-1} within the temperature range of 473 K to 973 K. The discrepancy may come from the difference in the thermal expansion coefficients for the two substrates which could lead to microstructural changes, such as cracking in the coating during curing [21-23]. Nevertheless, the deviation of the measured results is still within 15% between the two samples. Figure 2-18c shows the thermal responses of coatings with different thicknesses on SS304 substrates at 973 K. The thermal response curves for other temperatures (from 473 K to 973 K) can be found in Figure 2-19 below. All the curves show similar slopes in the low frequency range because they all have SS304 as the substrate. However, due to the different coating thickness, the transitional frequency or penetration depth, where the slope starts to change, varies for different samples. The transitional penetration depth increases with the coating thickness, e.g., ~ 80 μm for the 45 μm Pyromark 1200 and ~ 50 μm for the 30 μm Pyromark 1200. It is noted that all the curves converge in the high frequency range which is dominated by the properties of the coatings, indicating similar thermal conductivities of these coatings. As shown in Figure 2-18d, thermal conductivities for the Pyromark 1200 and Pyromark 2500 are determined to range from 0.4 to 0.6 W m^{-1} K^{-1} in the temperature range from 473 K to 973 K. The thermal conductivity for the black spinel oxide coating is slightly higher, ranging from 0.6 to 0.8 W m^{-1} K^{-1} in the same temperature range, and it is also much

lower than that the dense pellet made of a similar spinel oxide material (2-2.5 $W\,m^{-1}\,K^{-1}$, Figure 2-15b), due to the porous structure of the coating.

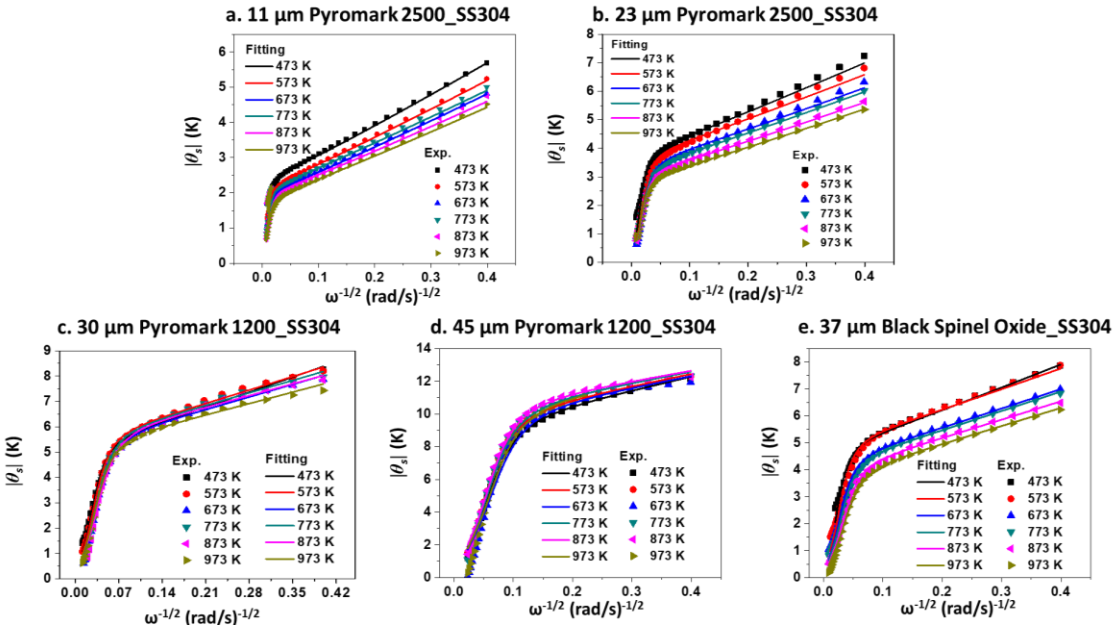

Figure 2-19. Thermal responses of different solar-absorbing coatings sprayed on SS304 substrates from 473 K to 973 K, as a supplementary to Figure 8 in the manuscript. (a) 11 µm Pyromark 2500. (b) 23 µm Pyromark 2500. (c) 30 µm Pyromark 1200. (d) 45 µm Pyromark 1200. (e) 37 µm black spinel oxide.

In this work, we fit both the thermal conductivity and volumetric heat capacity of the coating using the amplitude of the thermal response, based on the two-layer heat transfer model (Equation 2-4). In the meantime, we can also obtain the thermal conductivity using the equation in the low frequency range (Equation 2-5), in which thermal conductivity of the coating can be obtained from the intercept of the linear curve at low frequency. We compare the thermal conductivity obtained by the two different methods for the 23 µm Pyromark 2500 on SS304 as shown in Table 2-7. It is seen that the difference of fitted results is only ~ 10%, indicating that both methods give similar results. However, to obtain both the volumetric heat capacity and thermal conductivity at the same time, we use Equation 2-4 in the fitting.

Table 2-7. Comparison of fitting results for coatings using two-layer model for the entire frequency range and intercept at low frequency

T_a (K)	Extracted *k* using Equation 2-4 (W m^{-1} K^{-1})	Extracted *k* using Equation 2-5 (W m^{-1} K^{-1})	Difference (%)
473	0.501	0.547	-8.4
573	0.512	0.571	-10.3
673	0.550	0.617	-10.9
773	0.575	0.616	-6.7
873	0.616	0.660	-6.7
973	0.658	0.687	-4.2

The phase fitting is also widely used for the frequency-domain measurements. However, in our measurements, we measure both the bulk and coating materials. In bulk materials under the 1-D planar heat source heat transfer assumption, the phase lag is always 45° and thus we cannot extract the thermal properties of the bulk materials. In the coating measurements, we can also extract the thermal properties of the coatings using the phase signal, using Equation 2-4. As shown in the Figure 2-20 below, we demonstrate the measurement of thermal properties of the 20 μm thick Pyromark 1200 coated on SS304 at 573 K. The fitted thermal conductivity is 0.627 W m^{-1} K^{-1} which is close to that measured by the amplitude signal shown in Table 2-7.

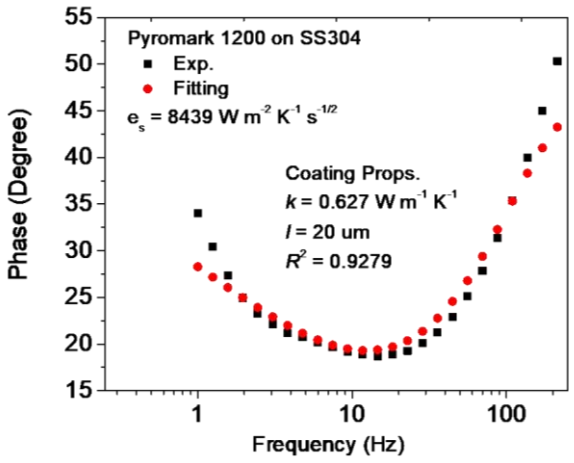

Figure 2-20. Fitting of phase for thermal conductivity of 20 μm thick Pyromark 1200 coated on SS304.

The low thermal conductivity of the solar-absorbing coatings indicates a possibly considerable temperature drop within the coating under high solar flux. For example, the temperature drop is estimated to be ~ 60 K for a 30 μm thick coating under the heat flux of 1000-sun. Figure 2-21 shows the schematic of a solar receiver tube for high-temperature CSP where a thin solar-absorbing coating (20 ~ 30 μm[77,78]) was applied on the external surface for solar absorption. Highly concentrated solar flux of 1000-sun is applied to yield 1000 K to achieve desirable thermal efficiency[79]. Under such a high solar flux, there is a considerable temperature drop within the coating. The temperature drop within a 30 μm thick Pyromark 2500 is as high as ~ 60 K assuming 1D steady state heat transfer:

$$\Delta T = \frac{l q_s}{k} \tag{2-20}$$

where q_s is surface heat flux, l is thickness and k is thermal conductivity. This is comparable to that within 2 mm thick tube wall. Therefore, it is imperative to take the thermal resistance of the solar-absorbing coating into account when designing the high temperature CSP receivers.

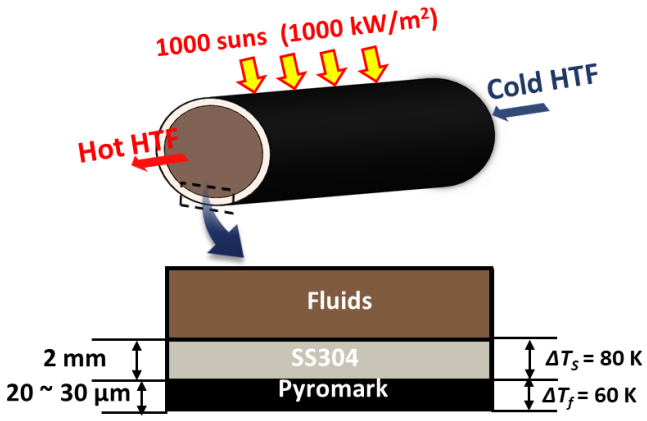

Figure 2-21. Estimation of temperature drop within solar-absorbing coating and tube under 1000 suns for high-temperature CSP receiver.

2.4. Conclusions

In this chapter, we develop a general high-temperature MPR setup to measure coating materials up to 973 K. The MPR takes the advantage of facile sample preparation on rough surfaces and high sensitivity at high temperatures due to the increasing emissive power. The designed sample holder can ensure the temperature uniformity for high temperature measurement within the infrared detection spot along the lateral direction and the thermal penetration depth of the measurements at high temperatures. The MPR setup is validated with the measurement on bulk materials with thermal conductivities ranging from 1 to 30 W m^{-1} K^{-1} from 473 to 973 K, with the maximum deviation of measured thermal conductivities from the literature or reference values less than 10%. Several types of solar-absorbing coatings are also measured, including Pyromark 1200, Pyromark 2500 and black spinel oxide coatings, with variation in the coating thickness of (10 ~ 50 μm) and substrate materials. Both the thermal effusivity and thermal diffusivity of the coatings are obtained to yield the thermal conductivity and volumetric heat capacity. We find that the thermal conductivity of Pyromark 1200 and Pyromark 2500

ranges from 0.4 to 0.6 W m^{-1} K^{-1} and that for the black spinel oxide coating is ranged from 0.6 to 0.8 W m^{-1} K^{-1}, within the temperature window of 473 K to 973 K. The measurement results indicate that it is necessary to consider the thermal resistance of the solar-absorbing coating in the design of CSP solar receivers, because the temperature drop within the coating can be significant. The MPR methodology demonstrated in this work may provide an attractive and convenient thermal conductivity diagnostic tool at high temperature on samples that are otherwise challenging to measure using other techniques, for example, specimens with surface roughness and/or small thickness down to ~10 μm. This technique sets the foundation for the measurements of flowing fluid and moving particle bed as shown in later chapters, which are of significance for the design and diagnostic of heat exchangers [79,80], nuclear reactors [81,82], thermal energy storage systems [83], and many other thermal systems.

Chapter 2, in full, is a reprint of the materials as it appears in 'Measurement of High-temperature Thermophysical Properties of Bulk and Coatings Using Modulated Photothermal Radiometry' *International Journal of Heat and Mass Transfer*, (170) 2021, 120989 by Jian Zeng, Ka Man Chung, Qingyang Wang, Xiaoxin Wang, Yu Pei, Peiwen Li and Renkun Chen. The dissertation author was the primary investigator and first author of this paper.

3. Chapter 3: *In-situ* thermal conductivity measurement of flowing fluid

3.1. Introduction

Measurement of thermal conductivity of fluids is important for the design of heat exchangers [79,80], nuclear reactors [81,82], thermal energy storage systems [83], and many other thermal systems. The ability of *in-situ* thermal conductivity measurement of flowing fluids could be useful for the operational safety and diagnosis of these systems [84,85]. Despite a multitude of techniques available for the thermal conductivity measurement of stagnant fluids, including the transient hot-wire (THW) method [86,87], steady-state method [88-90], laser flash analysis (LFA) [91,92], 3ω technique[84,93,94], and time or frequency domain thermo-reflectance techniques (TDTR/FDTR)[95], there are still challenges of applying these techniques for *in-situ* diagnostics, especially under the harsh environment (such as high temperature and/or with corrosive fluids). Hong *et al.* applied the 3ω technique for the thermal conductivity measurement of flowing water and ethanol where a thin metallic transducer layer in contact with the fluid serves as both the heater and the thermometer. They obtained the thermal conductivity of fluids at low flow velocity [93]. The 3ω technique was also used for the measurement of thermal properties of flowing gases [90,96]. Based on the similar principle, thermal conductivity of flowing fluids has been measured using the TDTR method[97]. Despite the successful implementation of the *in-situ* 3ω and TDTR measurements on common fluids, where dedicated metallic transducers are needed, it is still challenging to extend them for *in-situ* measurements under challenging conditions, such as at high temperature and for corrosive fluids (e.g., molten salts for nuclear reactors [98] and concentrated solar power (CSP) [99]). For example, to avoid the

corrosion by molten salts to the metallic transducer in the 3ω method, a thin protective coating (e.g., alumina) has to be applied, which not only requires time-consuming microfabrication, but also poses question on the long-term durability[100]. Therefore, a suitable technique for the *in-situ* thermal conductivity measurement of flowing fluids under harsh environment would be desirable.

Photothermal radiometry (PTR) using either modulated (continuous wave) or pulsed laser is a well-known non-contact thermal characterization tool for bulk and coating materials [37,57,101]. In the modulated photothermal radiometry (MPR), a sample is heated by an intensity-modulated laser to probe into different depths of the sample and its surface temperature response is measured with an infrared (IR) detector [37,38]. We have previously established the MPR technique for high-temperature measurements of bulk and thin coating samples, by using a refractory black coating for laser absorption and IR surface thermometry[101]. In this work, we applied the MPR technique for *in-situ* thermal conductivity measurement of flowing fluids within a pipe. By modulating the frequency of the laser and controlling the thermal penetration depth ($L_p = \sqrt{\frac{2\alpha}{\omega}}$ where α is thermal diffusivity of fluid and ω is the angular frequency) beyond the wall thickness of the tube and within the momentum/thermal boundary layer of the fluid, we could get high sensitivity of the surface temperature response to the thermal conductivity of the fluid while avoiding the convection effect within a certain range of flow velocity, thus obtaining the intrinsic thermal conductivity of the flowing fluid. We demonstrate the MPR measurement of flowing liquids (DI water, ethanol, Dowtherm A oil and Xcertherm 600 oil) in a pipe with flow velocity up to 550 mm s^{-1}. The Reynolds number (Re_D) is ranging from 0 to 13,000 at temperature from 30℃ to 170℃, thus covering the

stationary, laminar flow and turbulent flow regimes. Here Re_D is defined based on the pipe diameter D. At low flow velocity and low Re_D, the intrinsic thermal conductivity of fluid is obtained. At higher velocity, the forced convection effect becomes more prominent, and the obtained effective thermal conductivity is higher. This transition is found to relate to the dimensionless number $Re_D^{1/2}Pr^{1/3}$, where Pr is the Prandtl number. When $Re_D^{1/2}Pr^{1/3}$ is less than 100, we can obtain the intrinsic thermal conductivity of the flowing fluids. The MPR technique reported here can provide a facile *in-situ* thermal conductivity diagnostic tool for flowing fluids with broad applications. It may open an opportunity to simultaneously quantify both the thermal conductivity and local convective heat transfer coefficient in a fluid loop.

3.2. Modified MPR system for flowing fluid measurement

Figure 3-1a displays the schematic of the MPR system integrated with a flowing liquid loop. The MPR system is the same as what was reported in chapter 2 except that the test section is replaced with a circular tube connected to the fluid loop. A waveform-generator drove a continuous wave (CW) diode laser with its intensity modulated as sinusoidal function at the angular frequency of ω. The laser spot size was controlled to be around 10 mm in diameter and the laser beam was homogenized from Gaussian beam into a top-hat profile. Therefore, the heat flux is assumed to be uniform. The test section was heated up by the modulated laser flux, leading to the oscillation of the surface temperature rise θ_s of the sample at the same frequency (ω) as the heating laser. θ_s was measured based on the thermal emission from the surface collected by a HgCdTe (MCT) detector after proper calibration using a pyrometer. The IR-detection spot diameter is ~

0.5 mm and temperature is uniform within the detection point. The measurement was conducted after the fluid flow and temperature stabilized.

The schematic and photograph of the test section of the fluid flowing pipe are shown in Figures 3-1b and 3-1c, respectively. The wall thickness of the test section was set to be 100 μm to have high measurement sensitivity and accuracy as discussed in the later section. To ensure the mechanical strength of the setup, a 100 μm thick stainless steel 316 (SS316) sheet was wrapped into a round shape and welded onto two short tubes of 25.4 mm in outer diameter and 1 mm in wall thickness on both ends. The middle thin-walled section was ~10 cm long to minimize the edge effect due to the change in the wall thickness in this section. The laser spot was about 10 mm in diameter and was located at the center of the thin-walled region. The exterior surface of the tube was coated with a 30-μm-thick Pyromark 2500 black coating. During the MPR measurement, the laser beam irradiated the center of the middle thin-walled section. The tube was connected to the fluid loop with the fluid supplied by a pump from a liquid reservoir with heating capability (ZNCL Vevor 1584321637152051). Four types of fluids were measured: DI water, ethanol, Xceltherm 600 oil (Radco Industries Inc.), and Dowtherm A oil (Sigma Aldrich). Liquid was circulating at different flow velocities up to 550 mm s^{-1} driven by a mechanical pump (HD Portable oil transfer pump, Massive gears 3 phase, Goldenstream Pumps) with a VFD module (ABB ACS 150 Drive) to control the flow rate, which was also monitored using a flow rate meter. The pump has an operational temperature limit of ~200^{o}C, so our measurements were limited to 170^{o}C.

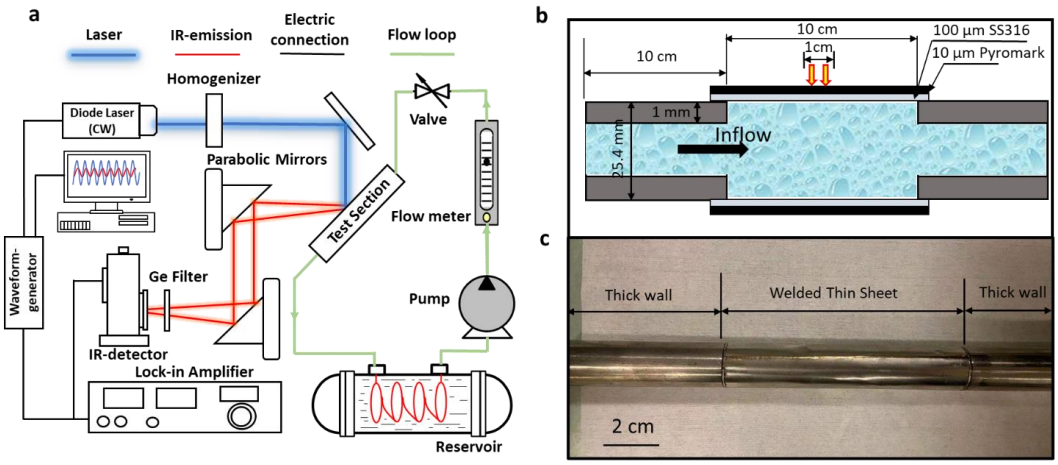

Figure 3-1. MPR system integrated with a flowing fluid loop. (a) Overview of the system. Schematic (b) and photograph (c) of the MPR measurement section of the pipe for the fluid flow.

Figure 3-2a shows the photo of the MPR setup integrated with the liquid loop. Figure 3-2b shows the MPR measurement section where laser irradiates the surface of the tube coated with a black coating, and the IR emission from the tube surface is collected by a pair of mirrors and focused to the MCT detector. Figure 3-2c and 3-2d show the photos of the tube.

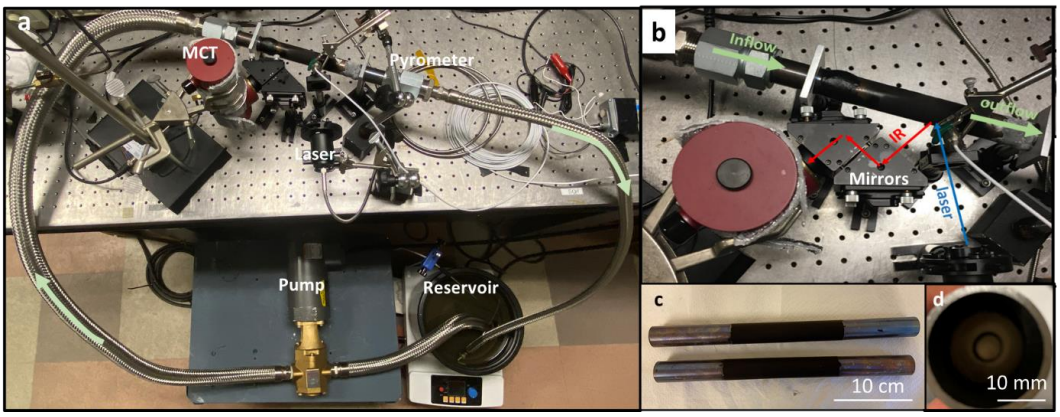

Figure 3-2. Photo of the MPR setup integrated with the flowing fluid loop. (a) Overview of the fluid loop. (b) Detail of the MPR section. (c) Photograph the tube. (d) Cross-sectional view of the tube.

3.3. Measurement principle and critical criteria.

Figure 3-3a shows the schematic of the MPR measurement of a flowing fluid inside a tube. The fluid is supplied from one end of the steel tube at a fixed bulk velocity u_b. An intensity-modulated laser at angular frequency of ω irradiates the surface of the middle thin-walled section. The surface temperature θ_s is oscillating at ω. The thermal penetration depth (L_p) can be adjusted by changing ω of the incident laser. The thermal emission from the tube surface is collected by an IR detector to measure the θ_s after calibration with a pyrometer as described in detail in chapter 2.3. Figure 3-3b shows the schematics of the momentum boundary layer Δ, thermal boundary layer δ and the thermal penetration depth L_p during the MPR measurement. Assuming laminar flow, the hydrodynamic entrance length L_{ef} and the thermal entrance length L_{eh} can be estimated by:

$$L_{ef} = 0.05 Re_D D, \tag{3-1}$$

and

$$L_{eh} = 0.033 Re_D Pr D, \tag{3-2}$$

where D is the diameter of the tube. In our measurement, Re_D is in the range of 100-13000 and Pr is in the range of 5-300. Therefore, L_{ef} and L_{eh} are in the range of 13-1650 cm and 42-5450 cm, respectively. The laser spot (~10 mm diameter) of the MPR measurement is located at middle of the 10-cm long thin-walled section. Therefore, the fluid flow is still in the hydrodynamic and thermal entrance region at the position of the MPR measurement. In this region, the thermal boundary layer (δ) is always thinner than the momentum boundary layer (Δ) as they are related by $\delta = Pr^{-1/3}\,\Delta$ and $Pr^{-1/3}$ is 0.15-0.58 for the fluids to be measured. To measure the intrinsic thermal conductivity of

a flowing fluid, the thermal penetration depth should be smaller than both the momentum boundary and thermal boundary layer thicknesses: $L_p < \min[\Delta, \delta]$. In our case, since δ is always smaller than Δ, $L_p < \delta$ should be satisfied.

As shown in Figure 3-3b, at high frequency, L_p is shorter than δ and thus the convection effect is minimized. In this case, the intrinsic thermal conductivity of the fluid can be obtained. On the contrary, at low frequency with $L_p > \delta$, the convection effect becomes prominent, leading to overestimation of the measured thermal conductivity of fluid. It is noted that δ depends on the flowing velocity and both the δ and L_p depend on the thermophysical properties of the fluid and the temperature, so the desirable frequency range to obtain the intrinsic thermal conductivity may change with the fluid properties, velocity, and temperature. In addition, L_p must be larger than the wall thickness of the tube (100 μm) such that the measurement is more sensitive to the fluid than the wall. Therefore, the frequency and L_p must fall within a suitable range. In general, L_p in the fluid is controlled to be around ~150 - ~300 μm in our experiments.

Although the measurement is conducted in a cylindrical tube, the 2-D heat transfer model based on the planar geometry can be applied (as justified later). Within the fluid, in the absence of heat generation or viscous dissipation and assuming constant thermal properties, the 2D heat transfer equation in the frequency domain for the flow in the entrance region is:

$$\frac{\partial^2 \theta_f}{\partial x^2} + \frac{\partial^2 \theta_f}{\partial y^2} = \frac{j\omega}{\alpha_f}\theta_f + \frac{\tilde{v}}{\alpha_f}\frac{\partial \theta_f}{\partial x}, \tag{3-3}$$

where *x* is the coordinate in the direction along the fluid flow and *y* is the direction perpendicular to the fluid flow as shown in Figure 3-3b. The position *y = 0* is defined at

the wall. θ_f is the temperature of the fluid, α_f is the thermal diffusivity of the fluid, j is the imaginary unit, $\tilde{v}$ is the velocity vector of flowing fluid and ω is the angular frequency. The velocity profile within the laminar boundary layer assuming a cubic polynomial is:

$$\tilde{v} = u_b\left(\frac{3}{2}\frac{y}{\Delta} - \frac{1}{2}\left(\frac{y}{\Delta}\right)^3\right), \tag{3-4}$$

where u_b is the bulk velocity. Within a short distance from the wall, the flow pattern can be assumed to be linear, which is valid when $L_p \ll \Delta$. As such, equation 4 is reduced to:

$$\tilde{v} = \frac{3u_b}{2\Delta} y\,. \tag{3-5}$$

Therefore, equation 3 becomes:

$$\frac{\partial^2\theta_f}{\partial x^2} + \frac{\partial^2\theta_f}{\partial y^2} = \frac{j\omega}{\alpha_f}\theta_f + \frac{3u_b y}{2\alpha_f\Delta}\frac{\partial\theta_f}{\partial x}\,. \tag{3-6}$$

Clearly, for $y \to 0$ (near the wall), Equation 3-6 is reduced to a pure heat conduction equation without the advection term. Therefore, the convection effect is only important when the temperature field reaches deep into the boundary layer, i.e., at the low frequency where L_p is large. By doing a dimensional analysis, it was found that the forced convection effect is negligible when the following condition is satisfied [93]:

$$\frac{u_b}{\omega} < L_c, \tag{3-7}$$

where L_c is the characteristic length scale of the fluid flow. For a fully developed flow, such as the one studied in Ref. [93], L_c is the radius of the flow channel. In our case studied here, the flow is still in the entrance region, so L_c should be the momentum boundary layer thickness Δ. If we take $L_c = \Delta$ and knowing $\Delta = 5\sqrt{\frac{\nu x}{u_b}}$ (for a laminar flow), equation 3-7 becomes:

$$u_b < \left(5\sqrt{vx}\omega\right)^{\frac{2}{3}} \tag{3-8}$$

where v is the kinematic viscosity of the fluid and x is the characteristic entrance length of the measurement section as shown in Figure 3-1b (x = 10 cm in our experiment).

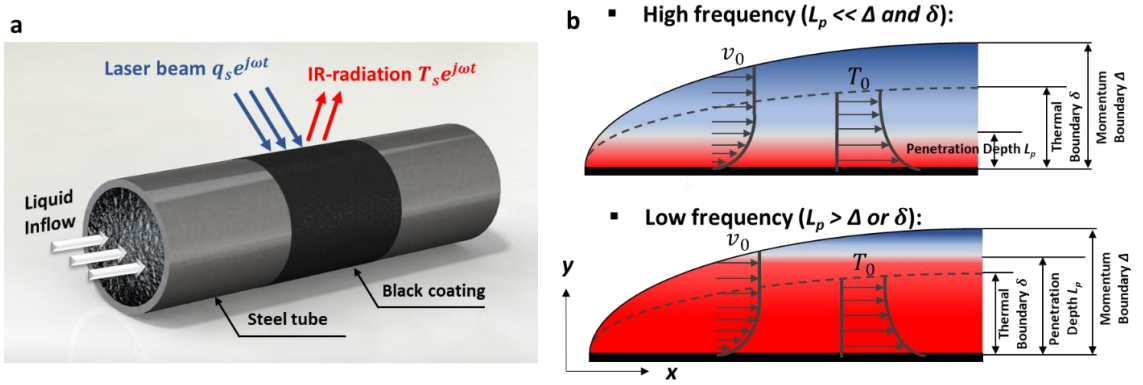

Figure 3-3. Schematic of MPR measurement on flowing fluid in a tube. (a) Schematic of the MPR measurement section. (b) Schematics of momentum boundary, thermal boundary and thermal penetration depth in the MPR measurement in a 2D model.

Figure 3-4a shows the critical velocity as a function of ω. The angular frequency is in the range of 3 – 12 rad s^{-1} (i.e., f = 0.5 – 2 Hz and L_p = 150 – 300 μm), and thus the critical velocity is ~ 70 mm s^{-1} to have the negligible forced convection effect. The critical velocity increases with increasing frequency because the penetration depth decreases with increasing frequency, and thus the effect of the momentum boundary layer diminishes.

The above analysis only examines the velocity and momentum equation. From the heat transfer point of view, $L_p < \delta$ also needs to be satisfied in order to measure the intrinsic thermal conductivity of the fluid, as discussed earlier. Here we set $L_p < 0.2\delta$:

$$\frac{L_p}{\delta} = \frac{\sqrt{\frac{\alpha_f}{\pi f}}}{5\sqrt{\frac{vx_1}{u_b}}Pr^{-1/3}} < 0.2, \tag{3-9}$$

where x_1 is the length of heater and is equal to the laser spot size, i.e., $x_1 = D_{laser}$. Rearranging equation 3-9 leads to:

$$Re_D^{1/2} Pr^{1/3} < \sqrt{\frac{DD_{laser}\pi f}{\alpha_f}}, \tag{3-10}$$

where D is the pipe diameter (25 mm), $Re_D = \frac{u_b D}{\nu}$, and $D_{laser} = 10\,mm$ in our experiment. Evaluating equation 3-10 at $f = 1$ Hz, we have $Re_D^{1/2} Pr^{1/3} < \sim 100$ as the condition to neglect the forced convection effect. On the other hand, when $Re_D^{1/2} Pr^{1/3} > \sim 100$, the forced convection effect becomes important, and the measured effective thermal conductivity is expected to be higher than the intrinsic thermal conductivity of the fluid. In our measurements, we vary the flow velocity u_b, laser modulation frequency f, and temperature (thus the viscosity) of the fluid to access both the intrinsic thermal conductivity (pure heat conduction) and forced convection regimes from the fluid flow (equation 3-8 and figure 3-4a) and the heat transfer (equation 3-10) points of view.

In addition, although the MPR measurement is conducted on a cylindrical tube, the heat transfer can be modeled based on the planar geometry under certain conditions. To specify these conditions, the thermal response of a cylindrical tube is compared to that of a flat plate. The surface temperature rise given by the heat transfer model for a cylindrical tube under the modulated laser heating is [102]:

$$\theta_{s,cyl}(r,\phi,\omega) = \frac{q_s}{2\pi k_s}\left(\begin{array}{c} \frac{2I_o(\sigma r)}{I_0'(\sigma D/2)}\sin\left(\frac{\theta_0}{2}\right) + \frac{I_1(\sigma r)}{I_1'(\sigma D/2)}(\theta_0 + \sin(\theta_0)) \times \cos\left(\frac{\pi}{2} - \phi\right) \\ +2\sum_{m=2}^{\infty} \frac{I_m(\sigma r)}{I_m'(\sigma D/2)} \times \cos\left[\frac{\mathrm{m}}{2}(\pi - 2\phi)\right] \times \left[\frac{\sin\left[\frac{(\mathrm{m}+1)\theta_0}{2}\right]}{m+1} + \frac{\sin\left[\frac{(\mathrm{m}+1)\theta_0}{2}\right]}{m-1}\right] \end{array}\right) \tag{3-11}$$

where k_s is the thermal conductivity of the solid tube, θ_0 is the center angle of the laser spot and is π/7.8 for a laser spot diameter (D_{laser} = 10 mm); ϕ is the angle of the

detection spot ($D_{IR} = 1\ mm$) relative to the horizontal position and is π/2 if the laser and IR-detector are well aligned. I_m is the m^{th} order modified Bessel function of the first kind and I'_m is the derivative of I_m. $\sigma = \sqrt{\frac{i\omega}{\alpha_s}}$, where α_s is the thermal diffusivity of steel tube.

The surface temperature rise of a planar plate under the modulated laser heating is:

$$\theta_{s,pl} = \frac{q_s e^{-\frac{\pi}{4}j}}{e_s\sqrt{\omega}} \tag{3-12}$$

where e_s is thermal effusivity of the plate. Figure 3-4b compares the thermal responses of a cylindrical tube and a plate using the thermal properties of steel in Table 3-1. To quantify the difference between the cylindrical and planar geometries, the ratio *R* of the $|\theta_s|$ of a cylindrical tube over that of a plate is also displayed in Figure 3-4b, where *R* is defined as:

$$R = \frac{\left|\theta_{s,cyl}\right|}{\left|\theta_{s,pl}\right|} \tag{3-13}$$

The figure shows that the maximum deviation between the two curves is 7% within the entire frequency range we will use in this experiment (0.5 to 2 Hz). Therefore, it is reasonable to use the simplified analysis based on the planar geometry. By neglecting the forced convection effect and temperature gradient in the *x* direction, and assuming the planar geometry, the frequency-domain heat transfer equation in the fluid domain (equation 3-6) can be further simplified as:

$$\frac{\partial^2\theta_f}{\partial y^2} = \frac{j\omega}{\alpha_f}\theta_f \tag{3-14}$$

Equation 3-14 is the same as the 1D heat conduction equation in a solid substrate. Therefore, the 1D heat conduction of the three-layered system (i.e., coating, steel containment and fluid, see Figure 3-3a) can be modeled as follows[101,103]:

$$\theta_s = -\frac{d}{c} q_s \tag{3-15}$$

where q_s is the AC component of the laser heat flux; $\theta_s = T_s - T_o$ is the temperature oscillation induced by the AC component of the heat flux, with T_s as the transient surface temperature and T_o as the baseline surface temperature due to the heating by the heaters and DC component of laser; *d* and *c* are obtained from the following transfer matrix:

$$M = \begin{pmatrix} a & b \\ c & d \end{pmatrix} = M_n M_{n-1} \cdots M_i \cdots M_1 \tag{3-16}$$

where M_i is the transfer matrix for the i^{th} layer, with i = 1, 2 and 3 referring to the coating, steel tube and fluid, respectively. The transfer matrix M_i is expressed as follows:

$$M_i = \begin{pmatrix} \cosh\left(D_i\sqrt{j\omega}\right) & -\frac{\sinh\left(D_i\sqrt{j\omega}\right)}{e_i\sqrt{j\omega}} \\ -e_i\sqrt{j\omega}\sinh\left(D_i\sqrt{j\omega}\right) & \cosh\left(D_i\sqrt{j\omega}\right) \end{pmatrix} \tag{3-17}$$

where $D_i = \frac{l_i}{\sqrt{\alpha_i}}$, l_i and α_i are the thickness and thermal diffusivity of the i^{th} layer, respectively. e_i is the thermal effusivity of the i^{th} layer, i.e., $e_i = \sqrt{(\rho c k)_i}$.

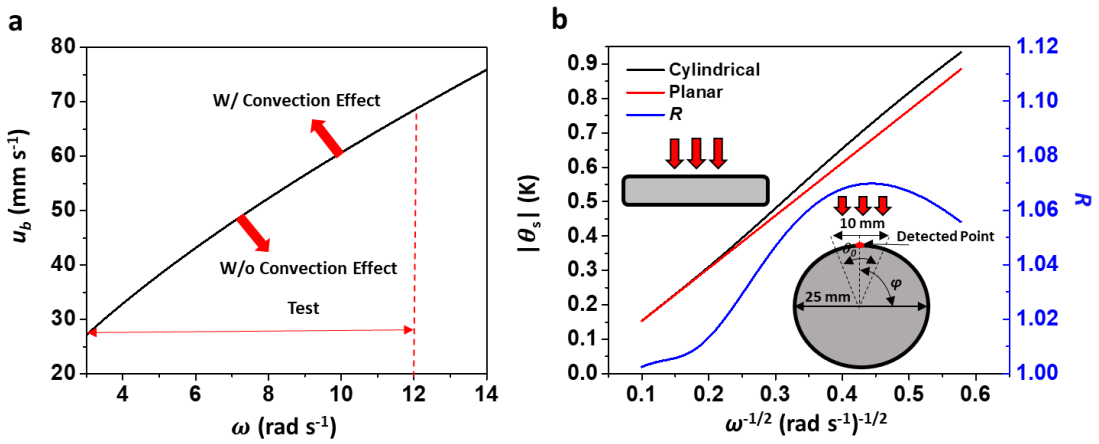

Figure 3-4. Simplification of heat transfer modeling in the fluid domain. (a) Configuration of MPR measurement on flowing fluid for minimum forced convection effect. (b) Comparison of thermal responses between the cylindrical and planar geometries. The left *y*-axis is the amplitude of surface temperature oscillation and the right *y*-axis (*R*) is the ratio of the $|\theta_s|$ between the cylindrical and planar geometries.

To quantify the forced convection effect on the thermal conductivity measurement, we compare the thermal responses predicted by the stationary fluid model in equation 3-15 and that numerically calculated with COMSOL simulation based on equation 3-3. The modeling parameters are shown in Table 3-1.

Table 3-1. Simulation parameters for stationary fluid within a tube

Parameter	Value	Unit
Tube Diameter D	25	mm
Thickness of Tube Shell l_s	100	μm
Thickness of Coating l_c	30	μm
Thermal Conductivity of Steel Tube k_s	20	W m^{-1} K^{-1}
Thermal Conductivity of Coating k_c	0.5 [101]	W m^{-1} K^{-1}
Thermal Conductivity of Fluid k_f	0.6	W m^{-1} K^{-1}
Thermal Diffusivity of Tube α_s	5	mm^2 s^{-1}
Thermal Diffusivity of Coating α_c	0.4	mm^2 s^{-1}
Thermal Diffusivity of Fluid α_f	0.16	mm^2 s^{-1}
Heat Flux q_s	13700	W m^{-2}
Heating Laser Diameter D_{Laser}	10	mm
Detection Spot Diameter D_{IR}	1	mm

The details of the COMSOL simulation are shown in Figure 3-5. Figure 3-5a shows the COMSOL simulation model of flowing fluid in a tube. We simplified the model into 2-dimensional. The harmonic perturbation solver is used. There are three domains in the model: the 30 μm thick coating, the 100 μm thick steel sheet and DI water channel with the half channel width of 12.5 mm. The model is symmetric about the center. The length of simulation domain is set to be 20 mm. A laser beam with the diameter of 10 mm is applied at the center of the domain on the surface of coating, with a uniform heat flux of 20,000 W m^{-2}. A fully developed laminar liquid flow is applied in the liquid domain as shown in Figure 3-5b with variation in the bulk velocity. The properties of materials are listed in Table 3-2. The surface temperature at the center of the laser spot is monitored. Figure 3-5c shows the temperature profile at different frequencies and velocities. It is obvious that as the frequency increases, the thermal penetration depth decreases. In addition, at high velocity, the temperature profile is asymmetric along the flow direction, indicating the strong forced convection, while at low velocity, the temperature profile is similar to that of bulk materials.

Table 3-2. Simulation parameters for flowing fluid in a tube using COMSOL.

Parameter	Value	Unit
Channel Height	25	mm
Channel Width	20	mm
Thickness of Tube Shell l_s	100	μm
Thickness of Coating l_c	30	μm
Laser Spot Diameter	10	mm
Detection Spot Diameter	1	mm
Thermal Conductivity of Steel Tube k_s	16	W m^{-1} K^{-1}
Specific Heat Capacity of Steel Tube c_s	500	J kg^{-1} K^{-1}
Density of Steel Tube ρ_s	8000	kg m^{-3}
Thermal Conductivity of Fluid k_f	0.6	W m^{-1} K^{-1}
Specific Heat Capacity of Fluid c_f	4182	J kg^{-1} K^{-1}
Density of Fluid ρ_f	997	kg m^{-3}
Heat Flux q_s	20000	W m^{-2}
Bulk Velocity u_b	0 - 800	mm s^{-1}
Thermal Conductivity of Coating k_c	0.5	W m^{-1} K^{-1}
Thermal Diffusivity of Coating α_c	0.4	mm^2 s^{-1}

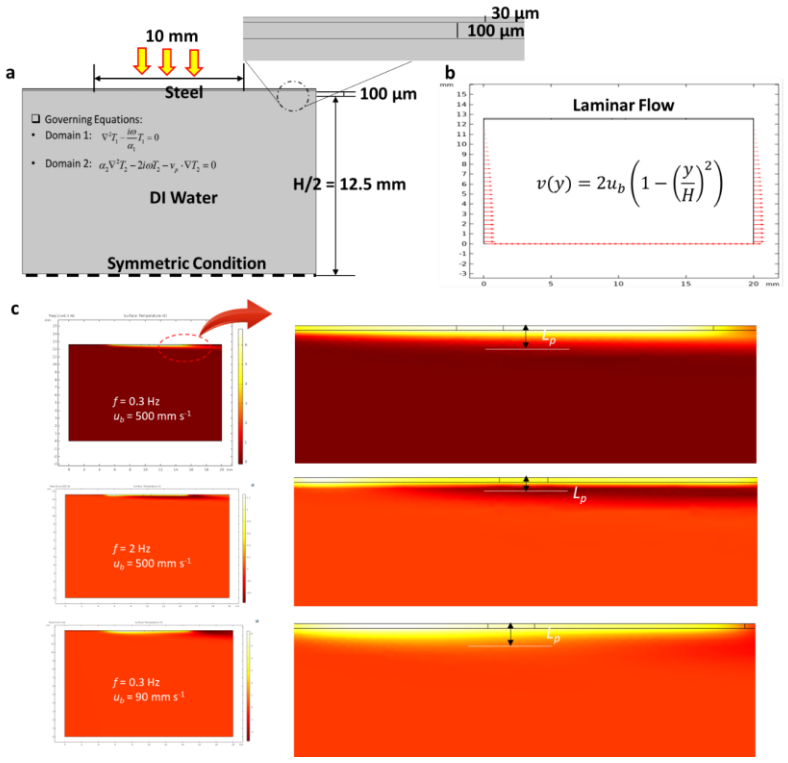

Figure 3-5. Schematic of 2-D COMSOL simulation of MPR measurement on flowing fluid in planar channel. (a) Simulation domain and boundary conditions. (b) Velocity profile of laminar flow (c) Temperature profile at different velocities and frequencies.

As shown in Figure 3-6a, at zero bulk velocity (u_b = 0 mm s^{-1}), the thermal responses of the analytical stationary fluid model (equation 3-15) and the numerical model in COMSOL for the flowing fluid (equation 3-3) agree well with each other. It is evident that the thermal response can be divided into three regions: the fluid dominated region at low frequency where the $|\theta_s|\ vs\ \omega^{-1/2}$ curve is linear; the steel dominated region at intermediate frequency where the slope of the $|\theta_s|\ vs\ \omega^{-1/2}$ curve becomes smaller because the thermal conductivity of steel is higher than that of fluid; the coating dominated region at high frequency where the slope is large due to the low thermal conductivity of coating. In an earlier study, we have experimentally demonstrated that the thermal conductivity and volumetric heat capacity of different layers can be obtained from the thermal responses at different frequencies [101]. At the low frequency limit when L_p is much larger than the thickness of coating and steel, the multilayer model (equation 3-17) can be simplified as [101,104]:

$$\theta_s = \frac{q_s e^{-\frac{\pi}{4}j}}{e_f\sqrt{\omega}} + q_s R_{cs} \tag{3-18}$$

where e_f is the thermal effusivity of fluid, defined as $e_f = \sqrt{k_f \rho_f c_f}$, where ρ_f and c_f are the density and specific heat of the fluid, respectively; R_{cs} is the total thermal resistance by the coating and the steel shell:

$$R_{cs} = \left(1 - \frac{e_s}{e_f}\right)\frac{l_s}{k_s} + \left(\frac{1}{2} - \frac{e_c^2}{e_f^2}\right)\frac{l_c}{k_c} \tag{3-19}$$

where e_s and e_c are the thermal effusivities of the steel shell and the coating, respectively; l_s and l_c are the thicknesses of the steel shell and the coating, respectively; k_s and k_c are the thermal conductivities of the steel shell and the coating, respectively. Notably, R_{cs} is

independent on the frequency in the low frequency range, therefore thermal effusivity of the fluid e_f can be directly obtained by measuring the slope of the $|\theta_s|\ vs\ \omega^{-1/2}$ curve according to equation 3-19. At low bulk velocity u_b = 10 mm s^{-1} as shown in Figure 3-6a, the thermal response remains the same as that of the stationary fluid. Therefore, the intrinsic thermal effusivity of fluid can still be obtained by measuring the slope at low frequency range (L_p = 150 – 300 μm). As u_b increases to above 50 mm s^{-1}, the thermal response starts to slightly deviate from that of the stationary fluid. The curves start to plateau at low frequency at u_b > 100 mm s^{-1}, indicating higher effective thermal effusivity in this regime, or the onset of the forced convection effect. At high flowing velocity, the forced convection effect becomes important, leading to a higher effective thermal conductivity. Therefore, the critical velocity is ~ 100 mm s^{-1} for MPR measurement of intrinsic thermal conductivity of the fluids with the experimental conditions used in this study. The critical velocity predicted by the COMSOL simulation agrees well with that predicted by the dimensional analysis shown in equation 3-8.

Figure 3-6b shows the sensitivity of $|\theta_s|$ on the thermal conductivity of the steel wall k_s, Pyromark coating k_c and fluid k_f, calculated based on equation 3-15 using the parameters in Table 3-1. The sensitivity of $|\theta_s|$ is defined as:

$$S_\theta = \frac{\Delta|\theta_s|/|\theta_s|}{\Delta k_i/k_i}, \tag{3-20}$$

where k_i is the thermal property of the steel wall, coating, or fluid ($k_s, k_c,$ or k_f). For example, the sensitivity of 1 to k_f means that 1% change in k_f leads to 1% change in $|\theta_s|$. As discussed above, $|\theta_s|$ is more sensitive to k_f at the low frequency limit (long thermal penetration depth) and to k_c at the high frequency limit (short thermal penetration depth), while in the intermediate frequency range, it is also sensitive to k_s.

Therefore, in this study, k_f is extracted from the thermal response in the frequency range of 0.5 to 2 Hz (L_p = 150 – 300 μm) where the sensitivity of $|\theta_s|$ to k_f higher than 0.2.

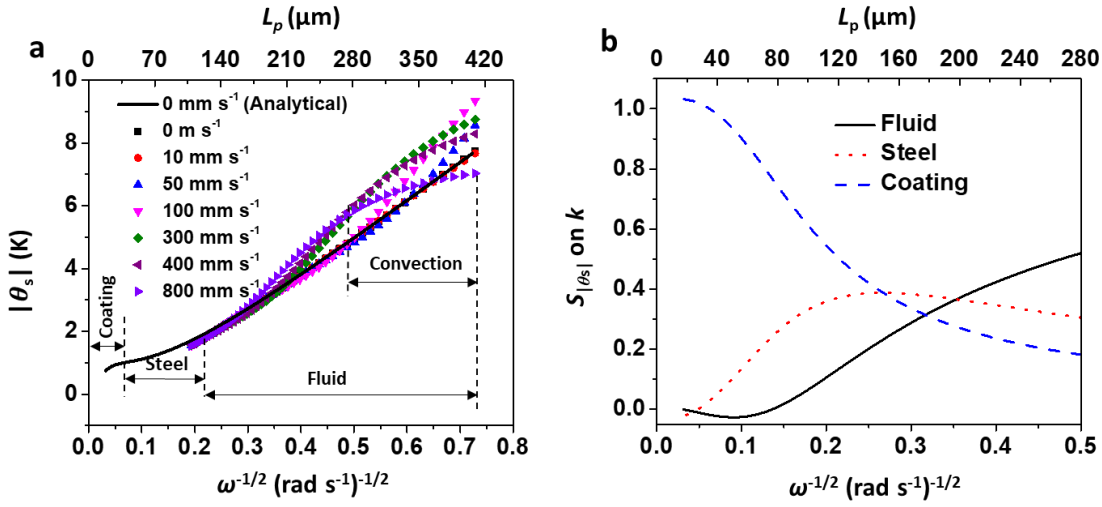

Figure 3-6. Numeric modeling of thermal response of flowing fluid and measurement error analysis of the thermal conductivity of fluid due to the forced convection. (a) Effect of flowing velocity u_b on the thermal response. The solid line from the analytical model is based on **equation 3-15** and the symbols are results from finite element modeling using COMSOL. (b) Sensitivity on the thermal conductivities of coating, steel tube and fluid at u_b = 0 mm s^{-1}.

Another important design parameter is the small wall thickness (100 μm) of the MPR section, which not only ensures high sensitivity of $|\theta_s|$ to k_f but also limits the lateral heat spreading effect. Equation 3-15 is based on the 1D heat transfer model, which is only valid when there is no significant lateral heat spreading effect, i.e., with small wall thickness. We analyzed the 2D heat transfer effect in the system and found that when the wall thickness is less than 100 μm, the measurement error of thermal effusivity of the fluid based on the 1D assumption (i.e., equation 3-15) is less than 10% with suitable steel cover thickness and laser spot size. The thermal effusivity of fluid is obtained from the slope of the thermal response at low frequency based on the assumption of 1-D heat transfer (equation 18). To ensure the 1-D heat transfer, the lateral spreading in the steel

should be minimized. To quantify this, we established a 2-D heat transfer model on a multi-layered system:

$$\theta_{S1} = \int_0^{\infty} -\frac{D}{C}\frac{Q}{\pi R x} J_1(xR) J_0(xr) x dx \tag{3-21}$$

where J_0 and J_1 are the Bessel functions of the zero and first order, respectively. R is the radius of the laser spot and r is the radial coordinate. Q is the laser heating power. D and C are the elements in the heat transfer matrix:

$$M = \begin{pmatrix} A & B \\ C & D \end{pmatrix} = M_3 R_{\text{int}} M_2 M_1 \tag{3-22}$$

where M_i is the thermal properties matrix of the i^{th} layer, and the first layer is close to the surface. R_{int} is the interfacial resistance matrix between the two neighboring layers.

$$M_i = \begin{pmatrix} \cosh(q_i l_i), -\frac{\sinh(q_i l_i)}{k_{zi} q_i} \\ -k_{zi} q_i \sinh(q_i l_i), \cosh(q_i l_i) \end{pmatrix} \tag{3-23}$$

$$R_{\text{int}} = \begin{pmatrix} 1, -\frac{1}{K} \\ 0, \quad 1 \end{pmatrix} \tag{3-24}$$

where K is the interfacial conductance (W m^{-2} K); l_i is the thickness of the i^{th} layer; k_{zi} is the through-plane thermal conductivity of the i^{th} layer; k_{ri} is the in-plane thermal conductivity of the i^{th} layer:

$$q_i = \sqrt{\frac{k_{ri} x^2}{k_{zi}} + i\,\omega/\alpha} \tag{3-25}$$

The lateral spreading can be minimized by reducing the wall thickness of steel or enlarging the laser spot size. Figure 3-7a shows the simulated thermal response at the center of the surface of a stainless tube with variation in the wall thickness filled with fluid using the parameters shown in Table 3-3. As shown in Figure 3-7a, the thermal

responses can be divided into three regions: the fluid governed region at low frequency; the steel governed region in the mediate frequency range and the coating govern region at high frequency. The thermal effusivity of fluid is calculated from the slope at low frequency range ($\omega^{-1/2} = 0.3 - 0.6$) and compared to the values input into the model. As shown in Figure 3-7b, the measurement error increases with increasing steel thickness. To reduce the measurement error to be ≤ 10%, the wall thickness is required to be ≤ 100 μm.

The thermal response is also affected by the laser spot radius. The lateral spreading effect is more prominent when the laser spot size is small. Figure 3-7c shows the simulated thermal responses of fluid in a tube with different laser spot radius and the simulation parameters are shown in Table 3-3. It is noted that the thermal responses for laser spot radius ≥ 3 mm coincide with each other while the curves start to plateau at the low frequency when the laser spot radius is reduced to 2 mm. The lateral heat spreading effect becomes more prominent for laser spot radius < 1 mm. The thermal effusivity of fluid is calculated from the slope at low frequency range ($\omega^{-1/2} = 0.3 - 0.6$) and compared to the values input in the model. Figure 3-7d shows the measurement error of thermal effusivity of fluid. To ensure the low measurement error (< 10%), the laser spot radius should be ≥ 3 mm.

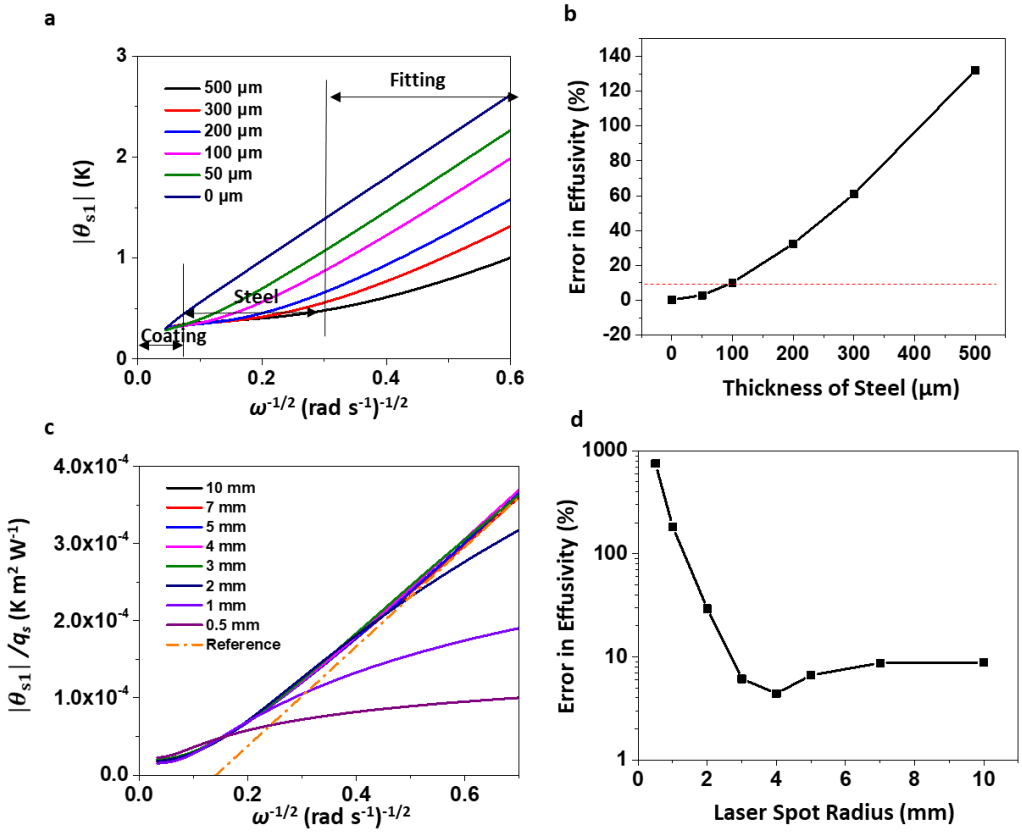

Figure 3-7. Analysis of MPR measurement error of fluids in a tube due to the limitation of thickness of steel wall and laser spot size. (a) Thermal responses with variation in the wall thickness of tube. (b) Measurement error of thermal effusivity of fluid as a function of wall thickness of tube. (a) Thermal responses with variation in the laser spot radius. (b) Measurement error of thermal effusivity of fluid as a function of laser spot radius.

Table 3-3. Simulation Parameters for the effect of wall thickness and laser spot size

Laser Power	2 W
Laser Spot Radius	0.5 - 10 mm
Interfacial Conductance	10^8 W m^{-2} K^{-1}
Coating	
Thickness	10 μm
In-plane Conductivity	0.6 W m^{-1} K^{-1}
Through-plane Conductivity	0.6 W m^{-1} K^{-1}
Diffusivity	0.4 mm^2 s^{-1}
Steel Tube	
Thickness	0.1 – 0.5 mm
In-plane Conductivity	20 W m^{-1} K^{-1}
Through-plane Conductivity	20 W m^{-1} K^{-1}
Diffusivity	5 mm^2 s^{-1}
Fluid	
Thickness	12 mm
In-plane Conductivity	0.6 W m^{-1} K^{-1}
Through-plane Conductivity	0.6 W m^{-1} K^{-1}
Diffusivity	0.15 mm^2 s^{-1}

In addition, to satisfy the 1D assumption, one should also ensure $D_{laser} \gg L_p$ [101]. In our measurement, L_p is ~ 150-300 μm which is much smaller than the D_{laser} (~10 mm). The natural convection effect induced by the temperature gradient is also negligible in the MPR measurement due to the short L_p as shown in Figure 3-8. In our measurement, the heating power is applied from the external surface which will induce a temperature gradient in the fluid, and thus the natural convection effect. If the liquid layer is thick, the natural convection effect is not negligible, leading to an overestimated thermal conductivity in most time-domain and back-side measurements where the liquid layer thickness is in the order of millimeters [100]. The natural convection effect is negligible when the Rayleigh number *Ra* is below 1100[105-107]:

$$Ra = \frac{\rho g \beta \theta_s L_p^3}{\mu \alpha} \tag{3-26}$$

where ρ is density, g is the gravitational acceleration, β is the coefficient of thermal expansion, μ is viscosity, θ_s is the surface temperature, α is the thermal diffusivity and L_p is the liquid thickness in the steady-state measurement and is the thermal penetration depth in the transient measurements. Notably, the *Ra* is linear to L_p^3 and thus the natural convection effect can be significantly suppressed if the liquid layer is thin. Figure 3-8a shows the *Ra* number as a function of liquid thickness for DI-water. The natural convection is negligible for the liquid layer thickness smaller than 1.5 mm. As shown in Figure 3-8b, the *Ra* number in the MPR measurement is < 10 in the frequency range of interest due to the short thermal penetration depth (< 300 μm) and thus the natural convection effect is negligible in our measurement.

The heat flux is calibrated using a standard material with known thermal effusivity *e* according to equation 3-12 as reported in chapter 2.3. This approach avoids

the need to precisely measure the laser spot size which is reported to be a major source of measurement uncertainty[108]. The MPR measurement uncertainty is 5.8% and the analysis can be found in chapter 2.2.

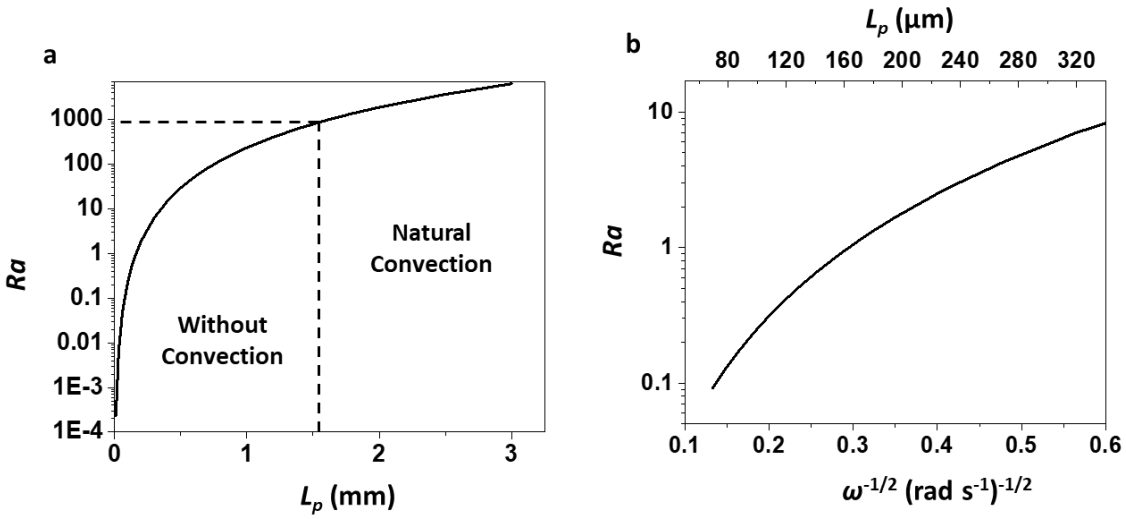

Figure 3-8. Evaluation of the Ra number in the MPR measurement. (a) *Ra* number as a function of the liquid thickness and (b) *Ra* number as a function of the modulation frequency and the corresponding thermal penetration depth.

3.4. Results and discussions

3.4.1. Measurement of stagnant fluids

Figure 3-9a shows the thermal responses of different fluids at stagnant state (i.e., u_b = 0 mm s^{-1}) and room temperature. All the thermal response curves can be delineated into three regions: (i) Pyromark coating dominated region at high frequency with L_p < 30 μm. (ii) tube wall (or substrate) dominated region in the medium frequency range where the slope is smaller due to the high thermal conductivity of the steel. The thermal responses in these two regions are the same for all the samples because the same tube with the same coating was used. (iii) fluid dominated region at low frequency with L_p > ~160 μm, where the slope is determined by the thermal effusivity of the fluid. According

to Equation 18, the thermal effusivity of the fluid e_f is obtained from the slope of the $|\theta_s|\ vs.\ \omega^{-\frac{1}{2}}$ curve in the low frequency regime, and the thermal conductivity of the fluid can be calculated based on the specific heat and density of the fluids reported in the literature [109-111]. Figure 3-9b shows the normalized thermal response by the heat flux ($\frac{\theta_s}{q_s}$) in the frequency range of 0.5-2 Hz, i.e., L_p in the range of 180-320 μm. e_f can be directly obtained from the slopes of the $\frac{\theta_s}{q_s}\ vs\ \omega^{-1/2}$ curves. Figure 3-9c compares the measured thermal conductivity of different fluid (e_{exp}) to the literature values (e_{lit}) while Figure 3-9d compares the measured thermal conductivity of different fluid (k_{exp}) to the literature values (k_{lit}) [109-111]. The measurement results are within 10% error from the literature values, validating the MPR measurement of stagnant fluids. This error is similar to what we have reported for MPR measurements on bulk materials [101]. The stagnant fluids can be treated as bulk materials if the natural convection effect is negligible. In our measurements, L_p in the fluids ranged from 180 to 320 μm in the low-frequency regime, leading to Rayleigh number (Ra) of 1 to 10 for these fluids (the critical Ra for the induction of natural convection is 1100 [105]) and consequently negligible natural convection effect.

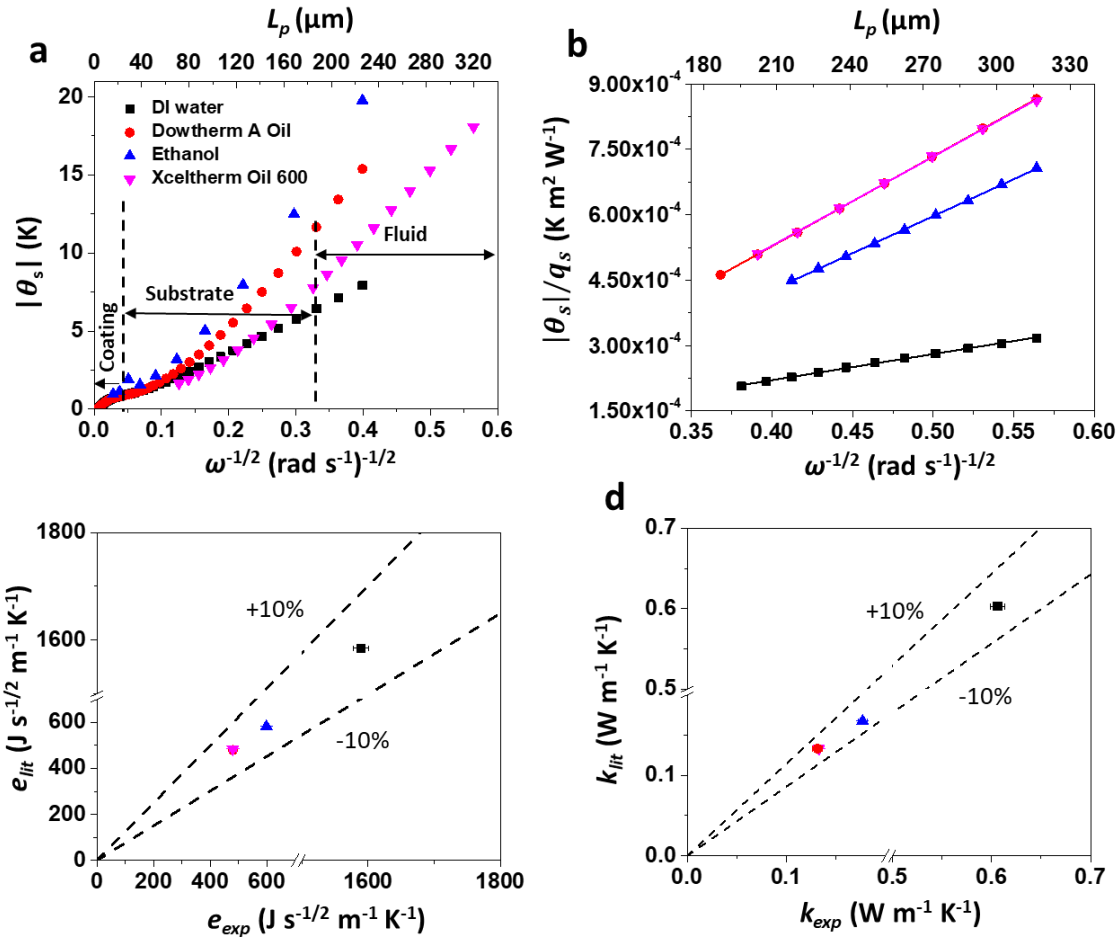

Figure 3-9. MPR measurement on stationary fluids at room temperature. (a) Thermal responses of different stagnant fluids filled in the MPR measurement section (tube wall thickness: 100 μm; Pyromark coating thickness: ~ 30 μm). L_P is estimated based on the properties of DI water. (b) Thermal responses of different stagnant fluids at the low frequency range of 0.5-2 Hz. (c) Comparison of the thermal effusivity measured using MPR and the literature values. (d) Comparison of the thermal conductivity measured using MPR and the literature values. Note the data of Dowtherm A oil and Xcetherm oil 600 are overlapped in (b), (c), and (d).

3.4.2. Measurement of flowing fluid

According to the analysis presented in chapter 3.3, to measure the thermal conductivity of flowing fluids, the flowing velocity should be lower than the critical velocity to satisfy the condition of negligible forced convection effect. In this section, we measured Xceltherm oil and DI water at room temperature with variable flowing

velocities to experimentally identify the critical velocity and compare it to the theoretical analysis. Figure 3-10a shows the thermal responses of Xceltherm oil. The thermal responses for u_b = 0 mm s^{-1} and 90 mm s^{-1} coincide, indicating negligible forced convection effect up to 90 mm s^{-1}. The thermal response curves shift downwards with increasing flowing velocities, indicating higher effective thermal effusivity and thermal conductivity due to the stronger forced convection effect. The effective thermal effusivity of the fluid (e_{eff}) is obtained from the slope of $|\theta_s|$ $vs.\ \omega^{-\frac{1}{2}}$ in the linear region with L_p = 150 - 300 μm (Equation 18) and the effective thermal conductivity (k_{eff}) is calculated with the literature values of specific heat and density of the fluids. Figure 3-10c shows k_{eff} normalized to the intrinsic thermal conductivity (k_0) of Xceltherm oil, k_{eff}/k_0 , as a function of u_b. k_{eff}/k_0 is within 5% of the unity when u_b = 0 - 90 mm s^{-1}. At higher velocity, k_{eff}/k_0 increases, reaching 118% at u_b = 250 mm s^{-1} and 151% at u_b = 500 mm s^{-1}. This result indicates that the intrinsic thermal conductivity of Xceltherm oil can be measured at u_b < 100 mm s^{-1} for the current MPR configuration, consistent with our theoretical analysis in Section 2.

Figure 3-10b shows the thermal responses of DI water. The slopes of the thermal responses from u_b = 0 mm s^{-1} and 90 mm s^{-1} are close, indicating negligible forced convection effect up to 90 mm s^{-1}. The thermal response curves shift downwards with increasing velocities, indicating higher effective thermal effusivity and thermal conductivity due to the forced convection, similar to the Xceltherm oil. The curve shows a plateau in low frequency region at u_b = 550 mm s^{-1}, indicating a significantly higher effective thermal effusivity in this region. Figure 3-10c shows k_{eff} normalized to the intrinsic thermal conductivity (k_0) of DI water, k_{eff}/k_0 , as a function of u_b. k_{eff}/k_0 is

within 5% of the unity when u_b = 0 - 90 mm s^{-1}. At higher velocity, k_{eff}/k_0 increases, reaching 118% at u_b = 190 mm s^{-1}. The above analysis indicates that the intrinsic thermal conductivity of DI water can also be measured at u_b < 100 mm s^{-1}, which is close to the prediction from the COMSOL simulation as shown in Figure 3-6a and the dimensional analysis shown in Figure 3-4a. It is also worth noting that the forced convection effect is stronger for DI water than Xceltherm oil at the same flowing velocity. The k_{eff}/k_0 reaches 310% at u_b = 347 mm s^{-1} and 1130% at u_b = 550 mm s^{-1} for DI water (versus 151% at u_b = 500 mm for Xceltherm). This is because the viscosity of oil is higher, leading to a lower Re_D number at the same flow velocity, which will be further discussed in the later section.

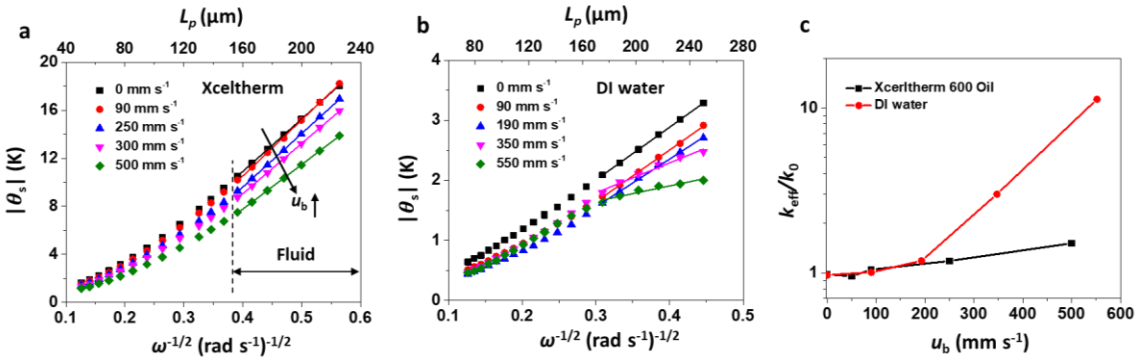

Figure 3-10. MPR measurement on flowing fluids at room temperature. (a) Thermal response of Xceltherm 600 oil in a tube flowing at different velocities. (b) Thermal response of DI water in a tube flowing at different velocities. (c) Normalized thermal conductivity as a function of flow velocity for DI water and Xceltherm 600 oil. The thermal effusivity measured from the slopes of the thermal response curves are used to calculate the thermal conductivity based on the density and specific heats in the literature [109-111].

Figure 3-11a and 3-11b show the thermal responses for DI water and Xceltherm 600 oil, respectively, at the same velocity of u_b = 90 mm s^{-1} with fluid temperature (T_0) ranging from 30°C to 170°C. The upper temperature limit is set so to avoid boiling of water or ignition of oil in air. Like the analysis done in the previous section, e_{eff} of fluid

is obtained from the slope at low frequency and then the k_{eff} is calculated. Figure 3-11d compares k_{eff} of DI water and the oil to the literature value k_0 at different temperature. k_{eff} of DI water is close to k_0 from 30℃ to 60℃. For the Xceltherm oil, k_{eff} is close to k_0 at T_0 < 100℃. However, k_{eff} of the oil increases significantly at T_0 > 100℃; k_{eff}/k_0 is 154.5% and 168.1% at 140℃ and 170℃, respectively due to the strong forced convection at higher temperature. The viscosity of the oil decreases with increasing temperature, and thus Re_D increases at higher temperature, leading to stronger forced convection effect. Figure 3-11c shows the thermal responses for the oil at the velocity of u_b = 50 mm s^{-1} with T_o from 90℃ to 170℃. As shown in Figure 3-11d, by reducing the flow velocity to 50 mm s^{-1}, k_{eff} of Xceltherm oil agrees well with k_0 at all the temperatures. Evidently, the critical velocity varies with the type of the fluid and the temperature, which will be discussed in the next section.

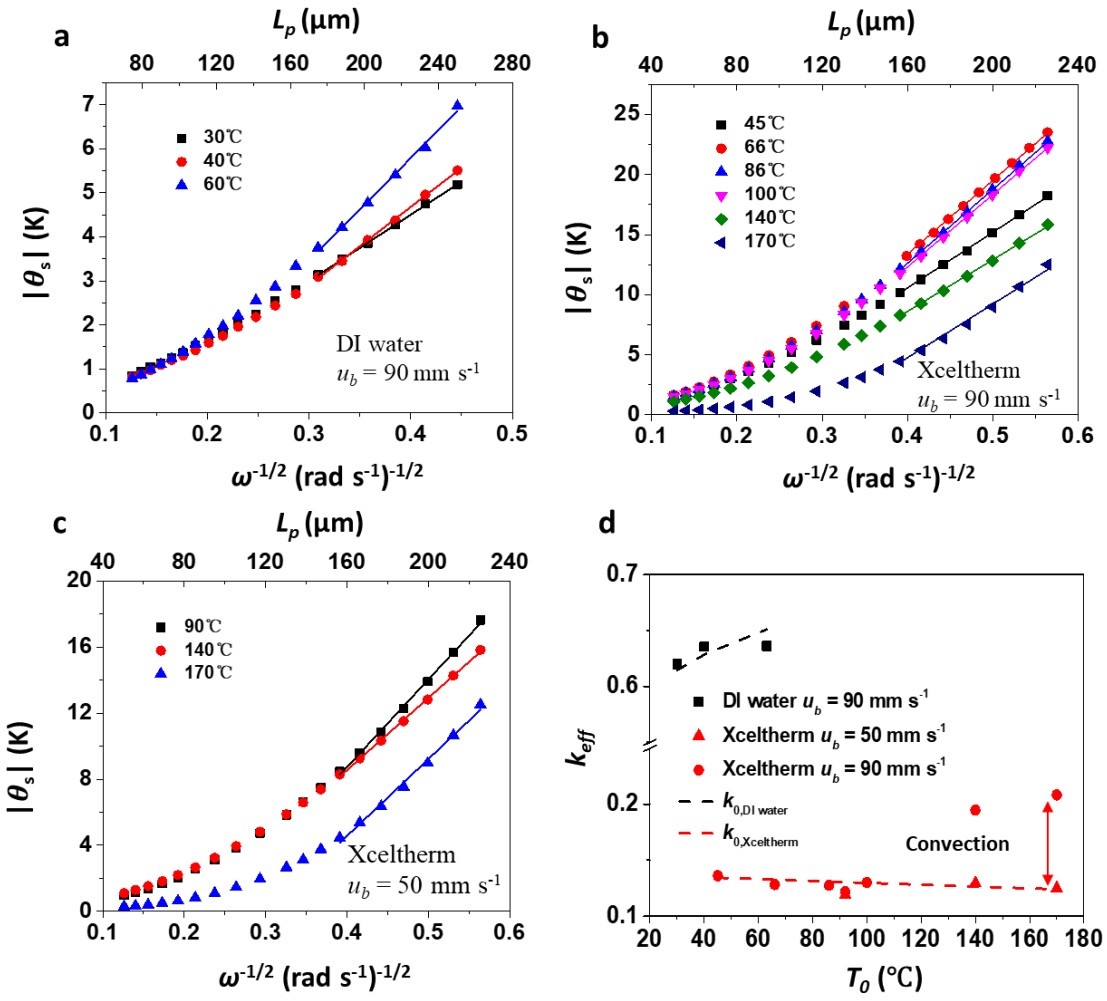

Figure 3-11. MPR measurement of flowing fluids at elevated temperature. (a) Thermal responses of DI water at u_b = 90 mm s^{-1} at 30-60℃. (b) Thermal response of Xceltherm 600 oil at u_b = 90 mm s^{-1} at 45-170℃. (c) Thermal response of Xceltherm 600 oil at u_b = 50 mm s^{-1} at 90-170℃. (d) Effective thermal conductivities of DI water and Xceltherm 600 oil as a function of temperature measured at u_b = 90 mm s^{-1} and u_b = 50 mm s^{-1}.

3.4.3. Analysis of Forced Convection Effect

To systematically study the forced convection effect, we further measured the two fluids at different velocities: (a) Xceltherm oil from 45-170℃ with flowing velocity of 50 mm s^{-1}, 90 mm s^{-1}, 250 mm s^{-1} and 300 mm s^{-1}; and (b) DI water at 30 ℃ with flowing velocity of 90 mm s^{-1}, 190 mm s^{-1}, 350 mm s^{-1} and 550 mm s^{-1}. Figure 3-12a shows the normalized thermal conductivity (k_{eff}/k_0) from all the measurements of DI water and

Xceltherm 600 as a function of Re_D. It can be seen that k_{eff}/k_0 increases with increasing Re_D. Although the range of velocity is the same for DI water and Xceltherm oil, Re_D for DI water is much higher due to the lower viscosity. At u_b > 190 mm s^{-1}, Re_D > 10,000, the flow of the water becomes turbulent, leading to strong forced convection effect. Therefore, k_{eff} also increases significantly. The viscosity of the oil decreases with increasing temperature, and thus Re_D is higher at higher temperature. As a result, k_{eff} directly obtained from the measurement is increasingly overestimated compared to k_0 as the temperature increases, as shown in Figure 3-11d. However, compared to DI water, Re_D for Xceltherm is less than 10,000 and the flow is still laminar within the entire flow velocity range.

Here we plot k_{eff}/k_0 as a function of $Re_D^{1/2}Pr^{1/3}$ in Figure 3-12b. Notably, k_{eff}/k_0 of both DI water and Xceltherm 600 follows the same trend as $Re_D^{1/2}Pr^{1/3}$ increases, except the outliner for DI water at high $Re_D^{1/2}Pr^{1/3}$value (>200) because the water flow is turbulent, which does not follow the Nu_D correlation for a laminar flow. The forced convection effect is negligible for both liquids at $Re_D^{1/2}Pr^{1/3}$ < 100 and becomes increasingly prominent as $Re_D^{1/2}Pr^{1/3}$ increases. This agrees well with the theoretical analysis as shown in equation 3-10. Therefore, we conclude that it is feasible to use the MPR technique developed here to measure the intrinsic thermal conductivity of flowing fluids under the condition of both low u_b and low $Re_D^{1/2}Pr^{1/3}$ (or more generally, equation 3-7 and equation 3-10 are both satisfied). On the other hand, this work also suggests that the MPR could be used to probe the convection effect of flowing fluids when u_b or $Re_D^{1/2}Pr^{1/3}$ is larger.

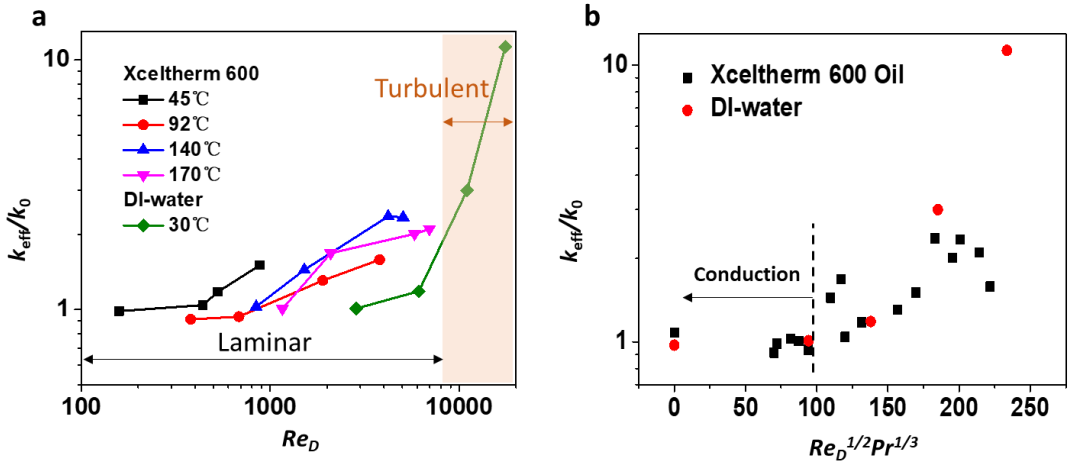

Figure 3-12. Analysis of forced convection effect in flowing fluid. (a) Normalized thermal conductivity as a function of Re_D number for DI-water and Xceltherm 600 oil. (b) Normalized thermal conductivities of DI water and Xceltherm 600 oil as a function of $Re_D^{1/2}Pr^{1/3}$ at different temperatures.

3.5. Conclusions

In this chapter, we develop an MPR setup to measure the thermal conductivity of flowing fluid in a tube by controlling the modulation frequency of heating laser beam and the corresponding thermal penetration depth. The MPR setup is first validated by the thermal conductivity measurement of stationary fluids, including DI-water, Dowtherm A oil, Xceltherm 600 oil and ethanol at room temperature. The measurement error of stationary fluid is within 10%. Subsequently, the MPR setup is extended for the measurement of flowing fluid in the velocity range of 0 – 550 mm s^{-1} and from room temperature to 170°C. The intrinsic thermal conductivity of fluid can be obtained at low velocity where the forced convection effect is minimized. The forced convection effect becomes prominent at high flow velocity and low frequency, leading to the overestimation of thermal conductivity. The critical velocity is determined by the dimensionless number $Re_D^{1/2}Pr^{1/3}$ modeled based on the laminar boundary layer. When

$Re_D^{1/2} Pr^{1/3}$ < 100, the intrinsic thermal conductivity of fluid can be obtained. The MPR technique reported here provides a convenient tool of *in-situ* thermal conductivity measurement of flowing fluid and shows the potential to characterize the local forced convection heat transfer close to the wall.

Chapter 3, in full, is a reprint of the materials as it appears in '*In-situ* Thermal Transport Measurement of Flowing Fluid Using Modulated Photothermal Radiometry', *International Journal of Heat and Mass Transfer*, 180 (2021), 121767 by Jian Zeng, Ka Man Chung, Sarath Reddy Adapa, Tianshi Feng and Renkun Chen. The dissertation author was the primary investigator and first author of this paper.

4. Chapter 4: Thermal transport of stationary granular media

4.1. Introduction

Particle beds are useful for a multitude of current and emerging systems and processes, such as catalytic reactors [112], nuclear reactors [113,114], heat exchangers[115], thermal and thermochemical energy storage[116,117], thermal insulation[118], adsorption bed[119], and additive manufacturing[56]. Heat transfer performance of these systems is highly dependent on the effective thermal conductivity of the particle beds (k_{eff}) [120,121], and it is thus important to model and predict the k_{eff} to optimize the system performance. Figure 4.1 shows the schematic of a sCO_2-particle heat exchanger used for concentrating solar power (CSP) plant. As shown in Figure 4.1a[122], there are arrays of mirrors on the ground to reflect and focus sunlight to the top of the solar tower. The particles fall from the top and are heated up to ~ $700°C$ by the concentrated sunlight at the receiver. The hot particles are stored in the hot tank and used to heat up the supercritical carbon dioxide (sCO_2) at the heat exchanger, which will drive the turbine for power generation. Figure 4.1b displays the schematic of the sCO_2-particle heat exchanger in greater details[36,123]. The hot particles are supply at $775°C$ from the top through parallel channels separated by the sCO_2 channels in between to enlarge the heat transfer area. As the particles flows down, the sCO_2 is heated up to $> 700°C$ whereas the particles cool down to $570°C$. The particles and sCO_2 flow at the counter directions and the effective heat transfer coefficient of the heat exchanger can be modeled as[36]:

$$U = \left(\frac{1}{h_{sw}} + \frac{\delta_w}{k_w} + \frac{1}{h_{CO_2 w}} \right)^{-1} \tag{4-1}$$

where h_{sw} is the heat transfer coefficient between particle and wall, δ_w is the thickness of wall, k_w is the solid thermal conductivity of wall materials (which is usually high-temperature alloy), and h_{CO_2w} is the heat transfer coefficient between the CO_2 flow and wall. Due to small thickness of wall and high velocity of CO_2 flow, the major thermal resistance lies in the particle-wall heat transfer, which can be modeled based on the semi-infinite continuum assumption[124,125]:

$$\overline{h_{sw}} = 2\sqrt{\frac{u_b \rho c_p k_{eff}}{\pi L}} \tag{4-2}$$

where $\overline{h_{sw}}$ is the average heat transfer coefficient over length of L, u_b is the bulk velocity of particle, ρ and c_p are the density and specific heat of particle, and k_{eff} is the effective thermal conductivity of particle bed. Obviously, k_{eff} of particle bed is a dictating parameter in the thermal performance of the sCO_2-particle heat exchanger. While other parameters can be accurately defined and modeled, the k_{eff} of particle bed is much more complicated and is yet to be well understood. Despite continuous efforts in the modeling of k_{eff} of particle beds since the 1960s [126-132] with varying materials, sizes, and packing structures, an accurate and predictive model still remains elusive due to the complexity of heat transfer in the particle bed. The k_{eff} represents the collective heat transfer performance from the solid conduction, gas conduction and radiation in a heterogeneous fluid and solid system. As such, the effective thermal conductivity is affected by numerous factors, such as particle size, porosity, the intrinsic thermophysical properties of the solid and fluid as functions of temperature and pressure, the interaction between the solid surface and the stagnant fluids and the mechanical adhesion between the solid surface, making it challenging to accurately model k_{eff} under a wide range of conditions.

The thermal transport in moving particle becomes even more complicated where the advection of individual particles increases the chaotic heat transfer pathways while interrupts the conduction pathways between particles. The aroused gas flow may also affect the thermal transport between the particles[133,134]. Up to now, there is limited knowledge about the effective thermal conductivity of moving particle bed and *in-situ* thermal conductivity measurement of a moving particle bed has been elusive.

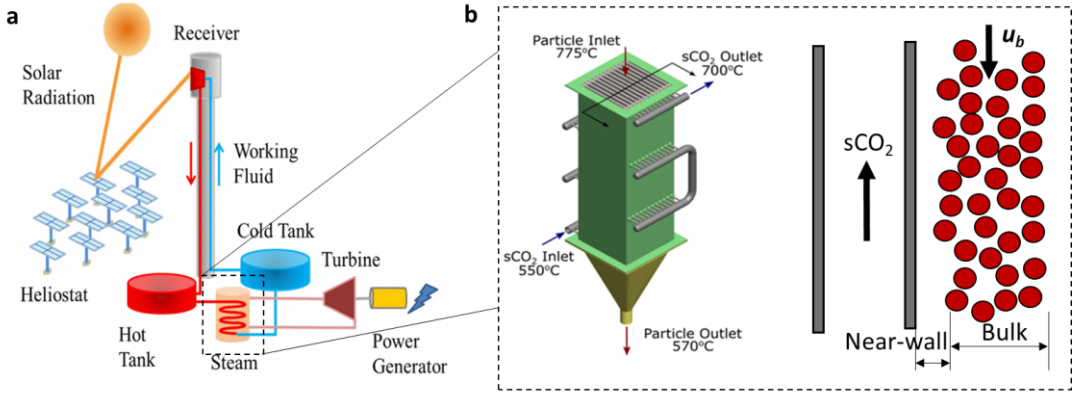

Figure 4-1. Schematics of particle-based concentrating solar power. (a) Overview of CSP plant.[122] (b) Schematics of sCO_2-particle heat exchanger without counterflows of sCO_2 and particle. The particle flow can be divided in the bulk and near-wall region with different packing density. The sCO_2 and particle flows are separated by the alloy wall.

Analytical models have been developed in the past few decades to capture k_{eff} of packed particles. The simplest models include the in-series and in-parallel thermal resistances between the solid and fluid phases. The in-series model predicts the lower bound of k_{eff} of a solid-fluid system while the in-parallel one represents the upper bound More sophisticated models for particulate media are based on unit cell with both in-series and in-parallel thermal pathways[126-132]. For example, in the models developed by Yagi and Kunni, Kunii and Smith, and Masamune and Smith [128-130], there are generally three different heat transfer mechanisms that constitute the effective conduction pathways: the

first is the heat transfer through the void fraction by gaseous conduction and radiation; the second mechanism is the solid-gas conduction where the solid and fluid layers are in series; and the third one is the heat transfer within the solid phase through the particle contacts. Their models, however, are limited to periodic packing structures which might not represent the realistic ones. On the other hand, the key parameters, for example, the particle contact fraction and effective solid-gas conduction pathway are empirically obtained based on experimental results. It might have oversimplified the solid-gas and solid contact pathways. Other types of unit cells have also been proposed to better capture the heat transfer mechanisms in packed particles[135,136]. For example, Hall and Martin [135] developed models for primitive cubic-packed array of spheres and for squared packed infinite cylinders. Although the models can include the low gas pressure and radiation effects, the models are limited to primitive cubic-packing structures. In addition, these models have not taken solid-solid heat conduction into consideration. The Zehner, Bauer, and Schlünder (ZBS) model is one of the widely used models, which considers packed particles within a cylindrical unit cell [136]. However, the ZBS model has limited accuracy under several conditions due to its simplified particle packing assumption. The analysis of the heat conduction through the finite solid-to-solid contact areas also requires the full knowledge of the elasticity of the solid particle. Thus, it is difficult to accurately predict k_{eff} of packed particles by simply applying the ZBS model. Therefore, the existing analytical models are usually limited by the assumption of regular particle packing and simplified particle-to-particle contact in a unit cell.

Realizing the importance of accurate packing structure on the prediction of k_{eff}, several studies have been carried out to model the structure of randomly packed beds via

the discrete element method (DEM) with great success on a few numbers of materials[137-140]. However, most of the prior studies were focused on large particles as the intended application was primary on nuclear reactors, e.g., 600 to 1000 μm diameter pebbles with standard deviations of ~ 150 μm[137,138,140,141] . It is still of fundamental interest to examine the impact of particle packing structure on a wider range of particle sizes and under various gaseous pressures. This is because the packing structure is expected to impact the solid-to-solid and the gas-solid heat conduction mechanisms, which are known to depend on particle size and gaseous pressure [115,142,143]. Therefore, examining the impact of the realistic random packing structure vs. the conventional periodic structure on k_{eff} modeling could be more relevant to assess the suitability of DEM over a wide range of experimental conditions. In this work, we aim to carry out a systematic study on monodispersed spherical particles within a wide range of particle size, temperature and gaseous pressure to evaluate the random particle packing structure derived from a DEM model and to quantify the contribution of different heat transfer pathways. Although the effects of the parameters (particle size, temperature, pressure) have been investigated separately in several earlier studies[139,144,145], the limited range of values in each of these studies and the different experimental conditions across different studies still inhibited effective validation of the DEM model and quantification of contributions of different heat transfer mechanisms.

While the modeling of particle thermal transport remains unresolved with many hypotheses under debate, much effort has been paid on the experimental thrust to measure k_{eff} of a variety of particles using different methods as summarized in Figure 4.2. The steady-state method is the most facile way to measure k_{eff} of particles where

the particles were clapped between a heat source and a heat sink, and the temperature drop across the particle bed with certain thickness is measured under a certain heat flux [146,147]. However, this method is prone to the artifact introduced from the particle wall contact and heat loss to the environment. Laser flash analysis (LFA) shines a pulse laser on the surface of the sample and detect the temperature rise delay at the back, which indicates the thermal diffusivity $\alpha = \frac{k}{\rho c}$ of the particles[148]. With the density ρ and specific heat c_p of particles measured separately, the effective thermal conductivity of particle can be obtained. However, similar to the steady state method, it is also a back-side measurement method, where the near-wall contact effect cannot be differentiated. Besides, if the near wall thermal resistance is too high, lateral heat dissipation becomes prominent, leading to the large measurement error. To avoid this problem, front-side measurement methods, such as transient hot-wire (THW) and transient plane source (TPS) methods[56,149,150] were employed. A heater line or heater plane was inserted into the particle bed, serving as both the joule heater and thermometer. The transient temperature rises after applying a constant current was recorded to back-calculate the thermal conductivity of media. While this method works well for a variety of particles, the measurement error becomes a concern for low thermal conductivity media in TPS and for large particles in THW. Besides, due to the weak mechanical strength of heater, it is not suitable for the high-temperature measurements or pressed particle bed measurement, which limits their attractiveness for the perspective moving particle measurements. 3-omega method[52,151] and frequency domain thermal reflectance (FDTR) [152] are frequency-domain methods where the thermal penetration depth could be adjusted by the modulation frequency as thus the near-wall and bulk region could be probed separately.

However, a thin metallic transducer layer (at the order of ~ 100 nm) was deposited on the sample surface, which not only requires the expensive nanofabrication but also places questions on their high-temperature stability under harsh environment. Therefore, there is so far still lacking a suitable measurement technique to measure the near-wall and bulk thermal conductivity of particle bed with high temperature stability and high accuracy.

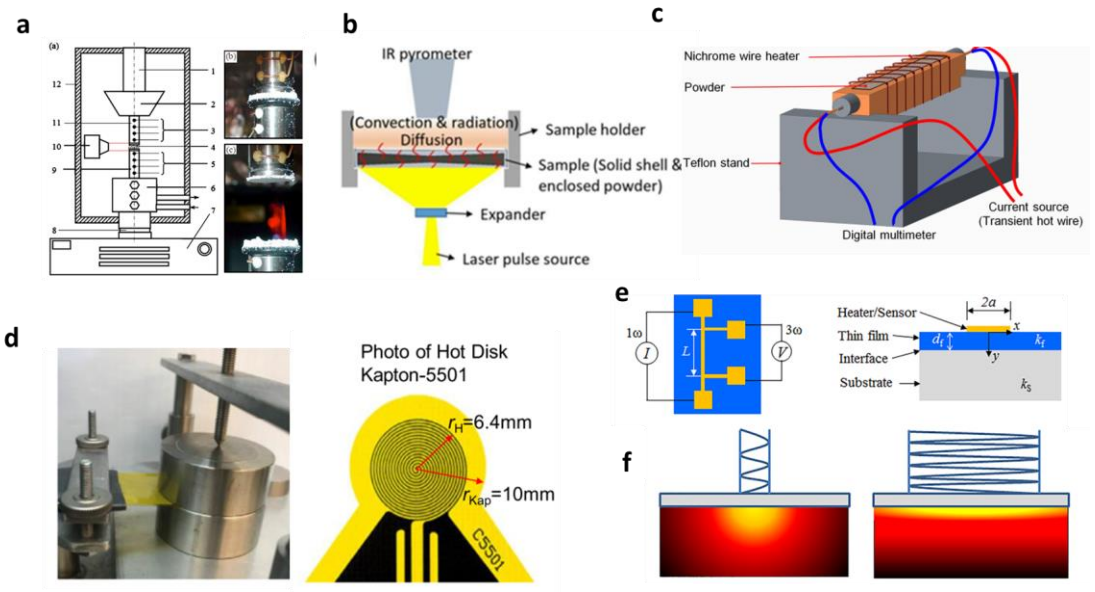

Figure 4-2. Conventional thermal conductivity measurement technique for particle bed. (a) Steady-state method[146,147], (b) laser-flash analysis[148], (c) hot-wire method[56,149], (d) plane-source method[150], (e) 3-omega method[52,151] and (d) frequency-domain thermoreflectance[152].

We first measured the effective thermal conductivity of stationary particles using transient hot-wire (THW) method as benchmark measurement, which was a popular technique for particle measurement[56,149,150]. We then modified the modulated photothermal radiometry (MPR) system developed in chapter 2 to be compatible with the stationary particle measurements up to 700℃. CARBO ceramic particles with the average particle diameter ranging from 150 μm, 275 μm and 400 μm, silica sand with irregular morphologies and particle sizes ranging 357 μm, 415 μm and 600 μm are

candidates for the particle based CSP. It is of significance to accurately measure their effective thermal conductivity for the optimum design of the particle heat exchanger. They were measured by both the THW and stationary MPR techniques. The measurement results were compared to the conventional simple-cubic based model. Subsequently, the mono-dispersed silica spheres with particles size ranging 23 μm, 67 μm and 330 μm were chosen as the model system to validate the k_{eff} of mono-dispersed spherical particle bed. k_{eff} of the silica spheres was modeled by COMSOL using discrete element modeling (DEM) to obtain the random packing structure as an input, which was compared to the conventional analytical models based on simple cubic structure.

4.2. Measurement system and principles

To measure the effective thermal conductivity (k_{eff}) of particle beds at different temperatures and gas pressures, we have established a high-temperature THW apparatus capable of measuring k_{eff} within a wide temperature range (room temperature to about 700^{o}C) and at different gas pressure levels (1 to 760 Torr) as shown in Figure 4.3. The THW method is a conventional thermal conductivity measurement method for various substances (i.e., liquids, compressed gases, and powders[56,87,153-156]. Figure 4.3a and 4.3b show the schematic and image of the high-temperature THW setup, respectively, while Figure 4.3c shows a photograph of the THW test section. The THW test section was made of mica (McMaster-Carr, Santa Fe Springs, California, USA) capable of withstanding the maximum operating temperature of ~798^{o}C. A cavity with a dimension of roughly 0.97 (width) × 1.50 (depth) × 11.6 (length) cm^3 was machined to contain the particles for the measurement. A Pt wire (Goodfellow Corporation, PT0005114) of 25.0

μm in diameter was embedded in the middle of the cavity, serving as the hot wire in the THW measurement as well as a resistive thermometer of the particles. The temperature of the particles was additionally monitored by a K-type thermocouple inserted directly into the particle bed. The thermocouple was connected to a thermocouple monitor (Stanford Research Systems SR630). Four Cu wires were fixed by set-screw connectors (Kurt J. Lesker Company, FTASSC050) at the end of the mica holder, enabling good electrical contacts to the Pt wire. This four-wire configuration is essential to eliminate the contact resistance when measuring the resistance of the Pt hot wire, as shown in the inset in Figure 4.3a.

To measure k_{eff} at different temperatures and gaseous pressures, the THW test section was placed inside a tube furnace (MTI GSL-1100X quartz tube furnace) with a maximum continuous operation temperature of 1000^{o}C. The furnace is connected to a gas cylinder in the upstream and a mechanical pump in the downstream. The four Cu wires were connected to pins of a vacuum feedthrough. The external terminals of the feedthrough were connected to a constant programmable current source (Keithley 220) and a digital multimeter (Hewlett-Packard 34401A, 6½ Digit), which are controlled by a computer through a GPIB interface. When the gas was introduced to the quartz tube, the gas flow rate was monitored and controlled by a mass flow controller (MKS Instruments 179C) that was connected to a 4-channel flow controller power supply readout (MKS Instruments 247D). On the downstream side, a pressure transducer (MKS Baratron Type 127A) and an exhaust throttle valve (MKS Instruments 253B-26373) were installed in series to monitor and regulate the gaseous pressure inside the tube furnace.

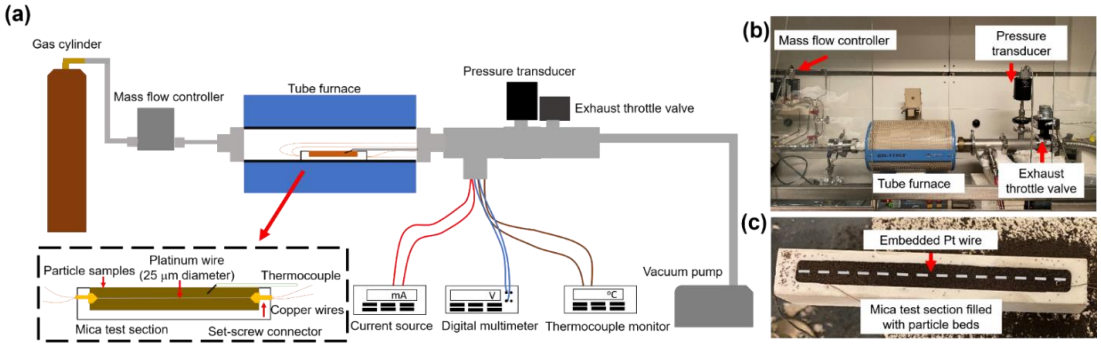

Figure 4-3. Schematics of THW measurement system. (a) Schematic of the THW set-up; (b) photograph of the THW measurement set-up; and (c) photograph of THW test section with particle samples filled inside.

In the THW measurement, with the assumption that a line heat source is embedded in an infinite particle bed, the effective thermal conductivity of the particles is given by the following equation[56,156-159]:

$$k_{eff} = \frac{q'/4\pi}{d(\Delta T)/d(\ln t)} \tag{4-3}$$

where ΔT is the temperature rise of the Pt wire induced by applying an electrical current I to it for a duration of time (t), q' is the heat rate per unit length of the Pt wire: $q' = I^2R/L$, where L is the length of the Pt wire, and R is the resistance of the Pt wire at the measurement temperature T. In our measurement, I usually ranged from 50-100 mA to achieve a sufficiently large ΔT in the particle samples. ΔT was determined from the measured resistance change (ΔR) of the Pt wire upon heating with the applied current:

$$\Delta T = \Delta R/(R_{ref}\beta) \tag{4-4}$$

where R_{ref} is the Pt resistance at room temperature (23°C) and the temperature coefficient of resistance β is evaluated at the measurement temperature T:

$$\beta = \frac{1}{\rho_{ref}}\frac{d\rho(T)}{dT} \tag{4-5}$$

where ρ_{ref} is the resistivity of Pt at room temperature and the temperature-dependent resistivity $\rho(T)$ of solid Pt was obtained from the known polynomial equation for the temperature range of 100 to 2041.3 K[160]. Additionally, to ensure that the thermometry based on the literature value of β for Pt is valid, we measured the temperature of the particle bed using a K-type thermocouple probe inserted in the bed. According to Equation 4-3, the effective thermal conductivity measured using THW method is given by $k_{eff} = \frac{q'/4\pi}{d(\Delta T)/d(\ln t)} = \frac{I^2 R V_{ref} \beta}{4\pi L d(\Delta V)/d(\ln t)}$, where $\Delta T = \Delta R/(R_{ref}\beta)$, ${}^{\Delta R}/_{R_{ref}} = {}^{\Delta V}/_{V_{ref}}$ and $V_{ref} = IR_{ref}$. The relative uncertainty of the effective thermal conductivity is then given by:

$$\frac{\delta k_{eff}}{k_{eff}} = \sqrt{(2\frac{\delta I}{I})^2 + (\frac{\delta V}{V})^2 + (\frac{\delta R}{R})^2 + (\frac{\delta \beta}{\beta})^2 + (\frac{\delta L}{L})^2} \tag{4-6}$$

Table 4-1 lists the uncertainty of the independent variables shown in Equation 4-6 in a typical THW measurement. The overall relative uncertainty of the THW measurement in k_{eff} determination is 2.35%.

Table 4-1. Uncertainty of each variable for k_{eff} measurement using THW

Independent Variable	Relative uncertainty
Current *I*	0.10%
Resistance *R*	0.01%
Voltage *V*	0.66%
Temperature coefficient of resistance β	1.44%
Length of Pt wire *L*	1.72%

The calibration of the THW setup was done by measuring three standard fluids: (1) DI water, (2) Dowtherm A oil, and (3) XCELTHERM 600. As shown in Figure 4.4a, the measured thermal conductivity of DI water, Dowtherm A oil and XCELTHERM 600 at room temperature are 0.6093±0.0084 $Wm^{-1}K^{-1}$ (literature value: 0.6009 $Wm^{-1}K^{-1}$ [47,

48]), 0.1382±0.0006 (literature value: 0.1380 $Wm^{-1}K^{-1}$ [47]), and 0.1366±0.0006(literature value: 0.1359 $Wm^{-1}K^{-1}$ [49]). For XCELTHERM 600, the thermal conductivity was also measured from 20°C to 225°C and was compared to the recommended values, as shown in Figure 4.4b. The standard deviation of each data point shown on the figure is generally less than 0.70%. The deviation of the experimental results from the literature values is < 0.50%. Therefore, the THW setup can be considered well calibrated.

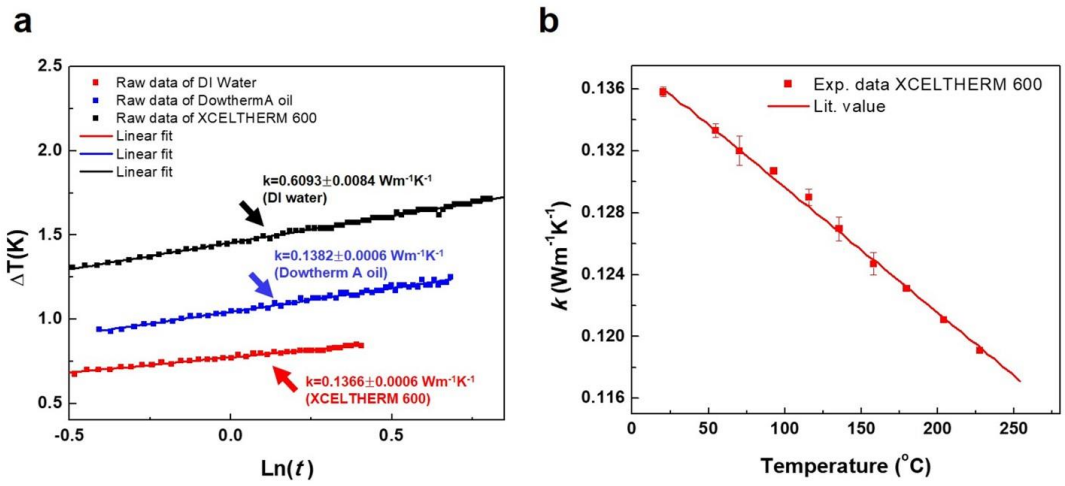

Figure 4-4. Calibration of THW system. (a) Plot of ΔT versus Ln (t) for DI water, Dowtherm A oil, and XCELTHERM 600 at room temperature. The extracted thermal conductivity values are shown next to the plots of each fluid. (b) Calibration results of the THW measurement using XCELTHERM 600 from 20°C to 225°C.

Figure 4.5 shows the MPR measurement setup for stationary particles, modified from the MPR system shown in chapter 2. Although the absorptance for CARBO ceramic particles is high (0.8-0.9[161]), the particle bed cannot hold as a pellet due to the large particle size (~ 300 μm) as our particle holder is vertically oriented. Besides, if the laser is directly irradiating on the particles, the laser can penetrate the voids between particles, leading to the uncertainty of laser absorption length. Therefore, the particles were filled

in a cavity with stainless steel cover. As shown in Figure 4.5a to 4.5c, the MPR holder was a three-layer system, where the particles were contained in a cell with a thin SS316 sheet as the front cover. The front cover was coated 10 μm thick Pyromark 2500 coating for laser adsorption and IR-emission. To ensure one-dimensional heat transfer, the thermal penetration depth should be much greater than the thickness of the steel plate while much smaller than that laser spot size. This is satisfied as the thermal conductivity of steel is high (~ 15-20 W m^{-1} K^{-1}) and the thickness is small (100 μm). The measurement method was similar to that for the bulk materials as shown in chapter 2. At the low frequency limit where L_p is much larger than the thickness of coating and steel, the multilayer model can be simplified as [101,104]:

$$\theta_s = \frac{q_s e^{-\frac{\pi}{4}j}}{e_f\sqrt{\omega}} + q_s R_{cs} \tag{4-7}$$

where e_f is the thermal effusivity of particles, defined as $e_f = \sqrt{k_f \rho_f c_f}$, where ρ_f and c_f are the density and specific heat of the particles, respectively; R_{cs} is the total thermal resistance by the coating and the steel shell:

$$R_{cs} = \left(1 - \frac{e_s}{e_f}\right)\frac{l_s}{k_s} + \left(\frac{1}{2} - \frac{e_c^2}{e_f^2}\right)\frac{l_c}{k_c} \tag{4-8}$$

where e_s and e_c are the thermal effusivities of the steel shell and the coating, respectively; l_s and l_c are the thicknesses of the steel shell and the coating, respectively; k_s and k_c are the thermal conductivities of the steel shell and the coating, respectively. Notably, R_{cs} is independent on the frequency in the low frequency range, therefore effective thermal effusivity of the particles e_f can be directly obtained by measuring the slope of the $|\theta_s|\ vs\ \omega^{-1/2}$ curve according to Equation 4-7. The effective thermal conductivity is

calculated based on the measured thermal effusivities, measured packing densities, and quoted specific heats from references[162,163], i.e., $k_{eff} = \frac{e_f^2}{\rho_f c_f}$.

It is noted that for smaller particles which can hold as a pellet, the front cover can be removed, and the system is reduced to a single-layer similar as for the bulk material measurement. As shown in Figure 4.5d to 4.5f, to show the versatility of the MPR setup, we also measured submicron black spinel oxide particles ($Cu_{0.5}Cr_{1.1}Mn_{1.4}O_4$) using MPR from 200℃ to 700℃, which is the starting material for the black spinel oxide coating we studied in the past [23]. When packed to a property density, the particles tend to coagulate and hold as a pellet as shown in Figure 4.5e. Since the particle bed is intrinsically black, it can be directly heated by the laser and detected by the IR detector without a front cover as shown in Figure 4.5f. Therefore, the particle bed can be treated as a single layer bulk material and the thermal effusivity can be obtained from the slope of the thermal response curve as for the bulk materials:

$$\theta_s = \frac{q_s e^{-\frac{\pi}{4}j}}{e_f \sqrt{\omega}} \tag{4-9}$$

Comparing to Equation 4-7, R_{cs} is missing in Equation 4-9 because it is a single layer system.

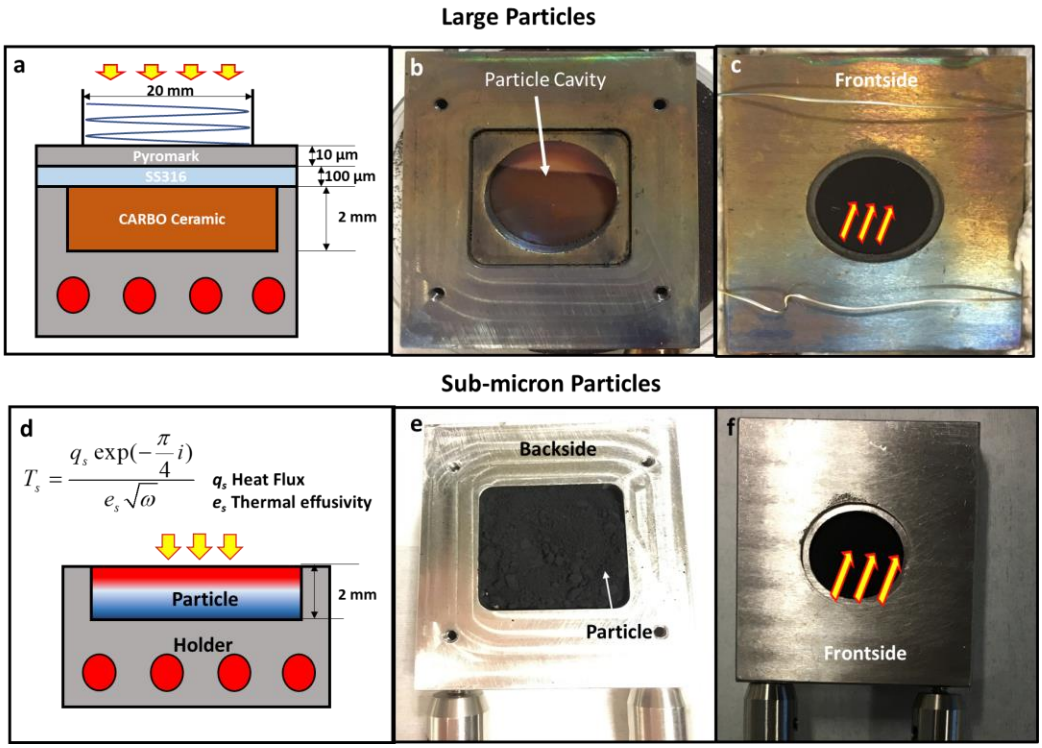

Figure 4-5. MPR holder for stationary particle measurement. Large particles. (a) Schematic of MPR measurement. (b) Cavity of the particle holder. (c) Frontside of the particle holder for laser access and IR-emission. Submicron particles: (d) Schematic of MPR measurement. (b) Cavity of the particle holder. (c) Frontside of the particle holder for laser access and IR-emission.

4.3. Measurement results and discussion

Two types of ceramic particle beds were investigated: (1) CARBOBEAD ID 50 and (2) CARBOBEAD HSP 40/70 (Carbo Ceramics, Inc., Houston, Texas, USA). The general physical properties and material characterization of the ceramic particles were obtained using the following methods. The particle densities (ρ_s) were measured based on the Archimedes' principle, while the apparent density of the particle bed (ρ_b) was determined from the measured weight of the particle bed in the THW holder and its occupied volume in the cavity. The average particle size and the surface morphology were determined by the images taken from FEI Quanta 250 scanning electron microscope

(SEM). Images of 100 particles were analyzed to determine the average diameter d_p, average circularity and roundness using the software imageJ[164-166]. In the software, the boundary of a particle in a SEM image was selected. The distances between the selected boundaries of the particles were then averaged out to obtain the average diameter d_p. Three additional parameters were used to quantify the morphology of the particles: circularity (C), aspect ratio (A_r), and roundness (R). C of a particle is defined as $C = \frac{4\pi A}{P^2}$ where A is the cross-sectional area (as viewed in the SEM images) and P is the perimeter of the particle. A_r is defined as the ratio between the major axis (a) and the minor axis (b) of a particle. R of a particle is defined as $R = \frac{4A}{\pi a^2}$. The chemical compositions of the particles were determined by the Energy Dispersive X-Ray Spectroscopy (EDS) in the SEM. X-ray diffraction (XRD) measurement was performed using the Rigaku Smartlab X-ray diffractometer to obtain the X-ray pattern of each particle for chemical identification. Table 4-2 summarizes the physical and geometrical properties of the ceramic particles. The density of fully dense ceramic particle is around 3500 kg m^{-3}, which is similar to the density of pure Aluminum Oxide (Al_2O_3) (range from 3000 to 3980 kg m^{-3}). This is consistent with the compositional analysis result showing that Al_2O_3 is one of the major constituents in the ceramic particles, with small amounts of SiO_2, Fe_2O_3, and TiO_2, etc. Aged HSP 40/70 particles were also tested to study the possible degradation effect. These aged particles have undergone multiple runs of testing in particle falling towers and heat exchangers at Sandia National Laboratory[167-169], thus having been exposed to high solar flux, attribution, and thermal cycles.

Table 4-2 Summary of the physical and geometric properties of the measured CARBOBEAD ceramic particles

Particle sample	Bulk Density ρ_s (kg m^{-3})	Apparent density ρ_b (kg m^{-3})	Porosity ε	Average diameter d_p (μm)	Circularity C	roundness R	aspect ratio A_r
Fresh ID 50	3530	2015	42.9	275	0.673	0.823	1.270
Fresh HSP 40/70	3480	2164	38.7	404	0.572	0.770	1.548
Aged HSP 40/70	3480	2083	41.0	403	0.508	0.722	1.600

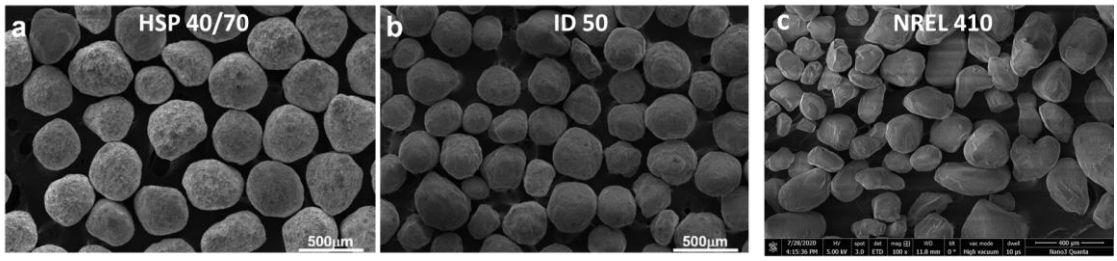

Figure 4-6. SEM images of CARBO ceramics particles and silica sand (a) HSP 40/70, (b) ID50 and (c) silica sand.

Figure 4-6 shows the SEM images of the CARBO HSP 40/70, CARBO ID 50. We also measured the irregular silica sands with the average particle size of 357 μm (NREL 410). Figure 4-7a to c shows the thermal responses of MPR measurement on Carbo HSP 40/70, Carbo ID-50 and Silica 410 particles, respectively, plotted as a function of the amplitude of surface temperature oscillation $|\theta_s|$ vs. $\frac{1}{\sqrt{\omega}}$. With a 100 μm thick stainless 316 front cover and 20 mm diameter laser spot size ($r_0 = 10\ mm$), error introduced by the 2D heat spreading effect is less than 10%, and the thermal masses in the coating and steel plate are negligible in the low-frequency region. As a result, at the low frequency range, the thermal response, $|\theta_s|\ vs\ \omega^{-1/2}$ is expected to be linear, similar to the case of bulk materials. As shown in Figure 4-7a, the thermal response curves can be delineated

into three regions: at low frequency range (long l_p), the thermal response is determined by the properties of particles. The slope in the linear range represents the effective thermal effusivity of particles. Due to the low thermal conductivity of particles compared to the cover and coating, the slope is large. The thermal effusivity of particle is obtained by fitting the data from 1 to 4 Hz with the penetration depth of 200-400 μm.; medium frequency range ($l_c + l_s > l_p > l_c$) where the thermal response is determined by the properties of the steel cover; at higher frequency ($l_p < l_c$), the thermal response only depends on the properties of coating. The thermal effusivity can be similarly obtained from the slope $\Delta T\ vs\ \omega^{-1/2}$, and the thermal conductivity can be calculated based on the specific heat of the same HSP 40/70 and ID50 reported in the literature (Ref.[162]) and that of the Silica in Ref.[163]. All the measurements show similar trend, i.e., at the low frequency, the thermal response is dictated by the properties of particle. Figure 4-7d to 4-7f display the effective thermal conductivities k_{eff} measured from the MPR experiment for HSP 40/70, ID-50 and silica 410, respectively. The k_{eff} measured from the MPR agree well with those obtained from our THW method on the same particles with similar packing densities (2100-2200 kg m^{-3}), with the maximum error < 20%, which validates the accuracy of the MPR measurement on stationary particles.

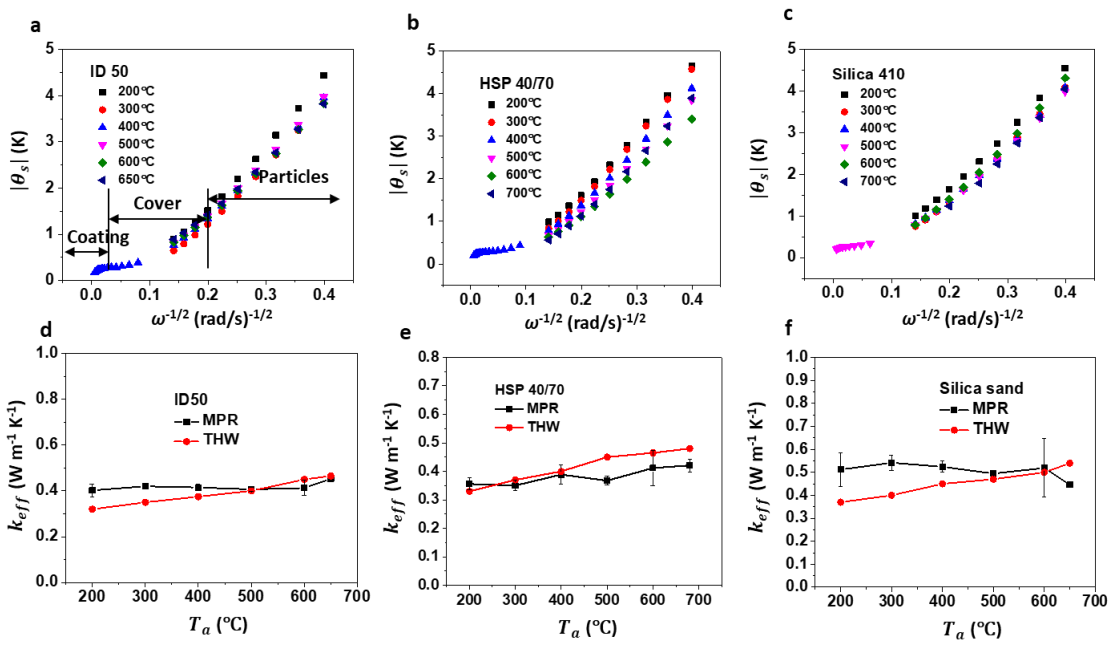

Figure 4-7. MPR measurement of stationary particles in a cell up to 700℃. Thermal responses of (a) HSP40/70, (b) ID-50 and (c) Silica 410. Comparison of Effective thermal conductivities of (d) HSP40/70, (e) ID50 and (f) Silica 410 measured by MPR and THW. The thermal conductivities are calculated based on the measured thermal effusivities, measured packing densities, and quoted specific heats from references[162,163].

We systematically analysed the effective thermal conductivity of CARBO ceramic particles under different gas environment, gas pressure, aging conditions, and temperatures using the THW system, with the aim to provide an abundant database to validate the k_{eff} models of particle bed. The effective thermal conductivity of HSP 40/70 and CP 40/100 under air and N_2 gas is shown in Figure 4-8a. The error bars in the figure include both the standard deviations of measurements of at least three samples for each type of particles and the systematic error obtained from the standard error propagation analysis. Under either air or N_2 gaseous environment, the HSP 40/70 particles with larger d_p possess higher thermal conductivity than CP 40/100. Both HSP 40/70 and CP 40/100 particles show similar k_{eff} between air and N_2 gas environments at 760 Torr. This is

reasonable because the bulk gas thermal conductivity (k_g) of air and N_2 are similar (k_g = 0.00263 $Wm^{-1}K^{-1}$ for air and k_g = 0.00259 $Wm^{-1}K^{-1}$ for N_2 gas at T = 300 K[109]). Therefore, the gas conduction contribution to the overall effective thermal conductivity of the ceramic particles is similar when the gas type is changed from air to N_2 gas.

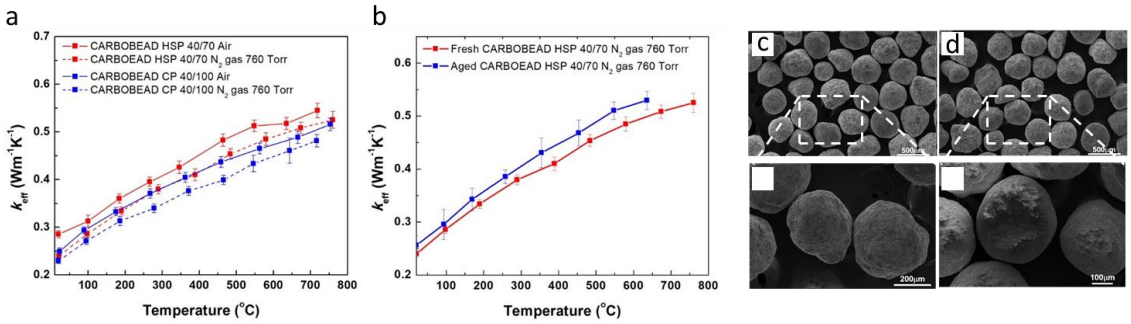

Figure 4-8. Effect of gas environment and aging conditions on k_{eff} of CARBO ceramic particles. (a) k_{eff} of fresh HSP 40/70 and fresh ID 50 under air and N_2 gas environment at 760 Torr. (b) Comparison of k_{eff} between fresh and aged HSP 40/70 under N_2 gas environment at 760 Torr.

Figure 4-8b shows k_{eff} of fresh and aged HSP 40/70 particles under 760 Torr N_2 as a function of temperature. There is no substantial difference in the thermal conductivity between the fresh and aged particles. From the material characterization, including SEM coupled with EDS and XRD (see Figure 4-9 and Figure 4-10 below), there is only minor difference in the particle size and shape between the fresh and aged HSP particles. Despite the cracks and fractures on the surfaces of some aged CARBO particles, which may have been caused by the collisions of particles during the free falling in the receiver during the on-sun tests, they do not change the general particle morphology significantly according to the particle shape analysis shown in Table 4-2. Therefore, the aging condition of the HSP particles has minimal effect on the heat transfer performance of the particle beds.

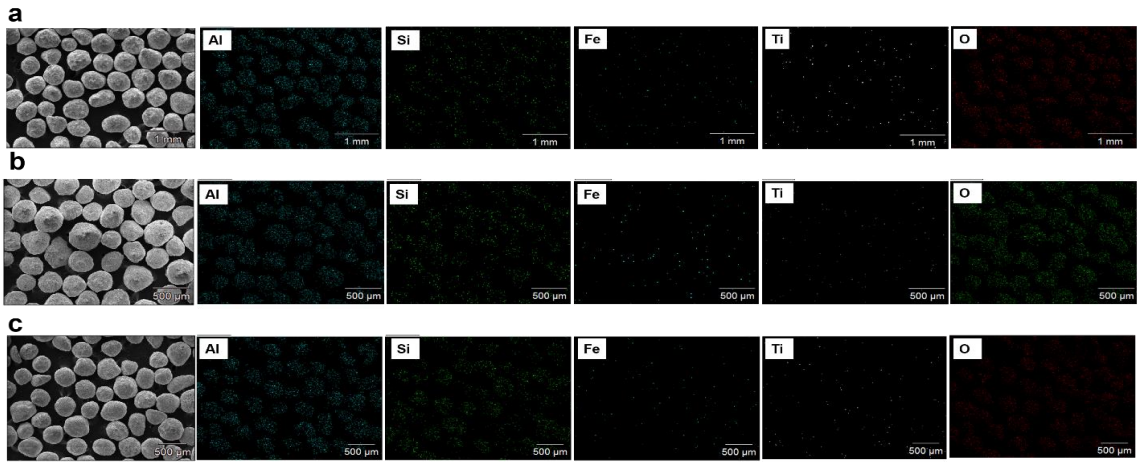

Figure 4-9. SEM-EDS mapping of **(a)** CARBOBEAD HSP 40/70; **(b)** CARBOBEAD CP 40/100; and **(c)** aged HSP 40/70.

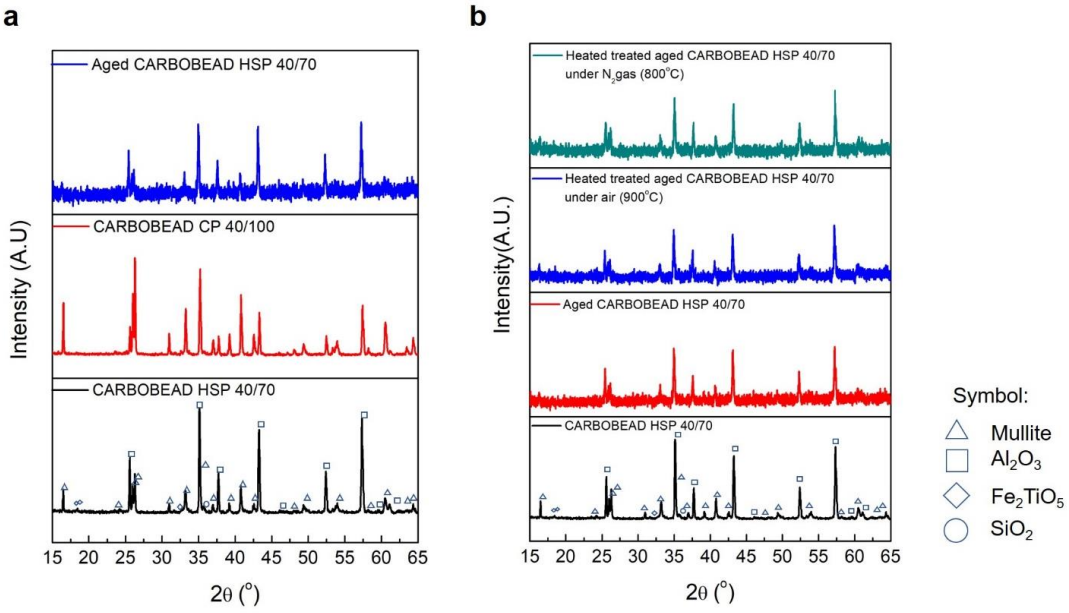

Figure 4-10. XRD Pattern CARBO ceramic particles. (a) CARBOBEAD HSP 40/70, CARBOBEAD CP40/100 and aged HSP 40/70; and (b) Fresh HSP 40/70 compared with aged HSP 40/70 and the heat-treated HSP 40/70 under N_2 gas (800ºC) and air (900ºC) The symbols represent the following phases: mullite (Δ), Al_2O_3 (□). SiO_2 (○) and Fe_2TiO_5 (◊).

The gaseous pressure dependence of k_{eff} of the packed particles are shown in Figure 4-11. Figure 4-11a and 4-11b show k_{eff} of the particles as a function of temperature under N_2 gaseous pressure from 760 Torr to 1 Torr. k_{eff} of the particle beds

drops substantially when the gaseous pressure decreases from 760 Torr to 1 Torr. At 1 Torr, k_{eff} shows a nearly constant value within the measured temperature range. The pressure dependent k_{eff} reveals that solid-to-gas and gas conduction play a dominant role in the entire temperature range. Solid-to-solid conduction, on the other hand, only contributes slightly to the overall thermal conductivity.

Figures 4-11c and 4-11d show k_{eff} as a function of gaseous pressure at 20, 200, and 400℃. The figures again show decreasing trends of k_{eff} with reducing gaseous pressure at all the temperatures for both types of the particles. At the high gas pressure limit (760 Torr), k_{eff} increases with the temperature, principally due to the increasing bulk gas thermal conductivity at high temperatures. At low gas pressure limit (1, 5, and 10 Torr), k_{eff} is greatly reduced with little to no temperature dependence below 400℃, as evidenced by the overlapped data below 10 torr in Figures 4-11c and 4-11d. This is because at low gas pressure and low-to-intermediate temperatures, the gas contribution is diminished and thermal radiation contribution is very small, and thus, k_{eff} is only a function of the solid conduction, which has weak temperature dependence. We also showed the k_{eff} modeled by the Zehner, Bauer, and Schlünder (ZBS) model which is one of the widely used models to predict the k_{eff} of stationary particle bed. The details of the modeling could be found in the next section.

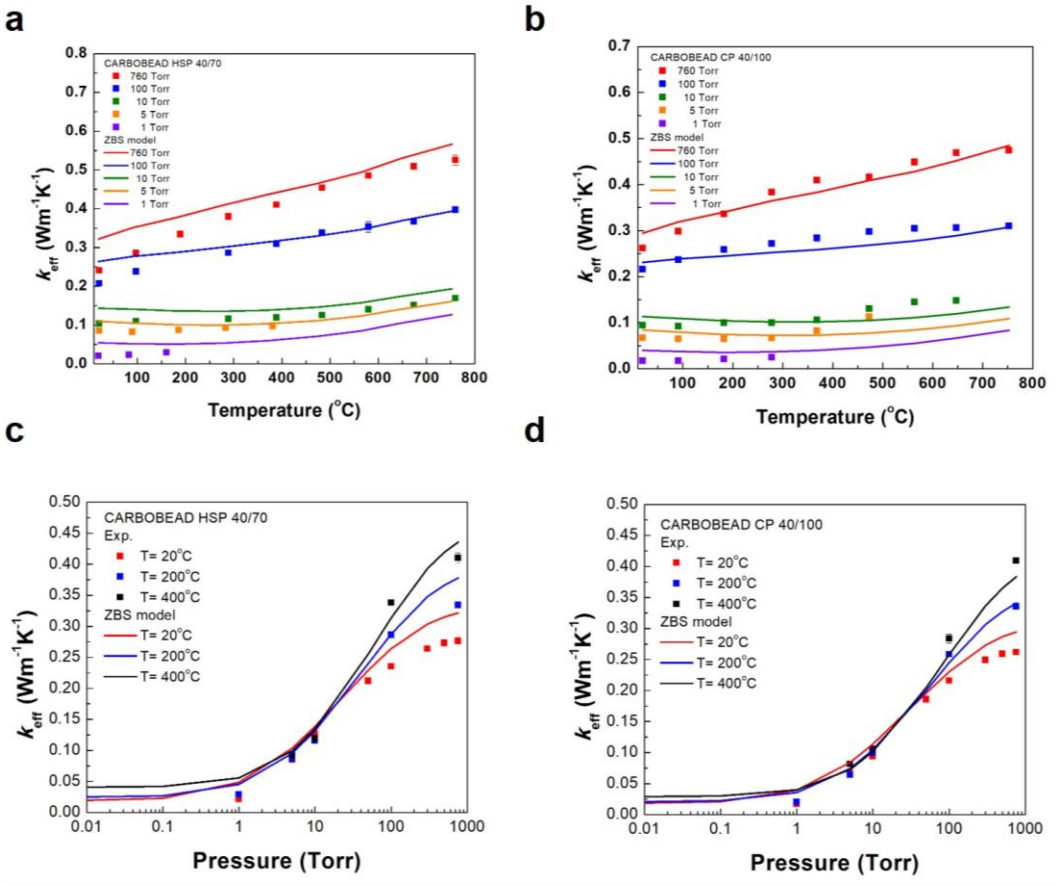

Figure 4-11. Effective thermal conductivity (k_{eff}) as a function of temperature for (a) CARBOBEAD HSP 40/70 and (b) CARBOBEAD CP 40/100 under different N_2 pressures, 760, 100, 10, 5 and 1 Torr; effective thermal conductivity (k_{eff}) as a function of gas pressure for (c) CARBOBEAD HSP 40/70 and (d) CARBOBEAD CP 40/100 at different temperatures, including 20 °C, 200 °C and 400 °C.

4.4. Thermal conductivity modeling of stationary particle bed

4.4.1. Conventional model based on simple cubic structure

The Zehner, Bauer, and Schlünder (ZBS) model is one of the widely used models to predict the k_{eff} of stationary particle bed. The ZBS model is based on simple cubic structure and has been proved to be suitable for large particles[121,123,170,171]. Although the ZBS model has been used to predict the thermal conductivity of HSP 40/70 and CP 40/100[123], it is yet to be validated with experimental measurements. In addition, due to

the uncertainty in the fitting parameters, the contributions of different heat transfer modes are still not accurately quantified.

The ZBS model was employed to fit the experimental results of the effective thermal conductivity of HSP 40/70 and CP 40/100, as a function of temperature and gaseous pressure. In the ZBS model, k_{eff} is given by[121]:

$$\frac{k_{eff}}{k_f} = \left[1-(1-\varepsilon)^{\frac{1}{2}}\right]\varepsilon\left[\left(\varepsilon-1+\frac{1}{\lambda_G}\right)^{-1}+\lambda_r\right]+(1-\varepsilon)^{\frac{1}{2}}[\varphi\lambda+(1-\varphi)\lambda_c] \quad (4\text{-}10)$$

where k_f is the thermal conductivity of the bulk gas at the corresponding pressure and temperature, ε is the porosity of the packed particle beds, and φ is the empirical contact fraction of the solid particle. The dimensionless parameters, λ_G, λ_r, and λ, correspond to the heat transfer processes through gas conduction, radiation, and solid conduction at the contact region, respectively. For the gas conduction,

$$\lambda_G = \frac{k_G}{k_f} = \left[1+(\frac{l}{d_p})\right]^{-1} \quad (4\text{-}11)$$

where k_G is the thermal conductivity of gas within the particle bed and l is the modified mean free path of the gas molecules, which can be calculated at a given temperature and pressure by following[121]. For the radiation parameter,

$$\lambda_r = \frac{4\sigma}{(\frac{2}{\varepsilon_r}-1)}T^3\frac{d_p}{k_f} \quad (4\text{-}12)$$

where σ and ε_r are Stephan-Boltzmann constant and emissivity of the particles, respectively. For the solid conduction parameter,

$$\lambda = \frac{k_s}{k_f} \quad (4\text{-}13)$$

and

$$\lambda_c = \frac{2}{N}\left\{\frac{B(\lambda+\lambda_r-1)}{N^2\lambda_G\lambda} ln\frac{\lambda+\lambda_r}{B[\lambda_G+(1-\lambda_G)(\lambda+\lambda_r)]}\right. \quad (4\text{-}14)$$

$$\left. + \frac{B+1}{2B}\left[\frac{\lambda_r}{\lambda_G} - B\left(1+\frac{1-\lambda_G}{\lambda_G}\lambda_r\right) - \frac{B-1}{N\lambda_G}\right]\right\}$$

where $B = 1.364(\frac{1-\varepsilon}{\varepsilon})^{1.055}$ is the deformation parameter and $N = \frac{1}{\lambda_G}\left(1+\frac{\lambda_r - B\lambda_G}{\lambda}\right) - B\left(\frac{1}{\lambda_G}-1\right)\left(1+\frac{\lambda_r}{\lambda}\right)$.

There are five parameters in the ZBS model: d_p, $\varepsilon, \varepsilon_r, k_s$ and φ. Among these, d_p, $\varepsilon, \varepsilon_r$, and k_s are experimentally determined: The measured thermal conductivity of fully dense bulk of the same CARBO ceramic material is shown in Figure 4-12. The fully dense CARBO ceramic pellet was prepared by hot pressing and the density is > 99%. Figure 4-12a show the thermal diffusivity (α_s) measured using the LFA, and the measured thermal conductivity of the CARBO ceramic pellet (k_P) determined from $k_P = \alpha_s \rho_p c_p$ of the pellet deceases from ~6.50 $Wm^{-1}K^{-1}$ to ~4.50 $Wm^{-1}K^{-1}$ as the temperature increases from 20℃ to 800℃, where ρ_p is the density of fully dense pellet and c_p is the specific heat of CARBO ceramic materials as shown in Figure 4-12b, which was measured by differential scanning calorimetry (DSC). The deceasing trend is consistent with the typical thermal conductivity of bulk solids with similar compositions (*i.e.*, Al_2O_3 and SiO_2). k_p is converted to k_s of a fully dense solid with the consideration of the porosity of the pellet (> 99%) using the effective medium theory; ε and d_p are obtained from Table 4-2, thermal emittance ε_r is extracted from Ref.[19] where ε_r is 90.8% for HSP 40/70 and is 86.8% for CP 40/700, leaving φ as the only fitting parameter, which was

obtained by fitting the modeling results to the experimental results for both types of particles at all the test temperatures and gas pressures, resulting in φ = 0.0031.

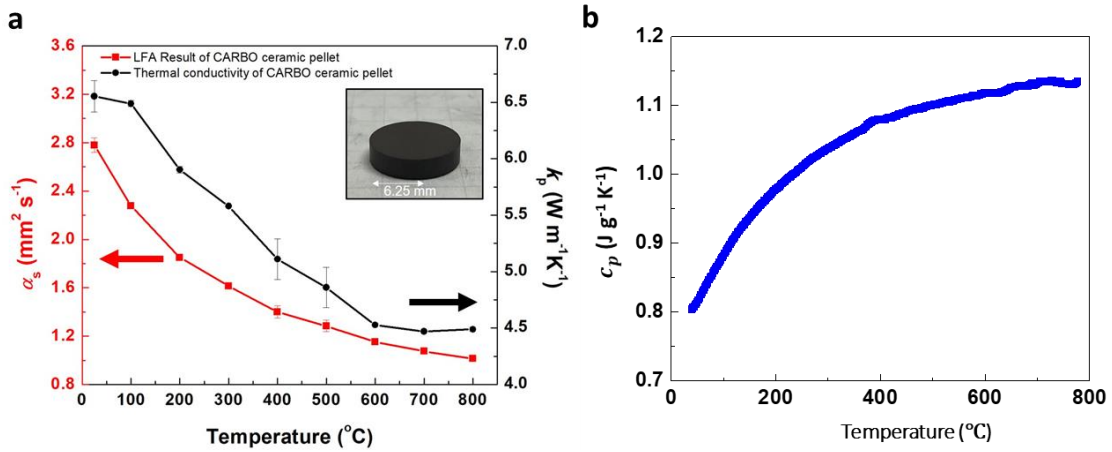

Figure 4-12. Measurement of bulk properties of CARBO ceramic pellet. (a) Measured thermal diffusivity (α_s) and thermal conductivity (k_P) of the CARBO ceramic solid pellet based on the LFA measurement. Inset: photograph of the solid pellet made from CARBOBEAD CP particles via hot pressing. (b) specific heat of CARBO ceramic particles measured by DSC.

The results from the ZBS model are shown alongside with the experimental data in Figure 4-11. The ZBS model can well capture the effective thermal conductivity of both HSP40/70 and CP 40/100 packed particle beds as function of temperature and gaseous pressure. For example, the curves representing the ZBS model in Figure 4-11a and 4-11b show substantial decrease in the thermal conductivity when the gas pressure changes from 760 Torr to 100, 10 and 1 Torr. From Figure 4-11c and 4-11d, the ZBS modeling results accurately predict the measured $k_{eff}$of HSP 40/70 and CP 40/100 in most of the gas pressure range except at 1 Torr. At 1 Torr, however, the ZBS model tends to overestimate the k_{eff} compared to the measured values. The overestimation by the ZBS model at the lowest gas pressure levels is not surprising because at this gas pressure level, gas conduction is greatly diminished and the solid conduction becomes more important, which can be highly dependent on the exact packing structure of the particles.

However, the ZBS model is based on a simple cubic arrangement of the particles, whereas the particle arrangement is random and more complex. This is evident from the difference between the experimental porosity ($\varepsilon \sim 38.7 - 42.9\%$, Table 4-2) and that of a simple cubic structure (ε is expected to be 48%). The lower porosity of the actual packing structure is possibly the cause of the overestimated thermal conductivity by the ZBS model at 1 Torr. The modeling of k_{eff} of the packed particles at this gas pressure requires a more realistic treatment of the particle packing structure, which is not within the scope of this study and warrants further investigation. Nevertheless, at higher gaseous pressures, especially at 760 Torr at which the particles are expected to be used in CSP systems, the gas conduction is the dominant heat transfer model and the effect of the packing structure is less important. This explains the applicability of the ZBS model at higher gaseous pressure despite its simplicity.

With this applicability in mind, we use the ZBS model to understand the roles of different heat transfer modes in particle beds under normal operation pressure of 760 Torr. Figure 4-13 shows the calculated effective thermal conductivity of the two types of the particles using the ZBS model and differentiates the contributions from solid conduction, gas conduction and thermal radiation. Based on Figure 4-13, gas conduction in these particle beds contributes to more than 80% of the total k_{eff} in the whole temperature range; solid conduction from particle-to-particle, on the other hand, contributes to around 5% of the total effective thermal conductivity at room temperature, with its relative contribution decreasing due to the increasing total thermal conductivity. Regarding the thermal radiation contribution, it is not important until at elevated temperatures. At 800^{o}C, around 15% (in HSP 40/70) and 11% (in CP 40/100) of the total

k_{eff} is contributed from the radiation heat transfer. The slightly larger radiation contribution in HSP 40/70 at 800 ^{o}C is due to the larger particle sizes, which lead to larger void sizes for longer photon propagation length. Nevertheless, in both types of particles, thermal radiation plays an insignificant role, due to the limited photon propagation length (optically thick) within the particle beds, which is caused by the high absorptance of the particles and the relatively small void size between the particles (comparable to the particle size, d_p). The analysis also suggests possible strategies to further enhance the thermal conductivity of the particle beds, *e.g.*, by filling the voids in the particle beds with smaller particles to increase the gaseous thermal pathways bridging solid particles.

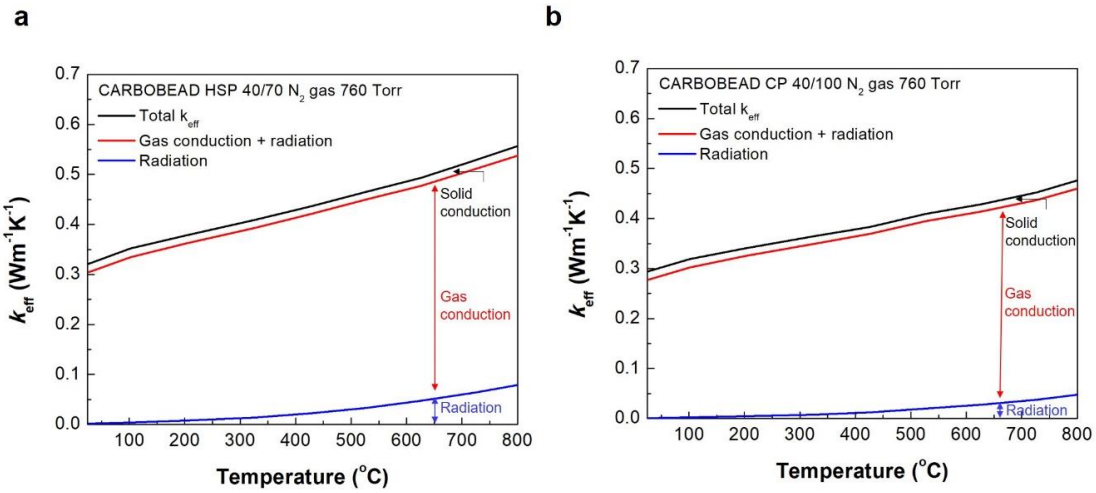

Figure 4-13. Plot of effective thermal conductivity prediction by the ZBS model to show the individual contribution from solid conduction, gas conduction and thermal radiation. (a) CARBOBEAD HSP 40/70; and (b) CARBOHEAD CP 40/100, under N_2 gas environment at 760 Torr.

4.4.2. Discrete element model for random packing structure

(a) Characterization and experimental method

As shown in the last section, the conventional k_{eff} models based on the simple cubic structure failed to capture the real packing of stationary particle bed and thus could not predict the k_{eff} at low pressure where the solid condition dominated. While much effort has been paid to include more details of the heat transfer pathway in the simple cubic framework to improve the models, the key to accurately model the k_{eff} is to acquire the realistic packing structure of particle bed. In this work, mono-dispersed silicon dioxide (SiO_2) microsphere particles of different sizes (~23 μm, ~67 μm and ~330 μm) were chosen as a model system to study the heat transfer mechanisms in pack particles. The effective thermal conductivity of the SiO_2 microspheres were experimentally determined by using a high-temperature transient hot-wire (THW) setup, in the temperature range of room temperature to ~500^{o}C. Gaseous pressures of the particle beds were systematically varied to tune the contribution from the gas pathway. We then developed a model using the discrete element method (DEM) to predict the packing structure of the particles, which is then incorporated into a COMSOL based finite element model (FEM) to predict the effective thermal conductivity. The DEM can simulate a more realistic three-dimensional (3D) structure of the mono-dispersed particles with the input of experimentally determined parameters. The simulation results based on the packing structure obtained from DEM shows excellent agreements with the experimental results within the entire temperature and gaseous pressure ranges, whereas the model based on a simple cubic packing structure shows large discrepancies with the experimental results.

Amorphous silica microspheres (Cospheric LLC, inc) with three different average particles sizes (23 μm, 67 μm and 330 μm) were chosen as the model system due to the near mono-dispersed nature of the particle size and the well-known properties of amorphous silica. The same microspheres were used and k_{eff} in vacuum was reported by Sakatani *et al.*[144], but in this work we measured and modeled k_{eff} of these particles under different gaseous pressures. The scanning electron microscopy (SEM) images of the particles are shown in Figure 4-14a. It can be seen that the particles are near-perfect spheres with smooth surface. To determine the particle size of the microspheres, the mean diameters of the particles are obtained by averaging the sizes of 100 particles in the SEM images. As shown in Figure 4-14b to 4-14d, the particle sizes follow the Gaussian distribution with a narrow deviation (< 10% of the mean particle diameters). The average particle sizes are measured to be 23±2.7 μm, 67±4.1 μm and 330±22.8 μm, respectively. Considering the small deviation of the particle size, it is reasonable to treat these particles as mono-dispersed microspheres in the modeling. The particles were also examined by the X-ray diffraction (XRD) as shown in Figure 4-14e. Evidently, these particles are amorphous silica. As such, the bulk thermal conductivity of amorphous SiO_2[172] is used (e.g., ~ 1.5 W m^{-1} K^{-1} at room temperature) for the modeling.

The effective thermal conductivity k_{eff} of the particle beds was measured using the same THW apparatus as the last section. The volume of the particles in the THW holder is $11.6 \times 1.5 \times 0.97$ cm^3. To systematically measure k_{eff} at different temperature up to 500℃ and gaseous pressure from 20 to 760 Torr, the THW test section was placed in a tube furnace equipped with N_2 gas supply and a pressure control system. In the THW measurement, the experimentally measured effective thermal conductivity ($k_{eff,exp}$) of

the particle bed was obtained from the transient temperature rise after applying a constant heat flux with the assumption of line heat source in an infinite medium.

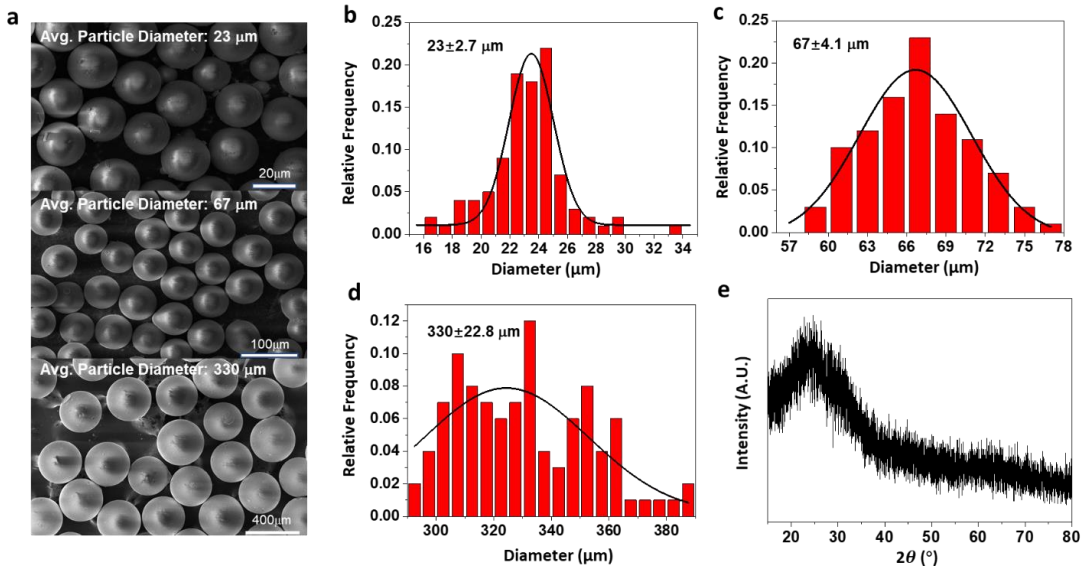

Figure 4-14. Characterization of SiO2 microspheres. (a) SEM images of SiO_2 microspheres. Particle size distribution of SiO_2 microspheres with average diameter of (b) 23 μm, (c) 67 μm and (d) 330 μm. (e) XRD pattern of SiO_2 microspheres.

(b) Discrete element modeling

We carried out DEM simulation using the LIGGGHTS package [LAMMPS (Large-scale Atomic/Molecular Massively Parallel Simulator) Improved for General Granular and Granular Heat Transfer Simulations][173]. To obtain the real packing structure of the particle beds, a rectangular container with the dimension of $15D \times 15D \times 20D$ $(L \times W \times H)$ was chosen as the simulation domain, where D is the particle diameter, as shown in Figure 4-15a. The dimension was set in order to reduce the computational complexity while avoiding the near wall effect [174-176]. The simulation domain was empty before the simulation as shown in Figure 4-15a at t = 0, with the particle injected from the top surface of the domain set with the dimension of $14D \times$

$14D$ $(L \times W)$. To randomly generate particles in the insertion surface, several prime numbers larger than 10000 were selected as seeds. In the simulation, the particles were generated with an initial downward velocity (v_0) of $\sim 0.1\ m\ s^{-1}$ and a global downward gravity $g = 9.81 m\ s^{-2}$ as shown in Fig. 4-15(a) at t_1 = 3.4 ms. The bottom of the domain served as the stopping surface and thus the particles were piled up from bottom to the top in the random fashion as shown in Fig. 4-15(a) at t_2 = 26.3 ms. The simulation stopped when the entire domain was filled with particles, denoted as the equilibrium state in Figure 4-15a.

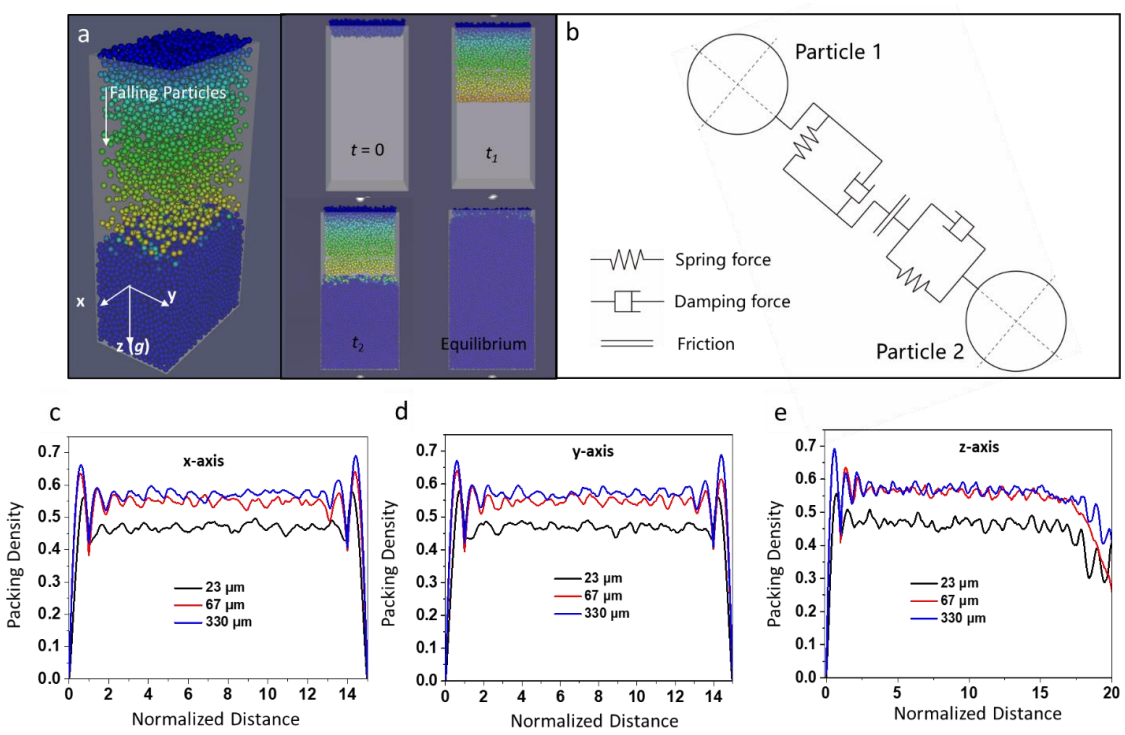

Figure 4-15. DEM simulation of packing structure. (a) Snapshots of randomly packed SiO_2 microspheres at different time. (b) Schematic of the forces between two adjacent particles in DEM. Distribution of packing density at (c) *x* direction (d) *y* direction and (e) *z* direction.

The particle properties for the simulations were based on the real particles (silica) used in our experimental measurements. The density $\rho = 2600\ kg\ m^{-3}$ indicated the

particle inertia. The Young's Modulus $E = 72\ GPa$, the Poisson's Coefficient $\nu = 0.278$, the Restitution Coefficient $C_R = 0.7$ and the Friction Coefficient $C_F = 0.3$ represented the inter-particulate contact behavior [177]. In addition, the cohesive energy density $e_{cohesive}$, implying the amount of energy needed to separate unit volume of particles, was applied to reflect the adhesive force between the particles at the interface [178,179]. We assumed that the cohesive energy density has the form of $e_{cohesive} = a \times D^{-b}$ and the parameter pair (a, b) is adjusted to get the optimum values of a = 0.25 and b = 2 so that the modeled density is close to the experimental value while the physical explanation is yet to be explored. Therefore, this property was optimized so that the simulated packing densities for all the three particles were close to the experimental values. The DEM simulation parameters are listed in Table 4-3. Thermal conductivities of bulk silica and N_2 gas are shown in Figure 4-16.

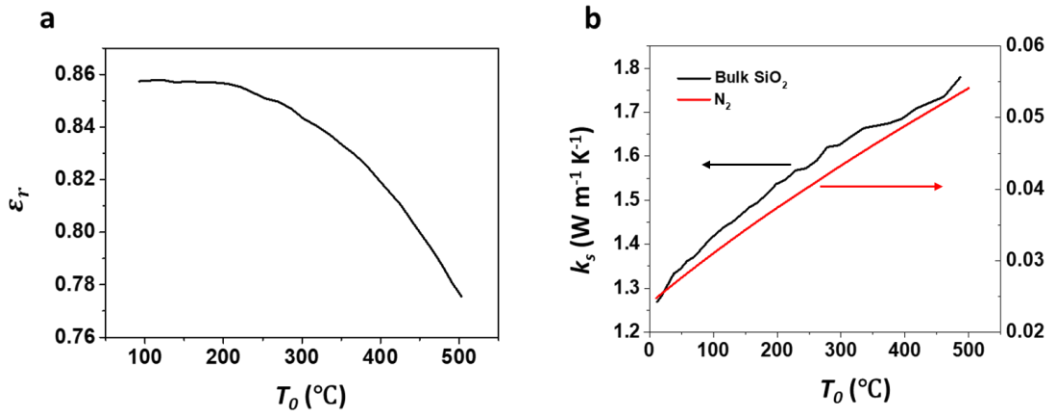

Figure 4-16. Parameters used for modeling of thermal conductivity. (a) Thermal emittance of SiO_2 [180]. (b) Bulk thermal conductivity of amorphous SiO_2[172] and N_2 gas.

Table 4-3. Simulation Parameters for DEM modeling

Parameters	Values
Particle Diameter	D
Skin Distance	$D/2$
Time Step	2.5×10^{-10} $[sec]$
Young's Modulus	72 $[Gpa]$
Poisson's Ratio	0.278
Coeff. Of Restitution	0.7
Coeff. Of Friction	0.3
Cohesion Energy Density	$0.25 \times D^{-2}$ $[J\ m^{-3}]$
Particle Density	2600 $[kg\ m^{-3}]$
Gravity	9.81 $[m\ s^{-2}]$
Initial Velocity	0.1 $[m\ s^{-1}]$

The Hertz contact model was implemented for modeling the contact force. This contact force can be divided into normal and tangential components Equation 4-15 and Figure 4-15b.

$$F_{contact} = F_{normal} + F_{tangential} \tag{4-15}$$

The normal force includes a spring force and a damping force, while the tangential force includes a shear force and a damping force. Each force was computed from the amount of overlap and the relative velocity between particles.

$$F_{normal} = F_{spring} + F_{damping,n} \tag{4-16}$$

$$F_{tangential} = F_{shear} + F_{damping,t} \tag{4-17}$$

F_{shear} in Equation 4-17 is proportional to the tangential displacement at the contact point, which can be calculated by integrating the relative velocity in the tangential direction over time. To take the shear force into account, we selected *tangential history* in the LIGGGHTS simulation. In addition, a simplified J-K-R (SJKR) model is used to include an additional normal force, which tends to keep particles in contact. With the

SJKR model and the definition of cohesive energy density, we simulated the cohesive effect. To ensure the accuracy, we defined the neighboring distance as the radius of the particle and set the time step less than 10% of the Rayleigh/Hertz time in our simulation. Once the simulation finished (i.e., all the particles were stable), the coordinates and velocity of each particle were saved as .txt files to extract the packing structure of particle bed to be imported into a COMSOL model.

Figure 4-15c to 4-15e show the packing structure of the loosely packed silica microspheres in the *x*, *y* and *z* directions, respectively. The normalized packing density is plotted as a function of the normalized distance by the particle diameter (i.e., *L*/*D*, where *L* is the real distance). It is noted that Figure 4-15c and 4-15d show the similar packing structures as the particle bed is symmetric in the lateral directions while Figure 4-15e shows packing structure in the vertical direction, with $z = 0$ as the bottom surface. As shown in Figure 4-15c and 4-15d, the near-wall effect exists within two particle sizes away from the wall, where the packing density oscillates, which agrees with the observations in the literature [174-176] as shown in Figure 4-17.

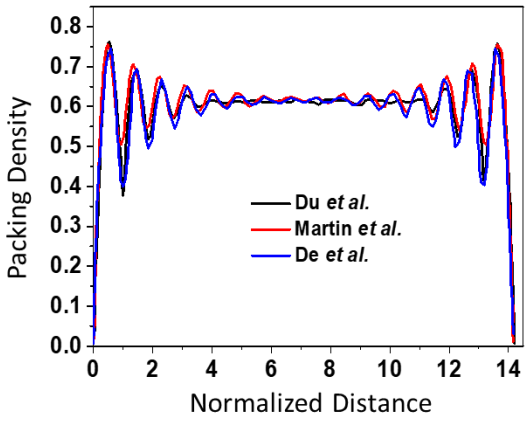

Figure 4-17. Packing structure of monodispersed particle bed to the literature. [174-176]

The packing density stabilizes in the bulk particle bed (i.e., more than two particles away from the wall). It is seen that the packing density decreases with the particle size increasing from 23 μm to 330 μm. As shown in Figure 4-15e, there is also near-wall effect close to the bottom surface within two particles away from the wall. Except that the packing density decreases close to the top surface because this surface is unconstrainted with continuous inflow of particles, the packing structure in the *z* direction is similar to that in the *x* and *y* directions, indicating that the packing structure is homogeneous in the bulk. As shown in Table 4-4, the average bulk packing density is 0.57, 0.55 and 0.46, respectively for 23 μm, 67 μm and 330 μm particles, respectively, which is closed to that measured in the experiment. The theoretical packing density of simple cubic structure is calculated to be 0.52 and is invariant with particle size. Evidently, the simple cubic structure fails to predict the packing density of real particle bed.

Table 4-4. Comparison of average packing density of SiO_2 particle bed.

Packing Structure	Packing Density (%)		
	D = 330 μm	D = 67 μm	D = 23 μm
Experiment	0.57	0.55	0.43
Random (DEM)	0.57	0.55	0.46
Simple Cubic (SC)	0.52	0.52	0.52

(c) Modeling of Effective Thermal Conductivity

Effective thermal conductivity of particle bed is contributed by gas conduction, solid conduction via contacts between particles, and radiation heat transfer. The modeled effective thermal conductivity ($k_{eff,calc}$) consists of two parts: solid and gas thermal

conductivity ($k_{s,g}$) modeled using COMSOL and radiation thermal conductivity (k_r) modeled analytically based on the optical properties of silica.

$$k_{eff,calc} = k_{s,g} + k_r \tag{4-18}$$

The coordinates of all the particles were extracted from the DEM simulation as the input into the COMSOL model to compute $k_{eff,calc}$. As shown in Figure 4-18a, a $4D \times 4D \times 4D$ ($L \times W \times H$) cube was chosen as the COMSOL simulation domain, which was truncated from the middle of the particle bed with a distance of at least two particles away from the walls to avoid the near wall effect. Since the packing structure is homogeneous as shown in Figure 4-15, the simulation result is insensitive to the particular position of the chosen domain, which is proven by the grid independence test in Figure 4-19. The cube contains ~140 sphere SiO_2 particles and the contact area between the particles was automatically given by the particle coordinates data from the DEM simulation based on the Johnson-Kendall-Robert (JKR) theory[181] using the mechanical properties of SiO_2. The gas gap between the particles is filled with N_2 with the Kapitza resistance (R_K) applied to the gas-solid interface:

$$R_K = \frac{2-\alpha}{\alpha}\frac{2}{\gamma+1}\frac{L}{\mu C_v} \tag{4-19}$$

where α is the accommodation coefficient (assumed to be 1 here), γ is the specific heat ratio of the N_2 gas (1.4), μ is the viscosity of the gas, C_v is the specific heat of the gas at a constant volume and L is the mean free path of the gas. For comparison, a $4D \times 4D \times 4D$ cube based on the simple cubic (SC) packing of silica microspheres was also established as shown in Figure 4-18b. For both models, the bottom surface was set at the ambient temperature T_0 and the top surface was set at $T_1 = T_0 + 1K$ to create a temperature gradient along the vertical direction. Other boundaries were set as symmetric boundary.

The heat flux q_s was extracted from the bottom surface and the conduction thermal conductivity is calculated by:

$$k_{s,g} = \frac{Hq_s}{T_1 - T_0} \tag{4-20}$$

where H is the height of the simulation domain ($H = 4D$).

The radiative thermal conductivity k_r is modeled based on the solid-to-solid radiative heat transfer between two particles which is valid for opaque materials in the IR spectrum of interest ($\leq \sim 600$ μm) [121,123,129]:

$$k_r = \frac{4\sigma}{(\frac{2}{\varepsilon_r} - 1)} T_0^3 \tag{4-21}$$

where σ is the Stephan-Boltzmann constant, and ε_r is the thermal emittance of silica quoted from Ref.[180], as shown in Figure 4-16b. This model has been proven valid for black ceramic particles with the particle sizes $< \sim 600$ μm[121,123]. With the $k_{s,g}$ and k_r, the total effective thermal conductivity $k_{eff,calc}$ was then calculated using Equation 4-18.

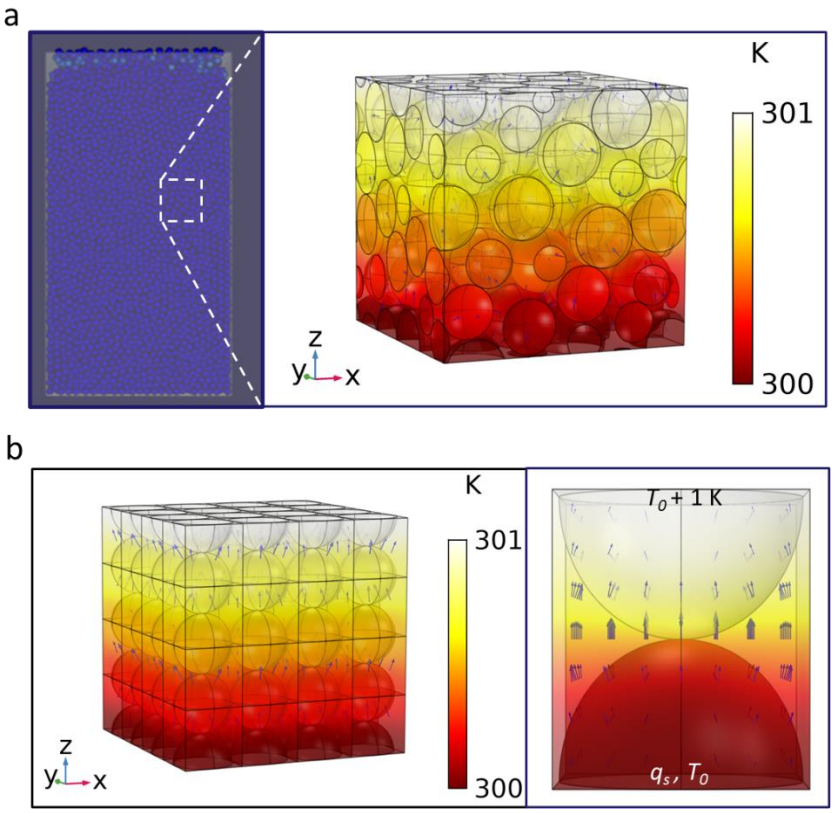

Figure 4-18. COMSOL simulation of thermal conductivity of SiO_2 particle bed based on (a) random packing structure obtained from the DEM simulation and (b) simple cubic (SC) structure.

Figure 4-19 shows the simulated thermal conductivity of three $4D \times 4D \times 4D$ units extracted from three different positions of the same particle bed obtained in the DEM. Position #1 is shown in Figure 4-18a. Position #2 is four particle diameters away from the edge of the position #1 in the x direction while Position #3 is four particle diameters away from the edge of the position #1 in the z direction. The simulation is conduction in N_2 at 760 Torr in the same fashion as shown in Figure 4-18a. The thermal conductivity does not change with the selected position, which validates the grid independence of our simulation.

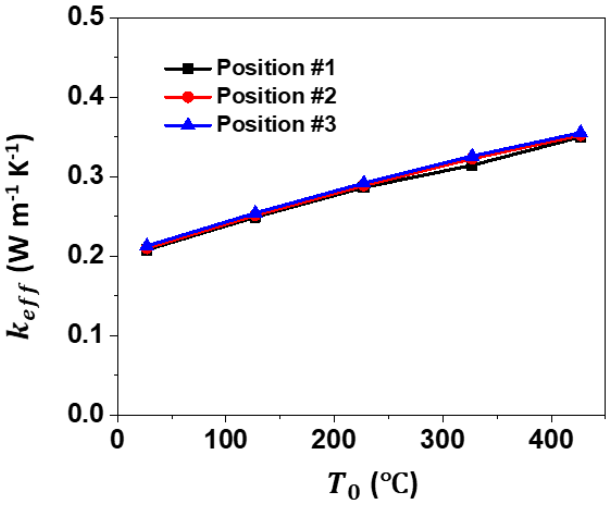

Figure 4-19. Comparison of thermal conductivities of three randomly packed bed selected from three different positions in the same particle bed obtained from DEM in 760 Torr N_2 environment for grid independence verification.

(d) Results and Discussions

Figure 4-20a to 4-20c show the experimental results of silica microspheres bed with the particle size of 23 μm, 67 μm and 330 μm, up to 500℃ under the N_2 gas environment with the gaseous pressure from 20 to 760 Torr. The maximum temperature was set to avoid the phase change and sintering of silica microspheres. For all the particles at 760 Torr, k_{eff} increases with increasing temperature mainly due to the enhanced gas conduction and a slight increase in k_r at higher temperature. It is noted that the radiation contribution is much less significant compared to the gas conduction within the temperature range in our measurement, which is shown by the fact the $k_{eff,exp}$ at 20 Torr is independent of temperature for the 23 and 67 μm particles and only slightly dependent on the temperature for the 330 μm particles because at this pressure, the gas conduction is suppressed. Previous studies indicate that the characteristic length scale for gas conduction $L_g \approx \frac{D}{7}$ instead of D because the gas bridge close to the contact point

dominates the gas conduction[142]. Therefore, L_g is ~ 3.3 μm, ~ 9.6 μm and ~ 47 μm for the 23 μm, 67 μm and 330 μm particles, respectively. For the 23 μm microspheres, the gas conduction is completely suppressed at 20 Torr (i.e., mean free path of N_2 at 20 Torr and room temperature is 2.3 μm, comparable to L_g). Therefore, it can be concluded that the contribution of the solid conduction to total k_{eff} for the 23 μm particles is less than 0.05 W m^{-1} K^{-1}. For the 67 μm and 330 μm particles, the gas conduction is not completely suppressed at 20 Torr, so k_{eff} at this pressure is higher than that of the 23 μm particles.

The modeled effective thermal conductivity ($k_{eff,calc}$) based on the simple cubic structure and the random packing structure by DEM is compared to the experimental results in Figure 4-20a to 4-20c. As shown in Figure 4-20a for the 23 μm particles, the modeling result based on the simple cubic structure is higher than the experimental one at all the temperatures and gas pressures while the results based on the random packing structure agree better with the experimental results. The reason is that the simple cubic structure overestimates the conduction heat transfer via the solid-solid pathway, caused by the overestimation of the particle packing density as shown in Table 4-4. This is clearly shown in the overestimation of k_{eff} at 20 Torr where the solid conduction k_s become relatively more important than the gas conduction k_g. As shown in Figure 4-20b for the 67 μm particles, both the simple cubic and random packing models capture the experimental results well because both models predict the real packing density of the particles of this size as shown in Table 4-4. As shown in Figure 4-20c for the largest particle size (330 μm), contrary to that for the 23 μm particles, the model based on the simple cubic structure underestimates k_{eff} while the model based on the random

structure agree well with the experimental results because the simple cubic structure underestimates the packing density of the large particles as shown in Table 4-4.

Figure 4-20d to 4-20f compare k_{eff} as a function of gas pressure of the three particle beds at 27℃, 220℃ and 420℃ respectively. It is seen that the random packing model captures the trend well for all the particle size and temperatures. Although the simple cubic model can roughly capture the k_{eff} trend for the large particles, it deviates drastically from the experimental results as the particle size decreases because the solid conduction become more significant as the particle size decreases, which strongly relies on the accurate packing structure.

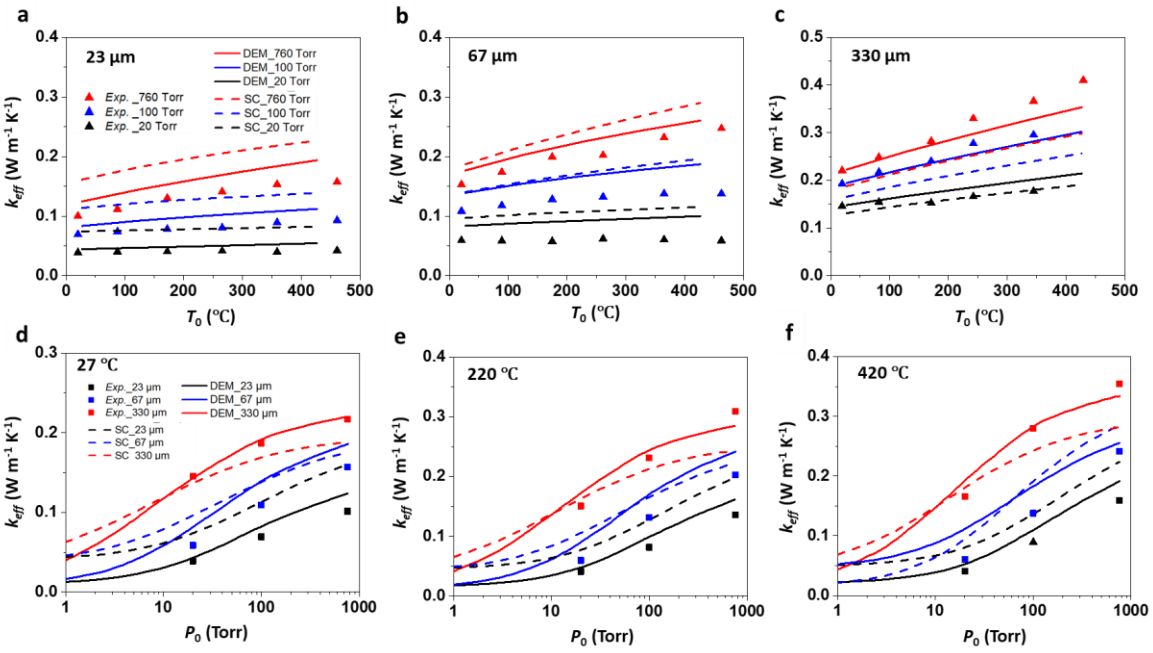

Figure 4-20. Comparison of experimental and simulated thermal conductivity of SiO2 based on simple cubic (SC) packing and DEM random packing. Thermal conductivity of SiO_2 particle bed as a function of temperature at different gaseous pressures for the diameter of (a) 23 μm, (b) 67 μm and (c) 330 μm particles. Thermal conductivity of SiO_2 with different particle sizes as a function of N_2 gaseous pressure at (d) 27℃, (e) 220℃ and (f) 420℃.

To quantify the deviation of the simulated thermal conductivity from the experimental values based on the simple cubic and DEM random packing structures, we define the relative deviation Δ_k as

$$\Delta_k = \left| \frac{k_{eff,calc} - k_{eff,exp}}{k_{eff,exp}} \right| \tag{4-22}$$

where $k_{eff,exp}$ is the experimentally measured thermal conductivity (Equation 4-3) and $k_{eff,calc}$ is the modeled thermal conductivity (Equation 4-18). Figure 4-21a to 4-21c show the Δ_k for 23 μm, 67 μm and 330 μm microspheres, respectively at various temperatures and pressures. It is evident that Δ_k for the DEM model is significantly smaller than that of the simple cubic model in all the cases. For example, for the 23 μm microspheres as shown in Figure 4-21a, Δ_k is within 30% for the DEM model for all the temperature and gas pressures while that for the simple cubic model is greater than 50%. The DEM model can also capture the thermal conductivity of the 330 μm microspheres with Δ_k less than 15% as shown in Figure 4-21c. For the 67 μm microspheres, Δ_k of the DEM model is less than 30% for gas pressure ≥ 100 Torr but it reaches 70% at 20 Torr and high temperature. A possible reason for this large Δ_k under these conditions is that the DEM model assumes the particles as monodispersed ones while as shown in Figure 4-14, the particle size follows the Gaussian distribution with a small but not negligible standard deviation. Further investigation on the polydispersity effect of particle size distribution is warranted to improve the accuracy of the DEM model at the low pressure. Nevertheless, except for the outliner for the 67 μm particle at 20 Torr, we can conclude that the DEM model agrees significantly better with the experimental results than the simple cubic model due to the realistic packing structure.

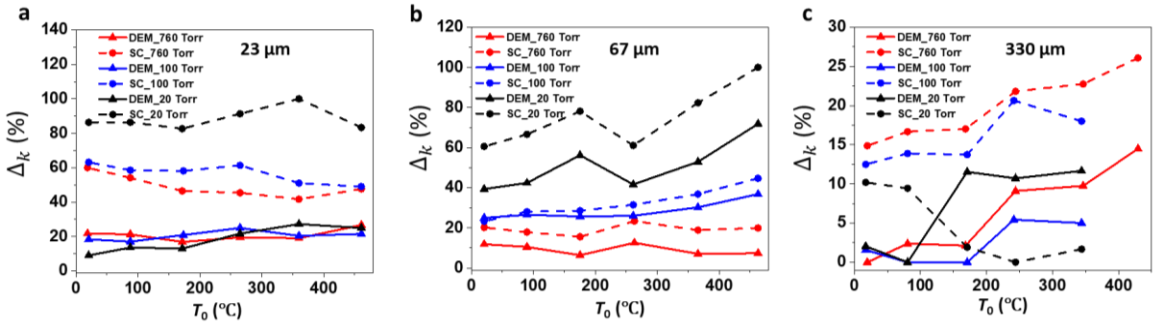

Figure 4-21. Comparison of deviation from the experimental value based on simple cubic (SC) and DEM packing structures at different temperature and gas pressure for (a) 23 μm, (b) 67 μm and (c) 330 μm particles.

The previous analysis demonstrates that the random packing structure obtained from the DEM is better for the prediction of the effective thermal conductivity of particle beds. Using this model, the contributions from different heat transfer modes are quantified, including the gas conduction in the void between the particles, solid conduction through the particle-particle contact, and radiative heat transfer. As shown in Equation 4-18, $k_{eff,calc}$ is determined from the combined solid and gas conduction components $k_{s,g}$ obtained from the COMSOL simulation and the radiative component k_r calculated from Equation 4-21. To further differentiate the gas conduction k_g and the solid conduction k_s components from $k_{s,g}$, COMSOL simulation on the random packing structure from DEM model was conducted under vacuum condition (i.e., gaseous pressure is 0), where the gas conduction is eliminated and thus $k_{s,g}$(vacuum) =k_s(P > 0 Torr). Therefore, we can also obtain k_g at 760 Torr by subtracting k_s from $k_{s,g}$ at the same pressure. Figure 4-22a to 4-22c show the contributions of k_s, k_g and k_r to $k_{eff,calc}$ under 760 Torr N_2 for 23 μm, 67 μm and 330 μm silica microsphere beds, respectively. The gas conduction is the dominant heat transfer mechanism for all the three particles.

For example, at $T_0 = 700°C$, k_g contributes to ~ 90% of $k_{eff,calc}$ to all the three particles. The solid conduction component k_s for the 23, 67 and 330 μm SiO_2 microspheres is calculated to be similar at ~ 0.007 W m^{-1} K^{-1} at room temperature. Because of the increasing total k_{eff} with particle size, the relative contribution of k_s becomes less important with increasing size. Measured k_s under vacuum of similar SiO_2 microspheres in Ref [144] also shows a near constant, albeit lower, value of 0.002 to 0.003 W m^{-1} K^{-1} for the particle size range of 50-500 μm. The higher k_s value obtained from our model could be due to the simplification of size distribution and particle morphology used in the DEM model. Specifically, it was found that the SiO_2 microspheres have μm-scale roughness and surface contaminants, which are expected to reduce the k_s due to the solid contacts[144], whereas in our DEM model the particles are assumed to be perfectly spherical and smooth. As such, a higher k_s value is expected from our DEM model compared to the experimental data on the real microspheres in Ref.[144]

The model allows us to quantify the relative contributions from each heat transfer mechanisms. The relative contribution of k_s becomes less important for the larger particles. For example, based on the DEM packing structure, at $T_0 = 700°C$, k_s contributes to ~ 11.8% of $k_{eff,calc}$ for the 23 μm particles, which decreases to ~ 4.5% for the 330 μm particles. On the contrary, the radiation contribution, k_r, increases with increasing particle size due to the longer propagation length of photons, e.g., at $T_0 = 700°C$, k_r only contributes to ~ 1% of $k_{eff,calc}$ for the 23 μm particles but it increases to ~ 7.7% for the 330 μm particles. To investigate the effect of packing structure on the heat transfer mechanisms, the gas conduction k_g and solid conduction k_s components from $k_{s,g}$ for the simple cubic structure are also differentiated in the same way as for the DEM

model and plotted in Figure 4-22a to 4-22c. Notably, the contribution of k_s is overestimated when using the simple cubic structure, e.g., $T_0 = 700°C$, k_s contributes to ~ 21.4% of $k_{eff,calc}$ for the 23 μm particles and ~ 13.9% for the 330 μm particles. On the contrary, the contribution of k_g is underestimated by the simple cubic structure, e.g., $T_0 = 700°C$, k_g contributes to only ~ 80% of k_{eff} for the simple cubic structure vs ~ 90--% for the random packing structure. A possible reason is that the in the random packing structure, the number of gas bridges between the particles (i.e., the region ~ 1/6 to 1/12 particle diameter away from the contact point[182,183]) increases, which reduces the effective length of gas conduction pathway. Although the theoretical coordination number of simple cubic structure is six, the effective coordination number for heat transfer should be considered as two because of the near one-dimensional heat transfer as shown in Figure 4-18b. The coordination number in the DEM for 23 μm, 67 μm and 330 μm diameter particle bed is calculated to be 4.2, 3.5 and 3.1, respectively, which should be considered as the effective coordination number due to the three-dimensional heat transfer in the random packing. The higher effective coordination number in random packing structure may explain the higher relative contribution from the gas conduction. Nevertheless, the effective length of solid conduction may be increased in the random packing structure because of the serpentine solid conduction pathway compared to the straight one in the simple cubic structure, which reduces the relative contribution from the solid conduction. The results above indicate that to accurately understand the heat transfer mechanism in a particle bed, it is imperative to obtain the real packing structure.

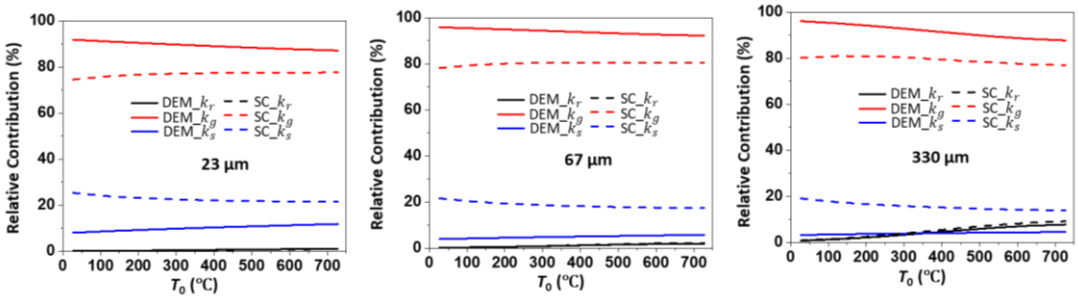

Figure 4-22. Relative contribution of different heat transfer pathways to the effective thermal conductivity of SiO2 particle beds calculated from Eq. (7) ($k_{eff,calc)}$ for (a) 23 μm, (b) 67 μm, and (c) 330 μm SiO_2 microspheres based on the simple cubic (SC) structure and the random packing structure from DEM.

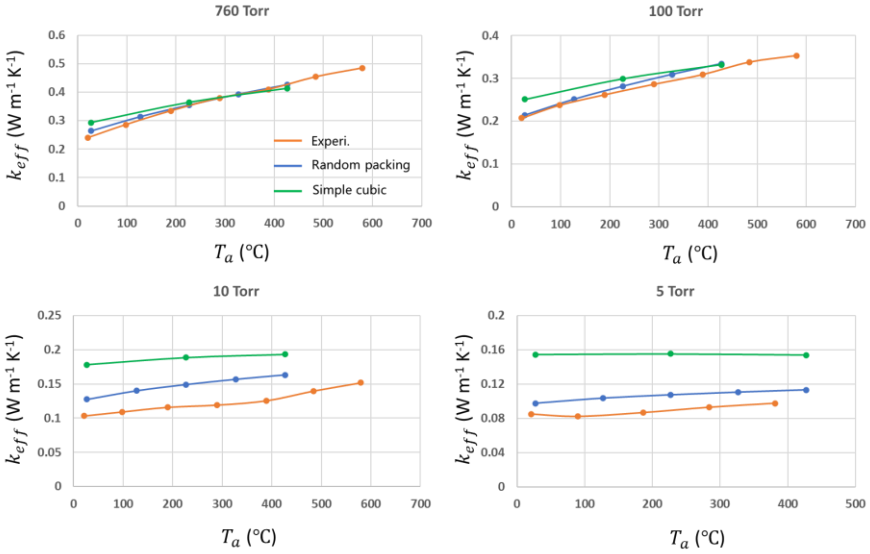

Figure 4-23. Effect of packing structure on the thermal conductivity of CARBO HSP 40/70 ceramic particles. Experimental results are obtained from the THW measurement as shown in the previous section. The simple cubic model is based on mono-dispersed particles of the average particle size of HSP 40/70 (~ 400 μm) The random packing structure is obtained from the DEM model and the k_{eff} is obtained by inputting the structure obtained in DEM into COMSOL model. Comparison of k_{eff} of HSP 40/70 obtained from experiment and predicted by simple cubic and random packing models at different gas pressures.

We also modelled k_{eff} of CARBO ceramic particles, i.e., HSP 40/70 with the average particle sizes of 400 μm based on simple cubic structure and random packing from DEM. The experimental results of HSP 40/70 were obtained from the THW measurement shown in the previous section. The simple cubic structure was input in the

COMSOL model, the same way as for the silica microspheres. The random packing structure was obtained from the DEM modelling as an input into the COMSOL model for k_{eff}. As shown in Figure 4-23, the modelled k_{eff} based on both the simple cubic structure and random packing structure agrees well with the experimental results for high pressure at 760 torr and 100 torr. The reason is that at high pressure, gas conduction dominates the heat transfer and thus k_{eff} is less sensitive to the packing structure, which is consistent with the findings for silica microspheres. However, at low pressure at 10 torr and 5 torr, the simple cubic model overestimates k_{eff}, while that based on the random packing structure agree well with the literature value, indicating that the random packing structure captures better the real packing structure of the CARBO ceramic particle bed.

4.5. Conclusions

A systematic study was performed to measure the effective thermal conductivity of ceramic particle beds, a promising heat transfer and thermal energy storage media for concentrating solar power (CSP). The thermal conductivity of the ceramic particle beds was measured using a transient hot-wire (THW) method within a temperature range of room temperature to 700℃, the target operating temperature of the next-generation CSP systems. Two different types of ceramic particles were examined: (1) CARBOBEAD HSP 40/70 and (2) CARBOBEAD ID50 with the average particle sizes of ~ 400 μm and ~280 μm, respectively, and thermal conductivities ranging from ~0.25 W m^{-1} K^{-1} to ~0.50 W m^{-1} K^{-1} from 20 ºC to 700 ºC in both air and N_2 gas. The gaseous pressure dependence of the thermal conductivity of the ceramic particle beds was also studied in the N_2 environment to differentiate the contributions from gas conduction, solid conduction, and radiation. Calculations using the Zehner, Bauer, and Schlünder (ZBS) model showed

good agreements with the measurements. Based on the model, it is concluded that the effective thermal conductivity of the packed particle beds is dominated by the gas conduction while the solid conduction and radiation contributes to about 20% of the effective thermal conductivity at high temperature. The ZBS model could predict the k_{eff} of large particles at high pressure accurately but showed larger error for smaller particles and at lower pressure where the packing structure became important.

To obtain a universal k_{eff} model of stationary particle bed, it is imperative to obtain an accurate packing structure. We measured and modeled the effective thermal conductivity of silica particle beds made of near monodispersed microspheres. $k_{eff,exp}$ of the particle beds was measured for particles with average diameter of 23, 67, and 330 μm and with varying N_2 gaseous pressure from 20 to 760 Torr and temperature up to 500 ^oC to quantify the relative contributions of solid conduction, gas conduction and radiation heat transfer in the particle beds. To better understand the effect of the particle packing structure on k_{eff}, modeling based on the discrete element method (DEM) was employed using the LIGGGHTS package to simulate the particle packing process. It was found that the random structure obtained from the DEM simulation better represents the real packing structure in the particle beds compared to the simple cubic structure normally assumed in common heat transfer models, as demonstrated by the good agreement of packing density between the experimental and DEM simulation results. The random packing structure extracted from the DEM was then imported into a COMSOL based FEM model to simulate the effective thermal conductivity ($k_{eff,calc}$) of the particle beds. $k_{eff,calc}$ based on the random packing agreed better with the experimental results for all the three particle beds with various gas pressures and temperatures. Compared to the

simple cubic model, the random packing model could better capture k_{eff}, indicating the importance of the actual packing structure of particles for heat transfer in particle beds. Based on the simulation results from the random packing, we found that gas conduction contributes to ~ 90% of the k_{eff} for the particle beds at 760 Torr while solid conduction and radiation heat transfer only contribute to ~ 10%. In contrast, the model based on the simple cubic structure predicts a lower contribution from gas conduction (~ 80%) while higher contribution from solid conduction possibly due to the longer effective length of gas conduction pathway in the simple cubic structure. This indicates that the packing structure impacts both the solid and gaseous conduction pathways. Additionally, the model confirms that the relative solid conduction is found to be more important for smaller particles while radiation heat transfer increases with larger particle due to the longer propagation length of photons.

Chapter 4, in full, is a reprint of the materials as it appears in 'Measurement and Analysis of Thermal Conductivity of Ceramic Particle Beds for Solar Thermal Energy Storage', *Solar Energy Materials and Solar Cells*. (230) 2021, 111271 by Ka Man Chung, Jian Zeng, Sarath Reddy Adapa, Tianshi Feng, Malavika V. Bagepalli, Peter G. Loutzenhiser, Kevin J. Albrecht, Clifford K. Ho and Renkun Chen. The dissertation author was the primary investigator and co-first author of this paper. It is also a reprint of the materials as it appears in 'Thermal Conductivity Modeling of Monodispersed Microspheres using Discrete Element Method' *Journal of Applied Physics,* (130) 2021, 165104 by Jian Zeng, Ka Man Chung, Xintong Zhang, Sarath Reddy Adapa, Tianshi Feng, Yu Pei and Renkun Chen. The dissertation author was the primary investigator and first author of this paper.

5. Chapter 5 Thermal transport of moving granular media

5.1. Introduction

Up to now, in-situ thermal conductivity measurement of moving particle bed has not been achieved not only because of the technical difficulty introduced by the high temperature and corrosive nature of particles but also the ambiguous definition of k_{eff} of moving particle bed. Nevertheless, several attempts have been made to extract the k_{eff} of moving particle bed from the global measurement on the thermal conductance of particle heat exchanger. As shown in Figure 5-1, the global heat transfer coefficient of the heat exchanger $\overline{h_L}$ over length of L can be calculated by measuring the inlet T_{in} and outlet temperature T_{out} and surface heat flux q_s:

$$\overline{h_L} = \frac{q_s}{T_{out} - T_{in}} \tag{5-1}$$

where T_{in} and T_{out} are the inlet and outlet temperature, respectively; q_s is the uniform heat flux on the surface. And the corresponding Nusselt number can be defined:

$$Nu_d = \frac{\overline{h_L} d}{k_g} \tag{5-2}$$

where d is particle diameter and k_g is the thermal conductivity of interstitial gas.

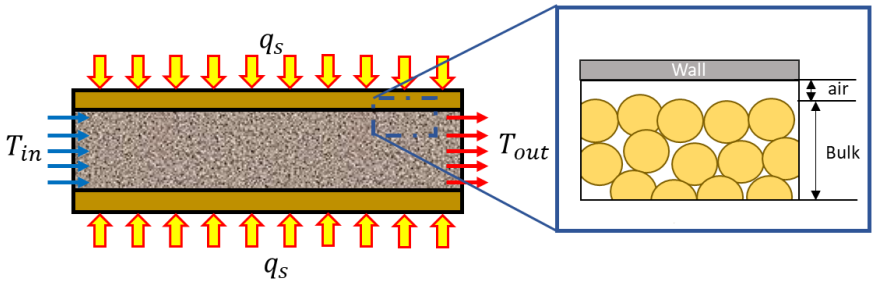

Figure 5-1. Schematics of particle heat exchanger with a uniform heat flux boundary condition.

Sullivan and Sabersky *et al.* pioneered the experimental work on particle flowing heat transfer in 1970s[124,184]. They compared the experimental results to the thermofluids model assuming continuum plug flow modeled by:

$$\frac{\partial^2 T}{\partial y^2} = \frac{u_b}{\alpha}\frac{\partial T}{\partial x} \tag{5-3}$$

where y is the transverse direction and $y = 0$ is the wall; x is the flow direction; u_b is the bulk velocity and α is thermal diffusivity of particle. The boundary conditions are:

$$T(0, x) = T_w \quad x \geq 0 \tag{5-4}$$

$$T(0, x) = T_\infty \quad x < 0$$

$$T(\infty, x) = T_\infty$$

With this, the modeled Nusselt number can be obtained:

$$Nu_{d,m1} = \frac{1}{\frac{\sqrt{\pi}}{2}\sqrt{\frac{1}{Pe_L^*}}} \tag{5-5}$$

where Pe_L^* is the modified Peclet number $Pe_L^* = \left(\frac{k_{eff}}{k_g}\right)^2 \left(\frac{d}{L}\right) Pe_L$ with k_{eff} as the effective thermal conductivity of particle, k_g as thermal conductivity of interstitial gas, L as the channel length, and Pe_L as the Peclet number $Pe_L = \frac{Lu_b}{\alpha}$. However, as shown in Figure 5-2a, they found that the modeled $Nu_{d,m1}$ could not fit the experimentally measured Nu_d unless a separated near-wall resistance was added to the model:

$$Nu_{d,m2} = \frac{1}{X + \frac{\sqrt{\pi}}{2}\sqrt{\frac{1}{Pe_L^*}}} \tag{5-6}$$

where X is the obtained from the definition of near-wall resistance:

$$R_{nw} = \frac{Xd}{k_g} \tag{5-7}$$

Therefore, X represents the thickness of an air layer between the wall and particle flow with respect to the particle diameter d. It was found that there was an effective airgap layer of $0.085d$ thick between the wall and particle flow[124], which consistently existed in different particles. As shown in Figure 5-2b, in a follow-up experiment[184], they pushed the Pe_L^* to a higher range by increasing the velocity and observed the decrease of Nu_d, which deviated from the modeled trend. They attributed this phenomena to the reduction of either bulk thermal conductivity of particle k_{eff} or increase of near-wall thermal resistance R_{nw}, induced by the change of density as velocity increased. However, further experimental evidence was lacking. Denloye and Botterill *et al.*[185] considered a packet of particles in conat with the heat transfer surface for a short residence time t then to be replaced by a fresh packet of inlet particles and derived a continuum heat transfer coefficient:

$$h_L = \left(\frac{k_{eff}\rho c_p}{\pi t}\right)^{0.5} \tag{5-8}$$

where t is the resident time of the packet of particles. Like Sullivan and Sabersky *et al.* [124,184], they released the significance of the near-wall thermal resistance in the modeling of heat transfer coefficient of particle flow. It was obtained by integrating the

$$h = \frac{1}{R_a}[1 - \frac{R_w}{2R_a}\ln(1 + \frac{2R_a}{R_w})] \tag{5-9}$$

where R_a is the average bulk thermal resistance of particles at the heat transfer surface and $R_a = \sqrt{\frac{\tilde{t}\pi}{4k_{eff}\rho c_p}}$. R_w is the near-wall thermal resistance. It was assumed that the near-wall region with the thickness of half particle had higher porosity than the bulk region, accounting for the near-wall layer:

$$R_w = \frac{d}{2k_{eff,nw}} \tag{5-10}$$

where $k_{eff,nw}$ is a modified k_{eff} at the near-wall region with higher porosity (i.e., $k_{eff,nw} < k_{eff}$). It has been well-known that the porosity of particle bed was higher close to the wall due to the less coordination number and reduced contact area[186,187] from both experiment and theoretical modeling. Its modeling can be found in Refs[36,186]. As shown in Figure 5-2c, after introducing the near-wall resistance, the modeled $Nu_{d,m}$ matched well with the experimental results. As shown in Figure 5-2d, After normalizing the k_{eff} to k_g and using a simple in-serial thermal resistance network (i.e., two-particle model), it was found that the near-wall thermal resistance could be represented by an gas gap with the thickness of $0.1d$ (i.e., $\frac{d}{2k_{eff,nw}} \approx \frac{0.1d}{k_g}$), which agreed well with the finding by Sullivan and Sabersky *et al.*[124,184].

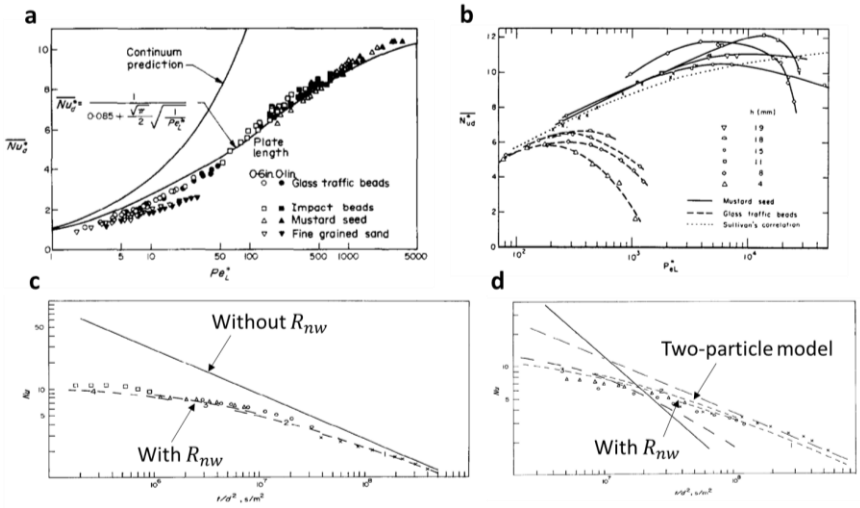

Figure 5-2. Pioneering work on modeling of Nu_d for particle heat exchanger in 1970s. Modeling based on plug flow assumption. (a) Comparison of Nu_d with and without near-wall airgap[124]. (b) Reduction of Nu_d in high Pe_L^* range due to the change in porosity[184]. Modeling based on the concept of periodically refreshing particle packet: (c) comparison of Nu_d with and without near-wall resistance. [185] (d) Comparison of modeled near-wall resistance based on effective near-wall thermal conductivity and effective airgap.

Recent works on the thermal performance of particle heat exchanger also revealed the significance of near-wall thermal resistance of moving particle bed. Albrecht *et al.* [36,169] modeled the particle-to-sCO_2 heat exchanger, treating the particle-to-wall thermal resistance like Sullivan and Sabersky *et al.* [124,184] (Figure 5-3a). The majority of the heat transfer resistance could be attributed to the particle-wall resistance[36] and the measured HTC agreed well with that modeled with a near-wall resistance (Figure 5-3b). Morris *et al.* [182] modeled the near-wall particle distribution of moving particle bed using discrete element method (DEM). The particle-wall distribution function was extracted and input into the single particle conduction model to reach a semi-continuum model. The modeled result captured the heat transfer coefficient better than the conventional continuum model (Figure 5-3c). Watkins *et al.*[188,189] also modeled the near-wall packing structure using DEM and found a much lower density close to the wall serving as the limiting factor in the heat transfer to a discrete particle flow (Figure 5-3d). More importantly, they found a higher near-wall porosity for higher velocity, which was related to the less particle in contact with the wall, indicating a higher near-wall thermal resistance for higher velocity. Fang *et al.* [190] systematically analyzed the sensitivity of heat transfer coefficient on different parameters and found that at low velocity, it was determined mainly by flow velocity and channel width, while at higher velocity, the effective thermal conductivity of particle flow dictated, which usually decreased due to the higher porosity in the near-wall region, albeit not providing further evidence (Figure 5-3e). Yu *et al.* [191]committed the most recent experimental effort to separate the near-wall thermal resistance from the bulk resistance and the convection resistance (Figure 5-3f). The authors established a continuum model considering the near-wall thermal resistance as an in-serial model, in an

essence like Sullivan and Sabersky *et al.* [124,184]. By fitting the Nu_D of a 1 m long particle heat exchanger, they concluded that increasing the flow velocity simultaneously increase the near-wall resistance and convection conductance, whereas a high velocity, the former one dominated, leading to the reduction of overall heat transfer coefficient. The near-wall thermal resistance was at the order of ~ 10^{-3} K m^2 W^{-1}, indicating an effective near-wall airgap thickness of 1/10 particle diameter. This finding matched well with that found by Spelt *et al.*[184], and Sullivan and Sabersky *et al.* [124,184]. However, up to now, there is not *in-situ* measurement on the near-wall thermal resistance. While the global heat transfer coefficient measurement might give us a hint on the development of near-wall thermal resistance, it is questionable if the R_n could be independently dissected from the convection and bulk resistances. These measurements also lost the local flow information from the global measurement, which warranted the development of *in-operando* measurement in the future to quantify the near-wall thermal resistance. Besides, the micromechanical explanation of the origin of the near-wall thermal resistance remained unknown. Although it has been often attributed to lower porosity in the near-wall region, how this happened and why it changed with flow velocity remain a puzzle.

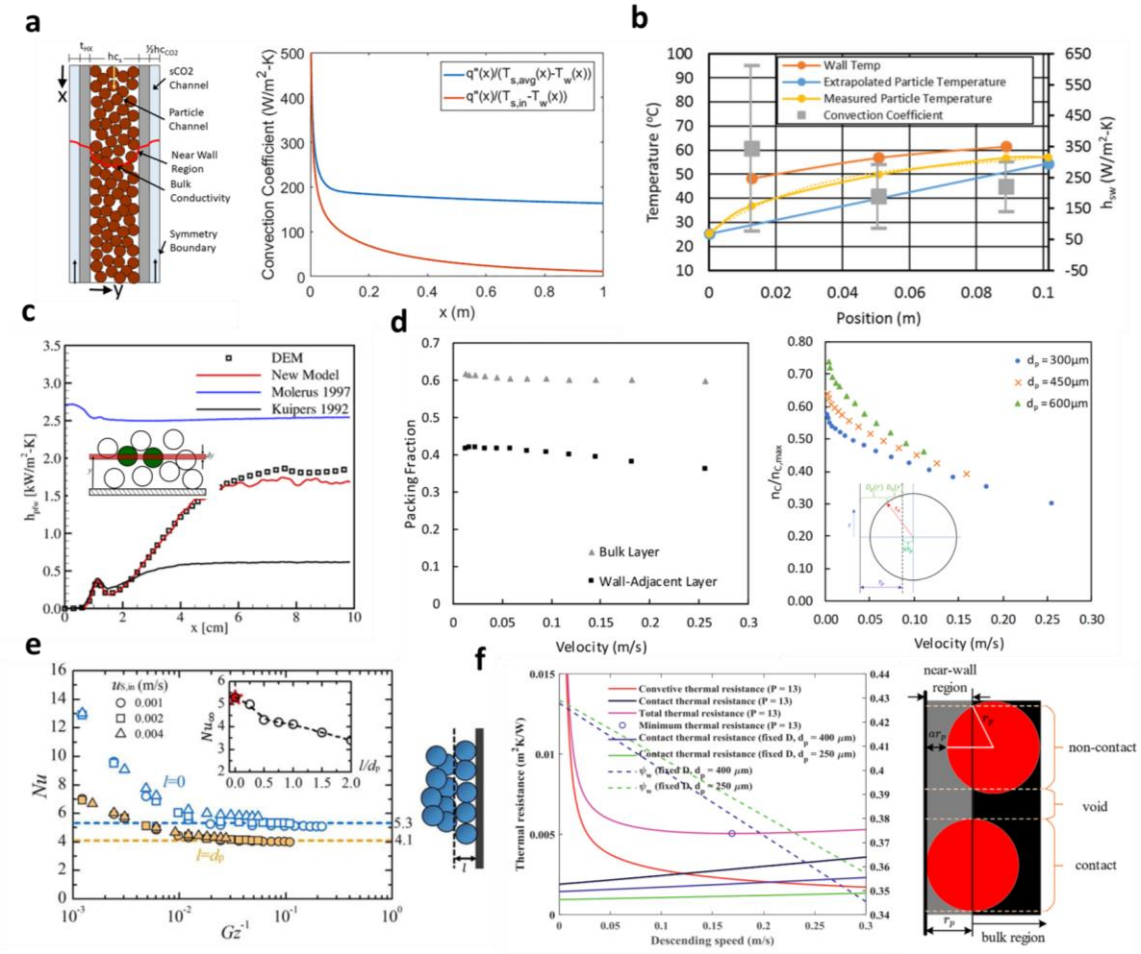

Figure 5-3. Recent progress on the experimental and theoretical modeling of moving particle heat exchanger. The near-wall thermal resistance was generally treated as an in-serial thermal resistance integrated with the continuum model. (a) Modeled HTC in a R_n-continnum model by Albrecht *et al.* [36,169]. (b) Measured HTC by Albrecht *et al.* [36,169] in good agreement with the modeling result. (c) Modeled HTC by Morris *et al.*[182] considering the near-wall distribution function. (d) DEM modeling of moving particle bed by Watkins *et al.*[188,189] for near-wall packing density and number of particle contact. (e) Comparison of modeled HTC with and without near-wall region by Fang *et al.* [190]. (f) Extracted near-wall thermal contact resistance from the global HTC by Yu *et al* [191].

While the origin of the near-wall thermal resistance is still not fully understood, there are two main assumptions that have widely been considered. There is an intrinsic near-wall region for the stationary particle bed where the porosity is higher due to the lower coordination number and smaller contact area compared to the bulk region. The

porosity variation with distance from the constraining surface usually took the form of a damped oscillator, having the maximum at the wall and minimum about half a particle diameter from the surface[187,192,193]. As displayed in Figure 5-4a, Farid modeled the near-wall porosity oscillation based on a modified Darcy's law with different airflow velocity (A = 0.0015 kg s^{-1} and B = 0.0030 kg s^{-1}) and found that the oscillation became more significant with higher velocity as the oscillatory profiles of porosity and velocity overlapped[193]. As shown in Figure 5-4b, the packing structure of stationary particle bed in a channel was modeled by Toit[174], Llerk[176], and Martin[175]. They showed similar oscillation of porosity and found the maximum at the surface. Although the porosity oscillation explained partly the origin of near-wall thermal resistance of stationary particles, it failed to match the order of magnitude of near-wall thermal resistance and explain why it increased with increasing velocity in moving particle bed.

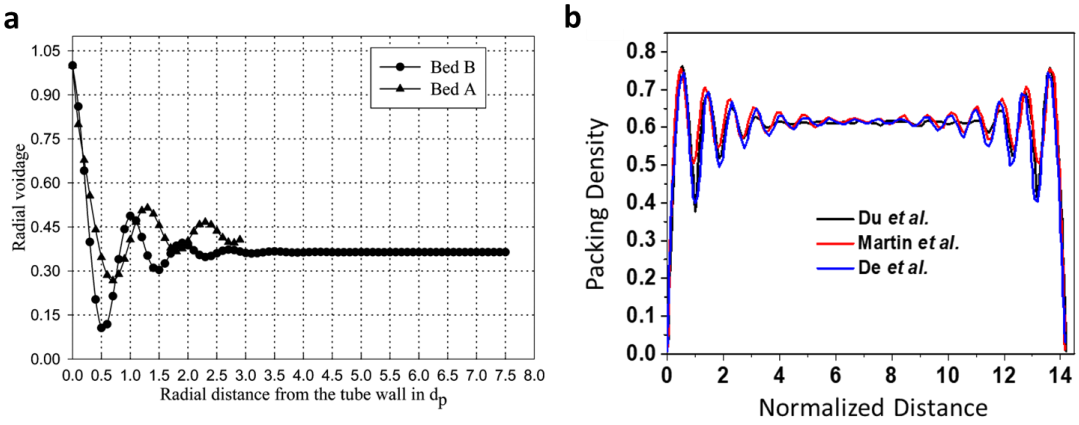

Figure 5-4. Oscillation of porosity of particle bed away from wall. (a) Modeling on a single-sided constraint particle flow[193]. (b) Modeling on particle flow in channel with symmetric constraint[175,176,193].

Due to due to the shear force between moving particles, particles close to the wall may move away from the wall. Therefore, an extra near-wall thermal resistance in a moving particle bed could also be induced by the formation of air cushion layer, or

effective airgap layer. It has been well-known that in addition to the bulk motion of particles, individual particles move randomly driven by the shear force between the particles and at the particle-wall interfaces. Due to analogy between the random motion of particle and gas molecules, the dense-gas kinetic theory has been developed to describe the particle flow[194-196].

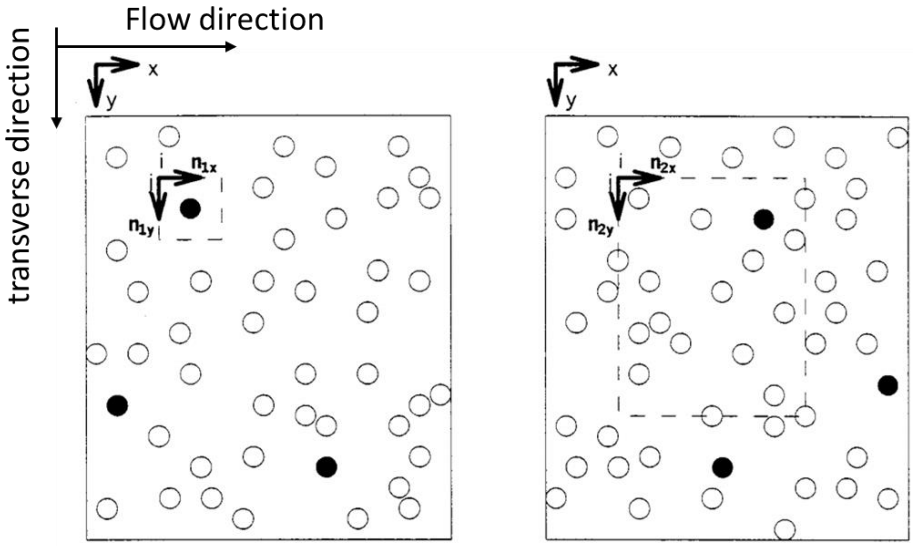

Figure 5-5. Schematics of granular diffusion in moving particle bed[196] (a) at initial time and (b) after a duration of t.

Figure 5-5 displays the schematics of random movement of particles in a bulk particle flow [196]. The average velocity can be calculated as:

$$u_a = \frac{\sum_{k=1}^{N} u_k}{N} \tag{5-11}$$

$$v_a = \frac{\sum_{k=1}^{N} v_k}{N}$$

where u_a and v_a are the average velocities in the streamwise and transverse direction, while u_k and v_k are the velocities of the k_{th} particles in streamwise and transverse

directions respectively, N is the total number of particles of interest. The fluctuation velocities in the two directions were:

$$u_f = \sqrt{\frac{\sum_{k=1}^{N}(u_k - u_a)^2}{N}} \tag{5-12}$$

$$v_f = \sqrt{\frac{\sum_{k=1}^{N}(v_k - v_a)^2}{N}}$$

Where u_f and v_f are the fluctuation velocities in streamwise and transverse directions respectively. In analogy to the thermodynamic temperature of gas, the granular temperature can also be defined based on the kinetic energy of particles. Since the random motion between particles are driven by the shear force, the granular temperature is expressed as the fluctuation velocity instead of the bulk or average velocities, i.e., $T_y \propto u_f$ and $T_x \propto v_f$[195]. From the dense-gas kinetic theory derivation in a homogeneous and stationary velocity field of granular flow, the self-diffusivity of particle in the specific vector direction is given by:

$$D_{ii} = \frac{D_p(\pi T_{ii})^{\frac{1}{2}}}{8(1+e_p)vg_0(v)} \tag{5-13}$$

where D_{ii} is the granular diffusivity in the ii direction, e.g., D_{xx} indicates the diffusivity in the x direction and the T_{ii} is the granular temperature in the corresponding direction, calculated based on the velocity component in the same direction. e_p is the coefficient of restitution of particle; v is the solid fraction and $g_0(v)$ is an equation of state of ridge spheres given by the Carnahan-Starting expression[197]:

$$g_0(v) = \frac{2-v}{2(1-v)^3} \tag{5-14}$$

Equation 5-13 is reduced to the classical Chapman-Enskog expression for gas diffusion in case of perfectly elastic particles[198,199]. In diffusion-governed motion, the particle displacement can be obtained from:

$$< {S_{xx}}^2 > = 2D_{xx}t \tag{5-15}$$

$$< S_{yy}^2 > = 2D_{yy}t$$

where S_{xx} and S_{yy} are the displacement in the *x* and *y* directions, respectively over the duration of *t*. Measurements on the fluctuation velocity in moving or rotating particle bed have been conducted since 1990s. Hsiau and Shieh[196] measured the diffusivity of particle flow driven by a rotating plate (Figure 5-6a). They found that the fluctuating velocities increases with increasing bulk velocity in both the streamwise (Figure 5-6b) and transverse direction (Figure 5-6c). In addition, the fluctuating velocity was higher anisotropic and was higher in the streamwise direction. The corresponding diffusivity in the streamwise direction was thus much higher than that in the transverse direction. Similar trend was observed by Utter and Behringer[195] on a rotating wheel as shown in Figure 5-6d where the tangential displacement (streamwise, Figure 5-6e) was an order of magnitude higher than that in the radial direction (transverse, Figure 5-6f). The diffusivity scaled with the particle diameter and shear rate $\dot{\gamma}$, i.e., $D_{ii} \approx \dot{\gamma} d^2$. In particular, diffusion appears to be 'superdiffusive' in the transverse and 'subdiffusivie' in the transverse directions. Another important fact is that the displacement was larger closer to the shear surface, indicating stronger diffusion close to the wall. Higher granular temperature at the wall than in the center of the shear gap was also reported in Ref.[200]. Hunt and Taylor[198] measured the fluctuating velocity of moving particles in a channel dragged by gravity. They found that compared to the smooth tube, the displacement was

larger in a rough tube (i.e., roughened inner surface), which might imply a larger near-wall thermal resistance in a roughened surface. However, although the particle diffusion theory has been well developed in the field of granular rheology, its connection with the thermophysical properties of particles have not yet been well explored. Hsiau and Hunt[201] attempted to model the effective thermal conductivity of granular flow using the kinetic theory of particle. Although the modeled results were not at the same order of magnitude to the experimental results, it captured qualitatively the trend of k_{eff} versus packing fraction. Hunt[202] later modified the kinetic theory to predict k_{eff} of granular flow and found that it matched relatively well with the discrete element model (DEM) at the low Biot-Fourier number << 1. The application of the granular kinetic theory on moving particle heat transfer has bee limited and the potential correlation between particle diffusion and near-wall thermal resistance has never been realized. One of the possible reasons is the limited experimental data for the near-wall thermal resistance over a wide range of conditions.

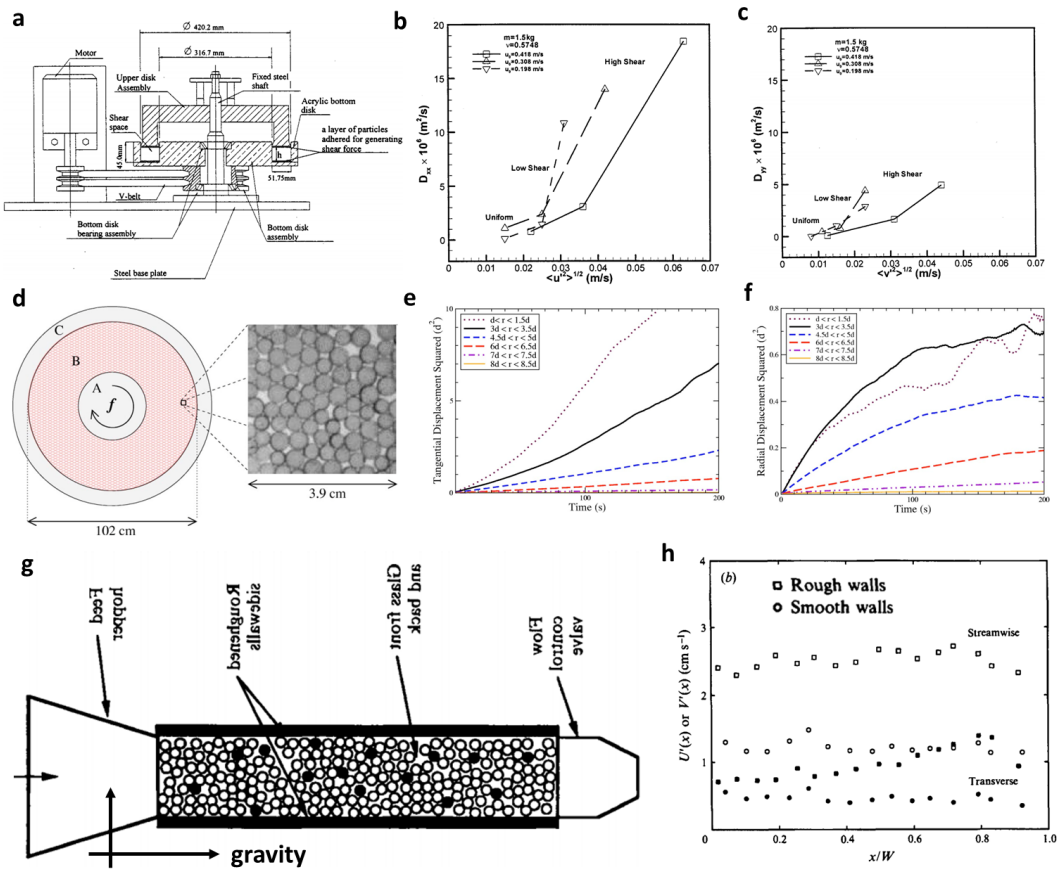

Figure 5-6. Measurement of particle diffusion in granular flow. (a) Measurement of particle diffusivity in rotating wheel and measured diffusivity in (b) streamwise direction and (c) transverse direction[196]. (d) Measurement of particle displacement in rotating wheel and measured displacement in (e) streamwise direction and (f) transverse direction[195]. (g) Measurement of fluctuating velocity in moving particle bed dragged by gravity and (h) measured fluctuating velocity in stream and transverse direction[198].

While the particle diffusion theory has been rarely coupled to the granular flow heat transfer, it has manifested its significance in predicting the near-wall thermal resistance. Ansary et al.[203] measured the HTC of particle flow in a vibrating channel and found that the HTC decreased under shaking. The enhanced particle diffusion away from the shaking surface has been repeatedly confirmed both experimentally and numerically[204-206]. As the particles diffuse further away from the wall, the near-wall thermal resistance may increase due to the reduction in the wall-particle contact time. As

already shown above, Hunt and Taylor[198] found that compared to the smooth tube, the displacement was larger in a rough tube (i.e., roughened inner surface). Presumably, a rough surface possibly induced extract perturbation of particle flow, leading to a highly porous near-wall region, and thus larger near-wall thermal resistance. We believe that the full understanding of the relationship between the particle diffusion behavior and thermal resistance of moving particle bed, especially in the near-wall region, will make an impact on the thermal performance of the particle heat exchanger.

In this section, a high-temperature thermal conductivity measurement system of moving particles using modulated photothermal radiometry (MPR) was established to measure effective thermal conductivity of particles. The effective thermal conductivity of different particle sizes and morphologies as a function of moving particle were investigated. The k_{eff} of stationary particle bed was first measured by MPR and modeled based on the realistic packing structure simulated by discrete element method (DEM). The measurement results were validated by the benchmark measurement from a transient hot-wire setup (THW). A more realistic model was established to predict the k_{eff} of stationary particle bed. The k_{eff} of moving particle were then measured by an improved MPR system for moving particle measurement. The near-wall thermal resistance was extracted from the k_{eff}. The near-wall thermal resistance was represented by an effective airgap layer close to the wall, which was found to be related to the particle size and velocity. The D_{air} of moving particle was modeled based on DEM and particle diffusion theory.

We modified the MPR system to measure moving particles in a channel. k_{eff} CARBO ceramics particles with the average particle diameter ranging from 150 μm, 275

μm and 400 μm were measured up to 700℃ and velocity up to 60 mm s^{-1}. The channel depth was changed from 2 to 6 mm to study the near-wall effect on the bulk flow. To separate the near-wall resistance from the bulk, a COMSOL model was established treating the bulk region with the properties obtained at the stationary state, and the near-wall region as an airgap with the properties of air at the specific temperature. The thickness of the airgap was acquired by best fitting the experimental results using the COMSOL model. To validate the measurement results, the packing structure of a moving particle bed was simulated by a discrete element model. We first extract the near-wall packing structure of the stabilized flow from DEM as an input in a COMSOL model for the k_{eff} of moving particle, and the near-wall airgap thickness was separated based on an in-serial model. Later, the fluctuation velocity was also extracted from DEM as an input into the particle diffusion model and the airgap thickness was obtained from the diffusion length.

5.2. Effective thermal conductivity of moving particles

5.2.1. Measurement system and principles

For the measurement of moving particle bed, we designed a high-temperature MPR system as shown in Figure 5-7. Figure 5-7a and 5-7b show the schematic and photograph of the overall setup, respectively. the system is similar to that for the measurement of stationary particles, where the sample surface (100 μm steel cover coated with ~ 10 μm thick Pyromark 2500 coating for laser adsorption and IR-emission) is heated by a modulated laser, and the thermal emission is collected by a pair of parabolic mirrors and focused to the MCT detector. Different from the stationary particle setup, particles are supplied continuous from the funnel on the top, serving as the particle

reservoir as shown in Figure 5-7c. The channel length is 30 cm. There are heaters and thermocouple inserted in the reservoir to control the particle temperature before entering the channel as shown in Figure 5-6d. There are also eight cartridge heaters inserted in front and back plate of the channel to heat up the particles along the flow direction. The flowing velocity of particles is controlled by a slide gate at the downstream of the channel. By controlling the opening size of the slit, we can control the flow rate from 0 mm s^{-1} (stationary) to ~ 60 mm s^{-1} [207]. The capacity is the particle reservoir is 27 liters, which is sufficient for the measurement at the highest flowing velocity (60 mm s^{-1}) with the channel depth D_c of 2 mm for about 30 mins. It is noted that the D_c can be adjusted from 2 mm to 6 mm to investigate of the near-wall effect on the heat transfer coefficient. Table 5-1 summarizes the key parameters of the moving particle channel. It is important to ensure the temperature uniformity in the particle reservoir to avoid the temporal change in DC temperature of the particle bed, which might affect the radiative signal received by the MCT detector. Therefore, we uniformly distributed 8 high-temperature heaters (temperature limit ~ 1200℃) in the particle reservoir as shown in Figure 5-7 d and 5-7e. During the heating process, the particles are stirred and mixed to further improve the temperature uniformity. To monitor the temperature uniformity, there are 4 thermocouples inserted in the particle bed from center to the edge as shown in Figure 5-7e.

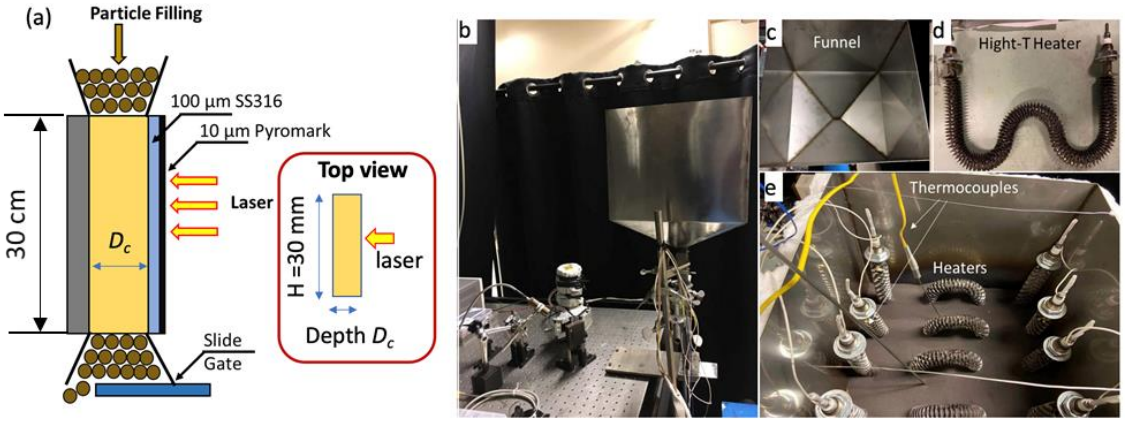

Figure 5-7. High temperature MPR setup for moving particles measurement. (a) Schematic of the setup. The depth of the channel (D_c) varies from 2 to 4 mm in our measurements. (b) Photograph of the setup. (c) Photograph of the particle reservoir. (d) High temperature heaters and (e) Reservoir with embedded heaters and thermocouples.

Table 5-1. Key parameters of MPR moving particles measurement setup.

Front Plate Thickness l_s	100	µm
Coating Thickness l_c	10	µm
Channel Depth D_c	6	mm
Flow Velocity u	0 - 60	mm s^{-1}
Particle Size	150-400	µm
Frequency Range	0.5-4	Hz
Channel Length	30	cm
Laser spot size D_{laser}	20	mm

Figure 5-8a shows the overview of the moving particle MPR system in operation. As shown in Figure 5-8a, particles flow out of the channel and turns red because of the high temperature (~ 700°C). There is temperature non-uniformity in the reservoir, indicated by the minor temperature fluctuation as shown in Figure 5-8b. To quantify the temporal temperature stability, the temporal temperature fluctuation at the flowing velocity of 10 mm s^{-1} was monitored the surface temperature of the MPR measurement section using a Pyrometer. Figure 5-8b shows that it takes about 5 mins for the system to reach an equilibrium after open the bottom slide gate (particles start flowing). The

maximum temperature change is < 10 K which is acceptable, leading to the uncertainty in the MCT signal of < 5%. Once the surface temperature stabilizes, the MPR measurement starts. After stopping the particle flow, the surface temperature drops because the channel wall temperature is lower than the particles temperature in the reservoir, due to the limited heating power in the channel.

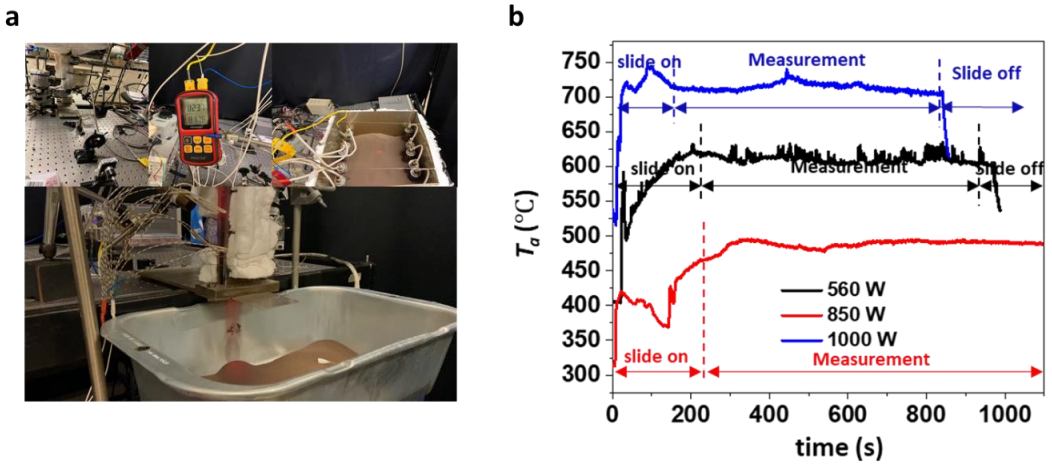

Figure 5-8. Testing of temperature (a) setup for the temperature measurement and, (b) stability of the surface temperature (measured from the front surface of the MPR window) during measurement.

We have shown in chapter 3 that at low velocity and medium frequency, where $Re_D^{1/2} Pr^{1/3} < \sqrt{\frac{D_c D_{laser} \pi f}{\alpha_f}}$, the moving particle bed can be treated as a stationary particle bed in terms of thermal conductivity measurement. Our measurements were conducted with the velocity v_b< 60 mm s^{-1} and frequency in the range of 0.5 – 4 Hz, and the above criterium was met. Besides, the penetration depth was ensured to be greater than the total thickness of the steel cover and coating. In this case, the moving particle channel can be modelled as a stationary three-layer system as for the stationary particle bed:

$$\theta_s = \frac{q_s e^{-\frac{\pi}{4}j}}{e_{eff}\sqrt{\omega}} + q_s R_{cs} \tag{5-16}$$

where e_{eff} is the effective thermal effusivity of particles, defined as $e_{eff} = \sqrt{k_{eff}\rho_f c_f}$, where ρ_f and c_f are the density and specific heat of the particles, respectively; R_{cs} is the total thermal resistance by the coating and the steel shell:

$$R_{cs} = \left(1 - \frac{e_s}{e_f}\right)\frac{l_s}{k_s} + \left(\frac{1}{2} - \frac{e_c^2}{e_f^2}\right)\frac{l_c}{k_c} \tag{5-17}$$

where e_s and e_c are the thermal effusivities of the steel shell and the coating, respectively; l_s and l_c are the thicknesses of the steel shell and the coating, respectively; k_s and k_c are the thermal conductivities of the steel shell and the coating, respectively. Notably, in this measurement, we only obtain the effective thermal conductivity k_{eff} of moving particle bed, which includes both the bulk thermal conductivity and near-wall thermal resistance. Figure 5-9 shows the thermal response of ID 50 particles moving in a 2 mm deep channel at the velocity of 10 mm s^{-1} and at the temperature of 300℃. Similar to the stationary particle measurement, the thermal response can be divided into three regions: at low frequency range (long l_p), the thermal response is determined by the properties of particles; at medium frequency range ($l_c + l_s > l_p > l_c$) thermal response is determined by the properties of the steel cover; at higher frequency ($l_p < l_c$), the thermal response only depends on the properties of coating. The effective thermal effusivity of moving particles can be similarly obtained from the slope at the low frequency range, i.e., from 0.5 to 4 Hz or l_p = 140-350 μm. The effective thermal

conductivity can be calculated based on the specific heat of the same HSP 40/70 and ID50 measured by DSC and that of the Silica in Ref.[163].

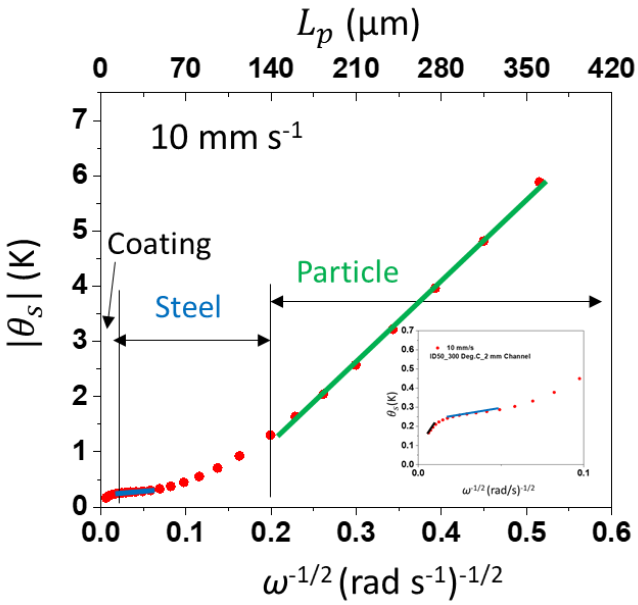

Figure 5-9. Typical thermal response of MPR measurement on moving particles. ID50 particles are moving in a 2 mm deep channel at the bulk velocity of 10 mm s^{-1} at 300°C.

5.2.2. Measurement results and discussion

Figure 5-10a shows the response of the amplitude of surface temperature oscillation ($|\theta_s|$) of HSP 40/70 at the stationary state (u = 0 mm s^{-1}) up to 500°C. The maximum temperature is limited by the heating power along the channel (when the particles are not flowing, the heaters in the top reservoir cannot heat up the particles residing in the channel). Figure 5-10b shows the thermal response of HSP 40/70 at the moving state (u = 10 mm s^{-1}) up to 700°C, where the particles are mainly heated up by the heaters embedded in the particle reservoir. It should be noted that we only focused on the low frequency regime from 0.5-4 Hz (i.e., l_p = 140-350 μm, roughly one particle away from the wall) where the thermal response

depends on the properties of particles. Figure 5-10c shows the measured k_{eff} of HSP 40/70 (average diameter d ~ 405 μm) at stationary and flowing states (with velocity of 10 mm s^{-1}) from 200 to 700°C with channel depth (D_c) of 4 mm. We compared the k_{eff} at the moving and stationary states to that measured by the stationary MPR setup (where the particles are packed in a holder, as reported in chapter 4) and the transient hot wire (THW) technique within the same temperature range. It is seen that k_{eff} measured by THW, stationary MPR, and moving MPR at u = 0 mm s^{-1} agree well with each other at all the temperatures, validating the measurement accuracy of the moving MPR setup. The k_{eff} at the moving state (u = 10 mm s^{-1}) is ~ 15-20% lower than that at the stationary state at all the temperature. The k_{eff} of ID 50 (average diameter $d \sim 275$ μm)was also measured using the moving MPR setup with channel depth (D_c) of 4 mm, stationary MPR setup and THW. Similar to that of HSP 40/70, k_{eff} measured by THW, stationary MPR, and moving MPR at u = 0 mm s^{-1} agree well with each other at all the temperatures, while that at the moving state is ~ 15-20% lower than that at the stationary state at all the temperature.

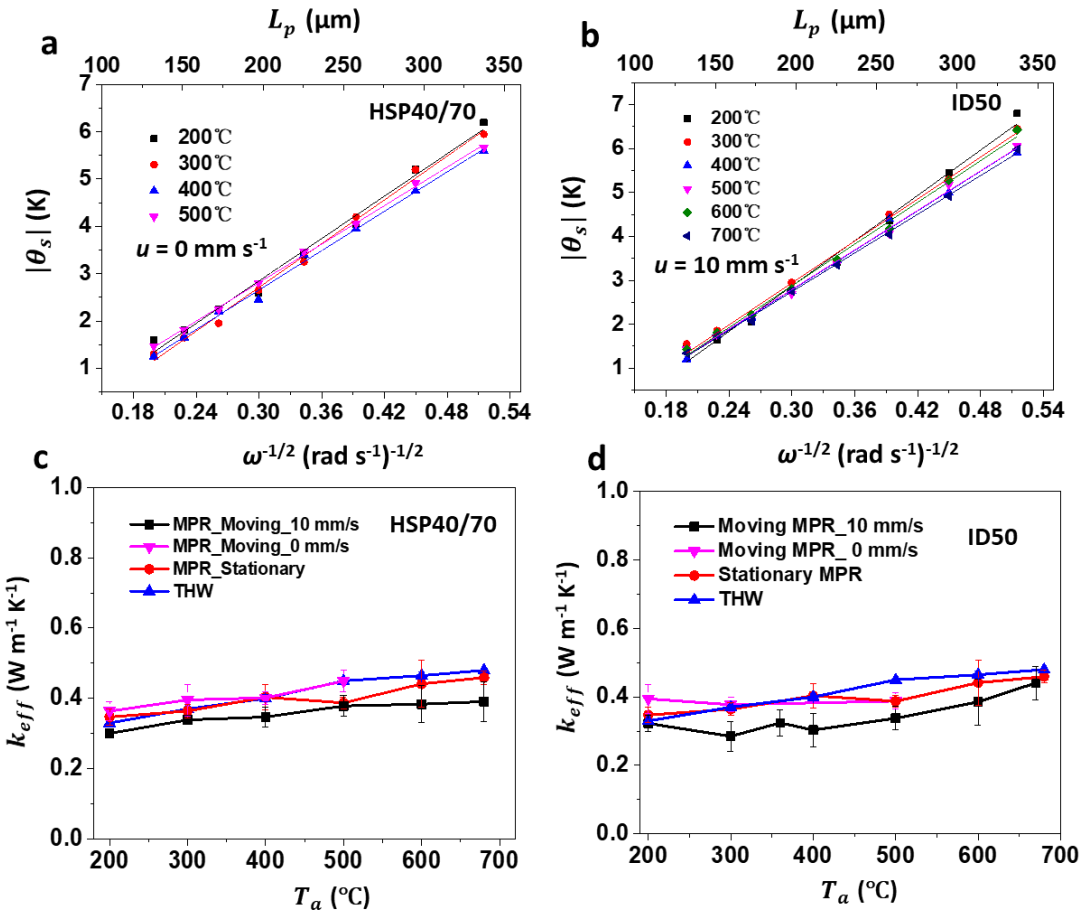

Figure 5-10. MPR measurement of moving CARBO ceramic particle up to 700℃. (a) Thermal response at 0 mm s^{-1} in the moving particle setup up to 500℃ for HSP40/70. (b) Thermal response at 10 mm s^{-1} in the moving particle setup up to 700℃ for HSP40/70. (c) Comparison of k_{eff} measured by the moving particle MPR with channel depth (D_c) of 4 mm, stationary particle MPR setup and THW techniques for HSP 40/70 (average diameter 405 μm). (d) Comparison of k_{eff} measured by the moving particle MPR with channel depth (D_c) of 4 mm, stationary particle MPR and THW techniques for ID 50 (average diameter 275 μm).

Figure 5-10c to 5-10d show the k_{eff} measured at different moving velocity (u = 0 mm s^{-1} and 10 mm s^{-1}) using the moving MPR with channel depth (D) of 4 mm and the comparison between the MPR and THW results for NREL 410, 430 and 480 silica particles. The average diameter of these particles is 300, 450, and 625 μm, respectively. The k_{eff} at u = 0 mm s^{-1} agree well with the THW results for all the three particles. As the u increases from 0 mm s^{-1} to 10 mm s^{-1}, k_{eff} decreases, e.g., by ~ 30% for the NREL

410, ~ 10% for the NREL 430, and ~ 20% for the NREL 480. The k_{eff} decreases more for the silica sands than the carbo ceramic because of their more irregular morphologies and wider dispersions of particle size as shown in Figure 5-12.

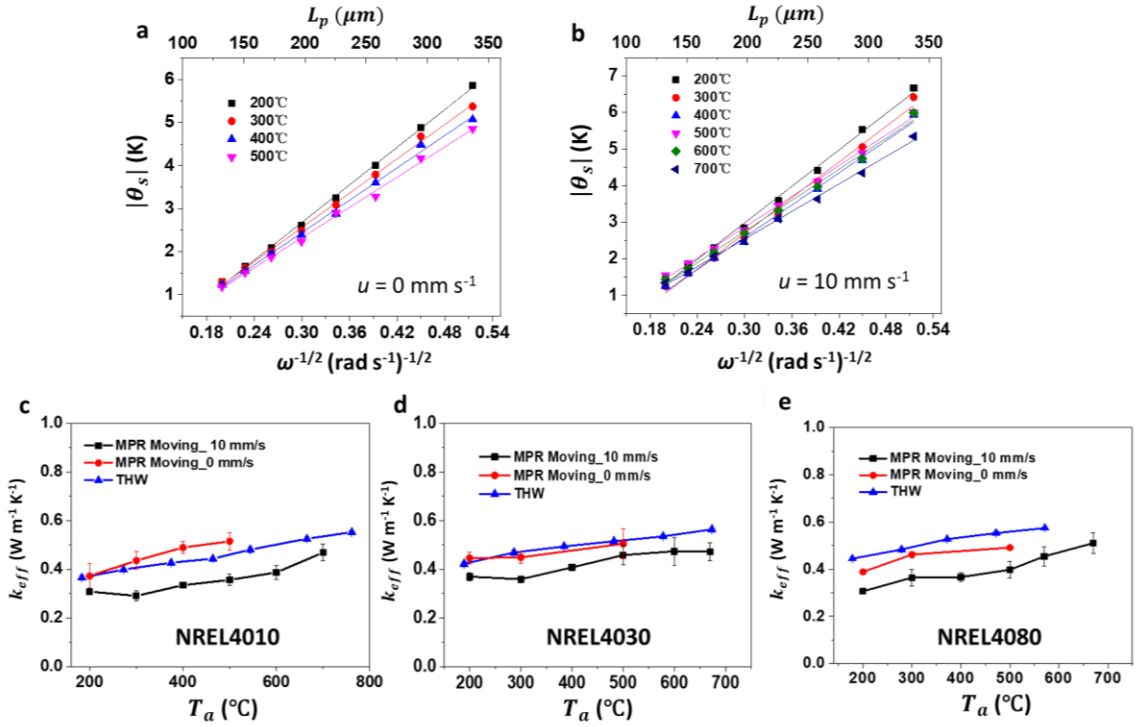

Figure 5-11. MPR measurement of moving irregular silica sands up to 700℃. (a) Thermal response at 0 mm s^{-1} in the moving particle setup up to 500℃ for silica 410 (average particle size 357 μm). (b) Thermal response at 10 mm s^{-1} in the moving particle setup up to 700℃ for HSP40/70.

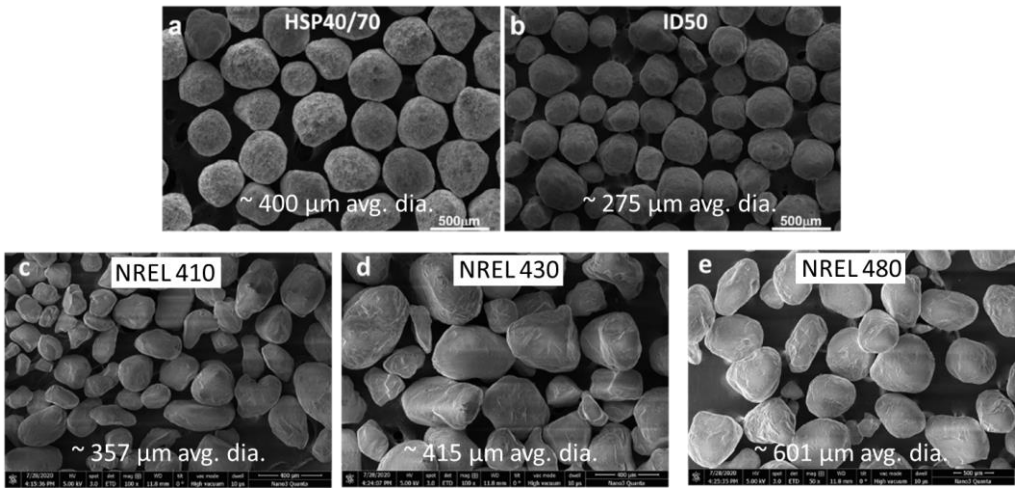

Figure 5-12. SEM images of tested particles. CARBO ceramic particles HSP 40/70 (a) and ID 50 (b), and silica sands (c) 410, (d) 430 and (e) 480.

To further investigate the effect of flow velocity on the k_{eff}, we measured the k_{eff} of CARBO ceramic particles HSP 40/70 (D_p ~ 400 µm), ID 50 (~ 275 µm) and silica sands, NREL 410 (D_p ~ 357 µm), NREL 430 (D_p ~ 415 µm) and NREL 480 (D_p ~ 601 µm) as shown in Figure 5-13, at the temperature T_a = 500 °C with the moving velocity from 0 to 30 mm s^{-1}. For the HSP 40/70 and ID 50, the k_{eff} decreases by ~ 15% and ~ 14%, respectively, as *u* increases from 0 to 10 mm s^{-1} and by ~31% and ~11%, respectively, as *u* increases from 0 to 30 mm s^{-1}. A greater reduction in the k_{eff} for the NREL silica sands can be observed as shown in Figure 5-12c to e. As *u* increases from 0 mm s^{-1} to 10 mm s^{-1}, the k_{eff} decreases by ~ 31%, ~ 10%, and ~ 23% for NREL 410, 430 and 480, respectively, in comparison to ~ 15% and 14% for HSP40/70 and ID50, respectively. From 0 mm s^{-1} to 30 mm s^{-1}, the k_{eff} decreases by ~ 38%, ~ 22%, and ~ 40% for NREL 410, 430 and 480, respectively, in comparison to ~ 31% and 11% for HSP 40/70 and ID 50, respectively. This trend is consistent with that observed in Figure 5-11, i.e., the

k_{eff} of silica sand decreases more at the moving state due to its irregular morphology and wide dispersion of particle size.

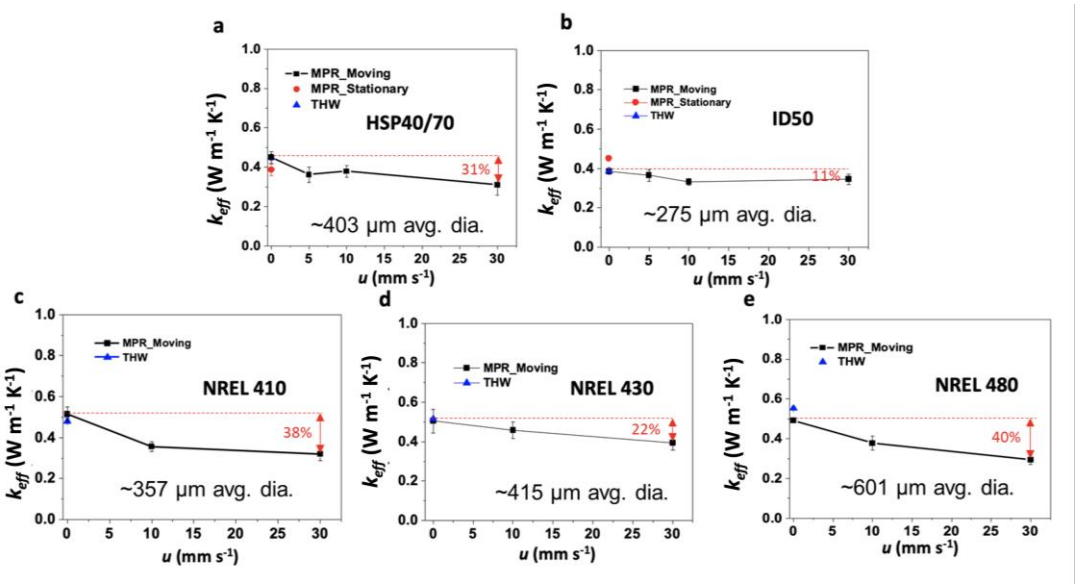

Figure 5-13. Effect of moving velocity u on the effective thermal conductivity of (a) HSP 40/70, (b) ID 50, (c) NREL 410 silica, (d) NREL 430 silica and (e) NREL 480 silica, measured with the moving MPR setup (all with 4 mm channel depth at 500℃).

The k_{eff} of CARBO ceramic with different particle sizes were measured as shown in Figure 5-14 at different temperature (300℃, 500℃ and 700℃) with the velocity up to 30 mm s^{-1}. It can be found at for all conditions and particle sizes, k_{eff} decreases by 15-30%. In general, the reduction of k_{eff} seems to be larger for larger particle sizes, e.g., at 700℃, as u increases from 0 to 30 mm s^{-1}, k_{eff} decreases by ~ 33%, ~ 30% and 27%, respectively. It is hypothesized that the reduction of k_{eff} is due to the increased near-wall thermal resistance as the velocity increases. For larger and more irregular particles, the particle-wall contact possibly deteriorates with increasing velocity, leading to a lower k_{eff}.

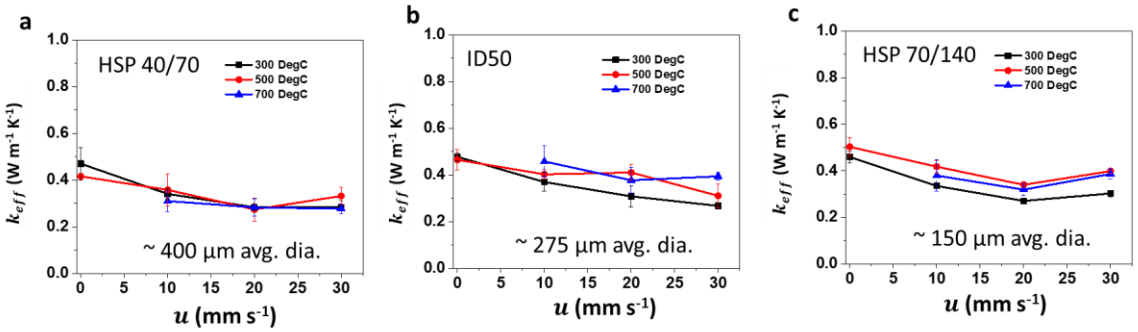

Figure 5-14. Effect of moving velocity u on the effective thermal conductivity of (a) HSP 40/70, (b) ID 50, and (c) HSP 40/70 at different temperature. All the three particles have the same material composition but different average particle sizes. The channel depth D_c is fixed at 2 mm.

To confirm if the reduction of k_{eff} arises from the near-wall thermal resistance or the bulk resistance, the bulk density of moving particle beds as a function of velocity was measured. As shown in chapter 4, the bulk effective thermal conductivity is highly dependent on the bulk density. To measure the bulk density, we modified the measurement setup by replacing the steel front plate with a transparent plastic cover to observe the flow pattern and the particle level to test the flowing velocity as shown in Figure 5-15a. Figure 5-15b shows the cross-section of the particle channel. The channel depth can be varied from 2 to 7.5 mm. As shown in Figure 5-15c, the position of the particle level is determined by the scales on plastic front cover. By counting the displacement of the particle level *s* over an interval of time *t*, the flowing velocity is calculated:

$$u = \frac{s}{t} \tag{5-16}$$

where *s* is the displacement of particle level and *t* is the interval of time. The channel depth and the channel width *W* are known. Therefore, the volumetric flow rate can be calculated with the knowledge of displacement *s*:

$$\dot{V} = \frac{V}{t} \tag{5-17}$$

where $\dot{V}$ is the volumetric flow rate and V is the displacement volume of particles over time of t. In the meantime, the mass m of particle for the displacement volume of V is measured by a balance. The mass flow rate $\dot{m}$ is calculated by:

$$\dot{m} = \frac{m}{t} \tag{5-18}$$

The bulk packing density is given by:

$$\rho = \frac{\dot{m}}{\dot{V}} \tag{5-19}$$

Figure 5-15d shows an example of the measurement, the particle level is flat because the flow pattern is plug flow, and thus the displacement can be easily obtained by the difference of particle level at different time. we measured the density of moving particles in 2 mm, 4 mm and 7.5 mm wide channels with the velocity up to 35 mm s^{-1} as shown in Figure 5-16. The density of moving particle is stable around 2278 kg m^{-3} with the uncertainty range of 5.9%, indicating that the density of particle is insensitive to the moving velocity. In addition, the density of particle bed is similar in channels with different channel depths. Therefore, it is believed that the reduction of k_{eff} is not attributed to packing density in the bulk regime at the flowing state.

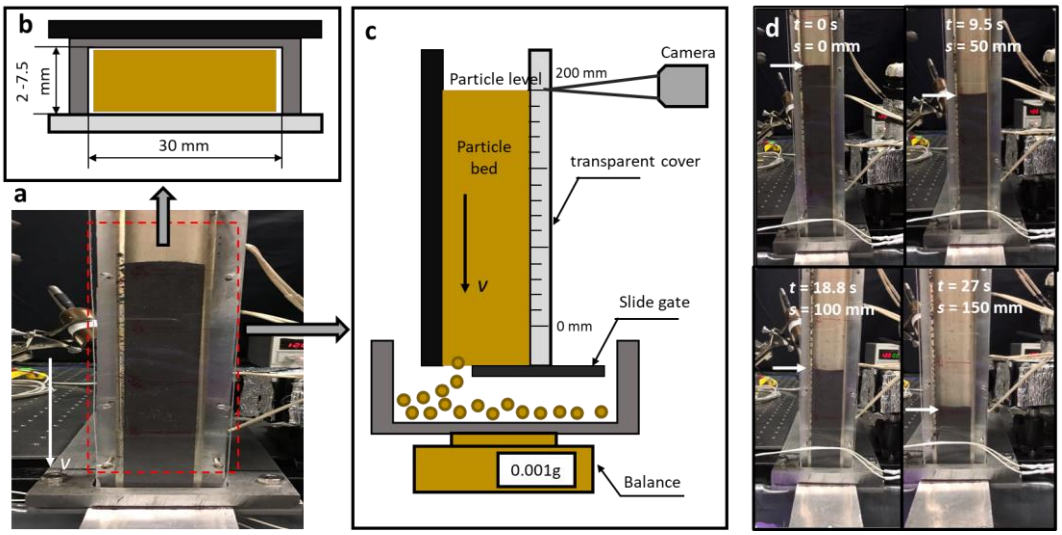

Figure 5-15. Measurement of bulk packing density of HSP 40/70 at different flowing velocity. (a) Observation of the flow pattern through the plastic front cover. (b) Cross-sectional view of the particle channel. (c) Schematics of the measurement. (d) Snapshot of particle level at different time and measurement of the displacement of particle level at u = 5.0 mm s^{-1}.

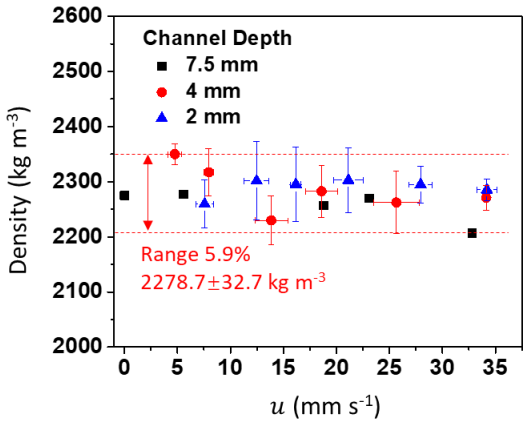

Figure 5-16. Measured packing density of particle bed at different moving velocity and with different channel depth.

5.3. Near-wall thermal resistance of moving particle bed

In the last section, we found that the k_{eff} of particle bed decreased with increasing moving velocity, which was likely due to the increased near-wall resistance. Although the existence of the near-wall thermal resistance R_{nw} has been known for a long time in the community of granular flow heat

transfer[36,124,182,184,186-190], it has not been well-quantified in an *in-situ* measurement. Most of the previous studies adopted a global measurement method to extract the near-wall thermal resistance from the global heat transfer coefficient, which not only lost the details of the thermofluid structures close to the wall but also failed to probe the micromechanical origin of the near-wall thermal resistance. In this regard, it is imperative to quantify the R_{nw} *in-situ* from the MPR measurement.

5.3.1. Measurement of near-wall thermal resistance

To separate the R_{nw} from the k_{eff} of the moving particle bed, we establish a 4-layer model using COMSOL on the moving particle as shown in Figure 5-17a (i.e., 10 μm Pyromark coating on 100 μm steel front cover, effective air-gap with the thickness $D_{air} = 0 - 50\ \mu m$ as a fitting parameter, and bulk particles in a channel depth of 2 mm). The laser heat flux is applied in the middle of the channel with the diameter of 10 mm at q_s = 13759 W m^{-2}, the same as the experiment. The flow pattern of the moving particle is a plug flow at a constant velocity u_b. The simulation parameters for 500°C are listed in Table 5-2 and the modeled temperature profile of the moving particles at different velocities is displayed in Figure 5-17b. The thermal properties of air, Pyromark coating and the bulk particles change with temperature which can be found in the literature and our prior studies in chapter 2[101,208]. The bulk region is treated as a uniform particle bed with the thermal conductivity of a stationary particle bed measured in chapter 4. It is noted that the near-wall resistance is treated as a uniform air gap layer with an effective thickness of D_{air} with the thermophysical properties of air at the specific temperature as found in many of the previous literature as shown in Figure 5-17c. Figure 5-17d shows

the sensitivity analysis of MPR measurement on near-wall resistance, where the sensitivity is defined as:

$$Sens. = \frac{\Delta\theta_s/\theta_s}{\Delta\gamma/\gamma} \tag{5-20}$$

where θ_s is the amplitude of the surface temperature oscillation and γ is the parameter of interest. The sensitivity on D_{air} of 1 indicates that 1% change in D_{air} leads to 1% change in θ_s. It is seen that at low frequency ($\omega^{-1/2} = 0.7 - 1.5$), the thermal response is mostly sensitive to the near-wall thermal resistance (with the sensitivity greater than 0.4), which is represented by the D_{air}. At higher frequency, where the penetration depth decreases, the sensitivity on D_{air} is reduced and the thermal response is more sensitive to the steel and coating. Therefore, to measure the D_{air}, it is imperative to lower the measurement frequency down to ~ 0.1 Hz (or $\omega^{-1/2} \sim 1$). However, further reduction in the measurement frequency would be challenging due to the thermal noise and the instrumentation limitation (e.g., high-pass filter in lock-in). Therefore, in the current measurement, the lower limit of measurement frequency is set at 0.07 Hz (as opposed to 0.5 Hz in the measurement of k_{eff}). Figures 5-17e and 5-17f show the thermal responses of ID50 particles at 0 mm s^{-1} and 20 mm s^{-1} from the experiment respectively. We modeled the thermal responses at the same moving velocity but with varying airgap thickness from 0 to 60 μm, which are plotted in the same figures along with the experimental results. As shown in Figure 5-17e, for $u = 0\ mm\ s^{-1}$, it is seen that the experimental results lie between the modeled results with $D_{air} = 0$ μm and $D_{air} = 10$ μm, indicating that the airgap thickness at u = 0 mm s^{-1} is 0-10 μm. The experimental curve does not show a plateau at low frequency because there is no convection effect. As shown in Figure 5-17f, due to the convection effect, the curve plateaus in the low

frequency range, similar to the result of flowing liquids reported in chapter 3. It is found that the experimental results lie between the modeled curves with $D_{air} = 20$ μm and $D_{air} = 40\ \mu m$, indicating that the effective airgap thickness for the moving particles at $u = 20$ mm s^{-1} is 20-40 μm.

Table 5-2. COMSOL simulation parameters of moving particle at 500℃

Name	**Expression**	**Description**
H	2e-3 [m]	Channel height
L	20 [mm]	Channel length
D_s	0.1 [mm]	Steel frontplate thickness
L_{laser}	10 [mm]	Laser spot diameter
k_{ss304}	18.5 [W/m/K]	Kappa of steel
c_{ss304}	624 [J/kg/K]	Specific heat of steel
ρ_{ss304}	8000 [kg/m^3]	Density of steel
L_{probe}	1 [mm]	Probe diameter
Q	13759 [W/m^2]	Harmonic Heat Source
u	20 [mm/s]	bulk velocity
$k_{particle}$	**From chapter 4**	Kappa of particle
$c_{particle}$	1038 [J/kg/K]	Specific heat of particle
ρ_{ss304}	2200 [kg/m^3]	Density of particle
$D_{coating}$	10e-6 [m]	Coating thickness
D_{air}	0-50e-6 [m]	Airgap thickness
$k_{coating}$	0.5 [W/m/K]	Kappa of coating
$c_{coating}$	1100 [J/kg/K]	Specific heat of coating
$rho_{coating}$	1100 [kg/m^3]	Density of coating
T_a	573 [K]	ambient temperature
k_{air}	0.042 [W/m/K]	Kappa of air

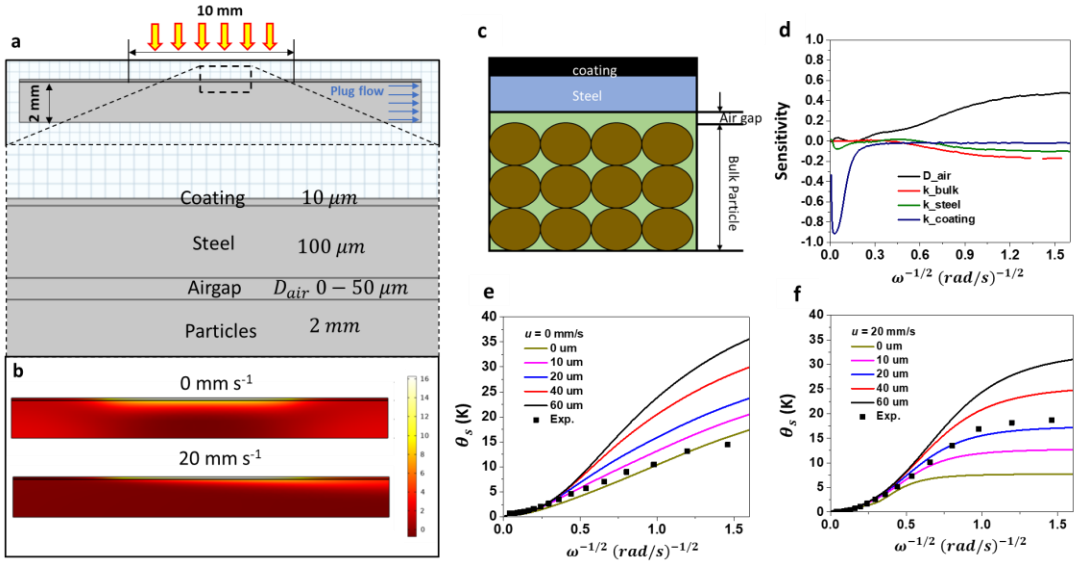

Figure 5-17. FEM modelling of moving particles using COMSOL. (a) Schematic of four-layer model in COMSOL. (b) Simulated temperature profile of moving particles at 0 mm s^{-1} and 20 mm s^{-1}, respectively. (c) Schematic of near-wall airgap. (d) Sensitivity analysis of the airgap thickness measurement in model. Preliminary fitting of the airgap thickness for experiment data of ID-50 particles at (e) 0 mm s^{-1} and (f) 20 mm s^{-1}.

To achieve the optimum fitting, a reverse fitting algorithm (Levenberg-Marquardt or LM method) is employed as shown in Figure 5-18a. In brief, the modeled result based on a random seed of D_{air} is obtained and a sensitivity matrix is obtained by changing D_{air} by 1%. According to the LM method, we could derive the next-step fitting parameters value based on the previous-step fitting parameters value and their Jacobin matrix followed by Equation 5-21,

$$P^{n+1} = P^n + [(J^n)^{Tr}J^n + \mu^n\Omega^n]^{-1}(J^n)^{Tr}[T_{meas} - T_{est}(P^n)] \quad (5\text{-}21)$$

where $\Omega^n = diag[(J^n)^{Tr}J^n]$, μ^n is damping factor (user defined). We defined the square root error $S(P^n)$ as shown in the Equation 5-22

$$S(P^n) = \sqrt{\sum_{i=1}^{N}(T_{exp-i} - T_{sim-i})^2} \quad (5\text{-}22)$$

We defined a convergence number δ=5%. If the value of error change is less than δ, we stopped the iteration, and the optimal D_{air} is obtained. More details of the reverse fitting algorithm can be found in Ref.[209]. Figure 5-18b to 5-18d display the fitting of ID-50 particles at 300℃, 500℃, and 700℃, respectively, with the variation in the flowing velocity from 0 to 30 mm s^{-1}. The model generally fits well with the experimental results with high R^2value (> 0.98). All the measurements have been repeated at least three times, and the average D_{air} for ID-50 as a function of velocity at different temperatures is shown in Figure 5-18e. It is seen that D_{air} generally increases with increasing velocity, e.g., at $v = 0\ mm\ s^{-1}$, D_{air} is 0-10 μm and increases to 30-40 μm at $u = 30$ mm s^{-1}, indicating an increasing near-wall thermal resistance $R_{nw} = \frac{D_{air}}{k_g}$, which explains the decreasing k_{eff} of moving particle bed.

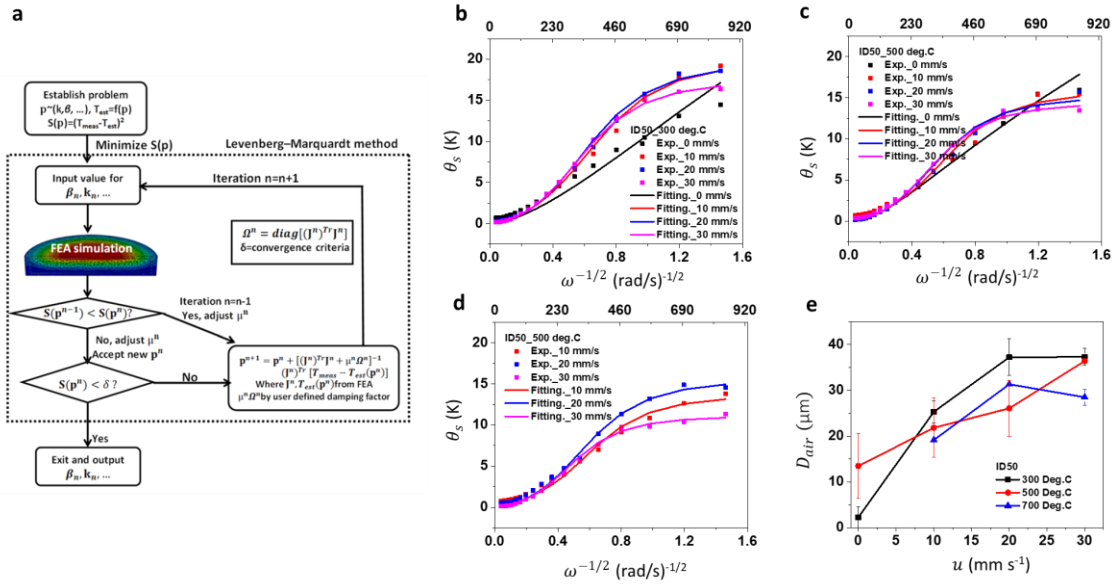

Figure 5-18. Thermal response and fitting of the airgap thickness for ID50 particles. (a) LM Algorithm of optimal fitting of airgap thickness D_{air}. Thermal responses and fitting of ID50 at different velocities at temperature of (b) 300°C, (b) 500°C and (d) 700°C. (e) Fitted D_{air} for ID50 as a function of moving velocity at different temperatures.

Figure 5-19 summarizes the raw data for ID 50 at different velocities up to 30 mm s^{-1} and temperature up to 700°C. The D_{air} is best fitted based on the L-M method. The particles were measured at least three times at a specific operational condition. Figure 5-20 compares the D_{air} of CARBO ceramic particles with different particle sizes (i.e., HSP 40/70 with D_p= 400 μm in Figure 5-20a, ID 50 with D_p= 275 μm in Figure 5-20b and HSP 70/140 D_p= 150 μm in Figure 5-20c). As shown in Figure 5-20b, Similar to the ID 50 particles, D_{air} for HSP 40/70 increases with increasing flowing velocity, e.g., at $T_a = 300°C$, D_{air} increases from 10 μm at u = 0 mm s^{-1} to 47 μm at u = 20 mm s^{-1}. In addition, it seems that D_{air} is slightly higher for the HSP 40/70 than for the ID 50, e.g., at $u = 20$ mm s^{-1} and $T_a = 500°C$, D_{air} for HSP 40/70 is ~ 40 μm while that for the ID50 is ~ 23 μm. Similar trend was also found for HSP 70/140 as shown in Figure 5-20c, where D_{air} increases from ~ 10 μm to ~ 40 μm. However, although the particle size of HSP 70/140 is much smaller than that of ID 50 (D_p of 150 μm vs 275 μm) but the D_{air} remains similar. This indicates that there are more factors at play than the particle size on the development of near-wall airgap layer. In general, the D_{air} for all the particles is in the range of 1/7 to 1/10 of particle diameter D_p, which agrees well with that found in the literature[124,184]. For example, Sullivan *et al.* [124] and Spelt *et al.*[184] measured the Nu_d *vs* Pe_L of various granular materials in a particle heat exchanger. The found that to fit the data, an effective airgap thickness of ~ $\frac{1}{10}D_p$ should be introduced. In general, it has long been assumed the existence of an effective airgap close to the heat exchanger wall, leading to the deterioration of heat transfer performance. The results reported in this section was the first in-situ

quantification of the D_{air}, which validates the assumption over half a century since 1970s. While we have confirmed the existence of a near-wall airgap and quantified it, the origin of such an airgap remains elusive, which limits our ability to improve the thermal performance of the particle heat exchanger. Therefore, in the next section, we will describe our effort in the DEM/FEM modeling to understand the heat transfer mechanism in the near-wall region.

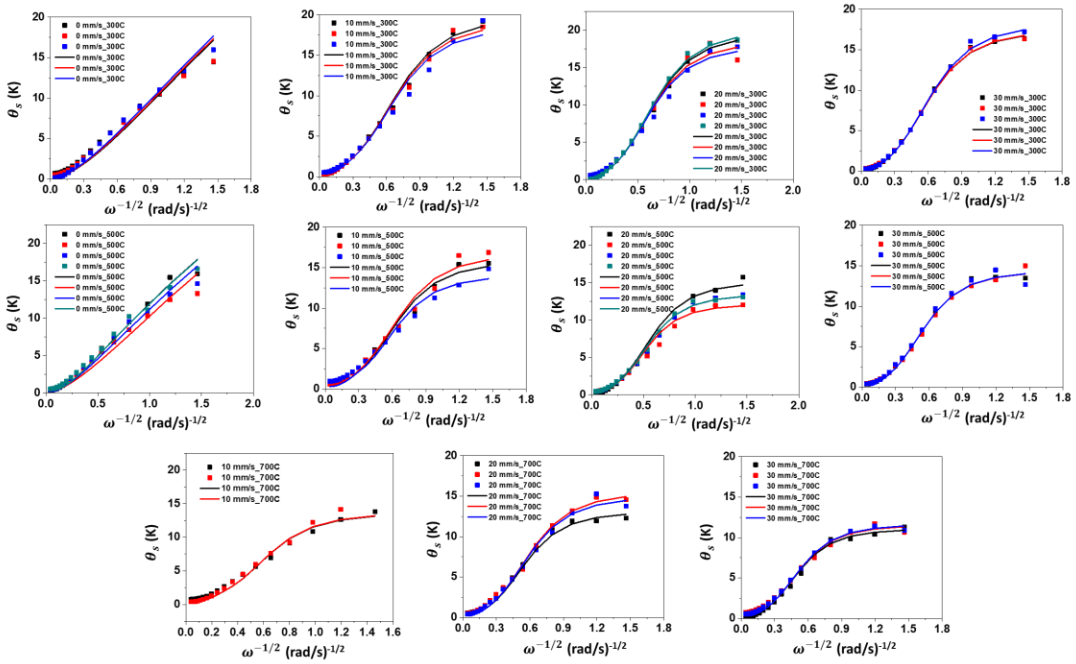

Figure 5-19. Thermal responses and curve fittings of ID 50 at different flowing velocities (0 to 30 mm s^{-1}) and temperature (300-700℃).

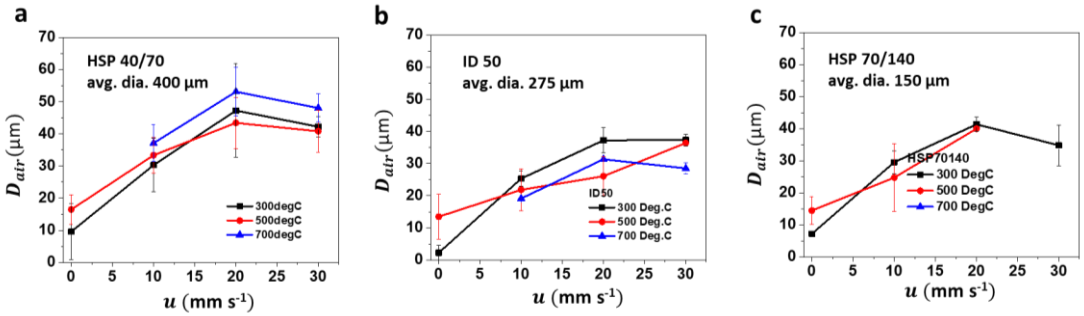

Figure 5-20. Measured D_{air} of CARBO ceramic particles as a function moving velocity up to 30 mm s-1 in a 2 mm channel with variation in temperature of 300℃, 500℃ and 700℃. Measurement results for (a) HSP 40/70 (D_p= 400 μm), (b) ID 50 (D_p= 275 μm) and (c) HSP 70/140 (D_p= 150 μm).

5.3.2. Discrete element modeling of near-wall resistance

We conducted DEM simulation of moving particle bed using the same method as shown in chapter 4.4.2 except that a stationary particle flow was sustained in this simulation to extract the packing structure of a stationary moving particle bed.

As shown in Figure 5-21a, there is an empty reservoir and channel with geometry similar to the experimental moving particle MPR setup. The channel is rectangular with the cross-section area of $20D_p \times 20D_p$. In the DEM simulation, the materials of particles and the channel are defined according to the experiment setup. All the simulation results are generated using the properties of CARBO ceramic HSP 40/70 (D_p ~ 400 μm) particles and steel walls. Particles are generated from the top of the reservoir at a constant speed while there is a stopper at the bottom of the channel. Therefore, the simulation domain will be filled with particles at the equilibrium state. The simulation is the same as that for the stationary particles up to this point. Subsequently, the stopper at the bottom of the channel will be opened to such an extent that the particles start flowing at a desired velocity u at t_0. By changing the opening size of the slide gate, the velocity can be changed from 0 – 35 mm s^{-1} to match with the range of velocity in our experiment. The packing structure of the moving particle flow will be obtained at the position of the measurement window, when the particle flow stabilizes, indicated by the stable distribution of flowing velocity extracted between t_0 and t_2, i.e., $t_1 = 0.01\ s$, $t_2 = 0.02\ s$ as shown in Figure 5-21b (flow direction) and 5-21c (transverse direction to the flow). It is seen that the packing structure becomes stabilized after 0.01 s.

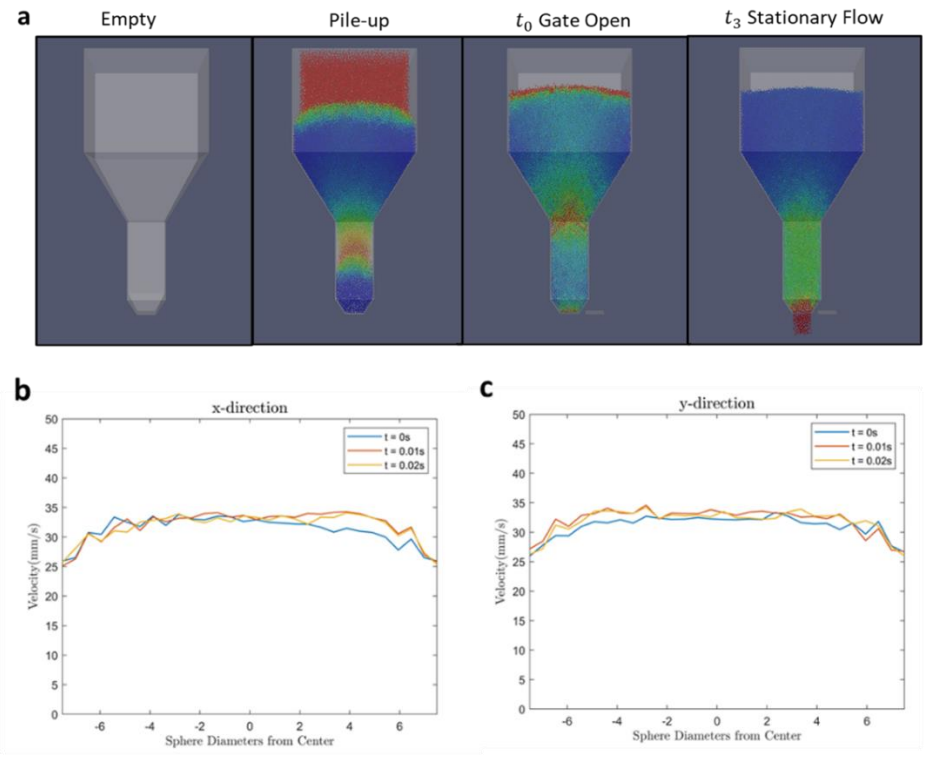

Figure 5-21. Schematic of moving particle bed simulated by discrete element modeling (DEM). (a) Procedures of DEM simulation. Distribution of flowing velocity at different time at $u = 30\ mm\ s^{-1}$ in the (b) *x* direction and (c) *y* direction.

Figure 5-22a compares the packing density of the particle bed at different moving states ranging from $u = 0\ mm\ s^{-1}$ to $35\ mm\ s^{-1}$. Notably, the packing density at the moving state is similar to that at the stationary state, which is around 54%. This result is consistent with the experimental observation shown in Figure 5-16. However, the contact length ratio between the particles decreases as shown in Figure 5-22b. Here, the contact length ratio (C.L.R.) is defined as the ratio of the overlap length between two particles over the particle diameter. The contact length ratio seems insensitive to the flowing velocity and stabilizes at 0.00095% when the flow velocity is greater than 5-10 mm/s, which is about 85% of the stationary state (0.0011%). Figure 5-22c indicates how the coordination number changes with an increasing flow velocity. The coordination number

shows a rapid reduction in the range of 0-5 mm/s, followed by a slower decreasing stage when $u > 10\ mm\ s^{-1}$. This implies that a higher flow velocity may weaken the solid conduction in the particle bed by reducing the inter-particle contacts. Moreover, we define a near-wall contact ratio as following:

$$N.C.R = \frac{n_{contact}}{n_{near-wall}} \tag{5-23}$$

where $n_{contact}$ is the number of particles in contact with the wall per unit area, $n_{near-wall}$ is the number of particles whose distances from the wall are no large than $\frac{D}{7}$ per unit area. Here, $\frac{D}{7}$ is an estimated thickness of a high thermal resistance layer caused by the lack of solid particles in the near-wall region. Figure 5-22d shows that the near-wall contact ratio has the similar trend to the coordination number with respect to the flow velocity. According to this, we may hypothesize that the heat transfer process will also be weakened by a higher flow velocity.

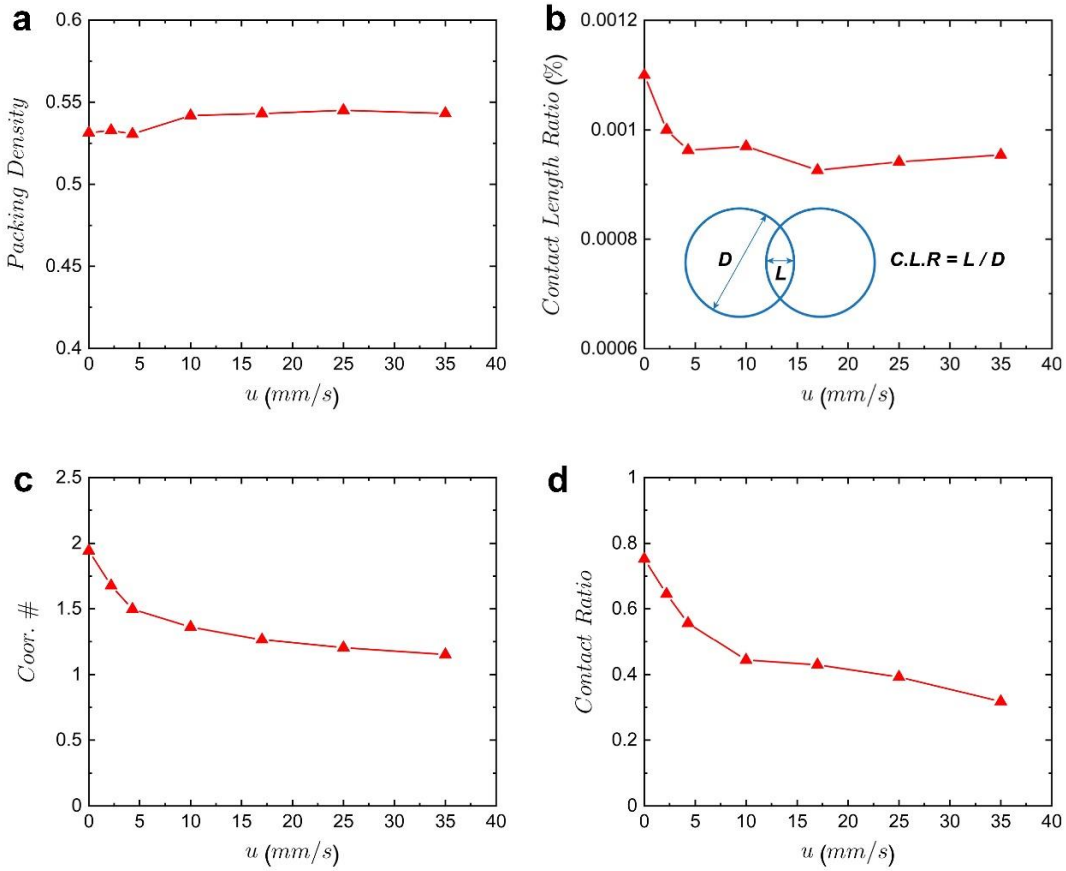

Figure 5-22. Packing structure of moving particle bed. (a) Packing density, (b) Contact length ratio, (c) Coordination number and (d) Near-wall contact ratio.

To model the k_{eff} of moving particle bed, we extract the packing structure from the near-wall region of a moving particle bed (when the flow stabilize and the position far away from the entrance and exit) and input it into COMSOL for heat transfer modeling as shown in Figure 5-23a. Similar to the modeling of stationary particle flow, we applied 1K temperature difference between the top and bottom surface of the simulation domain and record the normal heat flux through the bottom surface q_s. With the thickness of simulation domain known $L = ND_p$, where N is an normalized distance from the wall. As shown in Figure 5-23a, if we choose the thickness to be $L = 5D_p$, then N = 5. The effective thermal conductivity

k_{eff} is extracted from the applied temperature drop across the domain in the direction of heat flux and measured heat flux:

$$k_{eff} = \frac{q_s L}{\Delta T} \tag{5-24}$$

where q_s is the measured heat flux at the applied temperature drop $\Delta T = 1K$ in the *x* direction. However, it should be noted that as shown in Figure 5-23b**,** the effective thermal conductivity is related to the near wall resistance R_{nw} and bulk thermal resistance R_b by:

$$\frac{ND_p}{k_{eff}} = R_{nw} + \frac{ND_p}{k_{bulk}} \tag{5-25}$$

where *N* is the equivalent number of particles in the vertical direction of the simulation domain and $N = 5$ for the $5D \times 5D \times 5D$ unit, R_{nw} is the near-wall thermal resistance and $R_{nw} = \frac{D_{air}}{k_g}$. In this case, $R_b = \frac{ND_p}{k_{bulk}}$ is ~ 5E-3 $m^2 K^1 W^{-1}$, which is much greater than R_{nw} ~ 2E-4 $m^2 K^1 W^{-1}$ assuming 10 μm thick airgap. Therefore, the near-wall resistance cannot be observed for a large simulation domain because the majority of this domain has bulk-like thermal conductivity as shown in Figure 5-23c. As a matter of fact, in our study, the thermal penetration depth $l_p = \sqrt{\frac{2\alpha}{\omega}}$ is in the range of 500 μm to 1 mm, equivalent to 1 – 2 particle sizes, enabling us to observe the near-wall thermal resistance. Therefore, we reduce the simulation domain to $5D_p \times 5D_p \times 1.3D_p$ where $1.3D_p$ is along the heat transfer direction as shown in Figure 5-23d. As shown in Figure 5-23e, the simulation results have a similar decreasing trend with the experiment results for HSP 40/70, i.e., k_{eff} decreases with decreasing velocity monotonously, and the k_{eff} decreases by 16.3% as the velocity increases from 0 mm s^{-1} to 35 mm s^1. According to Equation 5-25, the air

gap thickness D_{air} can be extracted from the k_{eff}. Figure 5-23e shows that the D_{air} also increases with increasingly velocity but is weakly dependent on the temperature. The modelled D_{air} agrees well with the experimental data. The above results further confirm our experimental results and prove that the thermal resistance is a major resistance in the moving particle bed heat exchanger.

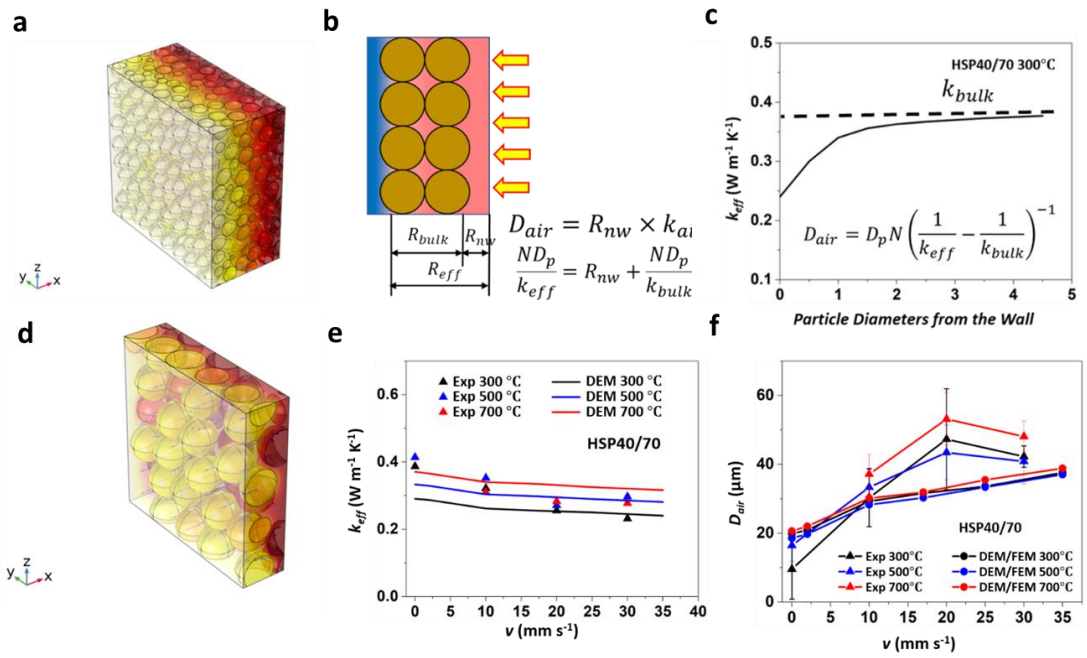

Figure 5-23. DEM and COMSOL modelling results of the near-wall region in the moving particle bed. (a) Snapshot of a $10D \times 10D \times 5D$ simulation domain. (b) An equivalent two-layered thermal resistance network of the near-wall region in the moving particle bed. (c) Predicted k_{eff} as a function of distance from the wall in the transverse direction. (d) Simulation domain of a $10D \times 10D \times 5D$ simulation domain for higher sensitivity on near-wall thermal resistance. (e) Comparison of experimental and modeled k_{eff} of HSP 40/70 based on a $5D \times 5D \times 1.3D$ unit as a function of velocity. (f) Estimated D_{air} of HSP 40/70 based on the DEM+COMSOL simulation results and the model shown in (c).

5.3.3. Micromechanical origin of near-wall resistance

To better explain the origin of the near-wall thermal resistance and to provide guidelines for the heat exchanger design, we probe into the particle rheology and study how the airgap develops in the moving particle bed.

In this section, we modelled the D_{air} of ID 50 (D_p ~ 275 μm) based on the granular diffusion theory. In this theory, we only need the information of the particle rheology from the DEM simulation without heat transfer modelling from COMSOL. In other words, we attempted to explore the micromechanical origin of the near-wall thermal resistance directly inherited from the particle motion. While the origin of the near-wall thermal resistance is still not fully understood, there are two main assumptions that have widely been considered. There is an intrinsic near-wall region for the stationary particle bed where the porosity is higher due to the lower coordination number and smaller contact area compared to the bulk region. The porosity variation with distance from the constraining surface usually took the form of a damped oscillator, having the maximum at the wall and minimum about half a particle diameter from the surface[187,192,193] as shown in Figure 5-4. Although the porosity oscillation explained partly the origin of near-wall thermal resistance of stationary particles, it failed to match the order of magnitude of near-wall thermal resistance and explain why it increased with increasing velocity in moving particle bed.

Due to the shear force between moving particles, particles close to the wall may move away from the wall. Therefore, an extra near-wall thermal resistance in a moving particle bed could also be induced by the formation of air cushion layer, or effective airgap layer. It has been well-known that in addition to the bulk motion of particles, individual particles move randomly driven by the shear force between the particles and at the particle-wall interfaces. Due to analogy between the random motion of particle and gas molecules, the dense-gas kinetic theory has been developed to describe the particle flow[194-196] as shown in Figure 5-5. Figure 5-5 displays the schematics of random

movement of particles in a bulk particle flow [196]. Here, we define the streamwise direction as x direction and the transverse direction as y direction. v and u are the particle velocity components in x and y direction, respectively. The average velocity can be calculated as:

$$\bar{v} = \frac{\sum_{k=1}^{N} v_k}{N} \tag{5-26}$$

$$\bar{u} = \frac{\sum_{k=1}^{N} u_k}{N}$$

where u_k and v_k are the velocity components of the k-th particle, N is the total number of particles of interest. The fluctuation velocities in the two directions were:

$$v' = \sqrt{\frac{\sum_{k=1}^{N}(v_k - \bar{v})^2}{N}} \tag{5-27}$$

$$u' = \sqrt{\frac{\sum_{k=1}^{N}(u_k - \bar{u})^2}{N}}$$

For a 2-D granular flow, the diffusivity tensor can be defined as:

$$D = \begin{bmatrix} D_{xx} & D_{xy} \\ D_{xy} & D_{yy} \end{bmatrix} \tag{5-28}$$

where D_{xx} and D_{yy} are the granular self-diffusivity in the x and y direction, respectively. D_{xy} is the off-diagonal diffusivity in the y direction influenced by the mean flow in the x direction. In analogy to the thermodynamic temperature of gas, the granular temperature can also be defined based on the kinetic energy of particles. Since the random motion between particles are driven by the shear force, the granular temperature is expressed as the fluctuation velocity instead of the bulk or average velocities, i.e., $T_y \propto u'$ and $T_x \propto v'$ [195]. From the dense-gas kinetic theory derivation in a homogeneous and stationary

velocity field of granular flow, the self-diffusivity of particle in the specific vector direction is given by:

$$D_{ii} = \frac{D_p(\pi T_{ii})^{\frac{1}{2}}}{8\left(1+e_p\right)\nu g_0(\nu)} \tag{5-29}$$

where T_{ii} is the granular temperature in the corresponding direction, calculated based on the velocity component in the same direction. e_p is the coefficient of restitution of particle; ν is the solid fraction and $g_0(\nu)$ is an equation of state of ridge spheres given by the Carnahan-Starting expression[197]:

$$g_0(\nu) = \frac{2-\nu}{2(1-\nu)^3} \tag{5-30}$$

Equation 5-29 is reduced to the classical Chapman-Enskog expression for gas diffusion in case of perfectly elastic particles[198,199].

In addition to the granular temperature, we can also calculate the entries of the diffusivity tensor by the mean-square diffusive displacement. The diffusive displacement of particles in the DEM simulation can be calculated by:

$$x = r_x - \sum_k \bar{v}_k \Delta t \tag{5-31}$$

$$y = r_y - \sum_k \bar{u}_k \Delta t$$

where r_x and r_y are the real displacement of particle in the x and y directions, respectively. Δt is the time step between two frames and k denotes the k-th frame in the DEM simulation. The diffusivity can be calculated by:

$$D_{xx} = \frac{1}{2}\frac{d\langle xx\rangle}{dt} \tag{5-32}$$

$$D_{yy} = \frac{1}{2}\frac{d\langle yy \rangle}{dt}$$

$$D_{xy} = \frac{1}{2}\frac{d\langle xy \rangle}{dt}$$

Figure 5-24 shows the schematic of the moving particle bed in the DEM simulation and the particle trajectories from 13 different particles within a time period of 30 ms. There are more than 6000 particles in the white box in Figure 5-23. The displacement and velocity of the individual particles can be extracted from the difference of coordinates at as specific time interval.

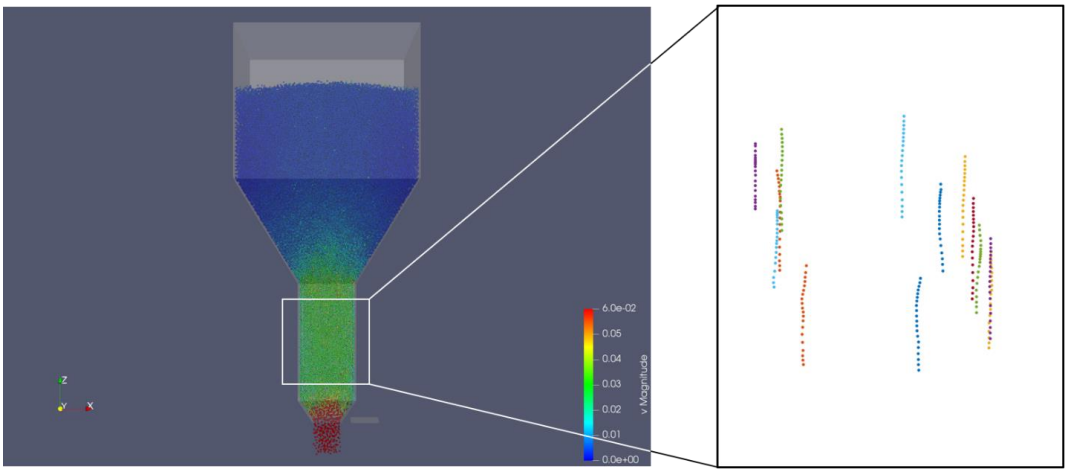

Figure 5-24. Schematic of DEM simulation of moving particle bed and particle trajectories in the channel within a time period of 30 ms.

The coordinates and velocity components of all particles can be extracted from the DEM files directly. Based on this data, the velocity fluctuation of ID50 (Figure 5-25) in the x (streamwise) and y (transverse) direction can be calculated. The higher mean flow velocity causes more frequent interaction between particles, hence higher velocity fluctuations in both x and y directions. In the fully developed region of the granular flow (> 5 particle diameters), as shown in Figure 5-25a and Figure 5-25c, the velocity fluctuation v' and u' are almost constant along the x direction. However, as shown in

Figure 5-25b and Figure 5-25d, both v' and u' reaches the maximum value at the wall, then decrease and form a plateau after 4 particle diameters away from the wall along the y direction. According to Equation 5-29, a higher velocity fluctuation results in a higher diffusivity. This indicates the wall has a significant effect on the diffusive behavior of granular flow. Besides, the magnitude of v' is twice as much as that of u', which is due to the mean flow in x direction.

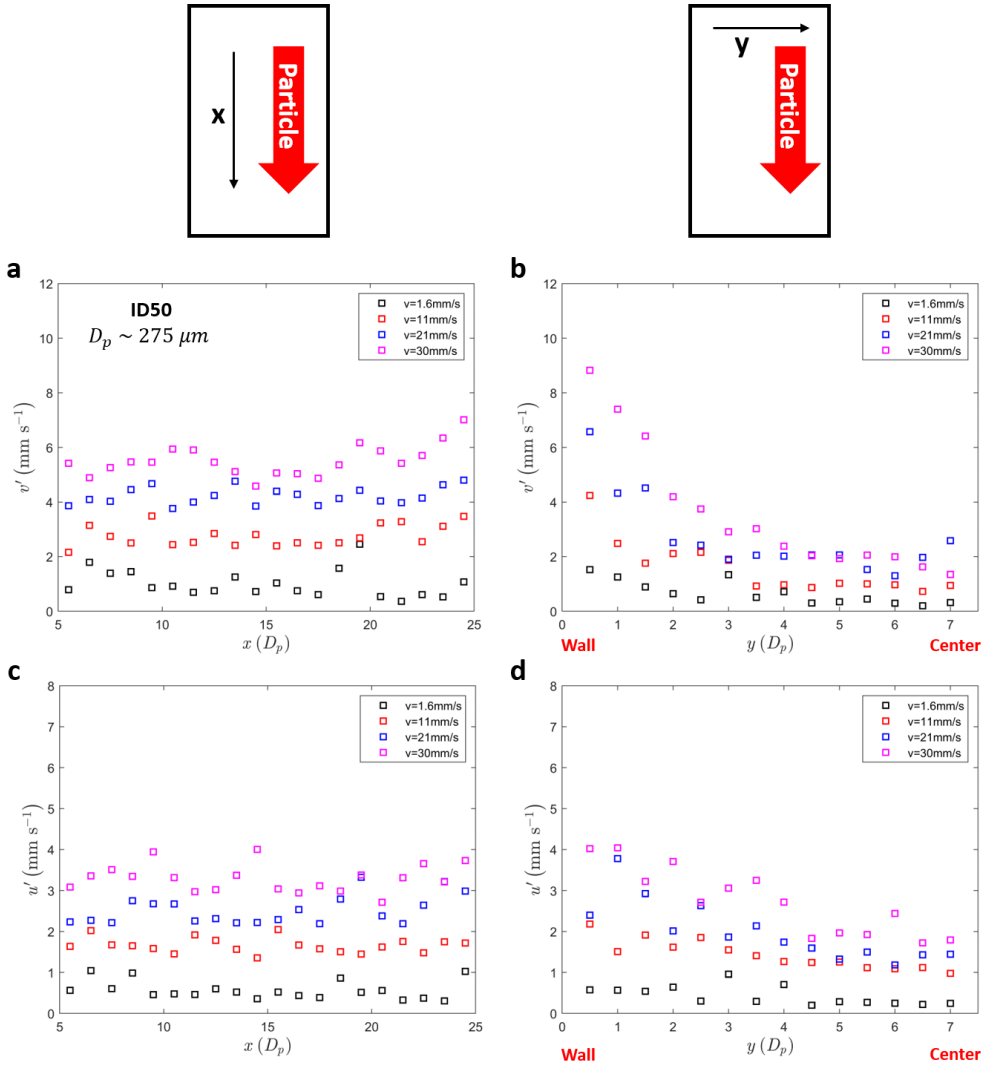

Figure 5-25. Streamwise velocity fluctuation v' of ID50 in (a) streamwise direction x and (b) transverse direction y. Transverse velocity fluctuation u' of ID50 in (c) streamwise direction x and (d) transverse direction y.

According to Equation 5-32, we can acquire the mean-square displacement and then the diffusivity of ID50 (Figure 5-26). Figure 5-26a to 5-26c show the mean-square displacement curve for bulk velocity of 11 mm^{-1}, 21 mm s^{-1} and 30 mm s^{-1}, respectively. The diffusivity can be estimated from the slope of the linear region. There is a short period of time around 20 ms to 30 ms before the curves reach the linear region. In that period, the particles need to experience enough interactions with other particles, e.g., collisions to sample the correct diffusive behavior. Trivially, the length of this period of time is shorter for a larger mean flow velocity. To get the accurate diffusivity, both linear fitting method and a second-order difference formula are implemented, and their results are consistent. Figure 5-26d shows the diffusivity of ID50 at different mean flow velocity. The diffusivity increases as the velocity increases, indicating a stronger disorder in the granular flow. In a condition where the near-wall resistance dominates, higher D_{yy} and D_{xy} in the transverse direction tend to worsen the contact between particles and the wall, and may cause a larger air gap thickness and a lower k_{eff}. This agrees well with experimental observation of increased near-wall thermal resistance with increasing velocity. Besides, D_{xx} is around 4 times greater than D_{yy} and D_{xy} attributed to the mean flow in x direction, which agree well with that reported in the literature[196].

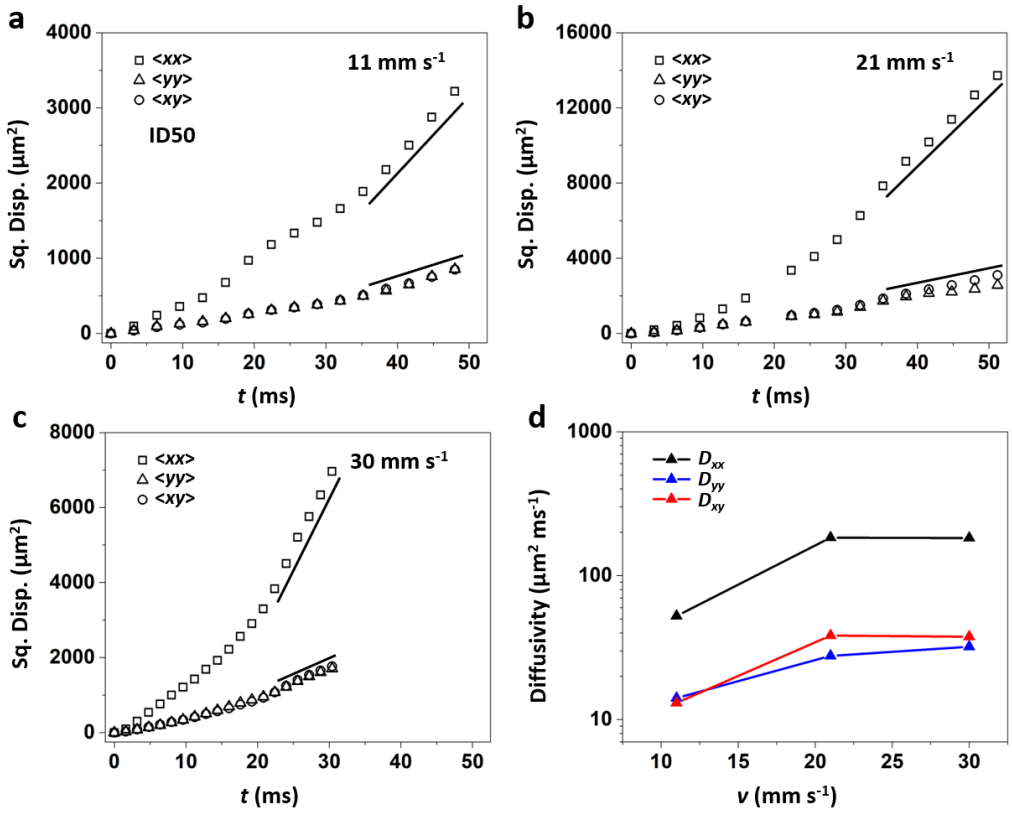

Figure 5-26. Mean-square displacement of ID 50 particle at different velocities of (a) 11 mm s^{-1}, (b) 21 mm s^{-1} and (c) 30 mm s^{-1}. (d) Diffusivity of ID 50 particle at different velocities obtained from equation 5-32.

The diffusivity of ID 50 particles at different bulk velocity can also be calculated based on Equation 5-29. The fluctuation velocity is shown in Figure 5-26. Since the fluctuation velocity u' decreases away from the wall in the y-direction as shown in Figure 5-26d, the calculated diffusivity also decreases away from the wall as shown in Figure 5-27a. It is noted that the diffusivity obtained from Equation 5-29 is slightly lower than that predicted by the displacement Equation 5-32 because in the later equation, perfect elastic collision between particles is assumed. If we set the coefficient of restitution e_p = 0 (i.e., elastic

collision), the same results can be obtained. Nevertheless, since both methods give similar diffusivity, we believe that the analysis of particle diffusivity is solid.

Based on the particle diffusivity D_{yy}, the airgap layer close to the wall can be estimated based on:

$$D_{air} = \sqrt{2D_{yy}t_c} \tag{5-33}$$

where t_c is the characteristic time for particle diffusion and $t = \frac{D_P}{u_b}$ where u_b is the bulk velocity of particle flow. Table 5-3 compares the transverse granular diffusivities in modelled from the diffusive placement and fluctuation velocity. It is seen that both models give similar results, confirming the accuracy of our models.

Table 5-3. Transverse diffusivities modelled by diffusive displacement and velocity fluctuation.

Diffusivity	Bulk velocity (mm s^{-1})		
	11	21	30
Method 1 D_{yy} (m^2 s^{-1})	1.5×10^{-8}	2.4×10^{-8}	2.8×10^{-8}
Method 2 D_{yy} (m^2 s^{-1})	1.41×10^{-8}	2.78×10^{-8}	3.21×10^{-8}

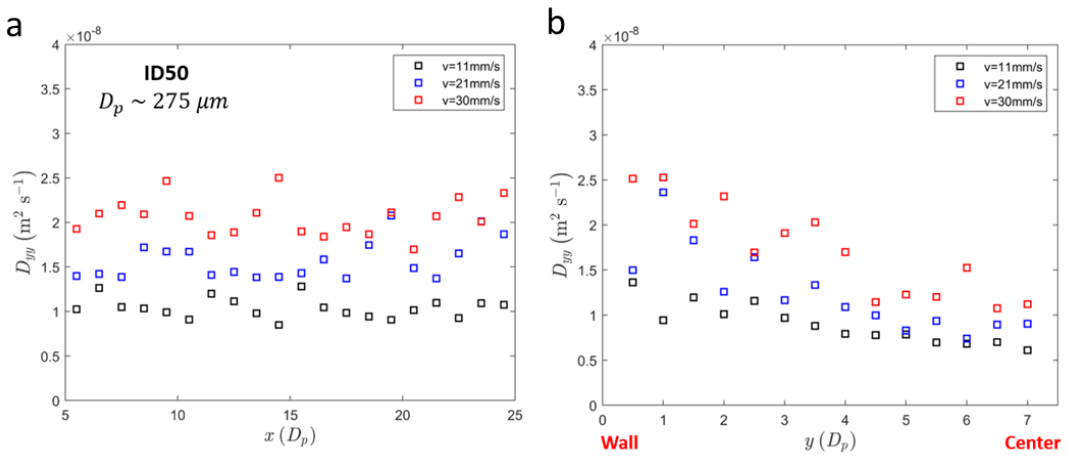

Figure 5-27. Particle diffusivity based on the granular temperature. Particle diffusivity of ID 50 at different velocity in the(a) flow direction (x-direction) and transverse direction (y-direction) obtained from Equation 5-29.

Table 5-4 compares the calculated D_{air}(based on Equation 5-33) from the particle diffusivities predicted by the displacement and granular temperature, respectively, D_{air} from the COMSOL modeling, and that obtained experimentally. It can be found that theoretically predicted D_{air} gap agrees well with the experimental results. Therefore, it is concluded that the near-wall thermal resistance can be well explained by the particle diffusion driven.

Table 5-4. Comparison of experimental and modelled D_{air}.

D_{air} (μm)	Bulk velocity (mm s^{-1})			
	0	11	21	30
Exp.	0	~ 20	~ 30	~ 30
DEM+COMSOL	~ 18	~ 28	~ 31	~ 33
DEM_Displacement	0	25.3	25.7	23.1
DEM_Fluctuation	0	26.1	23.9	21.6

5.4. Conclusions

In this chapter, we modified the modulated photothermal radiometry (MPR) setup for the thermal conductivity measurement moving particle bed at high temperature up to

700°C and bulk velocity up to 60 mm s^{-1}. Ceramic particles with different average particle sizes (150 μm, 275 μm and 400 μm) were measured. It is found that the k_{eff} decreased with increasing velocity for all the particles. The reduction of k_{eff} was larger for larger particles. Silica sands with more irregular particles were also measured. The k_{eff} of irregular silica sands decreased more than the ceramic particles at the same average particle size.

The k_{eff} decreased mainly due to the near-wall thermal resistance due to the invariant bulk density at different velocity. To extract the near-wall thermal resistance, we built a thermofluids model using COMSOL. At low frequency, the near-wall wall thermal resistance can be obtained by fitting the experiment data with the COMSOL model. The near-wall thermal resistance could be well represented by a near-wall airgap layer with the properties of air and thickness of 0 – 50 μm with the velocity increasing from 0 to 30 mm s^{-1}. The airgap layer was found to increase with increasing particle size and flowing velocity. The measured D_{air} agreed well with that reported in the literature, where the global heat transfer coefficient was measured.

While the existence of the near-wall airgap layer has been extensively recognized, there has been a lacking of knowledge how it develops due to the lack of *in-situ* measurement method and observation of granular motion at the microscale. To probe into the micromechanical origin of the near-wall airgap in the moving particle bed, we used discrete element method (DEM) to simulate the packing structure and particle rheology. We found that the particle motion in a moving packed bed was diffusion-like. In analogy to the dense-gas kinetic theory, the diffusivity of particle could be well defined based on the fluctuation velocity. The near-wall airgap could be estimated from

the diffusive displacement of particles away from the wall, which increased with increasing velocity and particle size. The modeled D_{air} matched well with the experiment, indicating that the diffusive behavior of particle close to the wall was the micromechanical origin of the near-wall thermal resistance in moving packed bed.

Chapter 5, in full, is being prepared for publication by Jian Zeng, Xintong Zhang, Ka Man Chung, Sarath Reddy Adapa, Tianshi Feng and Renkun Chen. The dissertation author was the primary investigator and first author of this paper.

Part II: Hydrogel materials for water harvesting and thermal management

6. Chapter 6: Thermo-responsive hydrogel for forward-osmosis desalination

6.1. Introduction

The mismatch between the soaring demand of fresh water due to the industrialization and ever-increasing life standards of mankind, and its less availability places emergence on the development of efficient and facile desalination technologies to exploit the vast storage of sea water. Forward-osmosis (FO) technology, which uses the ionic strength or osmotic pressure gradient across the membrane as the driving force to separate the salt and water molecules, has gained significant public concerns since the millennium due to the less membrane fouling, reduced reverse flux, and lower energy cost compared to the conventional desalination methods[210-217]. Nevertheless, the application envelope and marketing of the FO technique are still restricted by the lack of a suitable draw agent. Inorganic electrolytes with high ionic strength, such as NaCl, MgCl and NH_4Cl [218-220], are widely-used draw agents, which yield a high osmotic pressure of ~ 45 atm [220] and a favorable FO flux of ~ 20 LMH [219] with the concentration of 1 mol/L. However, the regeneration of the diluted draw agent into the concentrated state usually requires an energy intensive process, such as UF (ultrafiltration) and MD (membrane distillation), with the reported energy consumption of ~ 10 kWh/m^3 [221,222]. The large amount of energy required for the release of water in the follow-up treatment and the high reverse flux of inorganic solute [219,223,224] significantly undermine the

attractiveness of FO compared to the more prevailing RO process. Therefore, to justify the sustainability of FO desalination, it is imperative to develop a new class of draw agents with lower regenerative energy consumption, especially from more abundant and low-cost energy sources, such as thermal energy from the waste heat and sunlight.

One of the recently studied draw agents is based on thermo-responsive polymers, such as poly(N-Isopropylacrylamide) (P-NIPAAm) due to its potential to reduce the energy consumption [225-227]. The basic working principle of P-NIPAAm is its phase transition from a hydrophilic state to a hydrophobic one when heated up above its lower critical solution temperature (LCST). The LCST is caused by the rearrangement of water molecules around the hydrophobic and hydrophilic functional groups (alkyl and acrylate, respectively) in the polymer chain [227] leading to the collapse of the gel [226] and the fast release of the water (or dewatering) . Although P-NIPAAm has attracted an intensive interests from the field of drug delivery and release since 1990s [228-231], it is not until very recently that its potential for desalination was revealed [232]. Dan et al. [233] firstly demonstrated the P-NIPAAm-based FO desalination. It was found that the P-NIPAAm was able to regenerate ~ 70% of the absorbed water within 2 mins when only heated up to 50 °C. Because the latent heat penalty of water is avoided and the phase change latent heat for solid P-NIPAAm was low (~ 42 kJ/kg) [226,227,234], the energy consumption of the dewatering process is significantly lower compared to other methods such as traditional membrane distillation [221,222]. As a result of the high swelling ratio of P-NIPAAm (>10 times), the specific energy consumption for water production can be as low as 1.12 kWh/m^3 [235]. Besides, due to the low LCST (~ 32 °C [236]) of P-NIPAAm, it is possible to further decrease the specific cost of energy by utilizing low-grade heat, such as solar-

thermal energy (e.g., mixing the P-NIPAAm, with light-absorbing particles [235,237,238]) or waste heat. Similar to other organic draw agents, the P-NIPAAm, also takes the advantage of a negligible reverse flux due to its macromolecular structure [223,239]. However, polymers without ionic groups generally have lower osmotic pressure than those with ionic groups. It was found that the overall FO flux using pure P-NIPAAm is still very low (< 0.1 LMH) [240] compared with the inorganic draw solute (typically ~ 20 LMH [219]. In order to address these problems, polyelectrolytes, such as sodium acrylate (SA) [237,238], acrylic acid [241], polyvinyl alcohol [240] and sodium styrene-4-sulfonate (SSS) [242], etc., were co-polymerized with NIPAAm to increase the ionic strength. While the copolymers have indeed demonstrated enhanced FO flux, the addition of excessive polyelectrolytes hindered the phase transition of P-NIPAAm and thus compromised its key property of fast dewatering [243,244]. For instance, P(NIPAAm-co-SSS) with over 20 wt% of SSS did not show the LCST property [242]. Therefore, there is an inherent tradeoff between the high osmotic pressure and preserving the suitable LCST for fast dewatering when it comes to the choice of polyelectrolyte concentration. Amir et al. [235] attempted to solve this problem by employing a novel bi-layer design where the bottom layer, i.e., the one that was in contact with the FO membrane, had a high concentration of SA while the upper layer has a lower concentration. It was demonstrated that such a design yielded a higher overall flux than either of pure P-NIPAAm and P-SA. However, it remained unclear the mechanism behind this observation. More importantly, it is necessary to provide a more comprehensive study on the effect of the gradient of polyelectrolyte concentration and configuration of layers on the overall performance of FO in order to provide guidance for optimization of P-NIPAAm-based FO desalination.

In this chapter, a multi-layer design of P-NIPAAm-based draw agent was systematically studied. The design was featured with a gradually decreasing concentration of sodium acrylate away from the FO membrane, thus combining both merits of the high FO flux contributed by the drawing layer with the highest SA concentration and the fast water release by the releasing layer with pure P-NIPAAm. The intermediate layer was introduced in between so as to reduce the mass transport resistance between the aforementioned layers. A systematic study was conducted with regard to the swelling kinetics and capacity, FO flux and dewatering ratio. The mechanism for the enhanced overall performance of the multi-layer material was also explained in detail. Our study contributes to a better understanding of enhanced performance of swelling and water release in P-NIPAAm for the energy- and cost-efficient FO desalination.

6.2. Material preparation

The sodium acrylate (SA, 99%) and N-isopropylacrylamide (NIPAAm, 97%) as monomers, ammonium persulfate (APS, 98%) as initiator for the thermally-activated synthesis, α-ketoglutaric acid (98%) as photo-initiator for the UV-light activated synthesis, N,N'-methylenebisacrylamide (MBA, 99%) as cross linker and sodium alginate (99%) as backbone of the hydrogel matrix were purchased from Sigma-Aldrich.

6.2.1. Preparation of drawing layer

The drawing layers, which would be in contact with the FO membranes to draw water molecules from the feed seawater solution, were made of P(NIPAAm-co-SA) copolymers. These layers were synthesized by the free-radical polymerization of monomers (NIPAAm and SA) using the thermal-initiated method with the APS as

initiator. The monomers were added with the variation of weight ratio, i.e., the ratio of SA:NIPAAm varies from 0.3:1 to 1.5:1, to investigate the influence of polyelectrolyte concentration. Sodium alginate was added as the backbone to increases the strength of the hydrogel [245,246], with 12.5 wt% of monomers in total. The monomers and sodium alginates were then dissolved in deionized water to obtain a 14% homogenous solution. Afterwards, MBA and APS were added into the solution with a fixed molar ratio of monomers, crosslinker and initiator of 50:1:1. After being fully dissolved, the homogeneous solution was degassed for 10 mins before being put into the oven of 70°*C*, where the hydrogel was copolymerized for 10 mins. The hydrogel was kept in the oven overnight to ensure the complete co-polymerization. Figure 6-1 shows the reaction and FTIR spectrum of the NIPAM-co-SA material. During the copolymerization, the NIPAM, SA and MBA are connected via the C=C bonds to create an inter-connected matrix as shown in Figure 6-1a. As shown in Figure 6-1b, the peaks at the 1650 and 1559 cm^{-1} represent the C=O groups in the $> C = O \cdots H - N <$ species (amide band I and II, respectively) in the NIPAM and MBA repeat units[247-251]. The 1386 cm^{-1} peak refers to the C-H vibrations of $CH(CH_3)^2$ in the NIPAM repeated units[251]. The peak at 1455 cm^{-1} is attributed to the stretching vibration of the $–CH_2$ for SA [237]. In addition to that, the peak hump at 1705 cm^{-1} is due to the carboxylate anion of SA units[251].

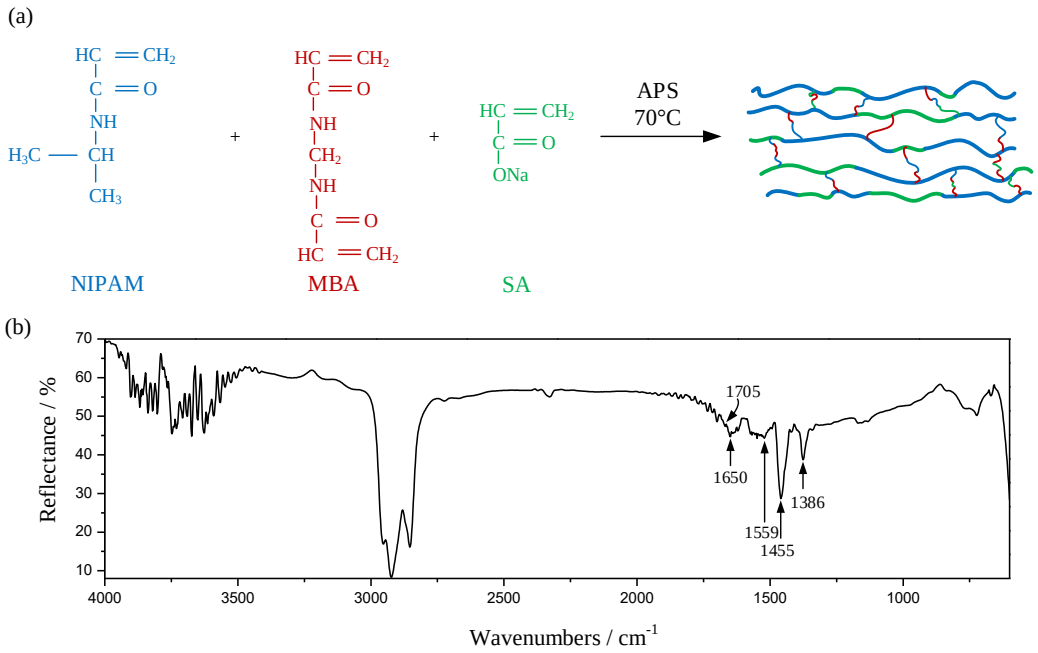

Figure 6-1. Characterization of NIPAM-co-SA (a) Chemical reaction (b) FTIR spectrum.

6.2.2. Preparation of releasing layer

The releasing layer is made of P-NIPAAm without SA. It was synthesized on the substrate of drawing layer obtained in the last step by the free-radical polymerization of NIPAAm using the UV-light initiated method with the α-ketoglutaric acid as initiator. The NIPAAm and sodium alginate, with the same weight ratio stated above, were dissolved in deionized water to produce a 14 wt% homogeneous solution. Afterwards, MBA and α-ketoglutaric acid were added into the solution with a fixed molar ratio of monomers, crosslinker and initiator of 50:1:1. The solution was degassed for 10 mins before it was added onto the top of the P(NIPAAm-co-SA) drawing layer in a mould. The ensemble was then exposed to UV-light to induce the copolymerization of the releasing layer for 12 hours. During the synthesis, some of the NIPAAm solution penetrated into the P(NIPAAm-co-SA) layer which created a solid bonding between the two layers as shown in Figure. 6-2c.

6.2.3. Description of samples

We prepared three types of samples: multi-layer (ML), bi-layer (BL), and uniform single-layer (SL). The sample IDs and their information are listed in Table 6-1. The characterization of the materials is given in the supplementary information (Figure S1). All the samples have the same total thickness of 3 mm for direct comparison of their swelling and dewatering characteristics. The single-layer samples (SL-1 to SL-5) have uniform SA concentration in each sample, with SA:NIPAM weight ratios ranging from 0:1 in SL-5 (pure P-NIPAAm) to 1:1 in SL-1. The bi-layer samples (BL-1 and BL-2) have a 1 mm thick P(NIPAAm-co-SA) drawing layer and a 2 mm thick pure P-NIPAAm releasing layer. The SA:NIPAAm ratios in the drawing layers are 1.5:1 in BL-1 and 1:1 in BL-2. The multi-layer samples have three layers (ML-1 to ML-3) or four layers (ML-4). In addition to a 0.5 mm thick drawing layer with high SA concentration and a releasing P-NIPAAm layer (2 mm thick in ML-1 to ML-3, and 1.5 mm thick in ML-4), the ML samples also have intermediate layers, with SA concentration between the drawing and releasing layers, as shown in Figure 6-2e. We expect that the intermediate layers would reduce the mass transfer resistance between the drawing and the releasing layers due to the osmotic pressure provided by the SA. The intermediate layers were synthesized in the same way as for the drawing layer. After dewatering and then cooling down below the LCST, the P-NIPAAm releasing layer is expected to draw the water molecules from the intermediate layer more easily when compared with the bi-layer hydrogels.

Table 6-1. Parameters for all the samples in study

Sample	1st Layer	2nd Layer	3rd Layer	4th Layer	Description
SL-1	1:1 (3 mm)				Uniform P(NIPAAm-co-SA) material with a single layer
SL-2	0.7:1 (3 mm)				
SL-3	0.5:1 (3 mm)				
SL-4	0.3:1 (3 mm)		-		
SL-5	0:1 (3 mm)				Uniform P-NIPAAm material without any SA
BL-1	1.5:1 (1 mm)	0:5 (2 mm)		-	Bi-layers sample with different amount of SA in the drawing layer
BL-2	1:1 (1 mm)	0:1 (2 mm)			
ML-1	1:1 (0.5 mm)	0.5:1 (0.5 mm)	0:1 (2 mm)		3-layers sample with variation of SA concentration gradient in thickness-wise
ML-2	0.8:1 (0.5 mm)	0.4:1 (0.5 mm)	0:1 (2 mm)	-	
ML-3	0.6:1 (0.5 mm)	0.3:1 (0.5 mm)	0:1 (2 mm)		
ML-4	0.8:1 (0.5 mm)	0.6:1 (0.5 mm)	0.4:1 (0.5 mm)	0:1 (1.5 mm)	4-layers sample with 2 intermediate layers in between

*The ratio in the table indicates the SA:NIPAAm ratio in weight in that specific layer with the layer thickness indicated in the parentheses. The total thickness of the as-synthesized gel was kept the same to be 3 mm.

6.3. Experimental method

We first measured the swelling ratio of the hydrogels in order to evaluate their water absorption capability. Before the swelling test, the hydrogel was placed in the freeze drier for 24 hours to ensure that it was completed dehydrated. And then the dry gel with the weight of m_{s0} was immersed in deionized (DI) water for a period of t_s to absorb water and swelled to m_{st}, where the swelling ratio within this period was calculated by:

$$R_s = \frac{m_{st} - m_{s0}}{m_{s0}} \tag{6-1}$$

To test the suitability of the hydrogels for FO desalination, two processes were evaluated: the forward-osmosis (FO) step where the water molecules were drawn by the hydrogel draw agents, and the water release step where the hydrogel was heated up above the LCST for the release of water. The FO flux was tested using a home-built setup as

shown in Figure 6-3, where the permeate side was the hydrogel that was in intimate contact with a FO membrane (CTA forward-osmosis membrane made from cellulose triacetate with an embedded polyester screen mesh as support layer by Fluid Technology Solutions, with an area of 9 cm^2 which was the same as that used in Ref.) and the feed side was 2000 ppm NaCl solution as benchmark to characterize the FO performance [237,240,252-254]. The feed solution was stirred at a constant speed of 100 rpm during the FO test in the reservoir to avoid salt accumulation close to the FO membrane. It should be noted that the thermo-responsive hydrogel was featured with multi-layers along the water transport pathway, as shown in Figure 6-2c and 6-2e, with the drawing layer in contact with the FO membrane had the highest concentration of SA (C_d) to provide a high osmotic pressure. The layer furthest to the FO membrane was the releasing layer with pure P-NIPAAm and zero polyelectrolyte concentration ($C_r = 0$) to enable fast dewatering above its LCST (~ 32 °C) [226,227] as shown in Figure 6-2d.

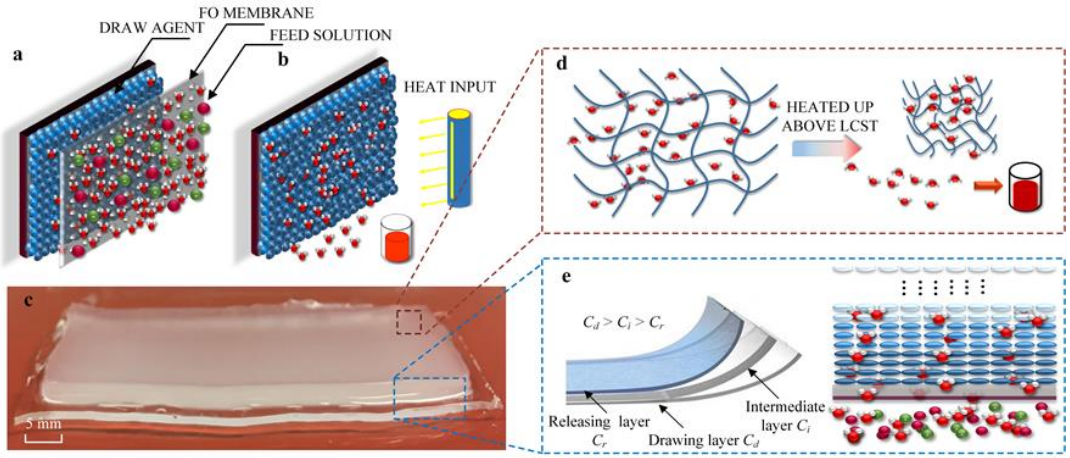

Figure 6-2. Schematic of experimental setup and characterization of material (a) forward-osmosis process (b) Dewatering process with thermal input (c) multi-layer material with the drawing layer for FO desalination and (d) releasing layer for fast water release (e) multi-layer design with gradual reduction of SA concentration along the water transport pathway.

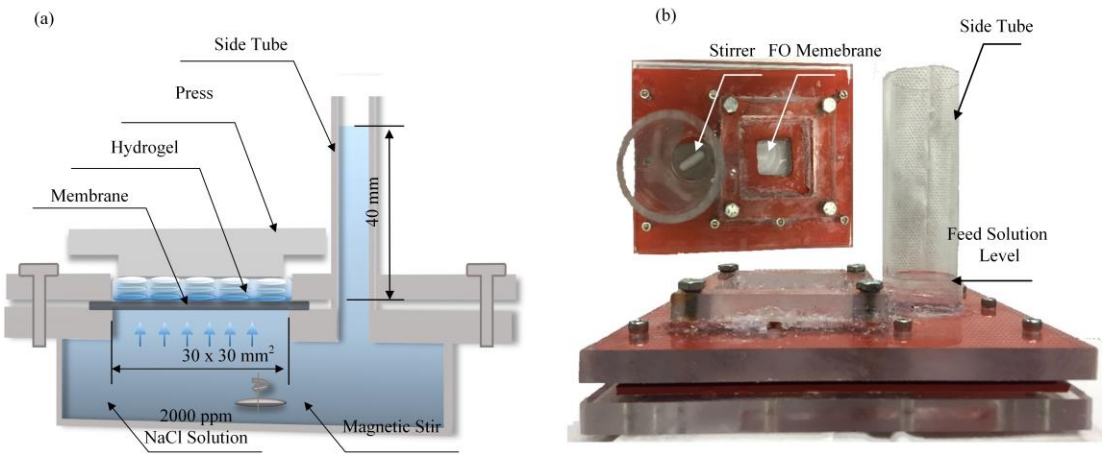

Figure 6-3. FO experimental setup (a) Schematics and (b) photo of setup from the side-view and top-view (insert). The hydrogel was pressed to ensure a good contact with the FO membrane. For the same purpose, there was a side tube connecting to the feed solution chamber, whose water level was higher than the FO membrane by 40 mm so that there was no gap between the feed solution and membrane. It was noted that the height difference was so small that the contribution of gravity was < 500 Pa, which was negligible compared with the osmotic pressure of hydrogel (~ 10 atm[236]).

The hydrogel was pressed to ensure a good contact with the FO membrane. For the same purpose, there was a side tube connecting to the feed solution chamber, whose water level was higher than the FO membrane by 40 mm so that there was no gap between the feed solution and membrane. It was noted that the height difference was so small that the contribution of gravity was < 500 Pa, which was negligible compared with the osmotic pressure of hydrogel (~ 10 atm[236]). Before the FO procedure, the as-synthesized hydrogels were fully swollen by immersing it in DI water for 24 hours and then dewatered to ~ 25 % of the weight at the fully swollen state. The FO flux was calculated for the first hour of the FO process as follows:

$$f_{FO} = \frac{(m_t - m_0)}{\rho_w A_m t_{FO}} \tag{6-2}$$

where m_0 and m_t are the weights of the hydrogel before and after the FO, respectively; ρ_w is the density of water and A_m is denoted as the area of the FO membrane; t_{FO} equals to 1 hour in this study.

The dewatering procedure was conducted in an oven at 60℃ for a specific period of time t_d where the average dewatering ratio within this period was given by

$$R_{dw} = \frac{m_{t0} - m_{td}}{m_{t0}} \tag{6-3}$$

where m_{t0} represents the weight of hydrogel at the fully swollen state (after being immersed in DI water for 24 hours) and m_{td} is the remained weight of the gel after dewatering for a period of t_d. We investigated two dewatering strategies: *continuous dewatering* by placing a sample in the 60°*C* oven throughout the test, and *intermittent dewatering* by periodically taking the sample out of the oven and cooling it at the room temperature (~23°*C*) for a specific period of time t_c. The idea is to restore the hydrophilicity of the P-NIPAAm releasing layer at room temperature, which would then drive the water from the drawing and intermediate layers to the hydrophilic P-NIPAAm releasing layer at this temperature. This cooling time (t_c) was varied from 2 to 25 mins in certain bi-layer and multi-layer samples. The dewatering (in the 60°*C* oven) and cooling (at 23°*C*) cycles were repeated until the cumulative dewatering time reached a certain value (e.g., 90 or 120 mins). During the cooling period, the samples were sealed inside a small container to avoid water evaporation.

The dewatering from the releasing layer in the oven has two contributions: evaporation of water and the (liquid) water release due to the LCST. The water release component is of interest to us as it contributes to the low-energy water recovery from the FO process. To quantify this component, we define the water release ratio R_{re} as:

$$R_{re} = R_{ML} - R_{SL} \quad (6\text{-}4)$$

where R_{ML} and R_{SL} represent the dewatering ratio of the bi-layer or multi-layer samples of interest, and that of the single layer sample, respectively. Here, we used the SL-1 sample (1:1 SA:NIPAAm ratio) as the reference to obtain R_{SL}. The SL-1 sample (and also SL-2 to SL-4) remained hydrophilic (no LCST phase transition) at 60°*C* as a result of its high SA concentration, thus the dewatering in this sample was solely due to the evaporation. Therefore, if a multi-layer sample showed a higher dewatering ratio compared to the SL-1 sample, we can attribute the extra dewatering ratio to the amount of liquid water release induced by the LCST phase transition, according to Equation 6-4.

The uncertainties for the measurements of m_{s0} and m_{st} are within 1.7% given the resolution of balance we used and the residual of water on the weighting paper. Thus, using the method in Ref.[255], the uncertainty of swelling ratio is within 2.9%. The uncertainty of membrane area due to the error of machining and cutting is assumed to be within 2%, and that for the m_o and m_t are both within 1%. Hence, the uncertainty of FO flux is within 2.5%. Similar to calculation for the swelling ratio, the uncertainty for the dewatering ratio is within 5.3%. The uncertainty for the water release ratio is thus calculated based on the error of dewatering ratio and is within 9.2%.

6.4. Results and discussions

6.4.1. Swelling rate and capacity

Figure 6-4 shows the swelling ratio of the hydrogels as a function time. In order to provide a reference for the capability of water absorption for the multi-layer samples, the uniform hydrogels with varying SA concentrations (SA:NIPAAm ratio from 0:1 to 1:1) were first tested using DI water at 23℃ as shown in Figure 6-4a. The hydrogel was

completely dry and white before the test (t = 0), and then it swelled and became transparent as shown in the inserts in Fig.2b and c (t = 900 mins). The curves in Figure 6-4a can be divided into two distinctive stages, i.e., the initial stage with a fast water absorption rate at t < 150 mins and a steady stage afterwards for all the samples with the SA:NIPAAm ratio higher than 0.3:1. However, the kinetics in the pure P-NIPAAm sample (SL-5) was substantially lower and the swelling was still not completed when the test stopped at t = 950 mins, which indicated that the addition of SA facilitated the kinetics of water transport due to the fact that the polyelectrolytes served as hydrophilic channels for water transport and more importantly, increased the osmotic pressure of the hydrogel [236,242]. The swelling ratio increased monotonously with increasing concentration of SA, e.g., the swelling ratio tripled from 44 to 135 for the first 15 mins while the swelling capacity increased from 60 to 147 as the SA:NIPAAm ratio changed from 0.3:1 to1:1, which was similar to the findings in earlier reports[237,238].

Similarly, the swelling curves for the multi-layers samples can also be delineated into the initial fast swelling stage and the subsequent steady stages after t = ~150 mins as shown in Figure 6-4b, which indicates that the multi-layer configuration does not affect the intrinsic swelling property of the P(NIPAAm-co-SA). However, it was observed that the swelling ratio did not just increase monotonously with the SA concentration, but was also dependent on both the composition and configuration of the material. For the same configuration (ML-1, ML-2 and ML-3), both the swelling rate at the initial stage (t < 150 mins) and the equilibrium swelling capacity increased with increasing SA concentration, e.g., with the SA:NIPAAm ratios increased from 0.6:1 (ML-3) to 1:1 (ML-1) in the drawing layer and from 0.3:1 to 0.5:1 in the intermediate layer, the swelling ratio in the

first 15 mins increased from 17 to 28 while the swelling capacity increased from 78 to 127, which was similar to the trend of the uniform samples. However, the swelling rate for the 3-layers sample was notably lower than that for the uniform one, e.g., the SL-3 swelled by 88 times at t = 15 mins, which was 200% higher than that for the ML-1 sample whose drawing layer had the same composition as its counterpart. This is because the drawing layer (0.5 mm) for the multi-layer sample is much thinner than the uniform sample, and thus, the swelling kinetics at the initial stage is mainly determined by the thicker P-NIPAAm layer (2 mm). In addition, the P-NIPAAm releasing layer tends to restrict the expansion of the drawing layer due to the difference of swelling rate[256,257], which further reduces the overall swelling rate. The dominant effect of the releasing layer on the swelling kinetics was justified by the gradual increase of the R_s at t >150 mins, which was similar to the trend for the SL-5 (pure P-NIPAAm) as shown in Figure 6-4a. This was also proven from Figure 6-4c, where the hydrogel tended to curl upwards from t = 15 to 45 mins, because the releasing layer swelled at a lower rate than that of the drawing layer. Interestingly, the effect of the releasing layer reduces as the material approaches its capacity limit. For example, the swelling ratio for the ML-1 sample reached 127, which ranged between that of the SL-1 and SL-3, indicating that the capacity of the multi-layer hydrogel was limited by the drawing layer. As shown in Figure 6-4c, the hydrogel unfolded at t = 105 mins because the P-NIPAAm was fully swollen and thus the restriction on the expansion of drawing layer was removed. The hydrogel became completely flat again at t = 900 mins as both layers approached their absorbing limit.

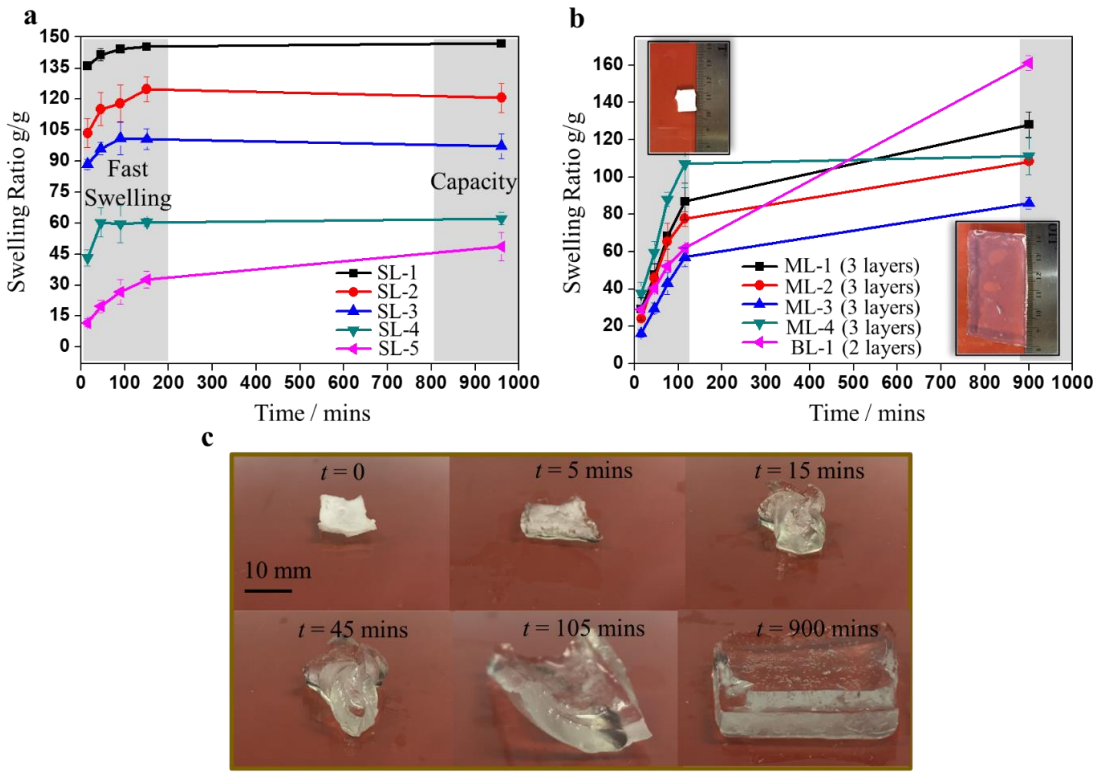

Figure 6-4. Swelling ratio as a function of time (a) for uniform P(NIPAAm-co-SA) samples with different concentrations of SA. (b) Multi-layer hydrogels with different configuration of layers along the direction of water transport. The inserted figures represent the ML-1 sample at t = 0 (top left) and t = 900 mins (bottom right), respectively. (c) Folding at the initial stage and unfolding at the saturated state of multi-layer hydrogel (ML-1) during swelling.

Another phenomenon worth discussing is that the swelling rate can be further enhanced by increasing the number of layers, and thus decreasing the gradient of SA concentration along the thickness direction with a fixed composition for the drawing layer. For example, although the drawing layer of the ML-1 sample had the same SA:NIPAAm ratio (1:1) as that for the BL-2 sample, it yielded a R_s of 87 at t = 150 mins, which was 40.3% higher than that for the latter one. As discussed above, the swelling kinetics at the initial stage is primarily determined by the releasing layer due to its restriction on the expansion of the drawing layer. Therefore, the small gradient of SA concentration between layers reduces the resistance of water transport from the drawing layer to the

releasing one, which facilitates the expansion of the P-NIPAAm layer, and thus, leads to a higher swelling rate. On the contrary, similar to the 3-layer samples, the swelling capability is still limited by the concentration and thickness of the P(NIPAAm-co-SA) layer. For example, at t = 900 mins, the R_s for the BL-2 sample reached as high as 160, which was 25.9% higher than the ML-1 sample and was close to that for the SL-1 hydrogel. The same trend still holds when comparing the ML-2 and ML-4 samples.

In brief, the multi-layer samples preserve the high swelling capability which is primarily determined by the drawing layer that has a high osmotic pressure, although the swelling kinetics at the initial stage is undermined by the water releasing layer due to its restriction on the expansion of the entire structures. Therefore, further increasing the SA concentration in the drawing layer could greatly increase the absorption capacity but not the kinetics. Increasing the SA concentration in the releasing layer could increase both the kinetics and absorption capacity of the whole structure. The overall swelling capability for the multi-layer hydrogels is still comparable to the uniform P(NIPAAm-co-SA) hydrogel. Therefore, it is concluded that the multi-layer hydrogel shows a favorable performance for water storage with a reasonable mass transfer rate.

6.4.2. Forward-osmosis flux

Figure 6-5 compares the average FO flux in the first hour for samples with different concentrations of SA and configurations of layers. The hydrogels contained water that was equivalent to 25wt% of that at the fully swollen state, e.g., the ML-3 sample had an equilibrium swelling ratio of ~ 80, and thus it contained ~ 5 wt% net hydrogel for the FO test.

It was seen that the FO flux increased monotonously with increasing concentration of SA, i.e., the FO fluxes were 0.08, 0.107, 0.191 and 0.295 LHM for the SL-5, SL-4, SL-2 and SL-1 samples, respectively, which agreed with the trends reported in the literature [236,240]. As expected, the FO flux for the multi-layer hydrogel is mainly determined by the composition of the drawing layer. For example, both the BL-2 and ML-1 had an drawing layer with the SA:NIPAAm ratio of 1:1, and the FO flux for them ranged from 0.236 to 0.292 LMH, which was similar to that for the SL-1 hydrogel having the same SA:NIPAAm ratio. As the SA:NIPAAm ratio for the releasing layer decreased from 1:1 to 0.8:1 (ML-2), the FO flux decreased from 0.292 to 0.22 LMH, which was between that of the SL-1 and SL-2 samples. The reason is that the FO is determined by the osmotic pressure of the drawing layer in contact with the FO membrane until the concentration of the polyelectrolyte decreases due to the hydrogel swelling so that the intermediate layer and releasing layer starts to attract water molecules. However, considering the fact that the FO flux is relatively low when compared to the swelling capability of the hydrogel, it would take a long time for the drawing layer to get saturated. Therefore, it is concluded that the FO performance of the multi-layered hydrogel is primarily determined by the drawing layer and it yields a similar FO flux to that of a uniform hydrogel with the same SA:NIPAAm ratio as the drawing layer of the multi-layer samples. The FO flux of multi-layer sample can be improved by increasing the concentration (e.g., using dry polymers rather than 5 wt% polymer in this study) or employing other types of polyelectrolytes in the drawing layer as to be discussed in later section.

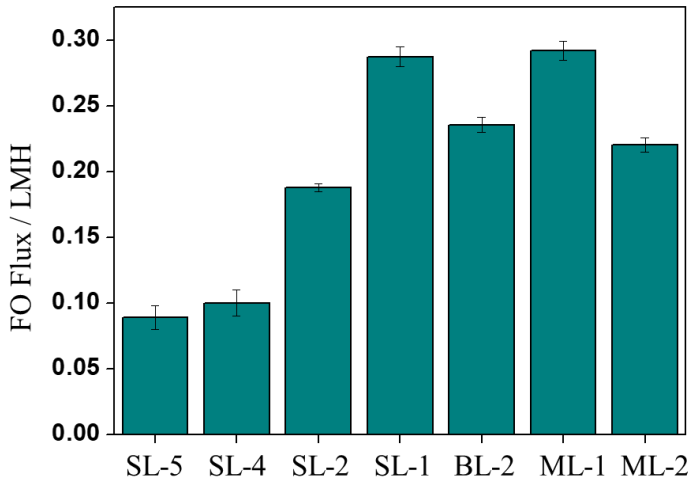

Figure 6-5. FO flux for different samples with variation of concentration of SA and configuration. The feed solution is NaCl (2000 ppm by weight) solution, that was continuously stirred by a magnetic stirrer at a constant speed of 100 rpm.

6.4.3. Dewatering ratio

As shown above, increasing the SA concentration increases the FO flux. However, the P(NIPAAm-co-SA) samples with high SA concentration lost the LCST phase transition LCST[241]. As shown in Figure 6-6a, the pure P-NIPAAm (SL-5) can be dewatered by over 95% in the first 15 mins, while the dewatering ratio for all the single-layer P(NIPAAm-co-SA) samples is lower than 20% under the same conditions. It was observed during the experiment that none of the uniform P(NIPAAm-co-SA) samples showed the LCST phase transition, and thus, the water was released from these hydrogels solely by evaporation. Such trend was also found in Refs [241,242] where the P(NIPAAm-co-SSS) lost the LCST when an excessive amount of sodium styrene-4-sulfonate (SSS) (> 20 wt%) or sodium acrylic (> 50%) was added because the hydrophilic groups in the polyelectrolytes tended to retain the water molecules, which naturally had an adverse effect on the release of absorbed water. Reducing the amount of SA only slightly increased the dewatering ratio, e.g., the dewatering ratio for the SL-4 sample at t = 120

mins was 71%, which was 22.4% higher than that for the SL-1. However, this was still significantly lower than that for the SL-5.

It is possible to increase the dewatering ratio more by further reducing the SA concentration, and is even possible to preserve the LCST phase transition for the P(NIPAAm-co-SA) if the SA:NIPAAm ratio is less than 0.08:1 as shown in Ref. [241]. However, reducing the SA concentration to such a lower level would have a negative effect on the FO flux, as shown by the lower FO flux (0.12 LMH) in the SL-4 sample (SA:NIPAAm ratio = 0.3:1). The multi-layer configuration, however, helps to increase the dewatering ratio while still maintaining a high FO flux. As shown in Figure 6-5, the BL-2 and SL-1 samples had similar FO fluxes, but the BL-2 sample had a dewatering ratio of 72% at t = 120 mins using the continuous dewatering strategy (t_c=0 mins), which was 16.2 % higher than that for the SL-1 hydrogel (Figure 6-6b). It even yielded a higher dewatering ratio than that of the SL-4 which had a lower SA ratio (0.3:1). The enhancement of the dewatering ratio can be attributed to the fast release of water caused by the LCST phase transition in the P-NIPAAm releasing layer.

To further increase the dewatering ratio, the intermittent dewatering strategy was applied, during which the dry releasing layer dragged water from the drawing layer after being cooled down below the LCST, as shown in Figure 6-6e. Evidently there existed two layers for the BL-2 sample immediately after it was taken out from the oven, i.e., a white, dehydrated layer on the top representing a shrunk P-NIPAAm after undergoing the LCST phase transition and releasing the water it initially contained, and a transparent drawing layer at the bottom which remained hydrated. The difference of the swelling ratios between the two layers induced the curvature of the sample as the releasing layer shrunk

(Figure 6-6e). After the sample was cooled to below the LCST, it became flat again, along with the gradual change of color from white to transparent of the P-NIPAAm layer. During this stage, water molecules were attracted from the drawing layer to the dehydrated P-NIPAAm releasing layer by the hydrophilic and charged groups in P-NIPAAm, leading to the re-swelling of this layer. This also confirmed that water molecules could be attracted by the concentrated P(NIPAAm) from the ionic drawing layer, or otherwise, the releasing layer could not swell and expand. The inter-layer water transport lasted for ~ 2 mins after which the balance of osmotic pressure was re-established, manifested by the steady curvature and color of the hydrogel at t > 2 mins. Such a water absorbing effect led to a higher dewatering ratio of the multi-layer hydrogel in the following dewatering cycle because the water transported to and stored in the P-NIPAAm would be released at the liquid state due to the LCST, which would otherwise have been evaporated had the sample been kept in the oven continuously. For example, with the intermittent dewatering strategy having a cooling time t_c = 2 mins, the dewatering ratio at t = 120 mins for the BL-2 increased to 78% (Figure 6-6b). However, further increasing the cooling time from t_c = 2 mins to 25 mins only leads to a slight increase of dewatering ratio to 85% (Figure 6-6b), which indicated that the inter-layer water transport at room temperature was largely saturated after 2 mins, which was in line with the visual observation shown in Figure 6-6e.

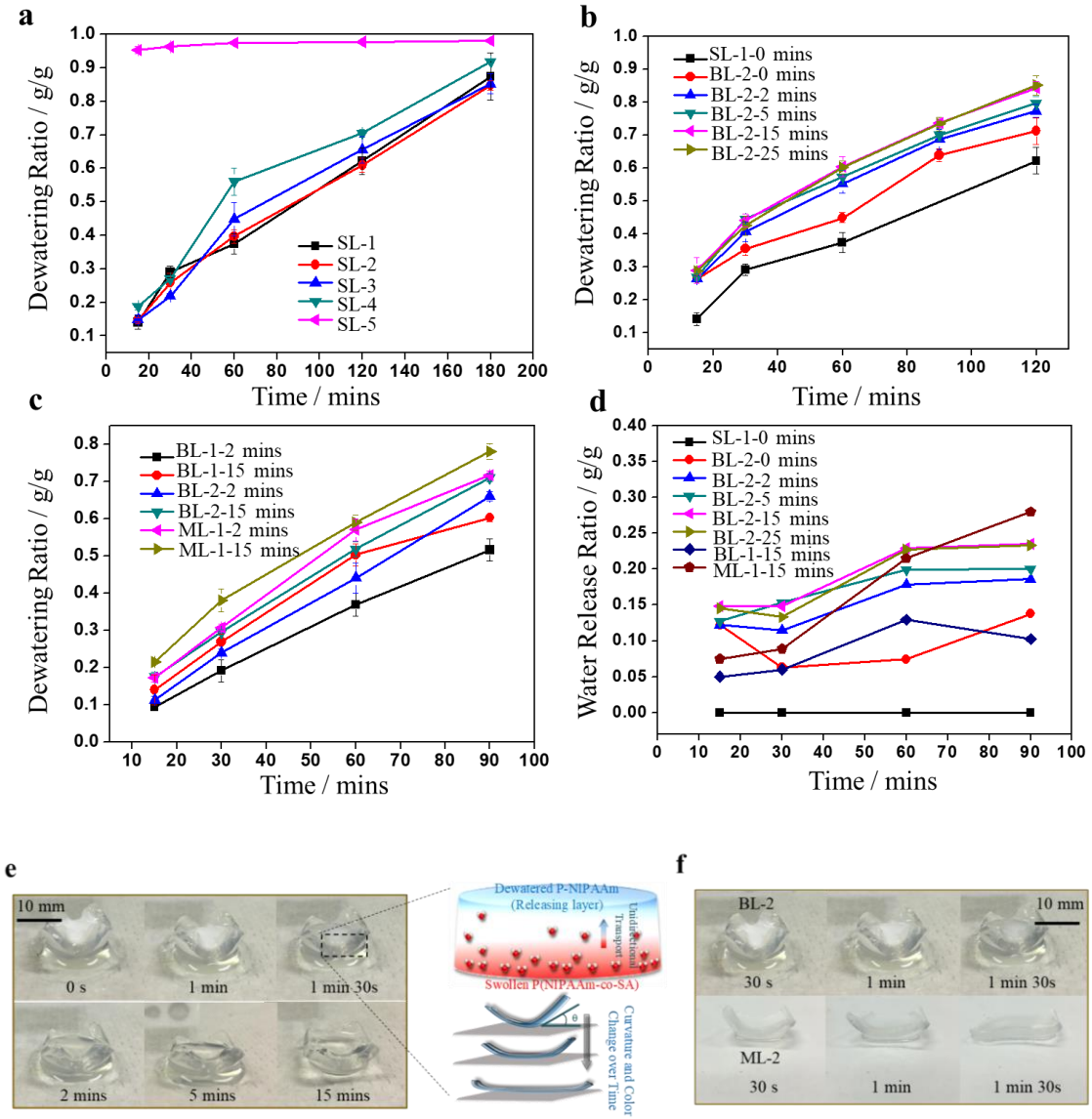

Figure 6-6. Dewatering ratio for different samples (a) Dewatering ratio for uniform P(NIPAAm-co-SA) hydrogels with different concentration of SA (b) Dewatering ratio for multi-layer sample (BL-2) with different dewatering strategies, where 0 – 25 mins indicates cooling time (t_c) when the hydrogel is placed in the ambient at room temperature (23ºC) before being put into the oven again after each measurement (c) Dewatering ratio for multi-layer hydrogels with different configurations (d) Contribution of water release to the overall dewatering ratio. The water release ratio is defined in Equation 6-4. (e) Photographs of the (BL-2) after being removed from the oven and cooling at the room temperature for various cooling time (t_c) of 0 to 15 mins. The schematics shows the inter-layer water transport from P(NIPAAm-co-SA) layer to the P-NIPAAm layer, leading to the reducing curvature in the multi-layer sample. (f) Photographs of the BL-2 (upper row) and ML-1 (lower row) after being removed from the oven and cooling at the room temperature for various cooling time (t_c) of 30 sec to 1 min 30 sec.

In order to quantify the contribution of liquid water release from the releasing layer caused by the LCST to the overall dewatering ratio that includes both liquid release and evaporation, the water release ratio, which is defined by Equation 6-4, is plotted as a function of time in Figure 6-6d. It can be seen that for the BL-2 sample, about 12% of water was released by the LCST phase transition before the cooling periods started (the first 15 mins). As expected, the contribution of water release increased with a longer cooling time (t_c) due to the inter-layer water transport, leading to the overall enhancement of water release by 23% as the t_c increases from 0 to 25 mins. Noticeably, the curves plateaus at t = 60 mins, indicating that the P-NIPAAm layer had reached its water release limit, after which there was only evaporation. This is because the ionic concentration of the drawing layer increased gradually after the loss of water so that the releasing layer could no longer attract water from the drawing layer, and thus, there was no inter-layer water transport.

Another point worthy of discussion is that the dewatering ratio can also be modulated by the configuration of the layers. As shown in Figure 6-6c, the dewatering ratio increased with the decreasing difference of SA concentrations between the drawing and releasing layers. For example, using the intermittent dewatering strategy with t_c = 2 mins, the ML-1 sample achieves the dewatering ratio of 72% at t = 90 mins, which is 9.1% and 39.5% higher than that for the BL-2 and BL-1 samples, respectively. It is noted that there was an intermediate layer for the ML-3 hydrogel, which had a SA:NIPAAm ratio of 0.5:1. Extending the t_c from 2 to 15 mins in intermittent dewatering process further increased the dewatering ratio due to the longer time for interlayer water transport. The increased dewatering ratio in the ML-1 sample with respect to the BL-1 and BL-2

samples can be attributed to the increased water release from the LCST phase transition in the releasing layer, as shown by the increased water release ratio in Figure 6-6d. For example, the water release ratio for the ML-1 (with t_c = 15 mins) reached 28% at t = 90 mins, which was 17% and 210% higher than that of the BL-2 and BL-1, respectively under the same conditions. We hypothesized that the intermediate layer in the ML-1 decreased the osmotic gradient along the path of water transport, facilitating the mass transfer from the drawing layer to the P-NIPAAm releasing layer. It is clearly seen in Figure 6-6f that the curvature for the ML-1 sample was smaller than that for the BL-2 sample, and it was almost flat after 1 min 30s cooling at room temperature, whereas the P-NIPAAm layer for the BL-2 hydrogel was still partially dry and the sample still had a large curvature. This means that the water was replenished in the P-NIPAAm layer at a faster rate in the ML-1 sample compared to the BL-1 sample, due to the enhanced water transport enabled by the intermediate bridging layer in ML-1. As a result, a larger amount of water could be released by the LCST phase transition from the ML-1 sample during the following heating cycle.

In brief, the analysis above confirms that the bi-layer samples yield a higher dewatering ratio than the uniform hydrogel due to the contribution of the releasing layer, and the multi-layer samples show an even higher dewatering ratio enabled by the enhanced inter-layer water transport. Interestingly, the releasing layer is able to attract water molecules from the drawing layer after being dried, which leads to the enhancement of water release in the intermittent dewatering process. Such an effect allows the optimization of both the layer configuration and the dewatering strategy of hydrogels to achieve the best tradeoff between the water production and energy-

effectiveness.

6.4.4. Fresh water yield and energy efficiency

Figure 6-7a compares the FO flux of ML-1 to that of other draw agents. The FO flux of ML-1 is comparable to data reported for PSA in literatures[220,233,235,237,238,240,242,252,258-260]. The FO flux depends on the concentration of draw agent, e.g., the FO flux of P(SA) reached > 1.35 LMH at the dry state[233] while at the swollen state (~ 25wt% P(NIPAAm-co-SA), the FO flux was 0.23 LMH [240]. The FO flux of ML-1, has comparable FO flux to other organic draw agents, e.g., poly(acrylamide) (PAM, ~0.45 LMH) [252], ionic liquid (IL, 0.8 LMH) [258] and hyaluronic acid/polyvinyl alcohol (HA/PVA, ~ 1.2 LMH) [259]. Inorganic electrolytes, such as NaCl generally yielded a higher FO flux (~ 8 LMH/M) than the organic ones mainly due to the smaller molecular size and higher mobility [220]. However, the post-treatment method, e.g., MD (~ 100 kWh/m^3) [261-267], is energy intensive which significantly undermines their attractiveness.

The multi-layer hydrogel in this study, although has a lower FO flux than that of the inorganic solutes, enables an impactful energy saving for water production (~ 13 kWh_{th}/m^3) due to the LCST phase transition as shown in Figure 6-7b. The sensible heat requirement can be calculated as:

$$Q_S = \int_{T_1}^{T_{LCST}} C_p dT \tag{6-5}$$

where C_p is the heat capacity with fixed pressure for water (4.2 kJ/kg·K) or P(NIPAAm) (1 kJ/kg·K on average from T_1=298 K ~ T_{LCST}=308 K)[225]. Assuming the hydrogel swells by the swelling ratio of 2, the specific energy consumption for water production is ***19*** $kWh_{th}/m^{3}_{(water)}$ as given by Equation 6-6.

$$Q = Q_S^w + \frac{Q_S^{NIPAAm}}{2} + \frac{Q_L}{2} \quad (6\text{-}6)$$

If the thermal energy of the released water (~ 35 °C) is recovered to heat up the feed solution from 25°C to 30°C assuming the ideal heat exchange as shown in Equation 6-7, the energy consumption can be reduced to *13 kWh_{th}/m^3* due to the reduction of sensible heating.

$$\int_{T_{LCST}}^{T_1} \frac{c_w}{T} dT + \int_{298}^{T_1} \frac{c_w}{T} dT = 0 \quad (6\text{-}7)$$

More importantly, the low LCST (~ 35 °C) [268,269] compared to that for MD (~ 75 – 90 °C [261,265,270,271]) allows us to use the low-grade heat, e.g., solar energy, as thermal input [237]. It has a competitive energy consumption when compared to that of other types of regeneration methods using solar energy, such as multi-stage flash (MSF) of ~ 70 kWh/m^3 [272], multi-effect distillation (MED) of ~ 50 kWh/m^3 [272], photovoltaic/reverse osmosis (PV-RO) of 22 kWh/m^3 [273,274] and so on, which were commonly used to regenerate the non-responsive draw agents. Therefore, although the theoretical energy consumption of RO can be as low as 2 kWh/m^3, we have to consider the energy conversion efficiency from the low-grade heat to electricity for the RO, which would have been very low even at the Carnot limit.

We have shown that the FO flux of multi-layer hydrogel is mainly determined by the drawing layer while LCST phenomenon is governed by the releasing layer, indicating that we may improve the FO flux by using other types polyelectrolyte in the drawing layer without undermining the dewatering ratio. For example, it is possible to yield a high FO flux of ~ 4 LMH by replacing the P(SA) with poly(sodium styrene-4-sulfonate) or

P(SSS) [242] and even ~ 10 LMH by using poly(acrylic acid-sodium salt) (PAA-Na) with a small molecular size of 1800 Da [260]. Both the P(SSS) and PAA-Na are hydrogel-like polyelectrolytes and compatible with NIPAAm [275]. The ionic strength of PAA-Na has similar osmotic pressure to P(SA) at the similar concentration (~ 30 atm at 20 wt.% [236,260]), and thus, the inter-layer water transport should not be compromised. Therefore, it is expected that we are able achieve a higher overall water production rate if we explore the multi-layer design to other types of polyelectrolytes. Although the FO flux achieved in the paper was still low compared to inorganic salt, but the insight of dual layer design provided us a new approach to achieve a high FO flux in the future by using highly ionic polymer for the drawing layer or reducing the size of the layer, e.g., using Janus microgel design.

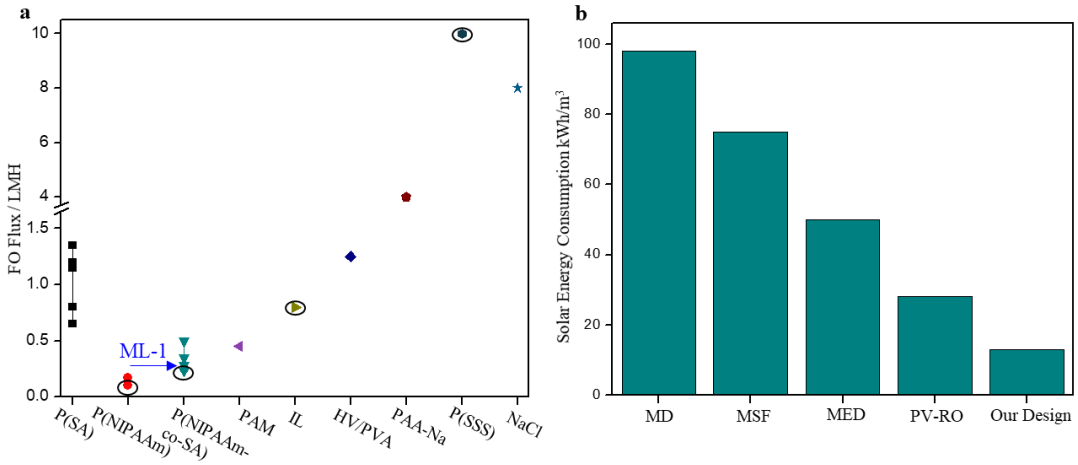

Figure 6-7. Comparison of FO flux and energy consumption with other draw agents (a) FO flux for various type polyelectrolyte at the dry state except for those circled in black. (b) Energy consumption for regeneration of non-responsive draw agents and multi-layer temperature-responsive hydrogels.

6.5. Conclusions

To combine both merits of the high osmotic pressure in the polyelectrolytes and the fast water release in the temperature-responsive P-NIPAAm, a novel multi-layer

temperature-responsive ionic hydrogel was developed for enhanced forward-osmosis desalination. The highlights of this study are as follows:

(1) The multi-layer hydrogel yielded a high equilibrium swelling ratio similar to their uniform counterparts, indicating that the water absorption capacity of multi-layer hydrogel was determined by the drawing layer. However, the swelling rate for the multi-layer hydrogel was low at the initial stage due to the constraint of the releasing layer.

(2) Similar to the swelling capacity, the FO flux of the multi-layer hydrogel was mainly determined by the concentration and composition of the drawing layer. Therefore, it is possible for the multi-layer hydrogel to yield a higher FO by replacing the releasing layer with more ionic polyelectrolytes.

(3) The multi-layer hydrogel (ML-1) released ~ 60% of the absorbed water at the fully swollen state in 60 mins due to the LCST phase transition of the P-NIPAAm releasing layer while the uniform hydrogels (SL-1) only released ~ 35% of the absorbed water purely by evaporation. Adding more intermediate layers or employing the intermittent dewatering strategy increased the dewatering ratio for the multi-layer hydrogel because water molecules could be transported from the drawing layer to the releasing layer more easily.

(4) The FO flux of multi-layer hydrogel is still low compared to the inorganic hydrogel which is a key obstacle for most organic draw agent. However, the multi-layer temperature-responsive hydrogel had a low energy-consumption compared to other regeneration methods for non-responsive draw agent due to the LCST phenomenon which was rid of the latent heat penalty. The concept of multi-layer designed showed promising application by replacing the releasing layer with highly-ionic polyelectrolytes.

Through a systematic study under various conditions and configurations of the materials, this study provides in-depth insights into the water swelling and releasing characteristics of the multi-layer hydrogels and could contribute to further development of hydrogel-based energy-efficient FO desalination.

Chapter 6, in full, is a reprint of the materials as it appears in 'Multi-layer temperature-responsive hydrogel for forward-osmosis desalination with high permeable flux and fast water release' *Desalination*, 459 (2019), 105-113 by Jian Zeng, Shuang Cui, Qingyang Wang and Renkun Chen. The dissertation author was the primary investigator and first author of this paper.

7. Chapter 7: Polyelectrolyte hydrogel for continuous solar-driven desalination

7.1. Introduction

Efficient harnessing of solar energy attracts wide-spread interest in the context of water-energy nexus. Recently, solar steam generation has become an attractive research area due to the promising application for water purification and desalination[212,276-278] assisted by the conceptual and technological breakthroughs in the fields of nanophotonics and nanomaterials that enabled the high solar-thermal energy efficiency. It is estimated that up to 325 GW of solar power is potentially available in the United State and the power density of natural evaporation is comparable to the current wind and solar technologies[279]. While the solar-thermal energy conversion efficiency was intrinsically limited by the performance of the absorber which already reached ~ 94%[12,13], the overall performance of the solar-thermal desalination system would be compromised without sufficient water supply and the ability to resist salt contamination. To solve this problem, several studies explored the capillary pumping effect as a passive liquid supply mechanism where liquid was driven by the capillary pressure in the micro-pores[280,281], micro-grooves[282], fibrous meshes[283,284] and carbon foam[285,286], etc. Although the capillary pumping is able to provide high liquid flux, there are two challenges associated with the capillary-driven desalination. First, there is an inherent tradeoff between capillary pumping pressure and flow resistance, as the former scales inversely with the pore size (i.e., $1/d$) and the latter as d^2 for the same flow rate. As a result, the pore diameter cannot be too small in order to ensure a certain flow rate. This tradeoff is even more prominent in solar desalination, as the thickness of the capillary pumping layer has to be large

enough to minimize the dissipation of solar heat to the underlying seawater, a major contributor to the total heat loss[283], which in term limits the overall flow rate due to the flow resistance. Typically, a thick thermally insulating layer was used to separate the absorber and seawater[287,288]. We calculated the maximum achievable flow rate for various foam thickness and thermal conductivity in a capillary pumping layer when the heat loss to the bulk seawater is less than 10% of the incident solar energy under the 1 and 3-sun condition. These optimal flow rates are far lower than the theoretical flow rate of solar evaporation due to the solar heat if the thick foam is used. Second, as the capillary pumping pressure is inversely proportional to pore size, so small pores, often at micron scale, are usually used for liquid pumping. The fine porous structures as liquid pathways were inherently prone to the clogging by contamination [12,289,290] during the evaporation, which undermined the liquid flux and stability in the long term. The salt sediment on the top of the absorber would reduce the solar absorbance[289] as well as the effective area for evaporation. Therefore, the absorber needed to be taken out for cleaning periodically[12], which may impact the durability of the absorber and stability of the entire system even though anti-scratching carbon-based absorber was developed for periodic salt-removal[291]. Although salt-dissoluble fabric[292] and Janus membrane [293] were developed to allow the salt crystal to diffuse back to the sea at night and thus systems were stable on the daily basis, it was still unclear if this system would sustain when operated under concentrated sun light or working with more concentrated brine water where the salt sediment rate could exceed the rate of salt back diffusion. Therefore, despite the great improvement in the material/structural designs with increasing efficiency over the years, interfacial solar desalination is still not ready for practical application due to the lack of efficient salt-

rejection strategies[294]. The problem of membrane fouling is also a critical concern in many other applications, including forward-osmosis (FO) and reverse-osmosis (RO) separations.

In this work, instead of capillary pumping, we proposed a new ionic pumping effect utilizing common highly ionic polyelectrolyte hydrogel for simultaneous high liquid flux and salt rejection. The high water flux is achieved through the osmotic pressure provided by the polyelectrolyte, e.g., 14 wt.% the Poly(Sodium Acrylate), or P(SA) have a high osmotic pressure of ~ 90 atm[236], which was a factor of 10^5 higher than the capillary pressure in micro-groove/pores (e.g., 360 Pa for micropore of 400 μm in diameter in the completely wetting state given by the Young-Laplace equation). Due to the high osmotic pressure, the ionic hydrogels (e.g., P(SA)[236], poly(sodium styrene-4-sulfonate (PSSS)[242], and poly(acrylate acid[260,295]), showed a high FO flux of > 10 LMH. The swelling ratio of P(SA), defined as the weight ratio of hydrogel at the fully swollen state to that at the dry state, could reach ~ 100[253]. The ionic hydrogel also showed promise for humid vapor absorption due to the favorable hygroscopic effect[296]. More importantly, the ionic hydrogel was able to resist ~ 35% of the salt molecules going through it [297,298] due to its high ionic strength. Although some salt molecules could enter the hydrogel, they were trapped inside the crosslinking network owing to electroneutrality[297]. And thus, there would be zero salt-sediment on the top of the solar evaporator if ionic hydrogel is used as the path for water pumping.

To demonstrate the ionic pumping effect as a new liquid supply mechanism for simultaneous high flux and salt-rejection, we developed a polyelectrolyte hydrogel foam (PHF) with P(SA) embedded in the micro-porous matrix. The PHF could provide high

flux of ~ 24 LMH, equivalent to the evaporative flux under 15 suns condition with DI-water and > 80% salt-rejection ratio for 3.6 wt.% NaCl solution. To demonstrate the practical application of the PHF, we applied the PHF for solar-driven desalination. Due to the efficient liquid supply, a thick (~ 5 mm) PHF could be used, which reduced the heat loss and thus yielded a high evaporative flux (~ 1.6 LMH under one sun condition with DI-water). The strong salt-rejection ability of the PHF help maintained a high evaporative flux of ~1.3 LMH (i.e., a high energy efficiency of ~ 79%) in the long-term test, i.e., 72 hours consecutively in the lab and 6 days outdoor using a 3.6 wt.% NaCl solution. The successful demonstration of PHF for solar-driven desalination could be extended to a broader range of application in chemical processing and separation where both high flux and salt-rejection are required.

7.2. Design of osmotic-driven solar-evaporator

To demonstrate the high flux and salt-rejection performance of the ionic pumping effect, we tested the PHF for solar-driven desalination using 3.6 wt.% NaCl solution mimicking the seawater. As shown in Figure 7-1a and 7-1b, the CF or PHF floated on the 3.6 wt.% NaCl solution in a glass beaker. The incident light (varying from 1 to 3 suns, i.e., 1 kW/m^2 to 3 kW/m^2) was absorbed by the carbon foam which heated up the thin layer of the foam close to the surface as well as the liquid trapped therein. It should be noted that water was driven by different pumping mechanisms between the CF and the PHF. In the CF, the seawater was driven upward from the bulk to the top surface due to the capillary force provided by the micropores, which was heated up and evaporated when transported close to the top surface. Due to the thick foam design (5 mm), little heat was dissipated to the bulk seawater. However, to sustain the high liquid flux through the

thick foam, the micropores in the CF were small (~ 400 μm) and thus were intrinsically prone to the clogging of salt and contamination during evaporation due to the lack of salt-resistance. In addition, the salt sediment on the top of the CF reflected some of the incident solar power which also degraded the performance of the CF absorber in the long term. The trade-off of pore size and thickness is resolved by the ionic pumping effect. The PHF avoided the clogging and sediment of salt while maintaining high liquid flux due to the ionic pumping effect of the P(SA) embedded in the micropores of the foam. As shown in Figure 7-1c, the PHF were filled with 20 wt.% P(SA) hydrogel which had a high osmotic pressure (> 100 atm[236]) to provide high liquid flux. The osmotic pressure of 20 wt.% P(SA) was measured to be 230 atm (see chapter 7.3) while that for the 3.6 wt.% NaCl solution was 27.6 atm. After absorbing water, the osmotic pressure of P(SA) close to the seawater decreased due to the reduced concentration while the top layer maintained a high concentration due to the continuous evaporation, and thus there was an osmotic pressure gradient established inside the hydrogel, which pumped water from the bottom to the top. The salt-rejection at the brine/foam interface was realized by the high ionic strength difference between the polyelectrolyte hydrogel and seawater. Although some ions (< 20%) might penetrate into the P(SA), they were trapped by the charged group in the P(SA) chains (e.g., negatively charged CH_2=$CHCOO^-$ acrylate groups and mobile Na^+) during the water transport in the micropores, and thus, there was little salt sediment on surface of the PHF absorber, which ensured the long-term stability of PHF. If polyelectrolyte hydrogels with higher ionic strength are used, we could obtain higher flux and better salt-rejection effect, e.g., the osmotic pressure doubles and the ionic strength

quadruples if poly(Magnesium acrylate) [P(MA)] is used because of the doubly-charged Mg^{2+}.

As shown in Figure 7-1c, the PHF was synthesized by copolymerizing the P(SA) hydrogel with SA monomers in the micropores of the porous carbon foam (CF). It should be noted that the CF was chosen for the demonstration of the solar-driven desalination due to its high solar absorbance, i.e., 97.8% in the solar spectrum (320 ~ 2600 nm) as shown in Figure 7-1d. Different types of microporous foam or membrane could be used based on the requirements for particular application. The sodium acrylate (SA, 99%) as monomer, ammonium persulfate (APS, 98%) as thermal initiator and N,N'-methylenebisacrylamide (MBA, 99%) as cross-linker were purchased from Sigma-Aldrich and used as-received. SA, MBA and APS were dissolved in DI-water with a fixed molar ratio of 50:1:1 to obtain a 20 wt.% homogeneous solution. Before the synthesis, the carbon foam (CF) was cleaned by sonication in DI-water for 30 mins and then was completely dried in an oven. The dry CF was immersed in the SA solution for overnight to ensure that the pores in the foam were filled with solution, after which it was put into an oven at 70 °C for 2 hour for copolymerization of SA. After the synthesis, the pores in the CF were filled with P(SA), and was named as PHF. The SEM images and EDS mapping of CF and PHF were captured with FEI Apreo SEM. The FTIR of P(SA) was conducted on a NICOLET 6700 FTIR (Thermoscientific Inc.), and the absorbance of CF before/after salt sediment and the PHF were evaluated with a UV-Vis spectrophotometer (JASCO V-770). Two sizes of samples were prepared: 5.52 cm^2 sample for bench-top experiment and 132 cm^2 (Figure S7) for long-term stability test at

the ambient environment. This also proved that our design could be easily applied for large-scale production.

To evaluate the contribution of ionic pumping by P(SA) to liquid supply and salt rejection, pure P(SA) hydrogel was also prepared with the same recipe described above except that the SA solution was poured into a mould to obtain P(SA) hydrogel sheet with the thickness of 2 mm. For comparison, copolymers P(N-isopropylacrylamide-co-SA) [P(NIPAAm-co-SA)] with the NIPAAm:SA ratio of 1:1 by weight and pure P(NIPAAm) are also prepared. The NIPAAm and SA monomers were dissolved in deionized water to obtain a 20 wt.% homogenous solution. And then MBA and APS were added into the solution with a fixed molar ratio of monomers, crosslinker and initiator of 50:1:1. After being fully dissolved, the homogeneous solution was degassed for 10 mins before being put into the oven of 70°*C* for copolymerization of P(NIPAAm-co-SA). The P(NIPAAm) was made by the free-radical polymerization of NIPAAm using the UV-light initiated method with the α-ketoglutaric acid as initiator. The NIPAAm were dissolved in deionized water to produce a 20 wt.% homogeneous solution. Afterwards, MBA and α-ketoglutaric acid were added into the solution with a fixed molar ratio of monomers, crosslinker and initiator of 50:1:1. The solution was degassed for 10 mins and then exposed to UV-light to induce the copolymerization for 12 hours. It should be noted that the NIPAAm monomers were not ionic and thus its osmotic pressure was much lower than that of the P(SA) and P(NIPAAm-co-SA). Similarly, due to the reduction of SA concentration, the osmotic pressure of P(NIPAAm-co-SA) was lower than that of the pure P(SA).

As shown in the SEM image in Figure 7-1c, the micropores in the CF matrix have a diameter of ~ 400 μm and are interconnected as liquid pathway driven by the capillary force. The chemical residual on the carbon fibers is adhesive for fiber connection. After copolymerization, the micropores were filled with P(SA) hydrogels, indicating the successful synthesis of PHF. The average absorbance value of the PHF is 97.7%, which indicates that the P(SA) does not changes the high absorbance of the active carbon foam. The Fourier-transform infrared spectroscopy (FTIR) spectrum of the P(SA) is displayed in Figure 7-1e. The peaks at the 1650 and 1559 cm^{-1} represent the C=O groups in the >C=O ··· H-N< species (amide band I and II, respectively) in the NIPAM (N-isopropylacrylamide) and MBA (N,N'-methylenebisacrylamide) repeated units [247-251]. The 1386 cm^{-1} peak refers to the C-H vibrations of $CH(CH_3)_2$ in the NIPAM repeated units [251]. The peak at 1455 cm^{-1} is attributed to the stretching vibration of the $–CH_2$ for SA [237]. In addition, the peak at 1705 cm^{-1} is due to the carboxylate anion of SA units [251]. The polyelectrolyte hydrogel, i.e., 20 wt.% P(SA), has two functions:

(i) the high osmotic pressure (Π), which is measured to be ~ 230 atm, drives the water from the bulk solution upwards to the top of the foam. The osmotic pressure of P(SA) is a factor of 10^5 higher than the capillary pressure in the micropores (e.g., 360 Pa for pore of ~ 400 μm in diameter assuming the completely wetted state).

(ii) The P(SA) resists the ions at the brine-foam interface due to the high ionic strength and entraps the ions which penetrate into the hydrogel by the charged groups (i.e., negatively-charged $CH_2=CHCOO^-$). Therefore, the PHF is expected to possess good anti-fouling capability. It is noted that we just used a common porous activated-carbon

foam and P(SA) hydrogel which could be easily replaced by other materials in different application scenarios.

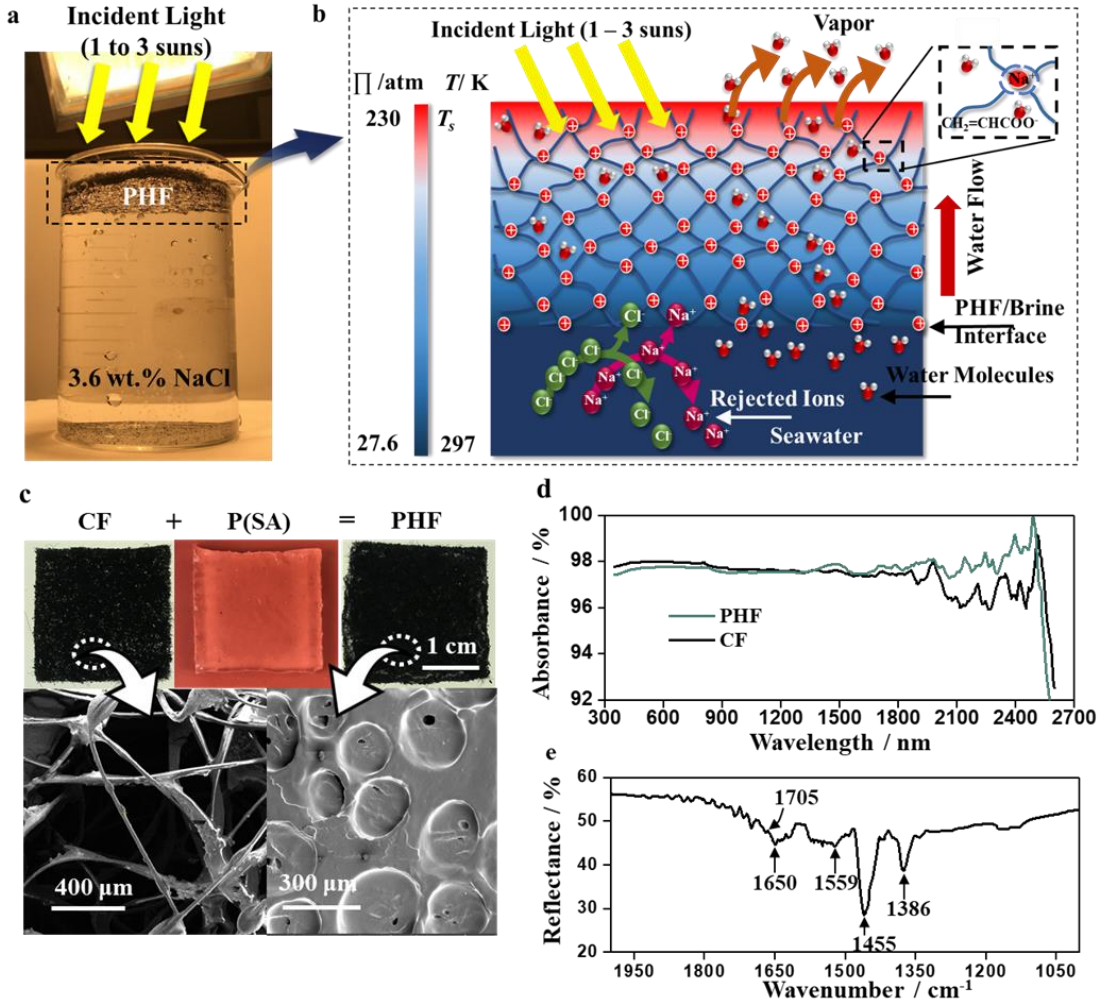

Figure 7-1. Experimental setup and schematics of dual ionic pumping and salt rejection effects offered by polyelectrolyte hydrogel poly(sodium-acrylate) [P(SA)]. (a) Bench-scale evaporation test with 3.6 wt.% NaCl solution mimicking the seawater. CF or PHF with the thickness of 5 mm floated on the bulk solution to receive solar radiation varying from 1 to 3 suns. (b) Polyelectrolyte hydrogel foam (PHF) absorber with its micropores filled with P(SA). Liquid flow is pumped by the osmotic pressure gradient between the bulk seawater (Π ~27.6 atm) and P(SA) hydrogel (Π ~230 atm). Salt ions are rejected at the PHF-seawater interface due to the high ionic strength of P(SA), and thus there is no salt clogging and sediment in the PHF. Liquid water is heated up close to the top of the PHF and evaporates. The surface temperature rises with increasing input solar flux. (c) Composition and microstructures of the PHF. The micropores with the diameter of ~ 400 μm are filled with P(SA) hydrogels after the copolymerization. (d) High absorbance of PHF and CF in the solar spectrum. (c) FTIR characterization of P(SA) hydrogel.

7.3. Characterization of osmotic pumping and design of evaporator

7.3.1. Diffusivity in hydrogel

Instead of the surface tension in the capillary pumping mechanism, in the ionic pumping mechanism, the liquid is pumped by the osmotic pressure difference between the polyelectrolyte hydrogel and seawater. Therefore, we first determined the osmotic pressure of the 20 wt.% PSA by comparing it to the NaCl solution of equivalent concentration as shown in Figure 7-2a. The average absorption flux in the first 5 mins, defined by Eq.3, decreased linearly from 2.3 LMH to 0.25 LMH as the osmotic pressure of the NaCl solution increased from 27.6 atm (equivalent to 3.6 wt.%) to 230 atm (equivalent to 30 wt.%), which was in line with the theory of diffusion. The diffusion-govern water transport in the hydrogel was also observed in literatures[253,299] and could be proven by the analysis of diffusive permeability. We record the water absorption by the 20 wt.% P(SA) hydrogel in the 7.2 wt.% NaCl solution as shown in Figure 7-3a. In this test, the as-synthesized 20 wt.% P(SA) hydrogel with the dimension of ~ 20×20×2 mm and initial weight of m_0, was immersed in the 7.2 wt.% NaCl solution for a specific period of time, after which the weight of the swollen hydrogel m_t was measured. This curve is in correspondence to that in Figure 7-2b under the condition of P(SA)-7.2 wt.% NaCl. The absorption results were fit to the following Fickian diffusion model Equation 7-1 [300-303] to calculate the water diffusivity in the Hydrogel D_w.

$$D_w = \frac{\pi l^2}{16}\left[\frac{d\left(M_t / M_\infty\right)}{d\left(t^{1/2}\right)}\right]^2 \tag{7-1}$$

where l is the thickness of the test sample (2 mm), M_t is the amount of water absorbed at time of t, and M_∞ is the total amount of water absorbed by the hydrogel at infinite time.

Although the curve did not complete plateau when the test was finished but it was reasonable to assume that the maximum mass was < 2 g as the curve stabilized after 1 hour. Therefore, the M_∞ was estimated to be 2 g. M_t / M_∞ was plotted as a function of $t^{1/2}$ in Figure 7-3b which showed a good linear fitting and gives the slope of 0.0193. Noted that we only chose the region of M_t / M_∞ < 0.6 for fitting as recommended in literature [303], which gave the diffusivity of water in P(SA) of 2.92E-10 m^2/s. This value was close to that reported for GMA, TEGDMA and HEMA hydrogels[299], which indicated the diffusion governed process instead of the viscous flow in the hydrogel as it was smaller than the self-diffusion coefficient of water (2E-9 m^2/s)[304]. It could be estimated from Figure 7-2a that the osmotic pressure of 20 wt.% PSA was around 240 atm although we did not further increase the NaCl concentration due to the dissolution limit, which was a factor of 10^5 higher than the capillary pressure of the CF with ~ 400 μm micropores assuming the completely wetting state (~ 360 Pa), and would still be ~1000 times higher than the capillary pressure of ~ 1 μm pores. More importantly, the osmotic pumping pressure is independent of the pore size and hence is independent of the flow resistance, and thus it can still be very high even with large pore sizes. The high osmotic pressure of P(SA) was attributed to the ionic SA monomers. By reducing the weight ratio of SA from 100 wt.% [pure P(SA)] to 50 wt.% [P(NIPAAm-co-SA)] and 0 wt.% [P(NIPAAm)], the equivalent osmotic pressure of hydrogels decreased to ~200 atm and < 30 atm, respectively.

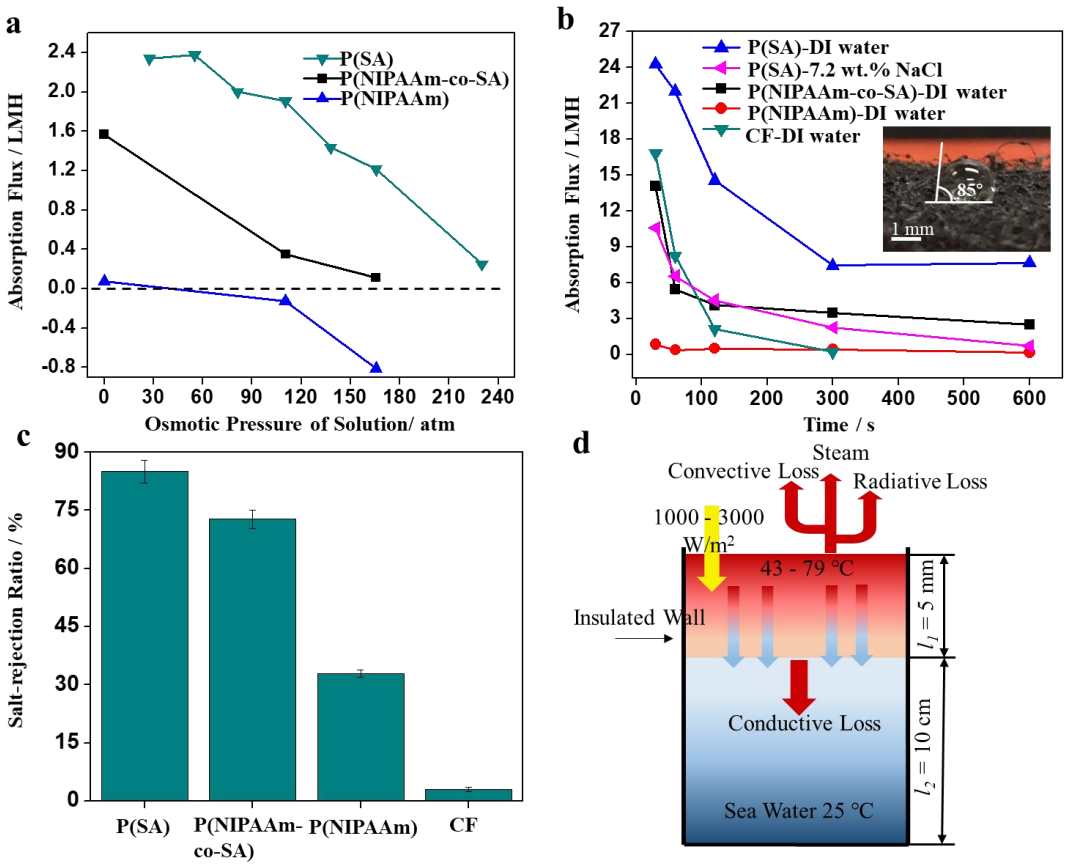

Figure 7-2. Ionic pumping mechanism for high flux and salt-rejection. (a) Average water absorption flux in 5 minutes of 20 wt.% P(SA), P(NIPAAm-co-SA) and P(NIPAAm) hydrogels with variation of osmotic pressure of NaCl solution. The osmotic pressure of solution at the flux of zero indicates the equivalent osmotic pressure for the hydrogels. (b) Instantaneous water absorption flux of hydrogels with different osmotic pressures and CF. The inset shows the contact angle on the surface of CF. (c) Salt-rejection ratio for hydrogels and CF using 3.6 wt.% NaCl solution, which is defined by the weight ratio between the NaCl salt rejected by hydrogels when it absorbs water from the 3.6 wt.% NaCl solution and that contained in the 3.6 wt.% NaCl solution of equivalent mass to the absorbed water (See Supplementary Information Section S1). (d) Heat transfer modelling of the solar desalination system.

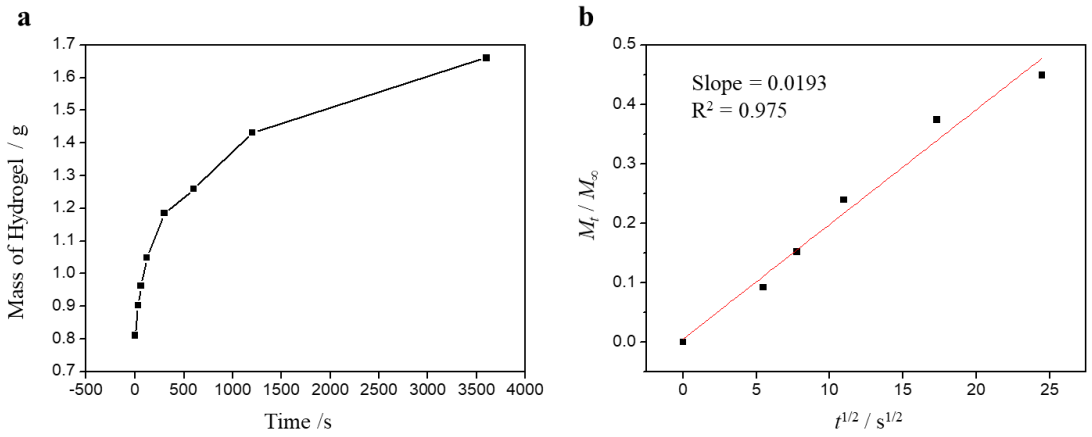

Figure 7-3. Measurment of diffusivity of water in P(SA) hydrogel (a) Mass change of 20 wt% P(SA) during the water absorption in 7.2 wt% NaCl solution (b) Linear fitting of M_t / M_∞ as a function of $t^{1/2}$.

7.3.2. Osmotic pressure and liquid flux

The high absorption flux was sustained by the osmotic pressure of the hydrogels. The osmotic pressure $\prod$ of strong inorganic electrolytes with certain molar concentration C (i.e., NaCl solution) can be calculated with the assumption of complete hydrolysis according to

$$\Pi = iCRT \qquad (7\text{-}2)$$

where i is the dimensionless van't Hoff index, R is the ideal gas constant and T is the temperature in K. However, it is still difficult to directly calculate the osmotic pressure of hydrogel. Instead of directly calculating the osmotic pressure of 20 wt.% P(SA), it was determined by comparing the concentration of NaCl solution C_{NaCl} where the immersed P(SA) could not swell, i.e., the P(SA) and the NaCl solution reach the thermodynamic equilibrium. Since the solubility limit of NaCl solution is 26.47 wt.% (~ 170 atm) where the absorption flux of P(SA) was still large as shown in Figure 2a, we further increased the osmotic pressure of solution to ~ 210 atm using 28 wt.% Na_2CO_3 solution (Only for this specific point). It is noted that the P(SA) swells when immersed in a solution of low

concentration, driven by the difference in the osmotic pressures until an equilibrium of $\prod$ between the swollen P(SA) and solution is reached. Therefore, the osmotic pressure of P(SA) was considered the same as that of the NaCl solution calculated from Equation 7-2.

To evaluate the liquid flux sustained by the PHF, we measured the absorption flux for hydrogels with different osmotic pressure (from 240 atm to 30 atm as described above) and CF as a function of time as shown in Figure 7-2b. A 20 wt.% P(SA) with mass of m_0 and external surface area of S_0 was immersed in DI water and 7.2 wt.% NaCl solution for a period of time t, and then the mass and external area of swollen P(SA) were recorded as m_1 and S_1, respectively. The absorption flux $\dot{m}_a$ during this specific period of time was given according to Equation 7-3.

$$\dot{m}_a = \frac{m_1 - m_0}{\rho_w A_a t_a} \tag{7-3}$$

The absorption flux of CF immersed in DI water was also given as comparison, which was driven only by the capillary force of the micro-pores. The tests were conducted under the ambient condition. The maximum real-time absorption flux of carbon foam was only 16.8 LMH, which was 16.8% lower than that of the P(SA) hydrogel. The reason is that the CF foam was merely hydrophobic as its contact angle with DI-water was ~ 85° as shown in the inset in Figure 7-2b, leading to the reduced capillary force from 360 Pa at the completely wetting state to ~ 30 Pa. The absorption flux monotonously decreased from 24 LMH [pure P(SA)] to 0.84 LMH [pure P(NIPAAm)] using DI water as the osmotic pressure decreased from 240 atm to 30 atm. Assuming that the evaporative flux is ~ 1.6 LMH/sun, the PHF using the P(SA) will be

able to provide stable liquid supply even under the 15-sun condition for DI-water and 6.6-sun for 7.2 wt.% NaCl solution.

7.3.3. Salt rejection ability

As shown in Figure 7-4a, to quantify the salt-rejection ability of the P(SA), P(NIPAAm-co-SA), P(NIPAAm) and the CF, the 20 wt.% P(SA)/P(NIPAAm-co-SA) and P(NIPAAm) hydrogels were firstly dried in the oven for 48 hours to the mass of m_1 and then immersed in the 3.6 wt.% NaCl solution for 24 hours to allow the fully swelling. Then the fully swollen hydrogel with the mass of m_2 was dried again in the oven for 3 days to the mass of m_3, which included both the dry mass of hydrogel (m_1) and the salt penetrated into the gel. The salt rejection ratio φ was given by Equation 7-2:

$$\varphi = 1 - \frac{m_3 - m_1}{0.036\left(m_2 - m_1\right)} \tag{7-2}$$

As shown in Table 7-1, the P(SA) was able to reject > 80% of the salt in the seawater when absorbed water. Due to the high ionic strength gradient at the brine/P(SA) interface, over 80% of the Na^+ ions were rejected by the P(SA). In the P(SA) hydrogel, the Na^+ ions are mobile while the negatively charged acrylate groups in the matrix are immobile. At the gel-brine interface, some Cl^- ions may still permeate through while most Na^+ ions are rejected. As a result, the gel side of the interface is locally negatively charged while the solution side is positively charged. The ionic strength decreased monotonously from P(SA), P(NIPAAm-co-SA) and P(NIPPAm) due to the decreasing content of SA monomers. And thus, the salt rejection ratio also decreased monotonously from 80% to 32% accordingly. For comparison, the salt rejection ratio for the CH was also measured using the same method descried above except that the CH did not swell after absorbing water. The CH did not show the ion-rejection ability because the ion-

rejection ratio was < 3.6%. Therefore, the PHF maintained a more stable evaporative flux in the long-term test compared to the CF. Figure 7-2c shows the salt-rejection ratio for the hydrogels and CF using 3.6 wt.% NaCl solution.

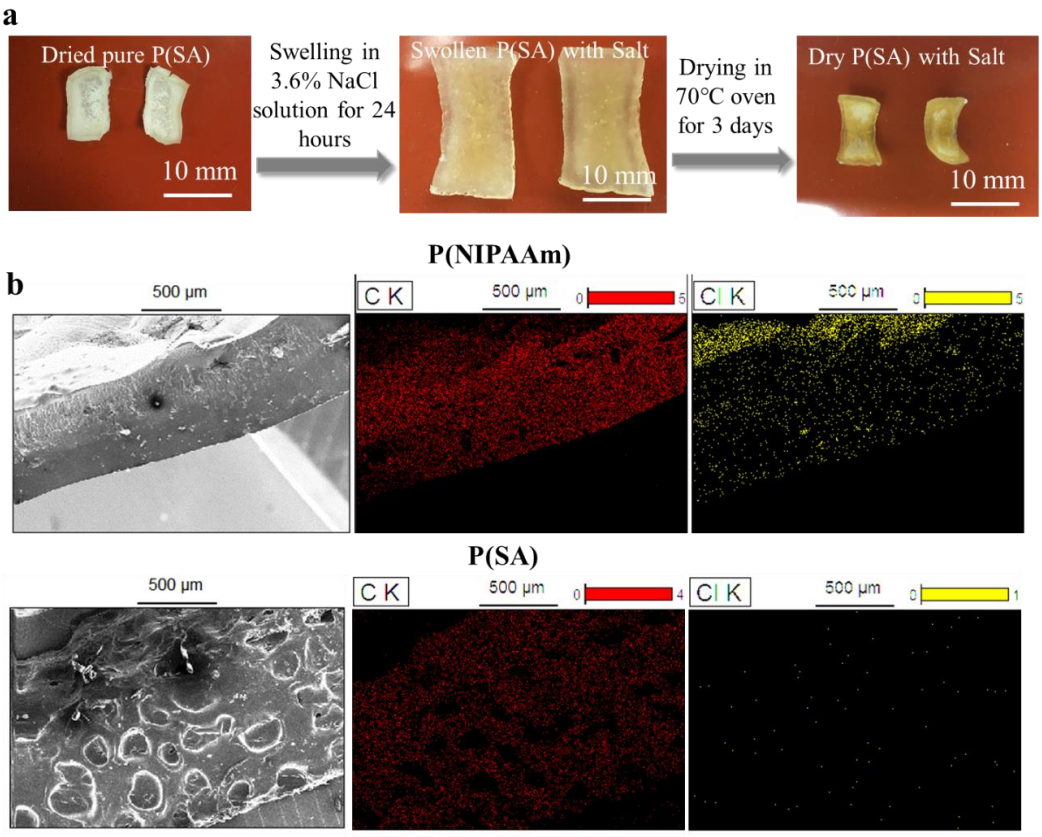

Figure 7-4. Characterization of salt-rejection ratio. (a) Measurement method of the salt-rejection rate for hydrogel. (b) EDS mapping of carbon and chloride elements in P(NIPAAm) (upper row) and P(SA) (lower row) after the salt-rejection ratio tests. A lot of Cl elements were identified in the P(NIPAAm) while little was found in the P(SA). Figures are SEM image, EDS mapping of carbon and EDS mapping of chloride from left to right.

Table 7-1. Salt rejection ratio of P(SA) and CF

Sample	Dry Mass m_1/ g	Swollen Mass m_2/ g	Dried Mass with Salt m_3/g	Salt Rejection Ratio
1	0.292	2.65	0.303	88.2%
2	0.273	2.57	0.288	81.9%
3	0.137	1.26	0.176	3.53%
4	0.136	1.19	0.173	2.49%
5	0.140	1.60	0.155	74.2%
6	0.165	1.93	0.186	70.3%
7	0.08	0.592	0.095	32.8%

*Sample 1 and 2 are P(SA); 3 and 4 are CF; 5 and 6 is P(NIPAAm-co-SA) with the NIPAAm:SA weight ratio of 1:1; 7 is the pure P(NIPAAm).

The unequal ion solute concentration distribution across the membrane across the membrane creates the Donnan potential which resist the ionic diffusion. We calculated the theoretical salt-rejection ratio for the 20 wt.% P(SA) hydrogel against the 3.6 wt.% NaCl solution based on the Donnon exclusion theory

$$C^s_{Na^{+1}} C^s_{Cl^{-1}} = C^m_{Na^{+1}} C^m_{Cl^{-1}} \tag{7-3}$$

where $C^s_{Na^{+1}}$ and $C^s_{Cl^{-1}}$ are the Na^+ and Cl^{-1} concentrations in the solution respectively, $C^m_{Na^{+1}}$ and $C^m_{Cl^{-1}}$ are the Na^+ and Cl^{-1} concentrations in the membrane respectively. Due to electroneutrality, $C^m_{Na^{+1}}$ can be expressed as:

$$C^m_{Na^{+1}} = C^m_{Cl^{-1}} + C^m_{R^{-1}} \tag{7-4}$$

and thus Equation 7-4 can be expressed as:

$$\left(C^m_{Cl^{-1}}\right)^2 + C^m_{Cl^{-1}} C^m_{R^{-1}} - \left(C^s_{Cl^{-1}}\right)^2 = 0 \tag{7-5}$$

Considering that only a small amount of Cl^{-1} penetrates into the membrane, i.e., $C^m_{Cl^{-1}} << C^s_{Cl^{-1}}$, the concentration of Cl^{-1} in the membrane can be expressed as:

$$C_{Cl^{-1}}^{m} = \frac{\left(C_{Cl^{-1}}^{s}\right)^{2}}{C_{R^{-1}}^{m}} \tag{7-6}$$

which allows us to evaluate the salt-rejection ratio by the P(SA) hydrogel. For example, we calculated that the $C_{R^{-1}}^{m}$ is ~ 7.3 M, and the $C_{Cl^{-1}}^{s}$ in the 3.6 wt.% NaCl solution is 0.64 M. Accordingly, the $C_{Cl^{-1}}^{m}$ is calculated to be 0.056 M. The salt rejection ratio, defined in Equation 7-7, is calculated to be 0.91, which is close to our measured value (0.85).

$$R = 1 - \frac{C_{Cl^{-1}}^{m}}{C_{Cl^{-1}}^{s}} \tag{7-7}$$

Although there were still 10 – 20% of the Na^{+} ions that penetrated into the P(SA), they would be trapped by the charged group of the P(SA). Ali *et al.* [298] confirmed that the P(SA-co-N-Isopropylacrylamide) was able to retain ~ 23% of NaCl. Therefore, we believe that there will be little salt sediment on the top of the PHF in practical application due to the salt-rejection and trapping of the P(SA). The high salt-rejection ratio of P(SA) was due to the ionic strength of the SA monomers, confirmed by the decreasing salt-rejection ratio from 85% to 32% with the decreasing SA concentration from 100 wt.% [pure P(SA)] to 0 wt.% [pure P(NIPAAm)]. On the other hand, the CF could not reject the ions, indicated by the salt-rejection ratio of < 3.6%. Due to the lack of ion-resistance, the CF would be prone to the salt crystallization and fouling of the foam in the long run.

Figure 7-4b shows the EDS mapping of P(SA) and P(NIPAAm) after the salt-rejection tests (i.e., with the mass of m_3) at the cross-sectional direction to qualitatively compare their salt-rejection ratios. It should be noted that the Cl elements are attributed to the NaCl salt absorbed by the hydrogel only because there was no Cl element in the composition of either P(SA) and P(NIPAAm). Due to the weak ionic strength, the

P(NIPAAm) had a low salt-rejection ratio and thus a lot of Cl elements could be found in the gel. On the other hand, little Cl element was found in the dry P(SA) because of its high ionic strength which helped rejected > 80% of the salt ions at the brine/gel interface when it absorbed water.

To evaluate the degradation effect of salt on the performance of P(SA) hydrogel and the lifetime of the membrane, we compared the absorption ratio of P(SA) hydrogels in several cycles using both DI-water and actual pacific seawater (collected from the La Jolla shore and provided by the Scripps Oceanography Institute). The 20 wt.% P(SA) hydrogel was dried in the 70℃ oven for 24 hours to the mass of m_1 and then immersed in the DI-water or actual seawater for 5 mins and 30 mins, respectively to let it swell to the mass of m_2. The swelling ratio R_s for the time period of interest was calculated as follows:

$$R_s = \frac{m_2}{m_1} \tag{7-8}$$

After the test, the P(SA) hydrogels were kept in the solution for 24 hours to allow it to fully swell. Subsequently, they were dried in 70℃ oven for 24 hours again before the next cycle. 3 cycles were done for the DI-water tests while 5 cycles were done for the actual seawater to better evaluate the salt degradation effect. Figure 7-5 shows the swelling ratio of P(SA) using DI-water and actual sweater as solution in the first 5 mins and 30 mins. It is seen that the swelling ratio of P(SA) is stable using DI-water, where the swelling ratios in the first 5 mins and 30 mins slightly decrease from 11.2 to 8 g/g and from 58.3 to 49.2 g/g over 3 cycles. The good salt-rejection effect of the P(SA) was proved by the stable swelling ratio using actual seawater over the 5 cycles. The swelling ratios ranged 6.7 to 9.3 (g/g) in the first 5 mins and from 11.6 to 14.8 (g/g) in 30 mins, indicating the minor salt degradation effect on the PHF. The swelling ratio of P(SA) in

actual seawater was significantly lower than that in the DI-water due to the much higher osmotic pressure of seawater.

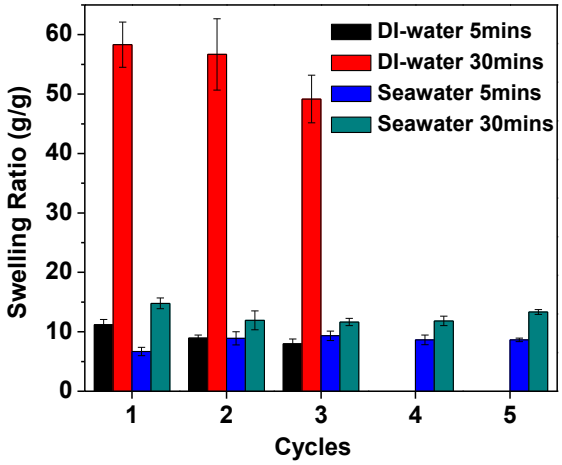

Figure 7-5. Swelling ratio of P(SA) hydrogel using DI-water and actual seawater in different cycles.

7.3.4. Thermal modeling

The results from these tests clearly demonstrated the high mass flux and salt-rejection capability of the ionic pumping mechanism using the polyelectrolyte hydrogel foam. We showed the high flux of up to 24 LMH and salt-rejection ratio up to 80% using the P(SA) ionic hydrogel. The simultaneous efficient liquid supply and salt-rejection achieved by the ionic pumping effect provide us an entirely new strategy to solve the tradeoff seen in capillary assisted solar desalination. Figure 7-2d shows the heat transfer model of the solar desalination system. The energy efficiency of the evaporator was calculated as follows:

$$\eta = \frac{q_{evp}}{q_{solar}} = \frac{q_{solar} - q_{c1} - q_r - q_{c2} - q_{de}}{q_{solar}} \tag{7-9}$$

where q_{solar}, q_{c1}, q_r, q_{c2} and q_{de} are the solar flux, convective heat loss, radiative heat loss, conductive heat loss and additional heat loss due to insufficient liquid supply, respectively, which are calculated based on the measured surface temperature of CF/PHF.

The radiative heat loss is given by Equation 7-10:

$$q_r = \varepsilon\sigma\left(T_s^4 - T_a^4\right) \tag{7-10}$$

where ε and σ are the emissivity at the peak radiation wavelength (~ 0.95 at 10 μm) and Stefan-Boltzmann constant; T_a is the ambient temperature in the lab environment (25 ℃). It gives the radiative heat loss of ~ 112.3 W/m^2.

The convective heat loss from the upper surface to the environment is given by:

$$q_{c1} = h_1\left(T_s - T_a\right) \tag{7-11}$$

where h_1 is the convective heat transfer coefficient and is given by the Nusselt number

$$Nu_1 = \frac{h_1 L}{k_1} \tag{7-12}$$

where L is the characteristic length of the surface (2.4 cm). And for the free convection condition on a horizontal hot surface, the Nusselt number is given by

$$Nu_1 = 0.54 Ra_1^{1/4} \tag{7-13}$$

where Ra_1 is the Rayleigh number which can be expressed as the product of Grashof number Gr and Prandte number Pr : $Ra_1 = Gr_1 \cdot Pr_1$

and

$$Gr = \frac{g\beta\left(T_S - T_a\right)L^3}{\nu^2} \tag{7-14}$$

where g is the gravity acceleration, β is the coefficient of thermal expansion of fluid,

$$\mathrm{Pr} = \frac{C_{p1}\mu_1}{k_1} \tag{7-15}$$

where C_p and μ are the heat capacity and viscosity of fluid, respectively. Plugging the physical properties of air at the average of T_s and T_a (i.e., at 34℃) into Equation 7-12 to

7-15, we obtain the heat transfer coefficient h_1 for the upper surface of 7.41 W/m^2-K. Thus, the convective heat loss of the upper surface to the air is 133.4 W/m^2.

To evaluate the conductive heat loss from the bottom surface to the bulk water, we firstly obtained the thermal conductivity of the PHF using a steady-state method which was found to be ~0.25 W/m-K. Assuming the one-dimensional heat conduction through the PHF with the thickness l_1 of 5 mm, the temperature of the bottom surface T_b was 28.6℃ using the Fourier's law:

$$q_s - q_{c1} - q_r = -k_{CFH} \frac{T_b - T_s}{l_1} \tag{7-16}$$

During the experiment, the bulk water was confined in the small reservoir and the hot surface was on the top without external perturbation, so we could assume that the heat loss to the bulk water was via thermal conduction instead of convection[292]. Thus, the heat loss from the bottom surface of the PHF to the bulk water is given by Equation 7-17 and is 21.6 W/m^2.

$$q_{c2} = -k_w \frac{T_a - T_b}{l_2} \tag{7-17}$$

It should be noted that although increasing the foam thickness helps reduce the conductive loss to the bulk water and increase the salt rejection ability, the energy efficiency is limited by the maximum liquid flux as shown in Figure 7-2b. Increasing solar power or thickness of the foam so that the sustainable liquid flux is lower than the theoretical maximum evaporative flux, the redundant solar flux will be dissipated, which leads to the q_{de} given by Equation 7-9. P(SA) was chosen to incorporate with the CF to produce the PHF to achieve the high salt-rejection ratio (85%). In the meantime, to achieve high energy efficiency > 70% with the

solar flux ranging from 1 to 3 suns, the thickness of the foam should be carefully chosen. Based on the absorption flux of P(SA), the foam thickness of PHF using the P(SA) was chosen to be 5 mm.

7.4. Demonstration of osmotic pumping for solar-driven desalination

Next, we set to demonstrate the feasibility of applying the ionic-pumping effect for continuous solar-driven desalination, which is an attractive topic in recent years in the context of water-energy nexus. Despite the abundant efforts in improving the energy efficiency of the solar absorber, the continuous solar-driven desalination is yet to achieve because most previous studies employed the capillary-pumping effect for liquid supply using microporous structure, which inevitably resulted in the salt clogging and sediments under the conditions of high solar flux, high salt concentration and long irradiation time. And thus, previous studies only achieved the stable solar-driven desalination on the daily-basis at best with self-diffusion at night [292,293]. In the previous section, we demonstrated the high flux using the ionic pumping effect, which enabled the efficient liquid supply even under the high suns condition. More importantly, due to the strong salt-rejection ability of P(SA), the problem of salt clogging in the foam and sediment on the top of the receiver were resolved. The sufficient liquid supply of ionic pumping was confirmed in the DI water test while the salt-rejection performance was evaluated in the test using 3.6 wt.% NaCl solution.

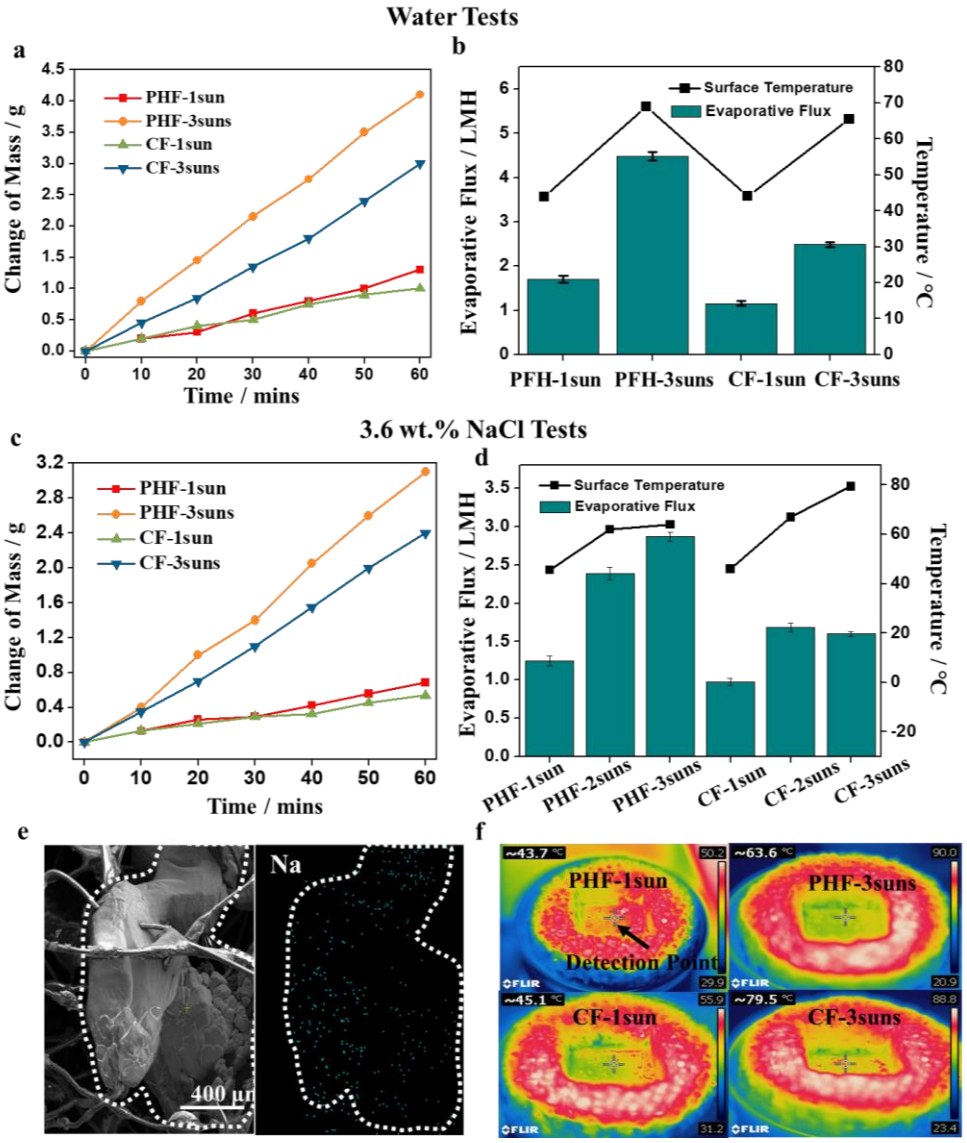

Figure 7-6. Ionic pumping effect for liquid supply and salt-rejection in solar-driven evaporation. (a) Evaporation mass loss of DI-water vs time under the 1-sun and 3-sun conditions, respectively. (b) Evaporative flux and surface temperature using DI-water under the 1-sun and 3-sun conditions, respectively. (c) Evaporation mass loss of simulated seawater (3.6 wt.% NaCl solution) with the solar flux varing from 1 to 3 suns. (d) Evaporative flux and surface temperature using the simulated seawater under 1 to 3 suns conditions. (e) Salt clogging in the micropores for the CF without salt-rejection effect. (f) Infrared thermal images of PHF and CF under the 1 and 3 suns conditions using simulated seawater. The surface temperature of CF was similar to that of PHF under the 1 sun condition but it was much higher than that of PHF under the 3 suns condition, due to the salt clogging in the micropores which led to insufficient liquid supply.

7.4.1. Osmotic-pumping assisted water supply

Figure 7-6a shows the mass loss of DI-water in the bulk due to evaporation using the CF and PHF as absorbers under the 1-sun and 3-sun conditions, respectively. The evaporation was stable during the one-hour test indicated by the linear relation of mass loss over time. The PHF absorber yielded 1.3 g mass change in 60 mins, which was 30% greater than that of the CF under the 1-sun condition. It showed a more evident advantage over the CF under the 3-sun condition where the PHF yielded 4.1 g mass change which was only 3.1 g for the CF. Figure 7-6b shows the evaporative flux for the CF and PHF under the 1 and 3 suns conditions in accordance to the mass changes shown in Figure 7-6a. The PHF yielded 1.65 LMH and 4.6 LMH under the 1 and 3 conditions, which were 42.2% and 79.9% higher than that for the CF, respectively. Interestingly, the surface temperatures for the PHF and CF were similar, which were ~ 43 °C and ~ 65 °C under the 1 and 3-sun conditions, respectively. This indicates that the heat loss due to radiation, convection to air, and convection to bulk liquid underneath the absorber were similar for the PHF and CF as shown in chapter 7.3.4, and thus both samples had similar energy efficiency η of ~ 75% under the one-sun condition, which agreed with that of CF (72.5%) given by $\eta = \frac{\dot{m}\, h_{lg}}{q_s}$ where q_s is the solar flux and h_{lg} is the evaporative latent heat. Therefore, we believe that the PHF yielded a higher evaporative flux than the CF due to the more efficient liquid supply.

To validate the measurement method, we measured the evaporative flux of pure water under 1 and 3 suns condition using DI-water with the surface area of 35.3 cm^2. The evaporative flux and temperature of the water surface under 1 sun condition were shown in Figure 7-7. The mass loss was 2.8 g in 1 hour, which was equivalent to 0.795 LMH.

The temperature increases slightly overtime from 33℃ to 40℃, and thus we took T_s = 311 K as the surface temperature and T_a = 300 K to calculate the theoretical evaporative flux, with the estimation of relative humidity RH of 60% and air velocity v of ~ 0.5 m/s in the lab environment.

The evaporative flux is given by an empirical equation

$$\dot{m} = \phi\left(x_s - x\right) \tag{7-18}$$

where $\dot{m}$ is the evaporative flux, φ (kg/m^2-h) is the evaporation coefficient and is estimated by:

$$\phi = 25 + 19v \tag{7-19}$$

Noted that theφ does not match the unit since this is an empirical equation. x_s is the maximum humidity ratio of saturated air at the surface temperature T_s and for ideal gas, it could be expressed as:

$$x_s = 0.62198\frac{P_{ws}}{P_a - P_{ws}} \tag{7-20}$$

where P_{ws} is the saturation pressure of water vapor at T_s, and P_a is the atmospheric pressure of moist air (1.01e5 Pa). The saturation pressure of water vapor is given by Eq. S4-4 and is 6555 Pa by plugging T_s = 311 K into the equation.

$$P_{ws} = \frac{\exp\left(77.345 + 0.0057T_s - \frac{7235}{T_s}\right)}{T_s^{8.2}} \tag{7-21}$$

The x is the humidity ratio:

$$x = 0.62198\frac{P_w}{P_a - P_w} \tag{7-22}$$

where P_w is the partial pressure of water vapor in the moist air which at T_a, and is given by:

$$P_w = RH \cdot P_{ws} \tag{7-23}$$

Noted that the P_{ws} in Equation 7-23 is calculated at T_a instead of T_s. With RH = 60% and $P_{ws}(T_a$ = 300 K) = 3524 Pa, the P_w is equal to 2114 Pa. By plugging in P_{ws} and P_w, we have x_s = 0.0436 and x = 0.0134. And thus, the evaporative flux of water at T_s = 311 K and RH = 60% is estimated to be 1.04 LMH, which is only 30% higher than the experimental value.

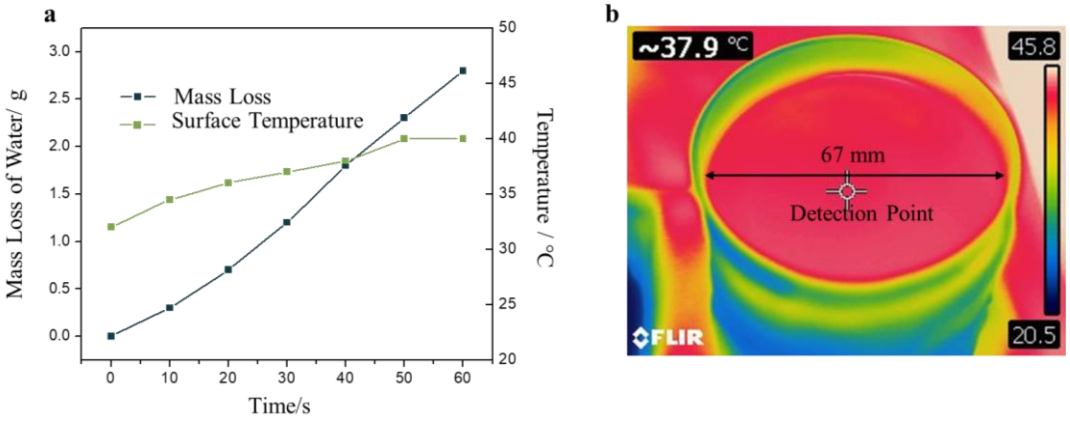

Figure 7-7. Evaporation of DI-water without receiver under 1 sun condition. (a) Mass change of water and water surface temperature during evaporation (b) IR-camera image of the water surface at T_s = 37.9℃.

Figure 7-8 showed the mass change and water surface temperature for DI-water under 3 suns condition. The surface temperature rose from 50 to 60 ℃ in the 1 hour test and thus we set T_s = 328 K as the characteristic surface temperature while keeping T_a = 300 K and RH = 60% as for the 1 sun condition test. The mass change was 12.6 g in 1 hour, which was equivalent to 3.58 LMH. Similar to the analysis for the 1 sun condition, we obtain the P_{ws} = 15583 Pa at T_s = 328 K and P_w = 2114 Pa at T_a = 300 K and RH= 60%, which gives x_s = 0.115 and x = 0.0134. And thus we obtain the theoretical

evaporative flux of 3.5 LMH, which is very close to the experimental data. Therefore, we believe that the experiments were solid.

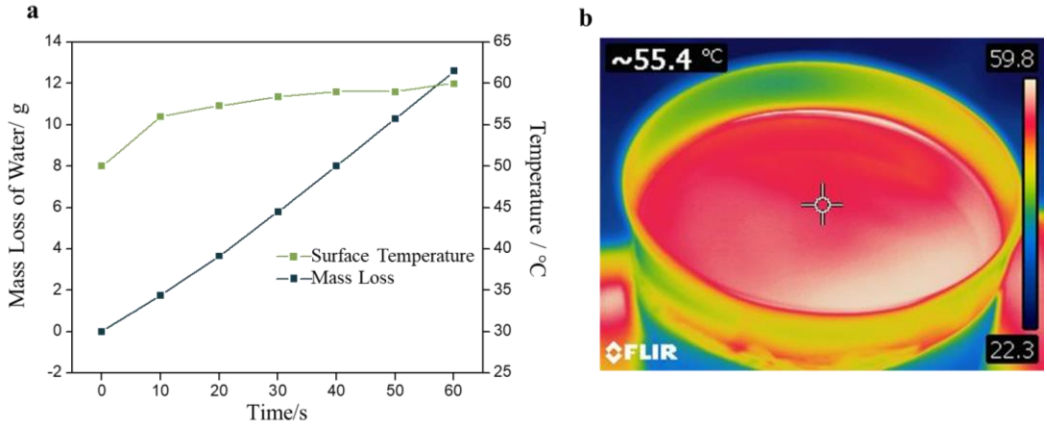

Figure 7-8. Evaporation of DI-water without receiver under 3 suns condition. (a) Mass change of water and water surface temperature during evaporation (b) IR-camera image of the water surface at T_s = 55.4℃.

7.4.2. Osmotic-pumping assisted salt-rejection

In addition to facilitate the water supply, the P(SA) also served as the salt-rejecting agent at the seawater-PHF interface due to its high ionic strength, which helped avoid the salt clogging in the porous foam and salt sediment on the upper surface of the receiver. Figure 7-6c shows the mass loss of 3.6 wt.% NaCl solution due to evaporation for 1 hour under the 1-sun and 3-sun conditions. It was found that the PHF and CF had similar mass change rate at the 1-sun condition but the PHF yielded a higher mass change rate under the 3-sun condition. Figure 7-6d compares the evaporative flux for the PHF and CF from 1 to 3 suns. The PHF yielded higher evaporative flux than the CF under all conditions, e.g., at the 1-sun condition, the evaporative flux for the PHF was 1.24 LMH, which was 27.8% higher than that of the CF. This could be attributed to the relatively insufficient liquid supply for the CF compared to the PHF. As discussed in chapter 7.3.2, the PHF yielded a higher water absorption flux than the CF due to its high osmotic

pressure. More importantly, although the absorption flux for the PHF slightly decreased when using 7.2 wt.% NaCl solution as shown in Figure 7-6b, the PHF still maintained a higher liquid flux than the CF due to the salt-rejection effect.

Figure 7-6e shows the SEM and EDS images of the CF after the 1 hour test under the 3-sun condition. It is clearly seen that the micropores in the CF were clogged by NaCl which crystallized in the pore as water evaporated. This undermined the liquid supply through the micropores. In addition, the salt sediments on the top of the foam reduced the solar absorbance because it reflected the sun light. As shown in Figure 7-9a, the solar absorbance of CF was reduced from 97.7% before the test (Figure 7-1d) to ~ 94.2% after the 1-hour test. As a result of the high ionic strength of the P(SA), most salt ions were rejected at the water-foam interface while the small amount of salt that penetrated into the foam were captured by the ionic group of P(SA) (acrylate group), and thus there was little salt sediment on the top surface of the foam. Figure 7-9b shows the absorbance of CF after the 6-hour test under 2-sun condition using 3.6wt.% NaCl solution. The average absorbance in the solar spectrum was reduced to 88.9% from 97.7% before the test.

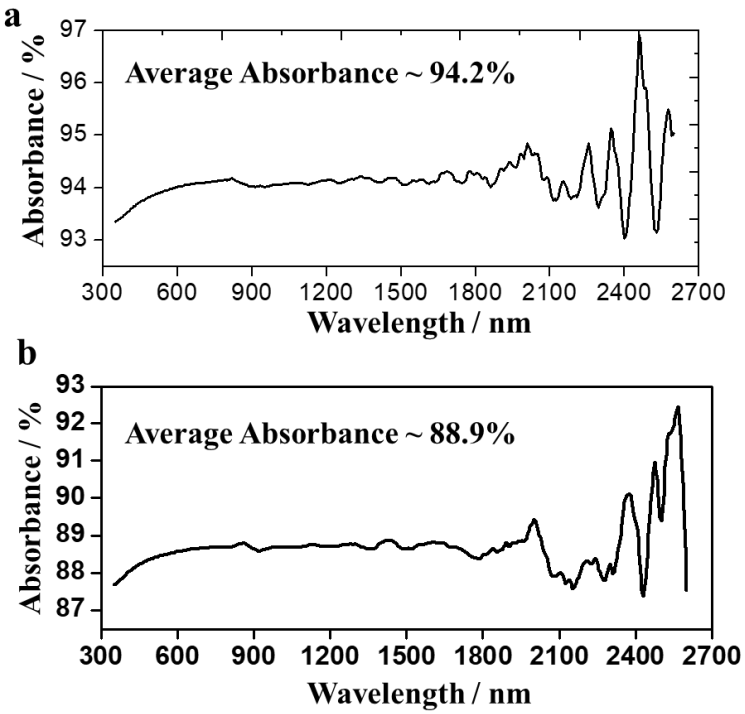

Figure 7-9. Solar absorbance of CF after (a) 1 hour under 1-sun condition with 3.6wt.% NaCl solution (b) 6 hours under 2-sun condition with 3.6wt.% NaCl solution.

The salt-rejection effect of the PHF became more prominent under the high sun condition where the salt crystal grew faster. For example, as the solar radiation increased from 1-sun to 3-sun, normalized the evaporative flux (i.e., the evaporative flux divided by the solar power, LMH/sun) for the CF decreased by 45.2% while that for the PHF only decreased by 23%. Due to the insufficient liquid supply, the surface temperature of CF was higher than that of the PHF, e.g., under the 3-sun condition, the surface temperature was 79°C for the CF and 63°C for the PHF as shown in Figure 7-6f and 7-6d. According to the calculation in chapter 7.3.4, the PHF had a 30% higher energy efficiency than the CF under the 3 suns condition using 3.6 wt.% NaCl solution.

7.4.3. Demonstration of continuous solar-driven desalination

Figure 7-10a compared the evaporation flux of the PHF and CF under the 2-sun condition with 3.6 wt.% NaCl in the bulk for 6 hours. In the first hour, the PHF yielded 2.4 LMH evaporative flux which was 41.2% higher than that of the CF. The PHF maintained a stable evaporative flux ranging from 2.36 to 2.56 LMH throughout the 6-hours test. However, the evaporative flux for the CF gradually decreased from 1.7 to 1.46 LMH in the first 4 hours and dropped to 1.1 LMH in the 5th hours where the salt crystallization became prominent as shown in Figure 7-10b. The absorbance of the CF decreased to 88.92% after the 6-hours test as shown in Figure 7-9b. This test also proved that the PHF was stable for 12 hours under 1 sun condition, which was equivalent to the stability on the daily basis. The stable solar-driven desalination on daily basis under the 1-sun condition was also demonstrated in Refs.[292,293]. However, without the salt-rejection effect, it is difficult to further increase the equivalent sun-hours stability because the rate of salt crystallization exceeds that of the dissolution and diffusion of salt under the high sun condition. Therefore, the stable solar-driven desalination exceeding the 12 sun-hours was challenging.

As shown in Figure 7-10c**,** we managed to achieve the continuous and stable solar-driven desalination exceeding the 12 sun-hours using the ionic pumping effect. The PHF was placed under 1-sun condition for 72 hours consecutively and its evaporative flux was measured every ~ 24 hours. The evaporative flux was an average value in 1 hour, the same way we measured the flux shown in Figure 7-6b and Figure 7-6d. The evaporative flux maintained stable between 1.2 and 1.3 LMH within 72 hours. It is evident that there was no

significant salt sediment on the top of the PHF (insets of Figure 7-10c). To further prove this, we did an EDS mapping on the PHF after test and compare it to the CF as shown in Figure 7-11. Salt crystals could be clearly seen on the surface of the CF as shown in Figure 7-11b after 2-days test under 1 sun, indicating by the existence of Cl element in the EDS figure. On the contrary, the PHF surface maintained smooth and salt sediment was not observed. In addition, we did not identify the Cl element in the EDS mapping.

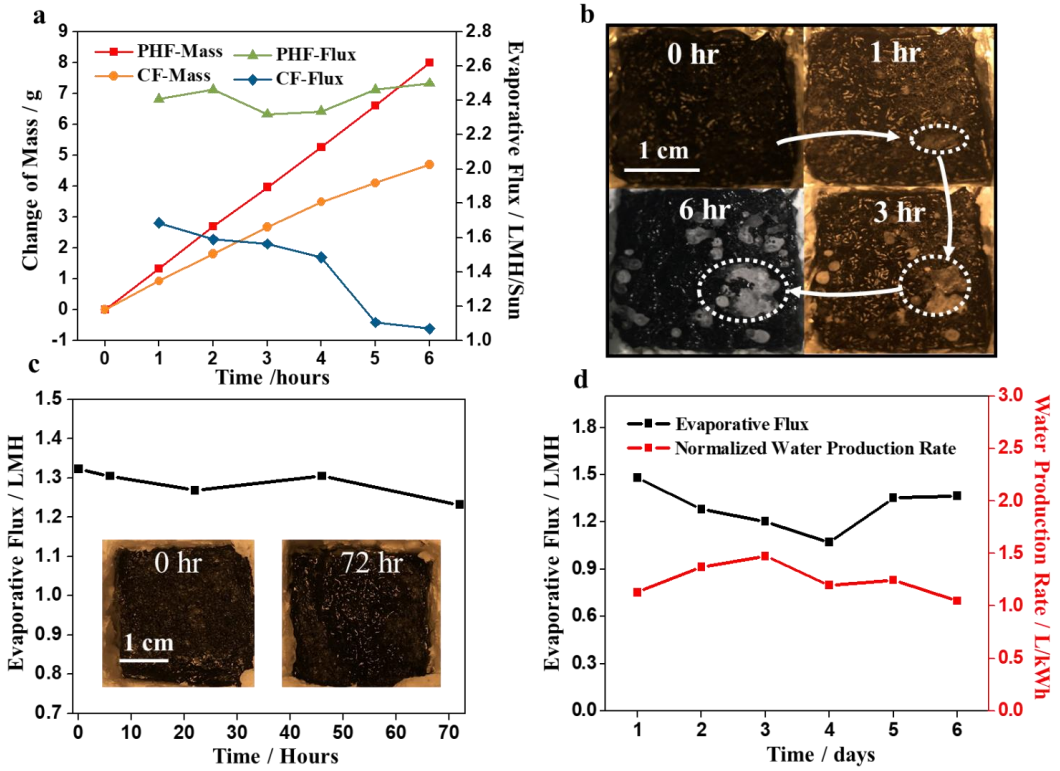

Figure 7-10. Continuous and stable solar-driven desalination exceeding 12 sun-hours sustained by the ionic-pumping effect. (a) Mass change and evaporation flux of CF and PHF under 2 suns condition for 6 consecutive hours. (b) Salt sediments (shown within the dashed circles) on the CF. (c) Stable evaporation flux for the PHF throughout the 72-hour test under 1 sun condition in the lab. The insets show the absence of the salt sediments on the PHF. (d) Evaporation flux (left axis) and daily water production rate normalized by daily solar irradiation (right axis) over the course of six days of continuous operation under natural solar irradiation on a rooftop. The daily solar irradiation flux was obtained from the NASA database[305].

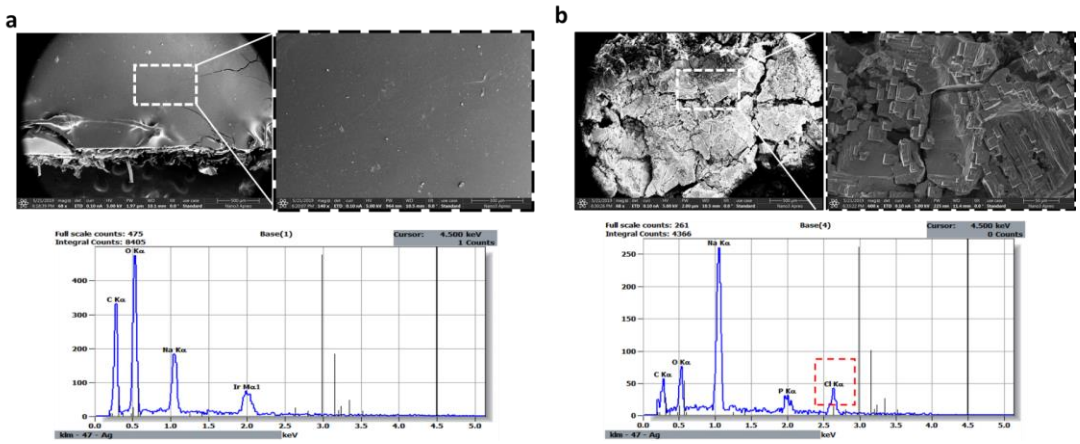

Figure 7-11. SEM and EDS of PHF and CF. (a) PHF after 12-days test under 1 sun condition using actual seawater. No salt sediment was observed from the SEM image and Cl element was not identified in the EDS mapping. (b) CF after 2-days test under 1 sun condition using actual seawater. Salt crystal could be clearly seen in the SEM image which was further confirmed by the existence of Cl element in the EDS mapping.

In the real application, assuming the 12-hour daylight, we can apply at least 6 suns onto the PHF while still maintaining the high evaporative flux of ~ 1.2 LMH/sun. The PHF was also tested under the natural sun light irradiation for 6 days consecutively (24 hours per day) on a rooftop without cleaning or replacing the receiver. The evaporative flux was measured at the mid-day where the solar irradiation was close to 1 kW/m^2 and was averaged over 1 hour. The evaporative flux still maintained stable over the course of 6-days. The small fluctuation of the flux was due to the unstable ambient conditions. Similarly, due to the variation in the total solar radiation energy from day to day in the 6-day test, the production rate (in L/m^2-day) fluctuated as shown in Figure 7-12a. However, after normalization with the daily solar radiation energy, which was quoted from the NASA database as shown in Figure 7-12b, the normalized water production rate was stable ranging from 1 to 1.5 L/kWh-day as shown in Figure 7-10d.

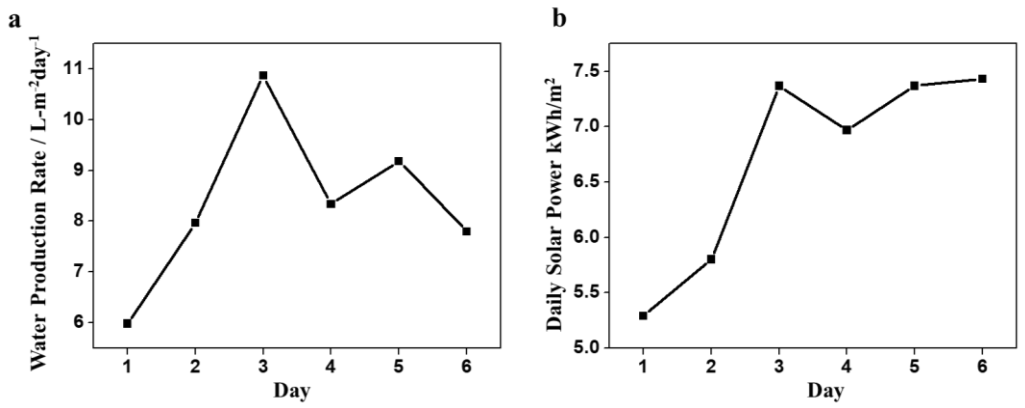

Figure 7-12. Long-term stability test. (a) Water production rate before normalization by daily solar radiation energy. (b) Daily solar radiation energy in the course of 6 days

We also demonstrated the long-term stability of PHF using actual seawater. Here we showed the PHF evaporative flux under 1 sun condition using actual Pacific Ocean seawater provided by Scripps Oceanography Institute, UCSD for 12 days consecutively, i.e., a 288 hours non-stop test. The evaporative flux was measured every 24 hours and the measurement lasted for 1 hour in the same way as we measured all other evaporative flux reported in this study. Figure 7-13a showed that the PHF yielded a stable evaporative flux around 1.3 LMH in the course of the 12-days test, indicating that the PHF was also stable in the real application scenario. It is seen from Figure 7-13b that there was no salt crystal on the surface of PHF. To further prove this, we have shown an EDS mapping on the PHF after test and compare it to the CF as shown in Figure 7-11. Salt crystals could be clearly seen on the surface of the CF as shown in Figure 7-11b after 2-days test under 1 sun, indicating by the existence of Cl element in the EDS figure. On the contrary, the PHF surface maintained smooth and salt sediment was not observed. In addition, we did not identify the Cl element in the EDS mapping. Figure 7-11c shows the stable surface temperature of the PHF over the 12 days test. The analysis above proved that the PHF was also stable using the actual seawater for at least 12 days under 1 suns.

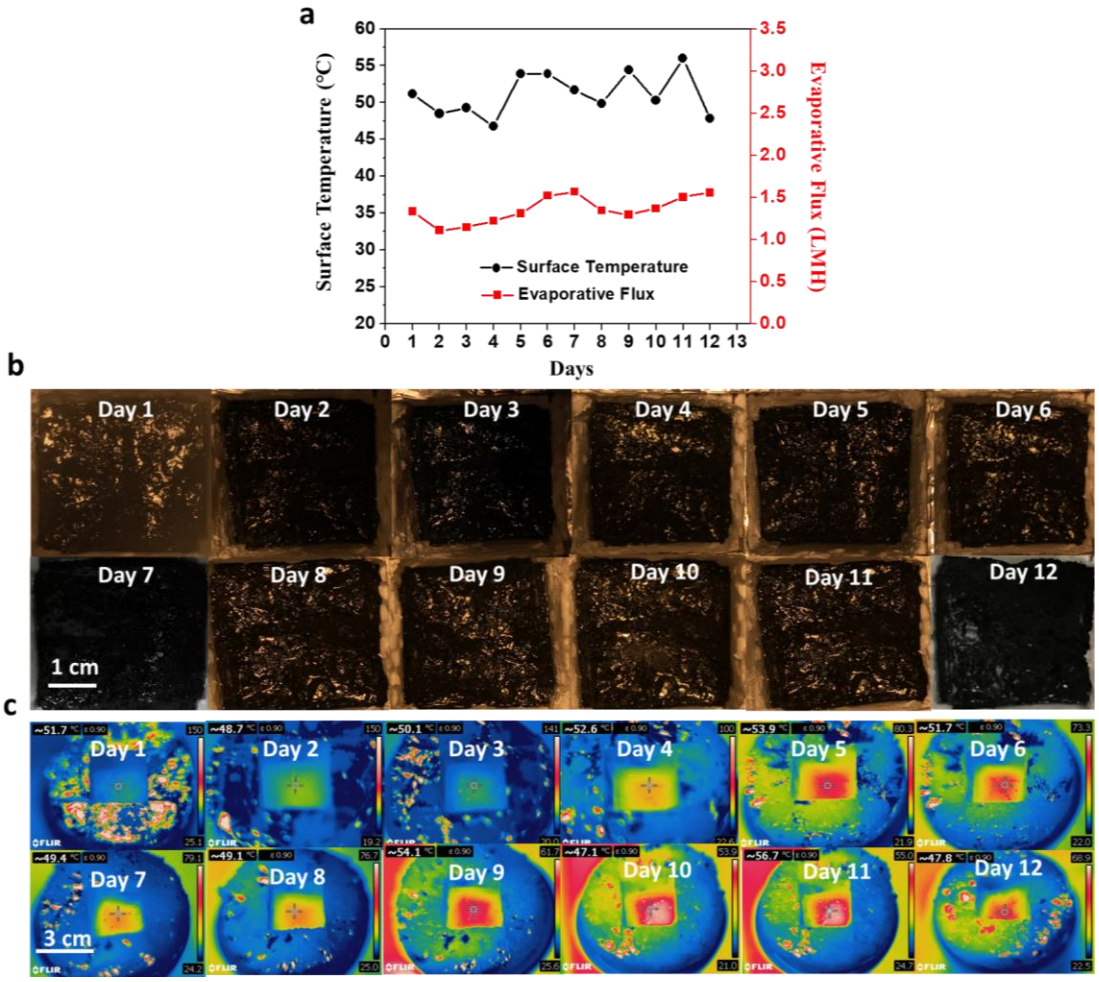

Figure 7-13. 12 days long-term test of PHF using actual seawater under 1 sun conditions in the lab. (a) Evaporative flux and surface temperature. (b) Surface condition on different days. (c) Surface temperature monitored with IR-camera.

To identify the critical condition that the PHF could sustain, we tested the PHF under 3 suns condition using actual seawater for 6 days consecutively, i.e., a 144 hours non-stop test as shown in Figure 7-14. Similarly, the evaporative flux was measured every 24 hours and the surface condition was monitored. We found that under the 3 suns condition, the evaporative flux was stable in the course of the 6-days test as shown in Figure 7-14a. As shown in Figure 7-14b, we did not observe salt sediment on both the top and bottom surface of the PHF until the day 5 when salt started to accumulate at the

bottom of the PHF. The surface temperature of the PHF was monitored as shown in Figure 7-14c. On day 6, salt start to accumulate on the top surface of the PHF. Therefore, under the 3 suns condition, the PHF was able to continuously reject salt for 5 days.

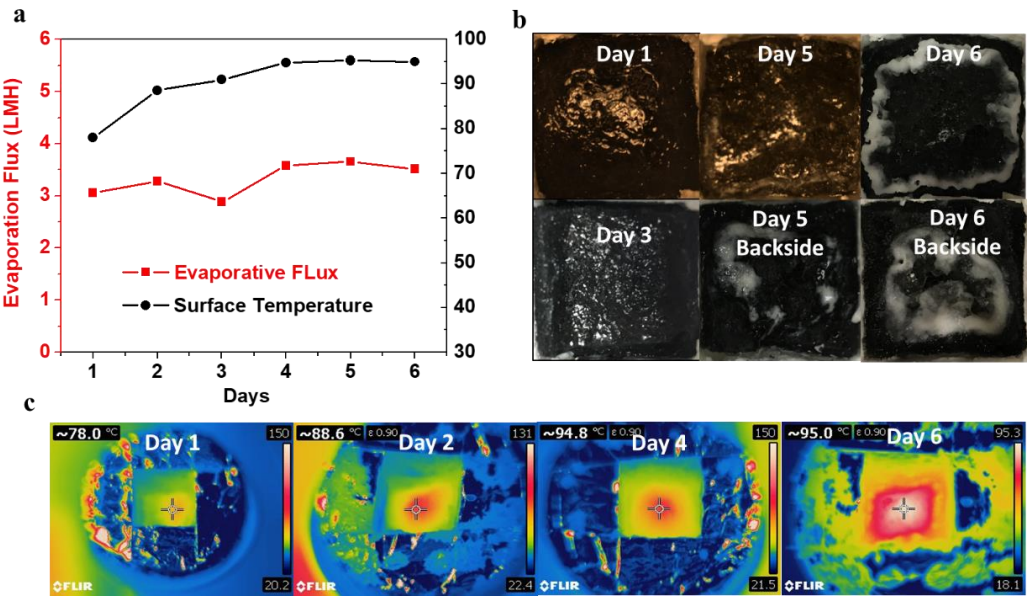

Figure 7-14. Evaporative of PHF under 3 suns condition using actual seawater for 6 days consecutively. (a) Evaporative flux and surface temperature on different days. (b) Surface conditions of PHF. (c) IR-image of the PHF top surface during measurement.

We demonstrated the facile purified water collection from vapor from the PHF using a desiccator as shown in Figure 7-15a. We collected the condensed water every 24 hours to show the stable yield of product water as shown in Figure 7-15b. The PHF was placed under 1 sun irradiation for 24 hours/day and for 12 days, i.e., a constant total daily solar energy of 24 kWh/day throughout the test. Since the setup was place in the lab, it was not prone the environmental change. We measured the weight loss of the bulk solution as well as the weight of collected condensed water every 24 hours to obtain the evaporative and condensation water yield on daily basis. As shown in Figure 7-15a, the PHF and bulk solution were placed in a desiccator. It is clearly seen that the vapor condensed on the inner surface of container which could be easily collected. As shown in

Figure 7-15b, the evaporative product water yield ranged from 23g to 26 g and we collected 18 g to 24 g of condensed water every day. The average evaporative and condensation flux stabilized around 1.2 LMH and 0.97 LMH, respectively. This result confirmed that the PHF can sustain a stable product water yield as long as the ambient conditions are stable.

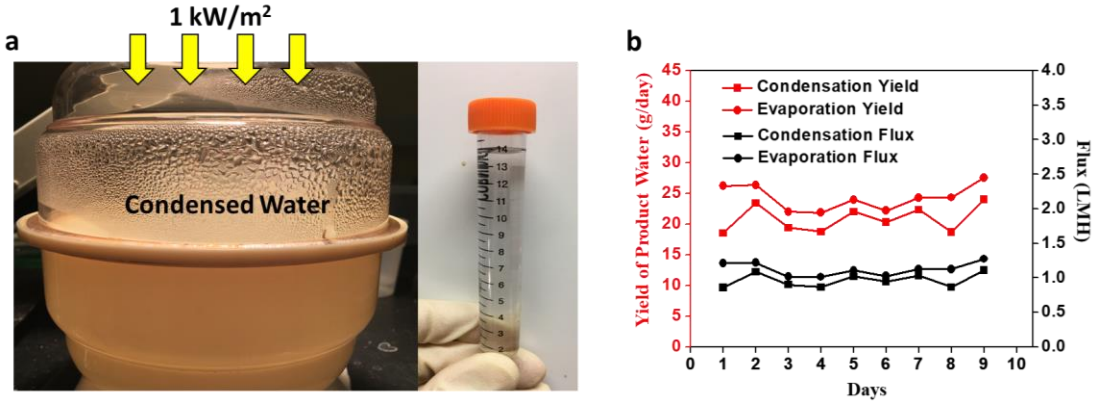

Figure 7-15. Water production rate test under 1 sun condition using actual seawater. (a) Photo of setup and product water. (b) Yield of product water and average flux on different day.

Figure 7-16 compares the salinity and specific ion concentrations for product water (collected from the condensed water as shown in Figure 7-15a and original seawater. The salinity of the seawater used in this study was 33180 ppm with the mass fraction of Na^+, Mg^{2+}, Ca^{2+} and K^+ ions of 10221 ppm, 1214 ppm, 390 ppm and 371 ppm, respectively. The salinity of the condensed water was 112 ppm with the mass fraction of Na^+, Mg^{2+}, Ca^{2+} and K^+ ions of 35 ppm, 4 ppm, 1.3 ppm and 1.3 ppm, respectively, indicating the high quality of the product water.

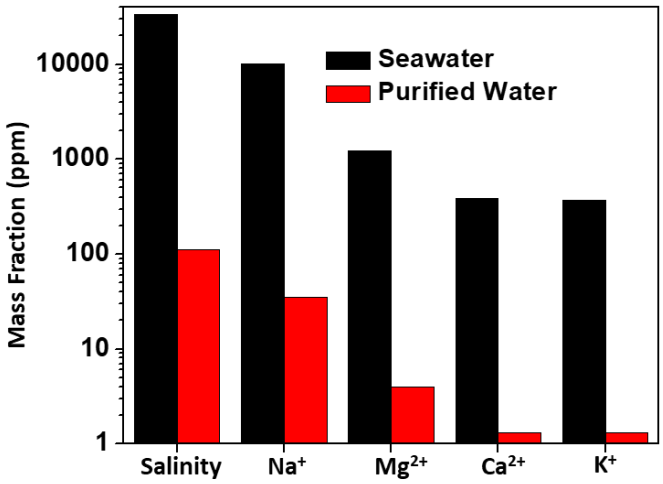

Figure 7-16. Salinity and specific ion concentrations in Pacific seawater and purified water from PHF.

7.5. Comparison between osmotic pumping and capillary pumping

Figure 7-17 compares the evaporative flux achieved by the PHF to that by other evaporators in literatures[12,13,278,280,281,287,289,293,306-322] using the capillary pumping effect under equivalent solar irradiation time. The evaporative flux was normalized by the solar flux for the convenience of comparison. The equivalent solar irradiation hour is defined as the multiplication of the concentration suns and time of test, e.g., in Ref.[316] the receiver was exposed to the 5 suns irradiation for 1 hour and thus the equivalent solar radiation time was defined as 5 hours. It is evident that the PHF yielded competitive evaporative flux to other evaporators. More importantly, it demonstrated a much longer continuous operational period than most of the previous evaporator, which makes it attractive in the real application. Although some studies showed higher flux than that of the PHF, they adopted the capillary wick for liquid pumping and did not demonstrate the continuous desalination, e.g., cyclic desalination with each evaporation period lasting 1- 2 hours and rinsing in between was demonstrated in Ref.[12,13,309,313,315,323]. Ni *et al.*[292] and Xu *et al.* [293]. demonstrated the stable evaporation on the daily-basis using salt-dissoluble foam and

Janus foam, respectively but the stability exceeding the 12 sun-hours was yet to be demonstrated. Without the self-dissoluble design, the foam was completely covered by salt sediments within 5 days[289]. Another advantage of the PHF is the cost-effectiveness because the chemicals and the activated carbon foam are inexpensive compared to the materials used for other studies, e.g., structured graphene[12,13,317,321], plasmonic nanoporous membrane[306,308] and so on, making it suitable for the large-scale production. In addition, due to the high liquid flux sustained by the PHF, it was able to maintain high energy efficiency even with a much thicker foam than that the CF, which was favorable for better salt-rejection.

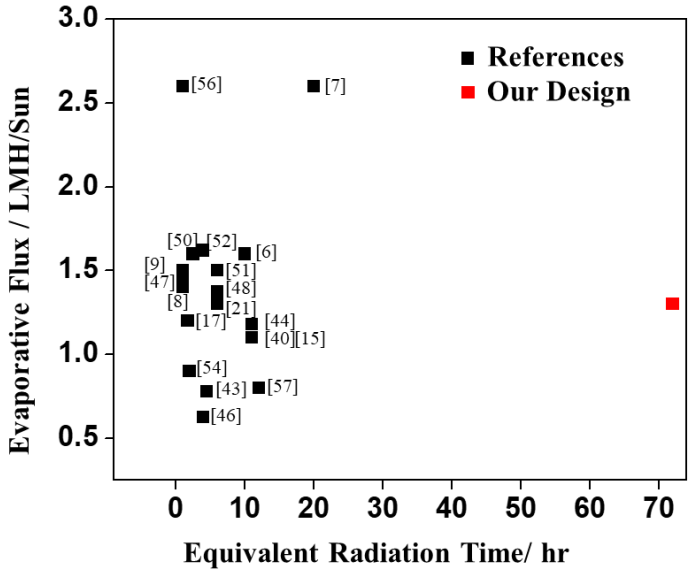

Figure 7-17. Comparison of evaporative flux and continuous operation time of PHF to other solar evaporators in literatures.

7.6. Conclusions

In this chapter, to provide simultaneously high flux and salt-rejection ability for chemical processing and separation, we proposed a new liquid pumping mechanism using the polyelectrolyte hydrogel which had high osmotic pressure for liquid pumping and

high ionic strength for salt-rejection. Different from the conventional capillary pumping effect, the ionic pumping effect tapped the water diffusion in the polymer network instead of viscous flow in the micropores, and thus it was not prone to the fouling for the porous wick. The ions were rejected at the solution/foam interface due to the strong ionic strength of polyelectrolyte. We successfully demonstrated the feasibility of ionic pumping for chemical separation in the solar-driven desalination test. The PHF using the ionic pumping effect always yielded higher evaporative flux than that of the CF using the capillary pumping effect both using the DI-water and brine water under different sun conditions due to the sufficient liquid supply and salt-rejection. For the first time, the continuous and stable solar-driven desalination with the operation period in 72 consecutive hours under 1 sun conditions was reported without cleaning or replacing the absorber, or equivalent to 12 hours under concentrated 6-suns condition. The high flux using the ionic pumping effect allowed us to use thicker foam to obtain better thermal insulation and foul-rejection without compromising the energy conversion coefficient. The successful application of ionic pumping effect in the solar-driven desalination showed its promise for miscellaneous chemical transport and separation processes where both high flux and good anti-fouling ability are required.

Chapter 7, in full, is a reprint of the materials as it appears in ‘Osmotic pumping and salt rejection by polyelectrolyte hydrogel for continuous solar desalination’ *Advanced Energy Materials*, 9(38), 2019 1900552 by Jian Zeng, Qingyang Wang, Yang Shi, Ping Liu and Renkun. . The dissertation author was the primary investigator and first author of this paper.

8. Chapter 8: Sorption-based water harvesting and thermal management

8.1. Introduction

The increasing power while miniaturizing design of power electronic devices, such as 5G antenna[324,325], electric-vehicle (EV) battery[326,327], wearable electronics[328], CPU/GPU[329], and photovoltaic (PV) panels[330,331], etc., places challenge on the high-performance thermal management. One of the challenges stems from the unsteady, fluctuating power of these electronics, for example, during on/off peaks hours for 5G devices and transient computing loads of a CPU/GPU. The unsteady heat loads require active control of power supply and cooling capacity[332,333]. Passive cooling methods, such as radiative cooling[334,335] and natural convection, failed to provide long-term and efficient cooling [heat transfer coefficient (HTC) of ~ 10 W m^{-2} K^{-1}) and their performances were highly contingent on the terrain and application scenario[336]. Active cooling techniques, such as forced convection by ventilating air and flowing liquid, provided high HTC ~ 10^3-10^4 W m^{-2} K^{-1} and critical heat flux ~ 100-1000 kW m^{-2} [337,338], but suffered from the bulky design, high energy consumption for coolant supply and flow instability. The key to suppress the temperature fluctuation is the adaptive thermal energy storage and release to mitigate the thermal mismatch between the on-/off-peak hours. Conventional phase change materials (PCMs), such as Paraffin wax, and salt hydrates,[339,340], have been widely used to buffer the temperature surge during the peak-hour by the solid-to-liquid phase change latent heat. The cooling potential was restored during the off-peak hour when the absorbed thermal energy was released to the ambient. However, the latent heat of traditional PCMs was only 50-200 J g^{-1}_{PCMs} (as opposed to ~ 2300 J g^{-1}_{water} for

evaporative latent heat of water) and thus their cooling power was limited. Besides, the PCMs needed to be sealed in an enclosure to avoid leakage, which exerted technical difficulty in many applications.

Water evaporative cooling utilized the high latent heat of water and thus provided high conductance, (~ 100 W m^{-2} K^{-1} [341]) and thermal energy density (> 200 kWh m^{-3} [342]). However, the difficulty in holding a thin water layer on the electronic surface, the risk of short-circuiting in water leakage, requirement of periodic liquid refill (or otherwise hermetic environment) and bulky design hindered its application in compact electronics. Recent advance on hygroscopic materials opens the possibility to explore the high latent heat of water while preserving the simple design. Several studies have been carried out on the sorption-based evaporative cooling where liquid-phase water was stored in the sorbent, such as hydrogel[328,330,331,341,343-350] and metallic-organic framework (MOF)[329,351] to avoid leakage. MOF absorbed moisture from air (~ 0.5 g_{water} $g^{-1}_{sorbent}$) at low temperature. Water stored in the sorbent evaporated under high heat flux for cooling and was regenerated during the off-peak hour for the long-term operation in the passive fashion. MOF was used for electronic cooling due to the high adsorption capacity[329,351], however, the high cost limits its large-scale application (124844 USD kg^{-1})[342]. Hydrogel simultaneously possess high adsorption capacity, low cost (e.g., ~ 10 USD kg^{-1} as shown in Table S3), and good mechanical strength[352,353]. Due to superior metrics of hydrogel, it has been used for cooling of battery[343,354], PV panel[330,349], building[341,344], thermo-galvanic cell[331] and wearable devices[328], but with active liquid-phase water refill. Recent progress on hydrogel-based water harvesting[14-18] showed that hydrogel absorbed 1-5 g_{water} $g^{-1}_{sorbent}$ (e.g., mixed with chloride-doped polypyrrole (PPy-Cl)[14,355], graphene[16] and Zn-O

network[296]) from air at relative humidity around 70-90%, showing their potential of passive liquid supply by absorbing moisture from air during the off-peak hour. It is of great interest to integrate high moisture storage in hydrogel and high evaporative conductance to make scalable passive cooling devices for high-power electronics.

In this study, we designed a hydrogel-based moisture thermal battery (MTB) for passive thermal management of electronics. The MTB was made by coating a thin polyelectrolyte hydrogel poly (sodium acrylate) [P(SA)] layer on the surface of an Al substrate with large effective surface area. This hydrogel has been used by the authors before for desalination[10,11]. The hydrogel layer captured and stored moisture from air during the off-peak hour and dissipated heat from the electronic by water evaporation during the peak-hour. The on-/off-peak fluctuation was mitigated via the synchronized thermal energy storage/release in MTB in pace with the on-/off-peak power of the electronics. While the thermodynamics of MTB (adsorption capacity) was determined by the intrinsic properties of hydrogel, the heat and mass transfer kinetics (thermal capacity and conductance) depended on the geometric design of the MTB at the meso- to macro-scale. The hydrogel thickness and surface area were carefully designed at the tradeoff between the HTC, thermal capacity and regeneration time. With ~ 100 μm thick hydrogel layer on ~ 760-fold extended effective surface area, we achieved high effective heat transfer coefficient (h_t) > 1000 W m^{-2} K^{-1}, cooling power (q_s) > 27 kW m^{-2} and thermal capacity (Q_s) > 200 kWh m^{-2}, which have not been achieved before by other passive cooling methods[328-331,341,343-345,347-351]. We first systematically analyzed the rational of MTB design and the effect of operational conditions on its performance. Later, as proof-of-concept demonstrations, we used the MTB for the thermal management of high-power

field-effect transistor (FET) and CPU and demonstrated the reduction in the electronic temperature by ~ 15 K and automatic regeneration in the long-term test. The achieved heat transfer coefficient and capacity met the daily cooling demand for 5G chips, power battery, server/data center and diode laser, etc., showing its general impact on residential and industrial cooling.

8.2. Sorption-based water harvesting from air using thermo-responsive hydrogel

Figure 8-1 shows schematics of water harvesting from air using thermo-responsive hydrogel based on sorption-water release process. As shown in Figure 8-1a, about 3% of the accessible freshwater on earth is trapped in the air, which is about 6 times higher than the total volume of freshwater storage in river[40]. However, compared to other resources, e.g., lakes and rivers, etc., it has been rarely developed to quench the worldwide thirst. As shown in Figure 8-1b, under the ambient temperature (T_a) of 22 ℃ and relative humidity (RH) of 85%, the moisture concentration in air is ~ 15 g m^{-3} [41], indicating that only a small space of 200 m^{-3} is needed to meet the daily need for human (~ 3 Liter). To explore the vast freshwater resources in air, we developed thermo-responsive hydrogel materials to harvesting moist from air based on sorption-desorption process. The hydrogel layer was synthesized by copolymerizing (N-isoproplyacrylamide, or NIPAm) in Poly (sodium-4-styrenesulfonate), or P(SSS) ionic liquid solution using ammonium persulfate (APS) as thermal initiator and N,N-Methylenebis(acrylamide) (MBAA) as crosslinker. As shown in Figure 8-1c, we developed a thermo-responsive P(SSS)-P(NIPAM) hydrogel to absorb water molecules from air at low temperature due to the high ionic strength of the hydrogel. The water molecules

are trapped in the polymeric network. It is noted that the hydrogel possesses the unique lower-critical temperature solution (LCST) phase transition, where when heated up above the LCST temperature (~ 35 ℃), water entrapped in the hydrogel will be released as liquid phase. Different from the conventional desorption process from sorbent where the high evaporative latent heat penalty is introduced, the LCST phase change is rid of the high latent heat penalty, and thus it is more energy-efficient (energy consumption < 1/10 of evaporative latent heat of water [10]) and the water release kinetic is much faster with the time constant of ~ 5 min. It is hypothesized that based on the fast adsorption-LCST release cycles, high water yield could be obtained with low energy consumption.

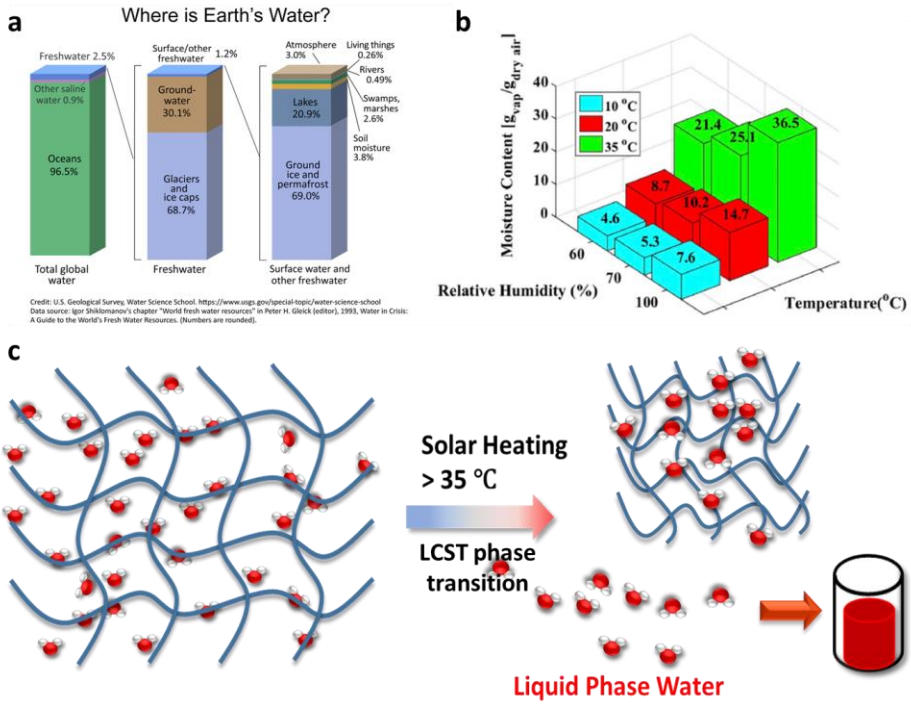

Figure 8-1. Schematics of adsorption-desorption based water harvesting from air using thermo-responsive hydrogel materials. (a) Water resource distribution on earth, cited from Ref. [40]. (b) Moisture content in air under different ambient conditions, cited from Ref. [41]. (c) Schematics of water harvesting using thermo-resposnive hydrogel by adsorption-LCST phase change process.

The freshwater yield not only depends on the thermodynamic (intrinsic properties of material) but also the kinetics, which is contingent on the scale-design of the hydrogel. As shown in Figure 8-2a, we test the adsorption kinetics of a 2 mm thick hydrogel under the condition of T_a = 22 ℃ and RH = 85%. It is obvious that the adsorption process is diffusion-driven. It can be well described by the diffusion theory at a constant concentration at the boundary:

$$\frac{\partial C}{\partial t} = D\frac{\partial^2 C}{\partial x^2} \tag{8-1}$$
$$C_{x=0,t>0} = C_0$$
$$C_{t=0} = 0$$
$$\frac{\partial C}{\partial x}|_{x=\delta} = 0$$

where C_o is the moisture concentration in the air. x is the coordinate in the thickness direction of hydrogel where $x = 0$ indicates the surface of hydrogel and $x = \delta$ indicates the center of hydrogel. Solving the above equation leads to:

$$\ln\left(1 - \frac{\Delta \mathrm{M}(t)}{\Delta M_\infty}\right) = \ln\frac{8}{\pi^2} - D\frac{\pi^2}{4\delta^2}t \tag{8-2}$$

where $\Delta \mathrm{M}(t)$ is the mass of adsorbed water by the hydrogel at a specific time and ΔM_∞ is the max amount of water adsorbed by the hydrogel. Notably, the adsorption time constant t_c scales as $t_c \sim \delta^2$, indicating that the adsorption kinetics could be significantly enhanced with reduced hydrogel thickness. Figure 8-2c shows the time constant experimentally determined for hydrogel layer with different thickness. It is seen that t_c decreases from 280 min for 2.8 mm thick hydrogel from ~ 10 min for 100 μm thick hydrogel. Therefore, to achieve high kinetics, we coat thin hydrogel layer on a porous scaffold with high

surface area. By doing so, a number of cycles can be done to obtain high water yield on daily basis.

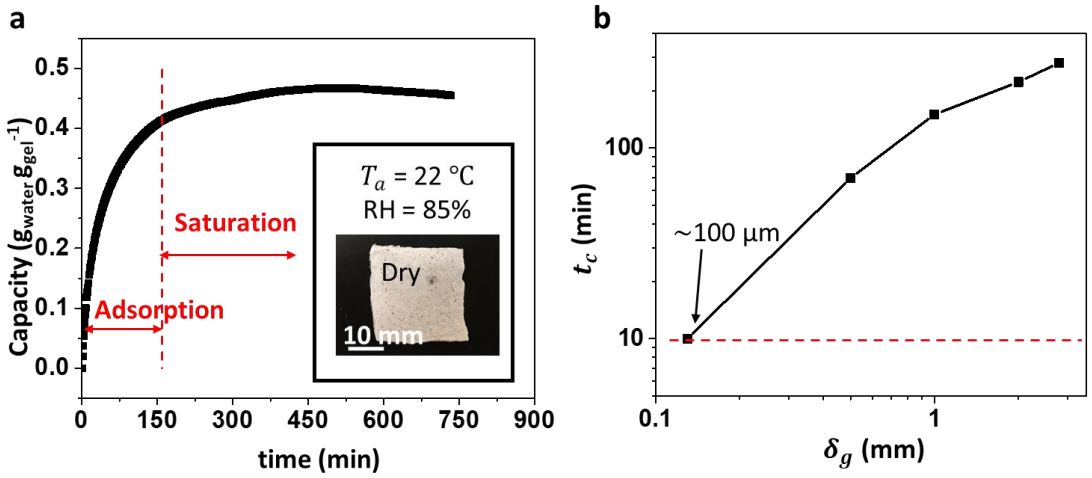

Figure 8-2. Adsorption kinetics of P(SSS)-P(NIPAMm) with the thickness of 2 mm under the condition of T_a = 22 ℃ and RH = 85%. (a) Adsorption capacity as a function of time. (b) Adsorption time constant (t_c) as a function of hydrogel thickness.

Figure 8-3a shows the photo of porous Al foam coated with 100 µm thick P(SSS)-P(NIPAMm) hydrogel layer on the surface scaffold. The porous Al foam provides 6-7 times extend surface area compared to the projection area. Figure 83-b shows the synthesis process of the hydrogel coated foam. The monomer solution was prepared as follows: 1.9 g of NIPAM was mixed with 0.2334 g sodium alginate (Alg) in 15 ml 30 wt.% PSSS solution and 13.9 ml of DI water. 0.075 g and MBAA and 0.075 g of APS were added and fully dissolved in the above solution. The amount of Alg should be well controlled to adjust the viscosity of monomer solution so that a thin solution adhered to the surface of scaffold after dip-coating. As shown in Figure 8-3b, the porous Al foam was immersed in the viscous monomer solution for 10 min, and was then placed on a spinning machine to remove the excessive solution. Subsequently, the foam was placed in an oven at 70 ℃ for 20 min for copolymerization and was kept at the ambient

temperature overnight for full reaction. As a result, we coat a 100 μm thick hydrogel layer on the surface of Al scaffold.

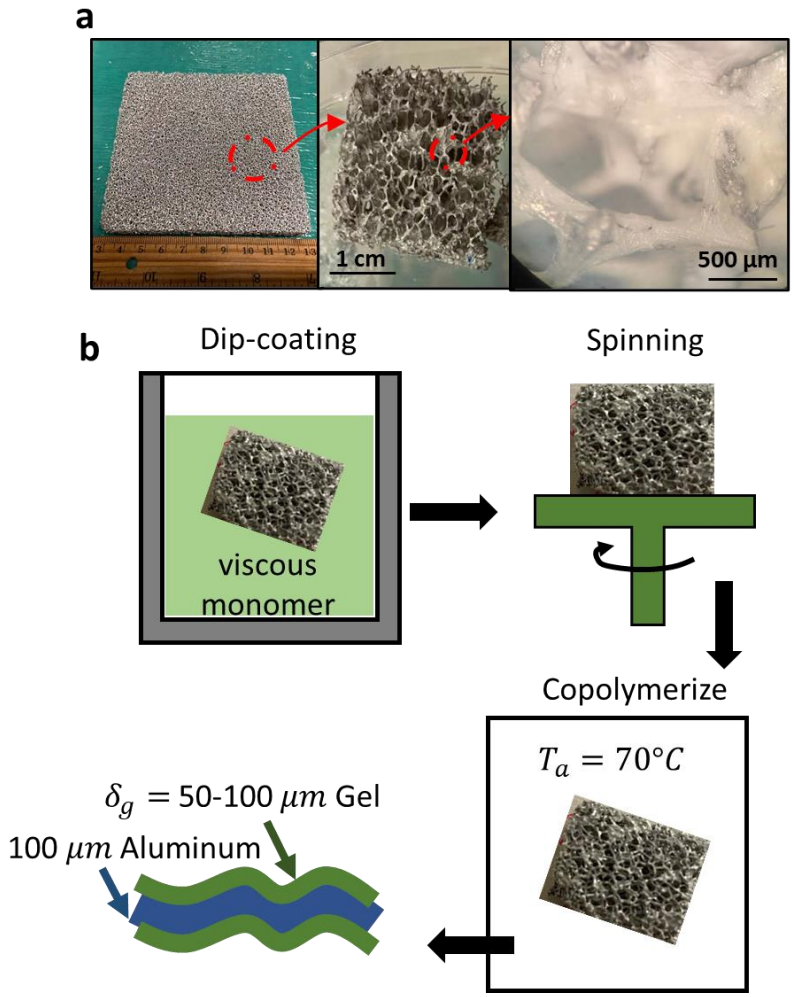

Figure 8-3. Porous Al foam coated with thin hydrogel layer. (a) Photo of the porous foam. (b) Schematics of synthesis procedures.

Figure 8-4 demonstrates water harvesting from air using the hydrogel-coated Al foam. As shown in Figure 8-4a, the foam was kept at T_a = 22 ℃ and RH = 85% for 10 min to adsorb moisture from air. Due to the small thickness of the hydrogel layer, the time constant is ~ 10 min as shown in Figure 8-2, and thus the hydrogel layer reached the adsorption capacity fast. Afterwards, the foam was heated up to 70 ℃ for 1.5 min to trigger the LCST phase transition when the adsorbed water molecules were released in

the liquid phase. It is noted that due to the low LCST temperature (~ 35 ℃), the LCST initiation is subject to the universal low grade heat source, e.g., solar energy and waste heat from industry, making a potentially energy-efficient water harvesting process. Figure 8-4b shows the cyclic adsorption-release process for 120 min, with t_r = 10 min and t_h = 1.5 min. The mass change of the foam was recorded, which was solely due to the mass change of water. Therefore, the cumulative water harvesting capacity could be obtained from the difference between the peak and valley. The water yield in 120 min is ~ 2.7 g_{water} g^{-1}_{gel}, which is projected to ~ 34 g_{water} g^{-1}_{gel} day^{-1}, or ~ 12-liter m^{-2} day^{-1} based on the projection area of the foam, both of which are higher than the state-of-the-art water harvesting capacity based on adsorption process[14,15,18,296,356-366].

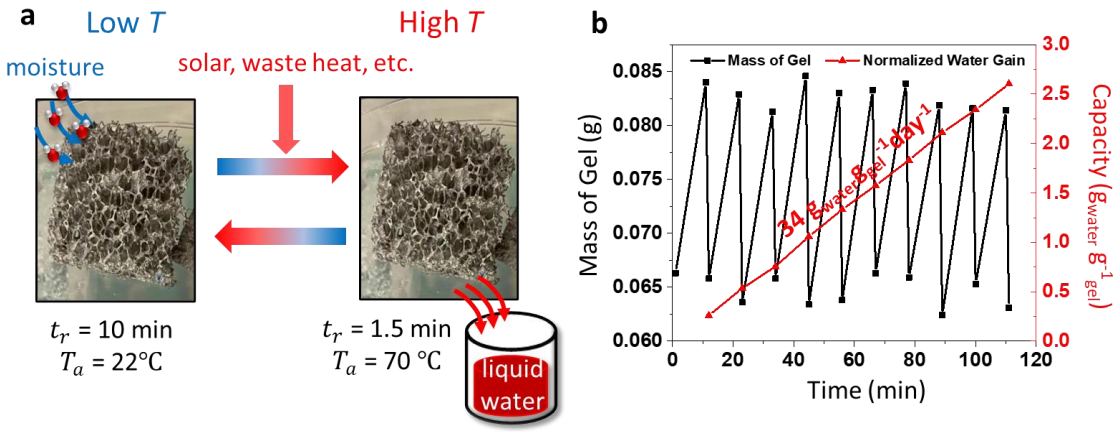

Figure 8-4. Water harvesting using hydrogel-coated Al foam. (a) Schematics of adsorption-LCST water release cycle. (b) Water yield from fast cycles.

8.3. Thermal management using hydrogel-based moisture thermal battery

8.3.1. Working principle of moisture thermal battery

Figure 8-5A shows the typical normalized operation power of data center[333] and cell tower[367] within a day. Due to the swinging dataflow between the daytime and nighttime, the operation power is high in the day and low at night, leading to the fluctuating temperature of the electronics. The key to suppress the temperature fluctuation is to store the thermal energy in the peak-hour and release it during the off-peak hour. This can be realized using a moisture thermal battery (MTB) as shown in Figure 8-5B. The hygroscopic sorbent inside the MTB stores liquid water by absorbing water moisture from air during the off-peak hour. The water stored in the MTB evaporates during the peak-hour and dissipates a large amount of heat from the electronics by the evaporation latent heat of water. Figure 8-5C shows the design of the MTB by coating a thin P(SA) hydrogel layer on the pin surface of a solid Al pin-fin heat sink (named as solid heat sink for convenience) to provide large effective surface area. The hydrogel layer absorbs and stores moisture from air in the off-peak hour. The hydrogel layer is 0.5-1 mm thick, and the fin geometry is as follow: fin length (L) is 45 mm, fin diameter (D) is 3.4 mm, and fin pitch (P_f) is 6.4 mm with the base diameter of 78 mm. The hydrogel thickness and geometry of the solid heat sink were carefully designed to ensure high water adsorption capacity and h_t of the MTB, which will be discussed in the next section. The hydrogel layer was coated on the surface of Al heat sink by dip-coating method (Figure 8-6). Before dip-coating, to ensure the good adhesive strength between the gel coating and pin surface, the surface of Al heat sink was sand blasted to increase the surface roughness (Figure 8-7A) and was treated with functional

silane solution (3-(trimethoxysilyl) propyl methacrylate) to form a strong covalent bond[352] (Figure 8-6C).

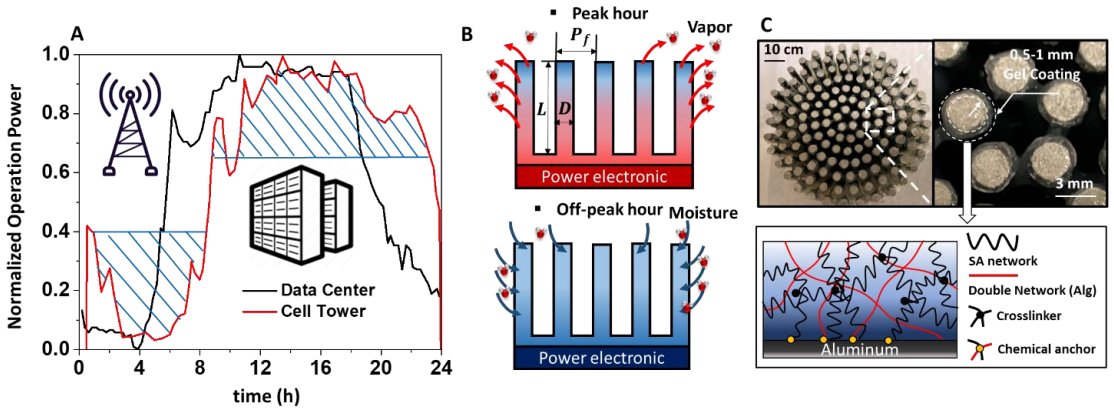

Figure 8-5. Working principle of moisture thermal battery (MTB) to mitigate on-/off-peak temperature fluctuation of electronics. (A) Typical normalized operation power of data center[333] and cell tower[367] in a day. The power fluctuates due to the swinging dataflow between the on-peak (daytime) and off-peak hours (nighttime) (Ref. Wang *et al.*[333] Copyright, 2018, IEEE and Ghatikar *et al.* [367], 2008, California Energy Comission). (B) Mitigation of thermal mismatch between on-/-off peak hours by an MTB. The MTB synchronizes the thermal energy storage/release with the on-/off-peak power, via moisture adsorption/vapor evaporation by the hygroscopic polyelectrolyte hydrogel layer on the extended surface of an Al heat sink. The MTB cools the electronic devices by evaporation of water stored in the hydrogel layer during the peak hour and regenerates during the off-peak hour by moisture adsorption. (C) Photography of the MTB consisting of a solid Al heat sink coated with a thin hydrogel layer. Pin-fin heat sink with length L = 45 mm, pin-diameter D = 3.4 mm, pitch P_f = 6.4 mm and a base diameter of 78 mm is coated with 0.5-1 mm thick D_g Poly (sodium acrylate) [P(SA)] hydrogel on the extended Al pin-fin surface. The surface is functionalized with silane to form covalent bonds with the hydrogel layer [352]. The double network of sodium alginate (Alg) increases the bulk mechanical strength of hydrogel.

The viscosity of monomer solution was adjusted by adding suitable amount of sodium alginate (Alg) so that a thin monomer solution layer adhered on the pin surface after dip coating. After dip-coating, the solid heat sink was placed in an oven at 80 °C for 30 mins for copolymerization of hydrogel and kept in the ambient overnight for full reaction. The thickness of the gel coating could be controlled by the viscosity of monomer solution and the number of dip-coating process. Increasing the Alg concentration in the monomer solution increased the viscosity (Figure 8-7 and Table 8-1).

In addition, as shown in Figure 8-5C, the toughness of the hydrogel layer was enhanced by the Alg double network[341].

8.3.2. Experimental method

Surface Treatment of Heat Sink

Pin heat sink was purchased from Newark Inc., (PINLED-7850, 2.33℃/W). The heat sink with embedded heat-pipe (HSHP) was purchased from DEEPCOOL, Inc., (GAMMAXX400). The surfaces of both heat sinks were sand blasted by silica bead (100-300 μm in diameter) to increase the surface roughness for better adhesion between the fin surface and gel coating (Figure 8-6A). The surface of pin-heat sink was originally coating with black coating for radiative cooling which was removed after the sandblasting (Figure 8-6A). Without sand-blasting treatment, the monomer solution could not adhere to the surface of heat sink even for the most viscous solution (Figure 8-7C). The monomer solution adhered well to the sand-blasted surface (Figure 8-7D). The sand blasted heat sinks were sequentially cleaned by acetone, ethanol and DI water, and was completely dried. Subsequently, they were immersed in a functionalization silane solution for 3 h at room temperature for strong chemical bonding between the polymer chain and metal surface[352] (Figure 8-6B). The silane solution was prepared by mixing 2 g of 3-(trimethoxysilyl) propyl methacrylate (TMSPMA; Sigma-Aldrich 440159) and 20 μL of acetic acid (Sigma-Aldrich 27225) with 98 g DI water under stirring for 30 mins. The functionalized heat sink was washed with ethanol and DI-water, and completely dried before it was ready for coating the hydrogels. After treating the Al surface by the functional silane solution, the hydrogel layer was crosslinked to the silane layer, which

was chemically bonded to the oxide layer on the Al surface by co-valent bonding, providing strong mechanical strength (Figure 8-6E).

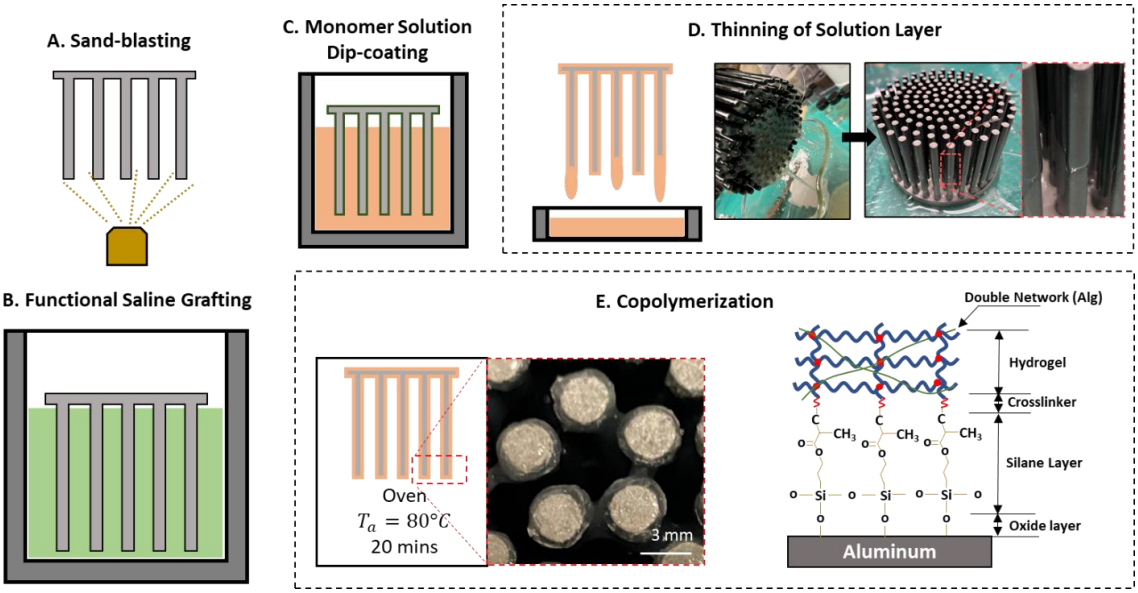

Figure 8-6. Schematics of hydrogel coating on heat sink surface. Solid heat sink is sand blasted with silica bead to increase the surface roughness (step A). It is then treated with function saline solution to create the silane layer for strong bonding between hydrogel layer and Al surface (step B). Functionalized heat sink is subsequently immersed in the monomer solution with proper viscosity (C). The excessive monomer solution was removed by hanging the hydrogel in the ambient for 5 mins. A thin monomer solution layer attached on the metal surface (step D). The heat sink with monomer solution layer was kept in the oven at 80℃ for 20 mins to initiate copolymerization and at the ambient temperature overnight for full reaction (step E). After treating the Al surface by the functional silane solution, the hydrogel layer was crosslinked to the silane layer, which was chemically bonded to the oxide layer on the Al surface by co-valent bonding.

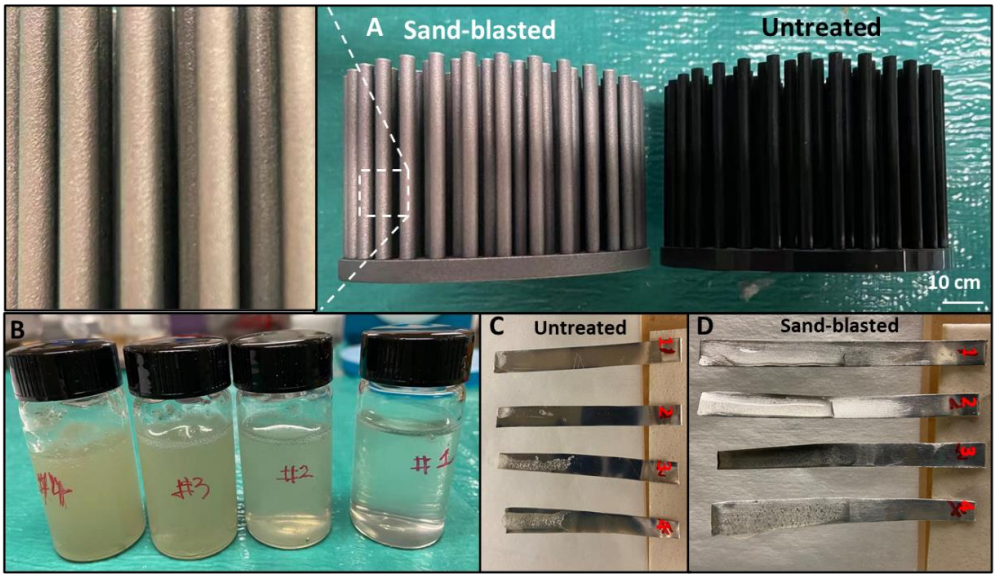

Figure 8-7. Surface treatment of solid heat sink and adjustment of solution viscosity. (A) Photo of sand-blasted (left) and un-treated heat sink (right). After sand blasting, the black coating was removed, and the surface was roughened (zoom-in figure). (B) Photo of monomer solution with different viscosity controlled by the amount of Alg. (C) Photo of adhesion of monomer solution on the smooth, untreated Al surface. (D) Photo of adhesion of monomer solution on sand-blasted, rough Al surface.

Dip-coating of Hydrogel Layer on Heat Sink Surface

The functionalized heat sink was immersed in a monomer solution to coat the hydrogel layers. The solution was prepared with the following procedure. 4.4 g of sodium alginate (Alg, Sigma-Aldrich W201502) was fully dissolved in 60 g DI water as solution A. 11.6 g of Sodium acrylate (SA, Sigma-Aldrich 408220) was dissolved in 35 g DI water as solution B. Solutions A and B were sufficiently mixed to form solution C. Alg and SA were separately dissolved due to the high viscosity of Alg solution. The viscosity of solution C could be further adjusted if needed by adding suitable amount of Alg (to increase viscosity) or DI water (to decrease viscosity). The Alg was also hygroscopic per se and it created a double-network structure to enhance the toughness of the hydrogel[341]. 0.4 g of *N*, *N*-methylenebisacrylamide (MBAA, Sigma-Aldrich 346136) as crosslinker and 0.4 g of ammonium persulphate (APS, Sigma-Aldrich A3678) as thermal initiator

were dissolved in solution C to form the monomer solution. The heat sink was immersed in the monomer solution for 2 min (Figure 8-6C). Subsequently, it was taken out slowly and hung at the ambient environment for 5 mins until the thickness of the monomer solution on the pin surface stabilized (Figure 8-6D). It was then kept in an oven at 80℃ for 20 mins to initiate the copolymerization and then placed at ambient temperature overnight for full reaction (Figure 8-6E). The thickness of hydrogel coating was controlled by the viscosity of the monomer solution, the surface roughness of the surface and the number of dip-coating process. We tried four different viscosities by adding different amount of Alg from 1.6 wt.% to 7.7 wt.% (Table 8-1 and Figure 8-7B). The viscosity increased with increasing Alg concentration. We found that if the solution was dilute (Sample #1 in Table 8-1), the monomer solution cannot attach on the surface. On the contrary, the hydrogel coating may be too thick with high viscosity (Sample #4 in Table 8-1). Moreover, hydrogel may not be copolymerized if the viscosity is too high. Therefore, a suitable viscosity should be selected. Based on the current surface treatment and viscosity of monomer solution (i.e., 5.8 wt.% Alg), the hydrogel coating thickness was 0.5-1 mm. The facile dip-coating method and inexpensive raw chemicals make this method suitable for large-scale production, e.g., the chemicals cost < 2 USD for the MTB (Table 8-2).

Table 8-1. Composition of monomer solution with different viscosity

Sample	Alg (g)	SA (g)	DI water
#1	0.3	2.9	15
#2	0.7	2.9	15
#3	1.1	2.9	15
#4	1.5	2.9	15

Table 8-2. Cost breakdown of MTB

Materials	Unit Price	Amount	Total Price (USD)
Sodium Acrylate	1 USD kg^{-1} [368]	46.4 g	0.046
Sodium Alginate	2 USD kg^{-1} [369]	17.6 g	0.035
MBAA	10 USD kg^{-1} [370]	1.6 g	0.016
APS	50 USD kg^{-1} [371]	1.6 g	0.8
Silane	50 USD kg^{-1} [372]	20 g	1
Al Heat Sink with Heat Pipes	10-30 USD [373-376]	1	10-30
Total			12-32

Measurement of Adsorption Kinetics and Capacity

The adsorption kinetic of P(SA) hydrogel was measured. The P(SA) hydrogel with well controlled geometries was prepared by pouring the monomer solutions into a mold. The P(SA) hydrogel was frozen in a refrigerator for 8 h and freeze-dried in a freeze-drier (Labconco Inc. LA-6LS) overnight. The dry hydrogel was cut into pieces of ~ 2×2 cm^2 in size (Figure 8-8A). The thickness of hydrogel was controlled by the volume of monomer solution in the mold and varied between 0.1 mm to 2.8 mm to study the effect of hydrogel thickness on the adsorption kinetics. The SEM image of freeze-dried P(SA) hydrogel is displayed in Figure 8-8B. The dry hydrogel was porous after freeze-drying. The dry hydrogel samples were placed in the humidity chamber (Linpin, Co., Ltd, LRHS-100) at a fixed humidity (RH = 20-90%) and temperature (T_a = 22 ℃) under natural convection (Figure 8-8C and 8-8D). The temporal mass change of the hydrogel was measured by using a balance, and the adsorption capacity R_m was calculated by the following equation.

$$R_m = \frac{m_t - m_0}{m_0} \tag{8-3}$$

where m_0 is the mass of dry gel before test and m_t is the instant mass of hydrogel including the dry gel and absorbed moisture, i.e., the R_m is evaluated by the mass of absorbed water per unit mass of dry hydrogel. Photo of the misted hydrogel is shown in Figure 8-7A.

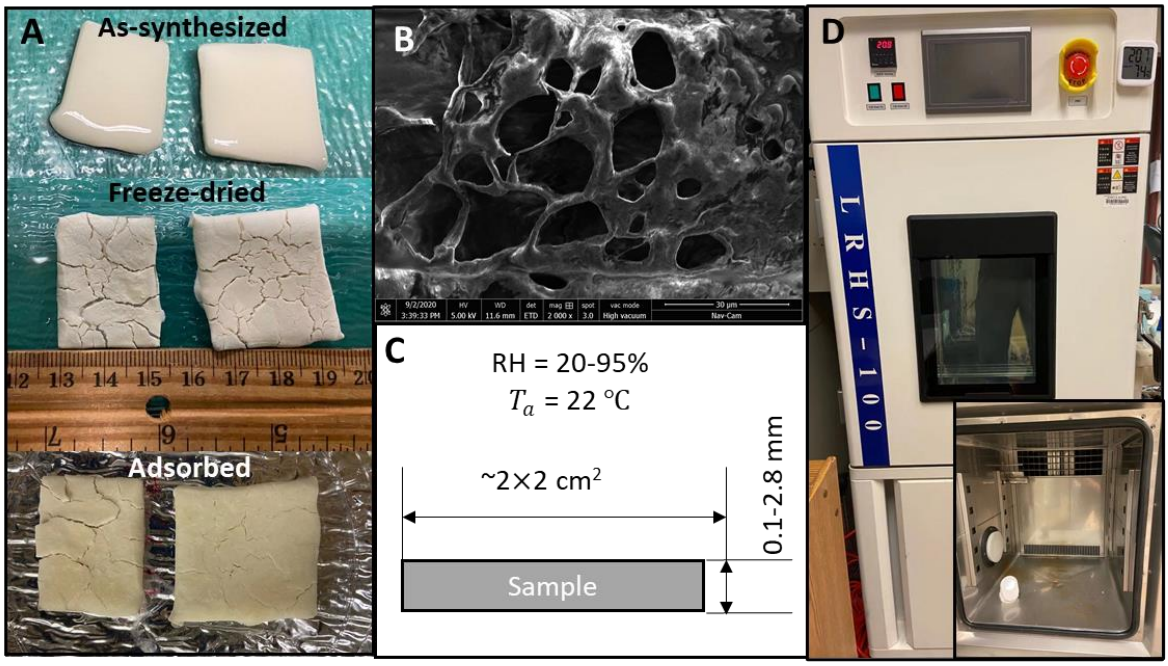

Figure 8-8. Samples and experimental setup for adsorption kinetic and capacity measurement. (A) Photo of 1 mm thick P(SA) hydrogel at different status, i.e., as synthesized (top), after freeze-drying (middle) and after the moisture adsorption test (bottom). (B) SEM image of freeze-dried hydrogel. (C) Schematic of the adsorption test. (D) Humidity chamber for adsorption test.

Temperature Rise Measurement

Temperature rise of MTB and solid heat sink was measured using a home-built setup. A constant heat flux q_s was supplied from the Al heating block at the bottom, powered by the cartridge heaters connected to a DC power supply. The heating block has the same size of the base area of the solid heat sink (i.e., 7.8 cm in diameter) and was wrapped with insulation foam to avoid heat loss. Thermal grease (Halnziye HY400) was applied at the interface between the heat sink and heating block to minimize the thermal

resistance. To ensure good contact between the heat sink and heater block, pressure was applied by a tie. Two K-type thermocouples were attached at the base of the heater sink to monitor the base temperature (T_b) and the average temperature was used, and another K-type thermocouple was attached on the tip of the fin to monitor the fin-tip temperature T_u. T_b and T_u were recorded by a data acquisition instrument (DAQ, Agilent 34970A). T_b was used to calculate the effective thermal conductance of the heat sink h_t based on Equation 2. In the meantime, the mass loss from the heat sink was also measured with a balance with a resolution 0.001 g to estimate the heat dissipated by evaporative latent heat. The setup was kept in the ambient environment at T_a = 22 ℃ and RH = 60%. For the forced convection condition, a circulation fan was placed 2 meters in front of the heat sink with controllable power and the air speed was monitored by an anemometer (BTMETER BT-100) in front of the MTB/solid heat sink. The anemometer was removed after measuring the air speed. The flow velocity was controlled to be ~ 1.5 m s^{-1} for the forced convection test. For natural convection condition, the fan was turned off and thus v = 0 m s^{-1}.

Before the test, the MTB was placed in the humidity chamber at T_a = 22 ℃ and RH = 85% overnight to absorb moisture. Under these conditions, the hydrogel absorbed ~ 0.9 g_{water} g^{-1}_{gel}. To demonstrate the effect of initial water loading on h_t and Q_t of MTB, we varied the initial loading from 0.9 to 4.3 g_{water} g^{-1}_{gel}. Due to the limitation of adsorption capacity of P(SA), for initial loading > 0.9 g_{water} g^{-1}_{gel}, liquid-phase water was supplied to the hydrogel layer by airbrush.

Regeneration Test of MTB

The cyclic measurement was done in the humidity chamber at T_a = 22 ℃ and RH = 85% under natural convection. The hydrogel layer was regenerated by moisture adsorption from ambient to demonstrate the autonomous operation of the MTB. The same setup for MTB cooling test was placed in the humidity chamber shown in Figure 8-8D. Before the test, the MTB was completely dried in an oven at 80 ℃ overnight to remove all the absorbed water and then placed in the humidity chamber for a specific regeneration time t_r varied from 36 min to 12 h for moisture adsorption. Subsequently, a constant heat flux q_s of 1 kW m^{-2} was applied from the bottom of the MTB for a fixed heating time (t_h) of 3 h, followed by the next regeneration period lasting for t_r. Such procedures were repeated for at least five cycles. Mass change of the MTB during the cyclic test with $t_h = 3$ h and $t_r = 12$ h was also measured to reflect the water evaporation/adsorption process. The corresponding water capacity was evaluated based on the dry mass of hydrogel coated on the MTB.

Proof-of-Concept Demonstration

A 100 W rated FET (STPS41H100CG) with base area of 2 cm × 1 cm was connected on an electronic load board (MakerHawk, 26111700) and its operating power was monitored by the board as shown in Figure 8-9B. The operating power of FET was ~ 85% of the total input power into the electronic load and was dissipated as heat. Therefore, q_s could be obtained based on the FET power and based area of FET. In this test, the MTB was made on a heat sink with four embedded heat pipes. The base area of the heat sink was 35 mm × 35 mm, which was used to calculate the heat flux q_s. Figure 8-9A shows the details of the HSHP. The outer dimension of HSHP is 135 mm × 80 mm ×

155 mm. There are 46 stacked fins separated at the pitch of 3 mm. The thickness of fin is 1 mm. 36 out of the 46 fins have the dimension of 135 mm × 8 mm and while the remaining 10 fins have the dimension of 100 mm × 8 mm, which in total enhance an effective surface area by ~ 760-fold compared to the base area. The surface of the fin was coated with P(SA) hydrogel layer, following the same dip-coating procedure for the pin-fin heat sink. The MTB was placed on top of the FET with thermal grease at the interface. The test setup was placed under the ambient environment of T_a = 22 °C, RH = 70% and natural convection throughout the experiments.

An 80-W rated CPU (Intel i5-4570 of 37.5 mm × 37.5 mm in area) was installed on a workstation. Its operating power and core temperature (T_{core}) were monitored by embedded diagnostic power meter and thermometer. The same HSHP-based MTB for the FET test was used. q_s was calculated based on the CPU area. The workstation was placed under the ambient environment of T_a = 22 °C, RH = 70% and natural convection throughout the experiments. In the transient test, the operation power of the CPU was controlled by a stress test program in a benchmark software 3DMark and fluctuated from 0 – 50 W, i.e., q_s = 0 - 41 kW m^{-2} based on the base area of the MTB. To demonstrate the passive regeneration, we run a numeric simulation program , discrete element modeling using LIGGGHTS [173], on the computer for 48 h.

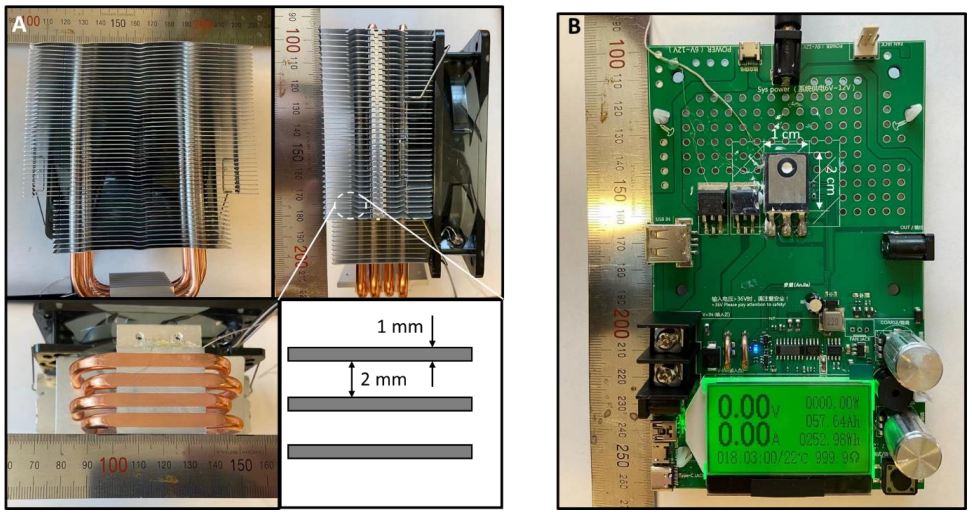

Figure 8-9. Photo and schematics of the HSHP and FET. (A) Details of the HSHP (B) electronic load board for FET.

8.3.3. Results and discussions

Design of Moisture Thermal Battery

While the moisture adsorption capacity depends on the intrinsic properties of the absorbent, the heat and mass transfer kinetics are determined by the meso- to macro-scale geometry of the MTB. As shown in **Figure 8-10A**, the surface of the fin (with diameter (D) of 3.4 mm, length (L) of 4.5 cm and separated at the pitch (P_f) of 6.4 mm) was coated with thin P(SA) polyelectrolyte hydrogel with the thickness of D_g. To maximize the fin efficiency, the fin geometry and hydrogel coating thickness should be well configurated. The temperature distribution along the fin can be modelled considering both the heat condition along the fin, and convective and evaporative heat losses from the external surface (derivation in **Appendix I**), and the final solution is given as follows:

$$T(x) = \frac{q_t}{k_s\sqrt{A}}\left(\frac{\cosh(\sqrt{A}x)}{\tanh(\sqrt{A}L)} - \sinh(\sqrt{A}x)\right) - \frac{B}{A} \tag{8-4}$$

where $A = \frac{h_c P + a\Delta H_{fg} P}{k_s A_c}$ and $B = \frac{\Delta H_{fg} Pb - h_c P T_a}{k_s A_c}$. k_s is the solid thermal conductivity of Al heat sink (~ 100 W m^{-1} K^{-1}); A_c, P and L are the cross-sectional area, perimeter and

length of the fin, respectively; q_t is the heat flux evaluated based on the cross-section area of fin and is related to the heat flux based on the base area (q_s) by $q_t = q_s(\frac{4P_f^2}{\pi D^2})$. T_a is the ambient temperature set at 22 ℃ and ΔH_{fg} is the evaporative latent heat of water (~ 2300 kJ kg^{-1}). $\dot{m}$ is the local evaporative mass flux and is a non-linear function of the local temperature [$T(x)$] and ambient relative humidity (RH) (Equation S2 Appendix I). To simplify the model, the mass flux can be linearized as a function of temperature, i.e., $\dot{m}(x) = aT(x) + b$ at a fixed RH within a certain temperature range (**Figure 8-11**). Within a small temperature range (< 50 K) and at a fixed RH, the mass flux estimated by the linearized function is close to that given by the non-linear function with the error less than 5%. The constants a and b have the units of kg m^{-2} s^{-1} K^{-1} and kg m^{-2} s^{-1}, respectively. h_c is the convective HTC of the external surface. It is evaluated separately for natural convection (Equation S10 Appendix I) and forced convection (Equation S11 Appendix I). $T(x)$ was obtained by iteration until $T(x)$, $\dot{m}$ and h_c converged and $T(x)$ was within the temperature range assumed for linearization of $\dot{m}$. For comparison, we also modelled and tested the solid heat sink with the same geometry of the MTB without the hydrogel layer. The same model could be used for the solid heat sink except that $\Delta H_{fg} = 0$ was set in the model. The base temperature (T_b) of MTB can be obtained at $T(x = 0)$. To validate our model, T_b was also estimated based on the energy balance and fin efficiency at the characteristic temperature $T_c = \frac{T_a + T_b}{2}$ (Equation S17 Appendix I). The maximum discrepancy of T_b estimated from the two models is only ~ 5%. It is noted that at this point, The thermal conductance of the hydrogel layer (G_g) layer is ignored but will be considered later.

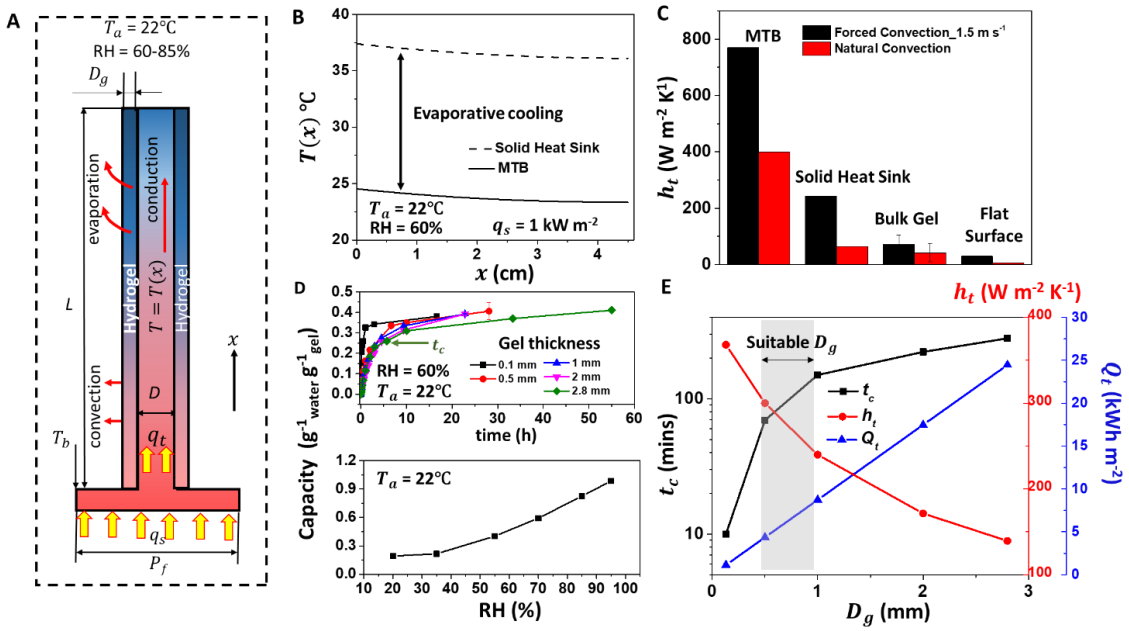

Figure 8-10. Rational of Geometric design of moisture thermal battery. (A) Heat transfer model of MTB based on Al solid heat sink coated with thin hydrogel coating. The same heat sink shown in Figure 8-5 is used. Heat conduction along the pin (*x*-direction), convection heat loss, and evaporative cooling on the external surface are considered. Heat flux is applied to the base and evaluated based on the base area $A_b = P_f^2$. The ambient temperature T_a is set at 22 ℃ while the relative humidity varies from 60% to 85%. HTC is evaluated based on T_b for natural convection and $T_c = \frac{T_a+T_b}{2}$ for forced convection. The evaporative flux is evaluated based on the local temperature $T(x)$, and specific T_a and RH. Detailed derivation of equations can be found in supplementary information section S3.1. (B) Modelled cooling performance of MTB and solid heat sink at T_a = 22 ℃, RH = 60% and q_s = 1 kW m^{-2} under natural convection. The fin temperature $T(x)$ is plotted as a function of distance away from the base where $T(x = 0)$ is the base temperature of the fin (T_b) as shown in Figure 8-10A. (C) Modelled effective heat transfer coefficient h_t of MTB in comparison to other heat sinks under both natural and forced convection at the airspeed of v = 1.5 m s^{-1}. Solid heat sink indicates the same Al heat sink shown in Figure 8-5C without gel coating, bulk gel indicates a flat P(SA) hydrogel with the thickness of ~ 1 mm on a flat surface, and the flat surface indicates a solid Al plate without extended surface. (D) Measured moisture adsorption kinetics and capacity of P(SA) hydrogel at T_a = 22 ℃ under natural convection in a humidity chamber. Upper row: effect of gel thickness on adsorption kinetics tested at RH = 60%. The adsorption time constant (t_c) is determined by fitting the curves with $c(t) = c_0(1 - e^{-t/t_c})$ where c_0 is the adsorption capacity. Lower row: the adsorption capacity of P(SA) hydrogel at different RH, measured as the mass of adsorbed moisture normalized by the mass of the gel. (E) Design of hydrogel layer thickness D_g showing the tradeoff between thermal capacity (Q_t), effective HTC (h_t) and regeneration time constant t_c.

Figure 8-10B compares the modelled $T(x)$ of MTB and solid heat sink at T_a = 22 ℃, RH = 60% and q_s = 1000 kW m^{-2} under natural convection. We find that the temperature can be reduced by ~ 13 K via the evaporative cooling of the MTB. Figure 2C compares the modelled effective heat transfer coefficient (h_t) of MTB, calculated based on:

$$h_t = \frac{q_s}{T_b - T_a} \tag{8-5}$$

h_t of the MTB ($h_{t,MTB}$) is calculated to be ~ 400 W m^{-2} K^{-1} under natural convection and ~ 770 W m^{-2} K^{-1} under forced convection condition (air speed v = 1.5 m s^{-1}, typical for a CPU fan) due to high evaporative HTC. On the other hand, h_t of the corresponding solid heat sink ($h_{t,solid}$) is only ~ 65 and ~ 240 W m^{-2} K^{-1} under natural and forced convection conditions, respectively. Since the evaporative and convective HTC are in-parallel, the evaporative HTC (h_{ev}) of MTB can be obtained from the difference of h_t between the MTB and the solid heat sink, i.e., $h_{ev,MTB} = h_{t,MTB} - h_{t,solid}$. $h_{ev,MTB}$ is calculated to be ~ 335 and ~527 W m^{-2} K^{-1} under natural and forced convection conditions, respectively. It is obvious that the HTC depends on the effective surface area of the fin. When evaluated based on the effective surface area of fin, i.e., $A_{fin} = PL$ (~ 10-fold increase compared to base area), h_{ev} is ~ 33.5 W m^{-2} K^{-1} under natural convection and ~ 52.7 W m^{-2} K^{-1} under forced convection, which are similar to the measured h_{ev} values for a flat bulk gel layer under the same conditions as shown in Figure 8-10C (42.1 W m^{-2} K^{-1} and 72.1 W m^{-2} K^{-1} for natural and forced convections, respectively). As a comparison, the HTC of a flat solid surface (without gel), i.e., h_c, is measured to be ~ 5 and ~ 18.5 W m^{-2} K^{-1} under natural and forced convection conditions, respectively. Due to the high HTC of

the MTB, the effective length of the fin ($L_{eff} \sim \sqrt{\frac{k_s D}{4h_{eff}}}$) for the MTB is only ~ 4.6 cm in comparison to ~ 13 cm for a solid heat sink. The h_{eff} is evaluated based on A_{fin} considering both convection and evaporation, i.e., $h_{eff} = h_{ev} + h_c$. Therefore, the length of fin is designed to be 4.5 cm, i.e., L = 4.5 cm. This also implies the compact design of MTB compared to a solid heat sink.

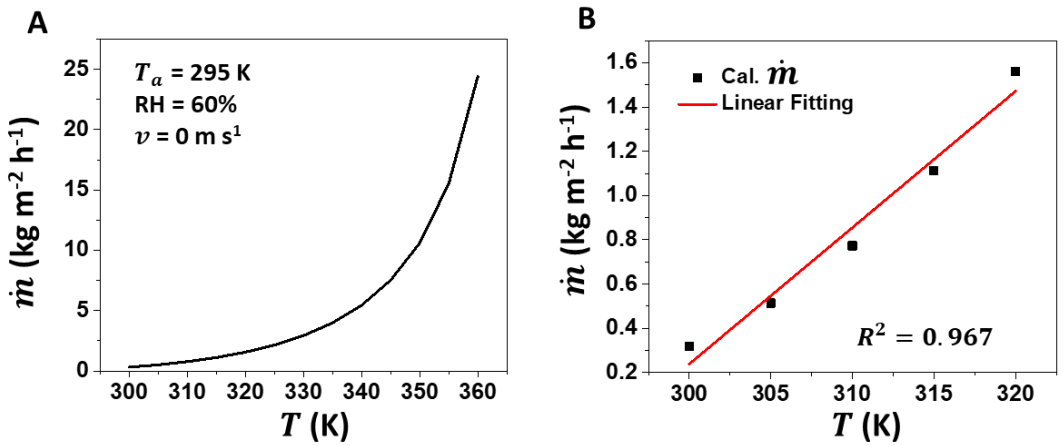

Figure 8-11. Modeling of evaporative flux at RH = 60% and T_a = 22 ℃. (A) Evaporative mass flux as a function of local temperature. (B) Linear fitting of evaporative mass flux within a specific temperature range from 300 – 325 K.

The above analysis has not considered the thermal conductance across the hydrogel layer (G_g) which scales as $G_g \sim D_g^{-1}$. Therefore, a thinner gel leads to higher G_g. Besides, the diffusion kinetics of moisture in the hydrogel is also determined by the gel thickness as the diffusion time constant (t_c) scales a $t_c \sim D_g^2$. Therefore, it is important to properly design the thickness of the gel coating to ensure fast heat and mass transfer. To this end, we first measured the moisture adsorption kinetic of P(SA) hydrogel with different thickness (D_g) ranging from 0.1 mm to 3 mm, as shown in Figure 8-10D (upper row). Before the test, the sample was freeze-dried (Figure 8-8A) and cut into ~ 2×2 cm^2 pieces (Figure 8-8C). The sample was porous after freeze-drying (Figure 8-8B). The test

was done in a humidity chamber at RH = 60% and T_a = 22 ℃ (Figure 8-8D) and the temporal change in the mass of hydrogel was monitored to calculate the instantaneous adsorption capacity. The moisture adsorption kinetics is governed by the diffusion process and thus the adsorption time constant scales $t_c \sim D_g^2$ while the specific adsorption capacity per unit mass of the gel is independent on the gel thickness, as shown in Figure 8-10D (lower row). t_c can be obtained by fitting the kinetic curves with $c(t) = c_0(1 - e^{-t/t_c})$, where c_0 is the adsorption capacity. The moisture diffusivity in the P(SA) hydrogel can also be obtained from the fitting the kinetic curves at the initial stage. Figure 8-12 shows the mass diffusion curve for the P(SA) hydrogel plotted as $\frac{M_t}{M_\infty} \sim t^{\frac{1}{2}}$ to calculate the vapor diffusion across the P(SA) hydrogel according to the Fickian diffusion model, in correspondence to the data shown in Figure 8-10D. Although the curves have not completely plateaued when the tests stop, it is reasonable to assume M_∞ to be 0.4 $g_{water}\ g_{gel}^{-1}$ under RH = 60%. It is noted that we only use the region of $\frac{M_t}{M_\infty} < 0.6$ for fitting as recommended in Ref.[303]:

$$D_w = \frac{\pi D_g}{16}\left(\frac{d\left(\frac{M_t}{M_\infty}\right)}{d\left(t^{\frac{1}{2}}\right)}\right)^2 \tag{8-6}$$

where D_g is the thickness of hydrogel, M_t is the amount of water adsorbed at time of t, and M_∞ is the total amount of water adsorbed by the hydrogel at infinite time. From the slope of the $\frac{M_t}{M_\infty} \sim t^{\frac{1}{2}}$ curve, the vapor diffusivity can be obtained and is found to be 10^{-12}-10^{-11} $m^2\ s^{-1}$ (Table 8-3) which agrees with that reported in the literature [364,377]. The adsorption capacity increases from 0.2 $g_{water}\ g^{-1}_{gel}$ at RH = 20% to ~ 0.8 $g_{water}\ g^{-1}_{gel}$ at RH = 85%.

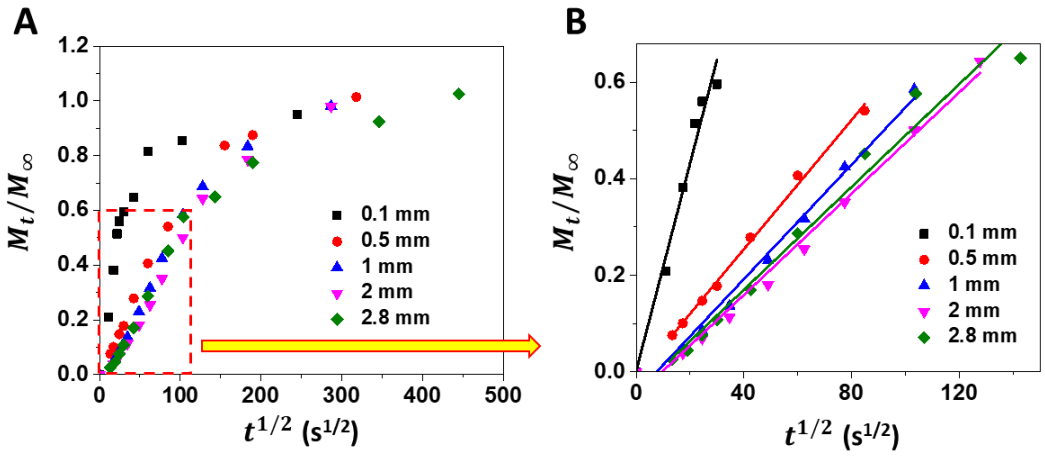

Figure 8-12. Fitting of moisture diffusivity in P(SA) hydrogel. (a) Normalized mass change of water in P(SA) hydrogel as a function of time. (b) Truncated diffusion kinetics with $\frac{M_t}{M_\infty} < 0.6$ for fitting of moisture diffusivity.

Table 8-3. Fitting of Moisture Diffusivity in P(SA).

Thickness of Gel (D_g, mm)	$\frac{d\left(\frac{M_t}{M_\infty}\right)}{d\left(t^{\frac{1}{2}}\right)}$	Diffusivity (m^2 s^{-1})
0.1	0.02147	1.12E-12
0.5	0.00669	2.19E-12
1	0.00592	6.88E-12
2	0.00524	2.16E-11
2.8	0.00532	4.36E-11

Although thinner gel leads to shorter t_c and thus faster regeneration rate and higher G_g, it reduces the thermal capacity of the MTB (Q_t), which is determined by the volume of the water storage and scales as $Q_t \sim PLD_g\rho_w\Delta H_{fg}$, where ρ_w is the density of water. Therefore, the gel thickness should be optimized due to the tradeoff between t_c, Q_t and G_g as shown in Figure 8-10E. With D_g = 2.8 mm, Q_t reaches ~ 24.5 kWh m^{-2} which is favorable for the long-term cooling (i.e., the MTB can operate for ~ 24 hours under q_s

= 1 kW m^{-2}). However, G_g is related to D_g by $G_g = \frac{k_w}{D_g}$ where k_w is the thermal conductivity of water. For D_g = 2.8 mm, G_g is low (~ 215 W m^{-2} K^{-1}) and thus it introduces a significant thermal resistance to the MTB, e.g., the $h_{t,MTB}$ decreases from 400 W m^{-2} K^{-1} to 139 W m^{-2} K^{-1} under natural convection as it scales $h_{t,MTB} \sim \left[\left(h_{ev,MTB} + h_{c,MTB}\right)^{-1} + G_g^{-1}\right]^{-1}$. In the meantime, t_c is 280 mins for D_g = 2.8 mm, indicating a slow regeneration process if the gel layer is thick. On the other hand, with D_g = 0.1 mm, the G_g is high (~ 4600 W m^{-2} K^{-1}) which is negligible compared to $h_{ev,MTB}$ and $h_{c,MTB}$, and the $h_{t,MTB}$ maintains at ~ 370 W m^{-2} K^{-1}. t_c decreases to 10 mins indicating a fast regeneration of gel. However, the thermal capacity is only 1.1 kWh m^{-2} due to the low water storage capability in the thin gel. Here, we designed the hydrogel layer thickness to range from 0.5 to 1 mm, leading to t_c ~ 70-100 min, Q_t ~ 5-8 kWh m^{-2} and $h_{t,MTB}$ ~ 240-300 W m^{-2} K^{-1}. It is noted that the thermal capacity increases linearly with increasing water capacity. In this work we chose P(SA) as the absorbent because of its facile and low-cost synthesis (~ 2 USD $kg^{-1}_{P(SA)}$ as shown in Table 8-4). In the literature, the moisture adsorption capacity of P(SA) hydrogel have been found to increase to 3-5 $g_{water}\, g_{gel}^{-1}$ by PPy-Cl doping or graphene grafting [14,355]. Additionally, the gel can be directly recharged with liquid water with over 130 $g_{water}\, g_{gel}^{-1}$ capacity within 10 mins[10].

Table 8-4. Cost breakdown of MTB

Materials	Unit Price	Amount	Total Price (USD)
Sodium Acrylate	1 USD kg^{-1} [368]	46.4 g	0.046
Sodium Alginate	2 USD kg^{-1} [369]	17.6 g	0.035
MBAA	10 USD kg^{-1} [370]	1.6 g	0.016
APS	50 USD kg^{-1} [371]	1.6 g	0.8
Silane	50 USD kg^{-1} [372]	20 g	1
Al Heat Sink with Heat Pipes	10-30 USD [373-376]	1	10-30
Total			12-32

Cooling Performance of Moisture Thermal Battery

The cooling performance of the MTB is evaluated by measuring the transient base temperature (T_b) of the MTB upon applying a heat load. A solid heat sink without gel coating under identical heating condition is measured for comparison. Figure 8-13A shows T_b of the MTB with the initial water load of 4.3 $g_{water}\, g^{-1}_{gel}$ and a solid heat sink at two heat flux values (q_s = 1- and 2-kW m^{-2}) under natural convection and the ambient conditions of RH = 60% and T_a = 22 ℃. T_b for the MTB is lower than that for the solid heat sink under all the conditions. At $q_s = 2$ kW m^{-2}, T_b for the solid heat sink stabilizes at ~ 46 ℃ after t = 1 h while that for the MTB at $t = 1$ h is only 36 ℃. Experimentally measured T_b of MTB and solid heat sink at the hydrated state agree well with that predicted by the model (Figure 8-14). However, T_b for the MTB gradually increases as water evaporates and eventually converges to that for the solid heat sink at t = 11 h when the stored water dries out. Figure 8-13B displays h_t of the MTB and solid heat sink corresponding to Figure 8-13A, as calculated by Equation 8-5. $h_{t,MTB}$ keeps decreasing as water evaporates and is eventually reduced to $h_{t,solid}$ when the gel coating dries out. $h_{t,MTB}$ stabilizes around ~ 200-250 kWh m^{-2} at q_s = 1 kW m^{-2} under natural convection

from t = 1 h to 4 h when the gel maintains hydrated. $h_{t,MTB}$ decreases faster for higher heat flux due to the faster dry-out, e.g., at $q_s = 2$ kW m^{-1} and under natural convection, $h_{t,MTB}$ is about 150-170 kWh m^{-2} from $t = 1$ h to 4 h.

Figure 8-13C shows the base temperature rise of MTB and solid heat sink at different heat flux (q_s = 1 and 2 kWm^{-2}, respectively) under forced convection (v = 1.5 m s^{-1}) with the initial water load of 4.3 g_{water} g^{-1}_{gel} under the ambient conditions of RH = 60% and T_a = 22 ℃. Like the case under natural convection, T_b for the MTB is lower than that for the solid heat sink under all the conditions. Due to the high forced convection HTC (h_c), i.e., ~ 35 W m^{-2} K^{-1} opposed to ~ 5 W m^{-2} K^{-1} for natural convection, at q_s = 2 kW m^{-2} and v = 1.5 m s^{-1}, T_b for the MTB at t = 0.5 h is 24.6 ℃ while that for the solid heat sink is ~ 29 ℃. Experimentally measured T_b for the MTB and solid heat sink under all the above conditions matches well with the modelled T_b (Figure 8-14). Figure 8-13D displays $h_{t,MTB}$ and $h_{t,solid}$ corresponding to Figure 8-13C, as calculated by Equation 8-5. Like the case of natural convection, $h_{t,MTB}$ decreases as water evaporates and eventually converges to $h_{t,solid}$ when the gel coating dries out at $t = 10$ hr. As expected, h_t is significantly higher with forced convection compared to natural convection, e.g., at q_s = 1 kW m^{-2} and v = 1.5 m s^{-1}, $h_{t,MTB}$ is > 1500 kW m^{-2} from t = 1 h to 4 h while at q_s = 1 kWm^{-2} and v = 0 m s^{-1}, $h_{t,MTB}$ is 200-300 kW m^{-2} from t = 1 h to 4 h.

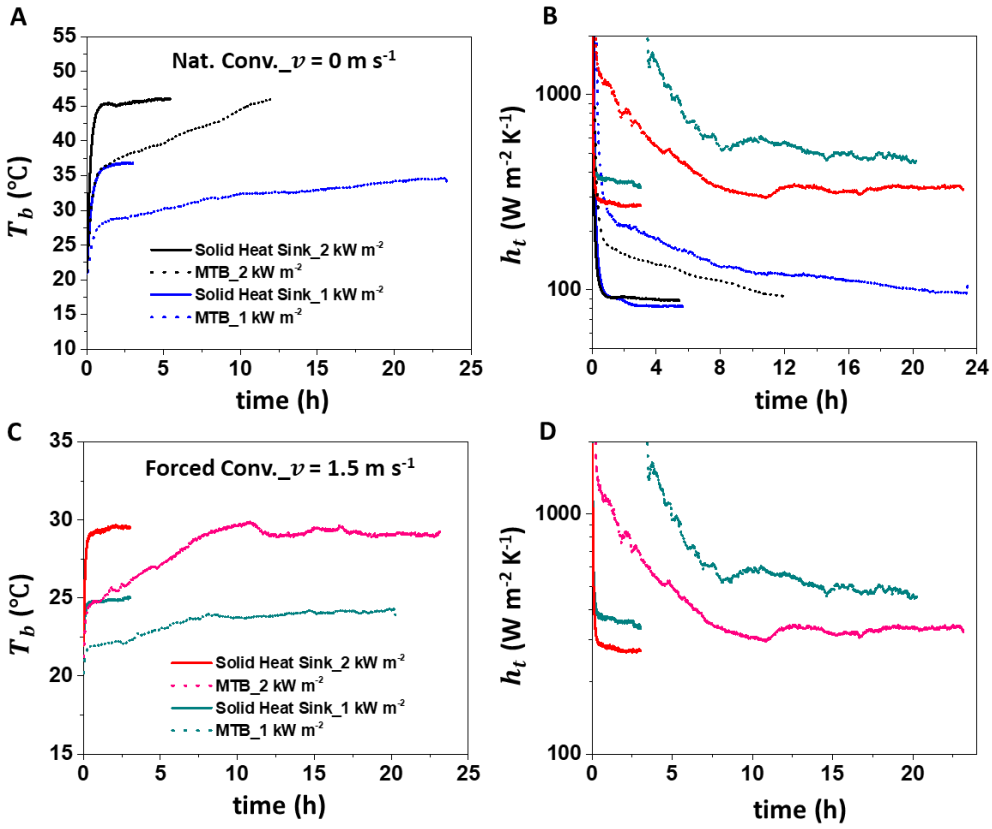

Figure 8-13. Cooling performance of MTB compared to solid heat sink under natural convection (A and B) and forced convection at v = 1.5 m s-1 (C and D). (A) Base temperature-rise (T_b) of the MTB and solid heat sink under natural convection at the heat flux of q_s = 1 kW m^{-2} and q_s = 1 kW m^{-2}, respectively. (B) Corresponding effective HTC (h_t) of MTB and solid heat sink to the conditions in Figure 3A. (C) T_b of the MTB and solid heat sink under forced convection with airspeed v = 1.5 m s^{-1} at the heat flux of q_s = 1 kW m^{-2} and 2 kW m^{-2}, respectively. (D) Corresponding h_t of the MTB and solid heat sink to the conditions in Figure 8-13C.

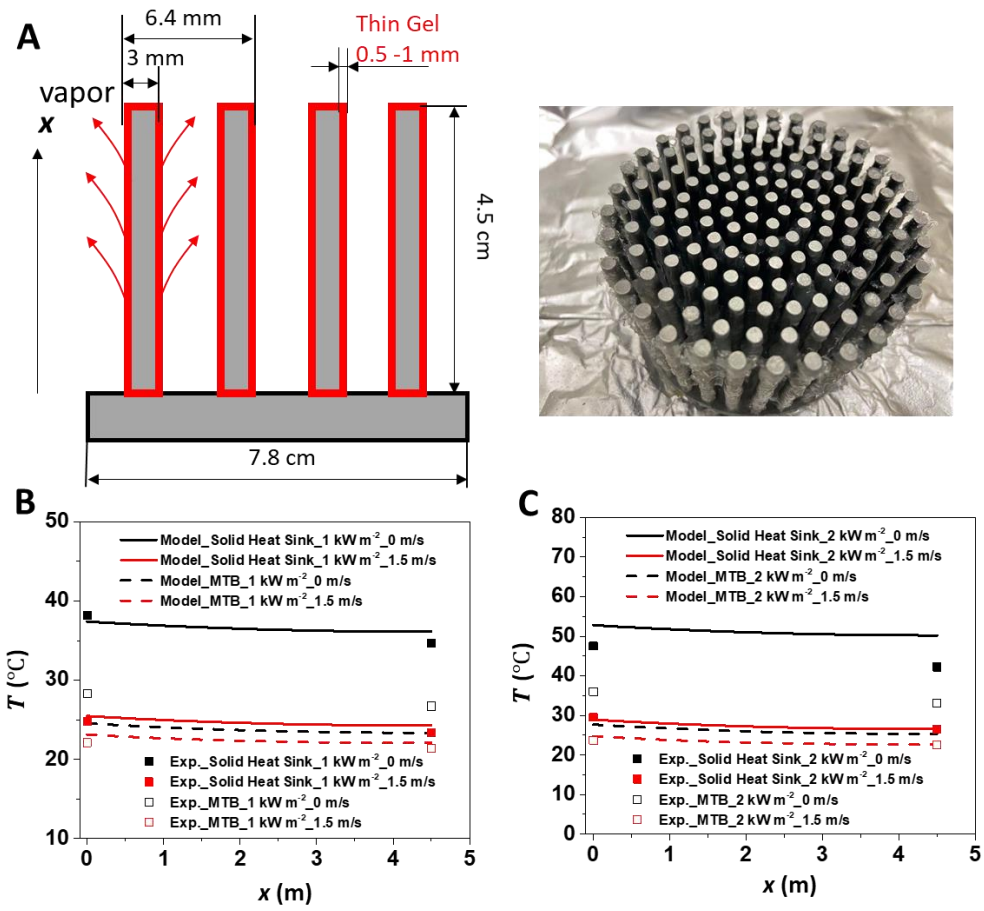

Figure 8-14. Heat and mass modeling of MTB at RH = 60% and T_a = 22 °C. (A) Schematic of the model and photo of the MTB. (B) Comparison of temperature distribution between solid heat sink and MTB at q_s = 1 kW m^{-2} under natural and forced convections. (C) Comparison of temperature distribution between solid heat sink and MTB at q_s = 2 kW m^{-2} under natural and forced convections.

Both the HTC and the thermal capacity strongly depend on the water content in the hydrogel layer. Therefore, it is important to investigate the performance of heat sink under different initial water loadings. Figure 8-15A shows the base temperature rise of the MTB with initial water loading ranging from 0.9 – 4.3 g_{water} g^{-1}_{gel} under the ambient conditions of RH = 60% and T_a = 22 °C at q_s = 1 kW m^{-2} under natural convection. T_b increases faster for lower water loading because the hydrogel layer dries out faster, e.g., for 0.9 g_{water} g^{-1}_{gel}, T_b reaches ~ 36 °C (dash line indicates T_b for the solid heat sink under

the same condition) at t = 6 h while that for 3.5 g_{water} g^{-1}_{gel} is only 30.5 ℃ at t = 6 h. T_b increases due to the dry-out of the hydrogel layer as shown in Figure 8-15B, where the water content indicates the total amount of liquid water left in the hydrogel layer. The slopes for different curves are similar indicating similar evaporative flux for different cases and that the thermal capacity is almost proportional to the initial water loading. Therefore, T_b increases more slowly for higher initial loading. As shown in Figure 8-15C, $h_{t,MTB}$ gradually decreases to that of the solid heat sink (dash-line) as the hydrogel layer dries out and decreases faster for lower initial loading. We also modelled the evaporative flux of the MTB and confirmed the increasing T_b with decreasing evaporative flux (Figure 8-16B). Based on the modelled relationship between T_b and evaporative flux, the transient mass flux was back-calculated (Figure 8-16C) based on the experimentally measured transient T_b in Figure 4A. The evaporative was found to decrease with time as the hydrogel dried out (Figure 8-16C). The cumulative mass loss can thus be obtained by integrating the transient mass flux over time (Figure 8-16E). The measured mass losses shown in Figure 8-15B agree weill with the modelled results, with the maximum discrepancy less than 30%, e.g., for initial loading of 2.5 g_{water} g_{gel}^{-1}, the measured mass loss was 29.1 g at t =12 h, which was ~ 25% lower than the model prediction (39 g). The model generally slightly overestimates the mass loss possibly because the mass transfer resistance in the hydrogel layer has not been considered.

Figure 8-15D displays T_b of MTB with initial loading of 4.3 g_{water} g_{gel}^{-1} under the ambient conditions of RH = 60% and T_a= 22 ℃ and natural convection, with variation in the heat flux (q_s = 0.5-2 kW m^{-2}). The corresponding mass loss is shown in Figure 8-15E. T_b increases much faster under higher heat flux, and the corresponding $h_{t,MTB}$ decreases

faster as shown in Figure 8-15F. The dash line indicates steady-state T_b and h_t of the solid heat sink under the same condition. The reason is that the evaporative flux is much higher for higher heat flux as shown in Figure 8-15E, leading to the faster dry-out of the hydrogel layer. As shown in Figure 8-15F, as the hydrogel dries out, $h_{t,MTB}$ is reduced to that of the solid heat sink and it decreases faster for higher heat flux. The transient evaporative flux (Figure 8-16D) and cumulative mass loss (Figure 8-16F) of MTB under 1- and 2- kW m^{-2} were modelled. The mass loss was faster for higher heat flux, which agreed well with the experimental results. For example, at t = 12 h, the experimentally measured mass losses are ~ 54 g and ~ 38 g for q_s = 2 kW m^{-2} and 1 kW m^{-2}, respectively, which were ~ 18.6% and 15.5% lower than the modelled mass loss for q_s = 2 kW m^{-2} (70 g) and 1 kW m^{-2} (45 g), respectively. The above analysis indicates that both h_t and Q_t rely on the water storage in the hydrogel layer, which at a fixed D_g, can be improved by increasing the effective surface area and the adsorption capacity of materials. Recent studies reported that the adsorption capacity of PPy-Cl doping or Graphene grafted hydrogel reached 3-5 g_{water} g_{gel}^{-1} at RH = 80% [14,355].

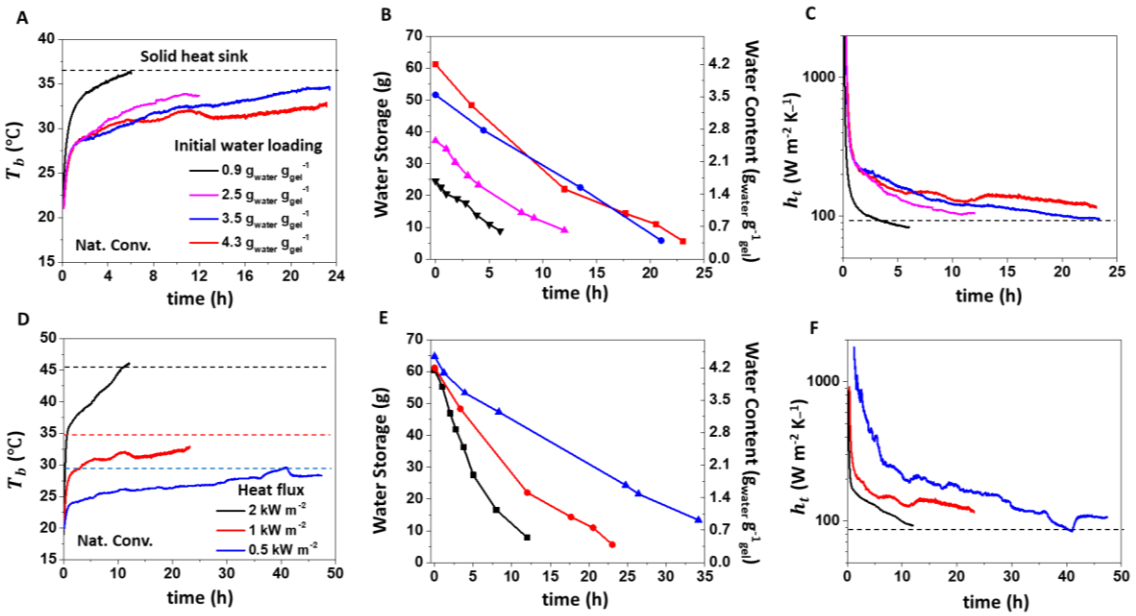

Figure 8-15. Parametric study on the cooling performance of the MTB at T_a = 22 °C and RH = 60% under natural convection. (A) Effect of initial water loading on the base temperature rise (T_b) of the MTB under natural convection and at q_s = 1 kW m^{-2}. The initial water loading in the hydrogel layer varies from 0.9 to 4.3 g_{water} g^{-1}_{gel}. The dash line indicates the steady state T_b of solid heat sink tested under the same condition. (B) Mass loss of water from the MTB during evaporative cooling in correspondence to Figure 8-15A. (C) Corresponding effective HTC (h_t) of the MTB and solid heat sink to the conditions in Figure 8-15A. The dash-line indicates the steady-state h_t of the solid heat sink. (D) Effect of heat flux on T_b of the MTB under natural convection with initial water loading of 4.3 g_{water} g^{-1}_{gel}. The dash line indicates the steady state T_b for the solid sink under the same condition. (E) Mass loss of water from the MTB during evaporative cooling in correspondence to Figure 8-15D. (F) Corresponding h_t of the MTB and solid heat sink to the conditions in Figure 8-15D.

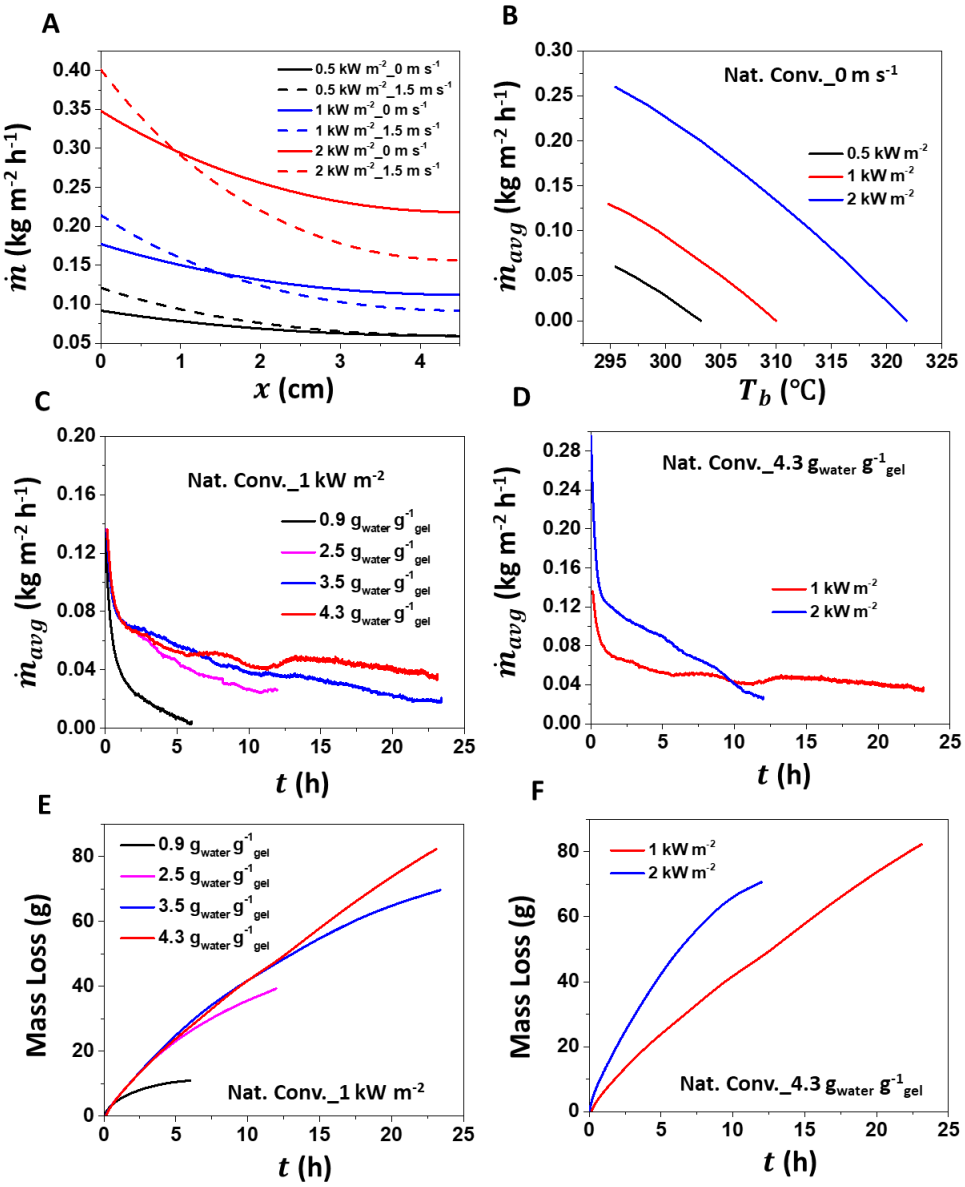

Figure 8-16. Modeling of evaporative flux of MTB at RH=60% and T_a = 22℃. (A) Distribution of evaporative flux along the fin at different heat flux at the hydrated state. (B) Relationship between T_b and $\dot{m}_{avg}$ under natural convection at different heat flux q_s = 0.5-2 kW m^{-2}. (C) Predicted evaporative flux as a function of time for MTB with different initial water loading 0.9-4.3 g_{water} g_{gel}^{-1} under natural convection at q_s = 1 kW m^{-2}, converted from the transient T_b shown in Figure 8-15A using the relation shown in Figure 8-16B. (D) Predicted evaporative flux as a function of time for MTB at different heat flux with the initial loading of 4.3 g_{water} g_{gel}^{-1} under natural convection, converted from the transient T_b shown in Figure 8-15E using the relation shown in Figure 8-16B. (E) Predicted mass loss as a function of time for MTB with different initial water loading 0.9-4.3 g_{water} g_{gel}^{-1} under natural convection at q_s = 1 kW m^{-2}. (F) Predicted mass loss as a function of time for MTB at different heat flux with the initial loading of 4.3 g_{water} g_{gel}^{-1} under natural convection.

Regeneration of Moisture Thermal Battery

The P(SA) gel adsorbs moisture by ~ 0.9 g_{water} g^{-1}_{gel} under the condition of T_a = 22 ℃ and RH = 85%, which enables the passive regeneration during off-peak hour. To demonstrate this, the MTB was tested in a humidity chamber at T_a = 22 ℃ and RH = 85% under natural convection, with periodic heat flux, i.e., q_s = 1 kW m^{-2} for t_h = 3 h, followed by the regeneration period with variation in the regeneration time (t_r) from 36 min to 12 h at q_s = 0 kW m^{-2}. The above process lasts for 5-6 cycles. Figure 8-17A to 8-17D displays the periodic base temperature rise of the MTB with t_c increasing from 36 min to 12 h. For comparison, the solid heat sink was supplied with periodic heat flux for t_h = 3 h and t_r = 3 h as shown in black curve in Figure 8-17B. Since the solid heat sink cannot absorb moisture, T_b of the solid heat sink is independent on t_r. The base temperature rise of the MTB is the same among different cycles for all the conditions, indicating the stability of the MTB. As shown in Figure 8-17B, T_b for the MTB is constantly lower than that of the solid heat sink, implying that water evaporates during the peak-hour and the hydrogel layer regenerates during the off-peak hour. t_r is determined by the adsorption time constant (t_c) of the hydrogel layer (~ 100 min as shown in Figure 8-10E). T_b at the end of the heating period, i.e., t = 3 h, was plotted as a function of t_r in Figure 8-17E. T_b decreases substantially as t_r increases from 36 min to 3 h because more moisture is absorbed by the hydrogel layer, leading to higher h_t and capacity. However, T_b is less sensitive to t_r when t_r > 3 h because the time constant (t_c) for 0.5-1 mm thick hydrogel is ~ 100 min. To obtain the time constant for the MTB ($t_{r,MTB}$), the adsorption kinetics of the MTB was tested by placing the freeze-dried MTB in the humidity chamber at T_a = 22 ℃ and RH = 85%. The adsorption capacity of the

MTB as a function of t_r is also plotted in Figure 8-17E in accompanied with T_b. The time constant could be obtained by fitting the kinetic curves with $c(t_r) = c_0(1 - e^{-t_r/t_c})$ where c_0 is the adsorption capacity. $t_{c,MTB}$ is found to be ~ 4 h, which agrees well with t_r when T_b starts to plateau.

The short t_c enables fast regeneration of the hydrogel layer and thus high equivalent thermal capacity on daily basis. For example, although the thermal capacity of the MTB in a single cycle is limited to ~ 6 kWh m^{-2} because the moisture adsorption capacity is ~ 0.9 g_{water} g_{gel}^{-1} (Figure 8-10E), the total daily equivalent thermal capacity is ~ 24 kWh m^{-2} day^{-1} if t_c is set at 3 h (i.e., 4 cycles per day). Several recent studies reported novel hydrogel materials with high adsorption capacity of ~ 5 g_{water} g^{-1}_{gel} [14,355]. However, due to the lack of structural engineering, t_c is 12 ~ 24 h[14,16,296], and thus only one cycle can be operated per day, limiting the thermal capacity. The equivalent thermal capacity of MTB could be much higher with active liquid refill for extreme heat flux condition, where t_c can be reduced ~ 30 min in cyclic operation and the adsorption capacity could be enhanced to ~ 100 g_{water} g^{-1}_{gel} [10]. This indicates the flexibility of the MTB for different application scenarios. Figure 5F shows the periodic water content in MTB for t_h = 3 h and t_r = 12 h at T_a = 22 ℃ and RH = 85%. The MTB evaporates and absorbs similar amount water in every cycle, validating the stable evaporation-desorption of MTB in the long-term operation.

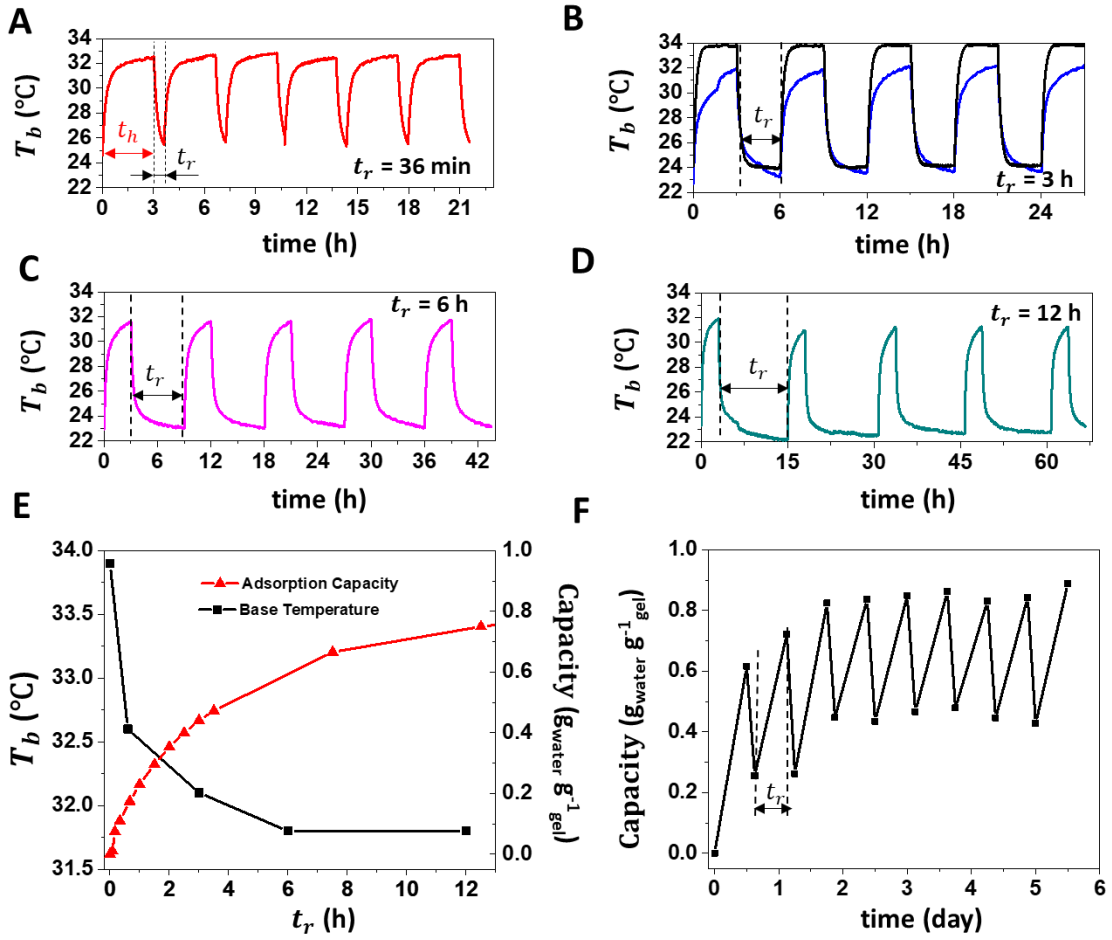

Figure 8-17. Evaporation-sorption cycle of MTB under the ambient condition of T_a = 22 °C and RH = 85% under natural convection. The MTB is subject to periodic heating (q_s = 1 kW m^{-2}) for heating time (t_h) of 3 h and regeneration (q_s = 0 kW m^{-2}) cycles for regeneration time (t_r) varied from 36 min to 12 h. The hydrogel layer absorbs moisture during the regeneration period and evaporates in the subsequent heating period. Periodic base temperature-rise of the MTB tested with t_r of (A) 36 min, (B) 3 h (the black curve indicates the solid heat sink), (C) 6 h and (D) 12 h, respectively. (E) T_b of the MTB recorded at the end of the heating period as a function of the regeneration time t_r and the transient water moisture content in the hydrogel layer of the MTB recorded during the regeneration period, which is calculated from the mass gain of the MTB with respect to the dry mass of gel. $T_b(t_r = 0)$ indicates that T_b of MTB when the hydrogel is not regenerated with moisture and is the same as that for a solid heat sink. (F) Water content in the MTB during cyclic operation with t_h = 3 h and t_r = 12 h.

Demonstration on Thermal Management of Field-effect Transistor

To demonstrate the thermal management of 5G devices, we applied the MTB for high-power field-effect transistor (FET), a key power element in 5G devices[324,378]. To maximize the performance of the MTB, we used a state-of-the-art solid heat sink with embedded heat pipes (HSHP) with ~ 760-fold enhanced surface area (Figure 8-18A), which was much larger than that of the pin heat sink characterized above (~ 10-fold enhanced surface area). The surface of the fins was coated with 0.5 mm thick P(SA) hydrogel using the same dip-coating method as in the pin-fin heat sink. Due to the larger surface area, both the effective HTC and thermal capacity were significantly enhanced. For example, at q_s = 7.5 kW m^{-2} under natural convection, when using the HSHP, T_b of the HSHP-MTB was consistently ~ 10 K lower than that of the MTB using the pin heat sink in a cyclic test for longer than 30 h (Figure 8-19A). The HSHP-MTB could sustain up to q_s = 60 kW m^{-2} for up to 3 h under natural convection condition which was 30 times higher than the maximum q_s demonstrated by MTB based on pin heat sink (Figure 8-19B). Under forced convection, the HSHP-MTB can sustain q_s = 60 kW m^{-2} for t_r longer than 3 h in cyclic operation (Figure 8-19B).

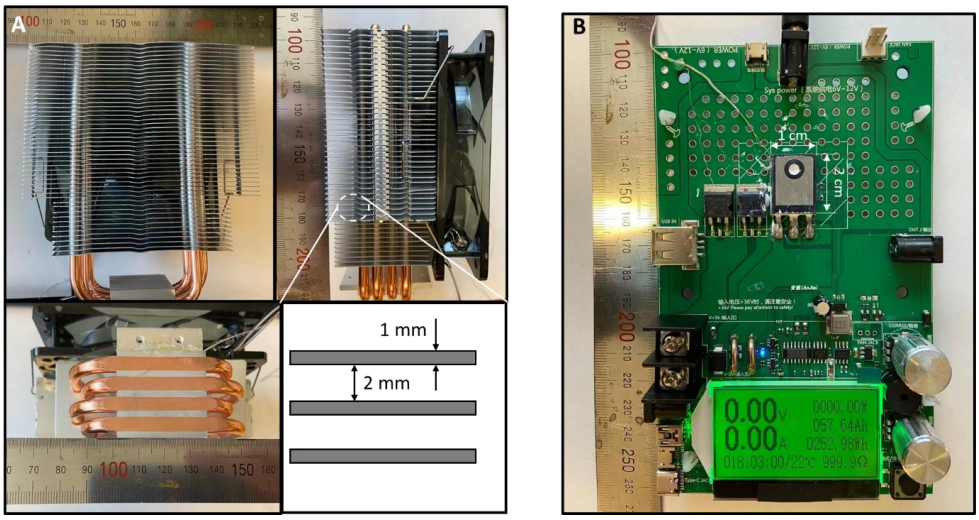

Figure 8-18. Photo and schematics of the HSHP and FET. (A) Details of the HSHP (B) electronic load board for FET.

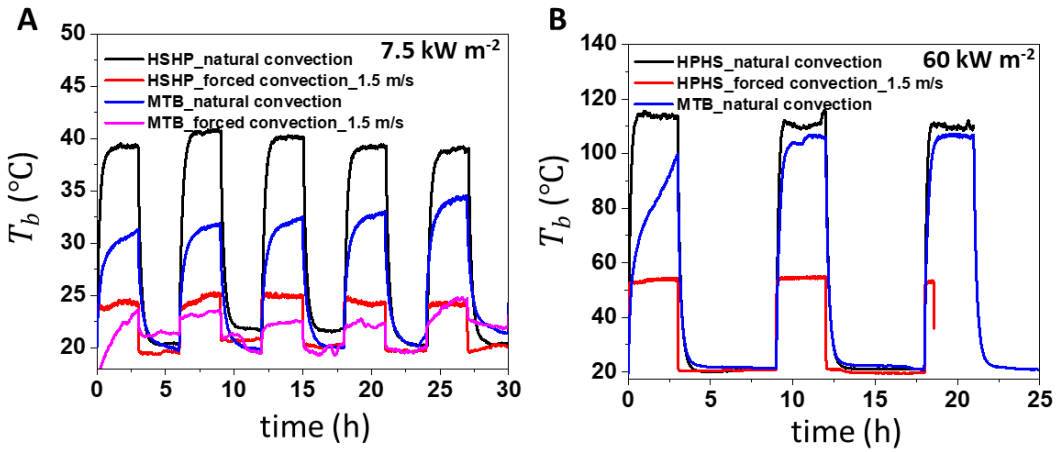

Figure 8-19. Comparison between HSHP (without gel) and HSHP-based MTB (with gel). The heat flux is supplied from a heater. The initial loading is 4.3 g_{water} g_{gel}^{-1} by liquid-phase water airbrushing. The setup is placed in the ambient environment of RH = 70% and T_a = 22 ℃. During the regeneration period, water is regenerated by moisture adsorption from air by the hydrogel layer without active liquid replenishment. (A) The base temperature rise (T_b) with q_s = 7.4 kW m^{-2} for t_h= 3 h and regeneration time t_r = 3 h. (B) T_b with q_s = 60 kW m^{-2} for t_h = 3 h and regeneration time t_r = 6 h.

As shown in Figure 8-20A and 8-20B, the HSHP-MTB (simply called MTB for convenience from now on) was placed on top of the FET of 10 mm × 20 mm in area and the setup was kept under the ambient condition of T_a = 22 ℃ and RH = 70% under natural convection. The chip temperature (T_c) was recorded by a thermocouple attached

on the side of the FET. The operating power of FET was controlled and monitored by an electronic load controller (Figure 8-18B). 85% of the operating power was dissipated by the FET as heat. The infrared images of the FET taken at q_s = 2.7 kW m^{-2} and, that of the HSHP (simplify called solid heat sink for convenience from now on) and MTB taken at the steady state at q_s = 27 kW m^{-2} are also displayed in Figure 8-20B. Figure 8-20C compares the temperature rise of the FET (T_{chip}) at different heat flux (q_s = 11.3 – 27 kW m^{-2}) cooled by the MTB with initial water loading of 4.3 g_{water} g_{gel}^{-1} and the solid heat sink. The heat flux q_s is adjusted by the input power to the FET, which is 11.3 kW m^{-2}, 18 kW m^{-2} and 27 kW m^{-2}, respectively, based on the base area of MTB (35 mm $\times$ 35 mm in area). T_{chip} of the FET cooled with the MTB is ~ 15 K lower than that cooled by the solid heat sink at all the heat fluxes. Fin temperature (T_{fin}) of the MTB is also lower than that of the solid heat sink as shown in Figure 8-20B (lower row), e.g., at q_s = 27 kW m^{-2}, T_{fin} of MTB is ~ 32.8 ℃, which is ~ 12 K lower that that of solid heat sink. Due to the high effective surface area of HSHP, the cooling power of HSHP-based MTB is much higher than that based on the pin heat sink studied above (i.e., 27 kW m^{-2} vs 2 kW m^{-2}). The effective HTC of the MTB, i.e., $h_t = \frac{q_s}{T_{chip}-T_a}$, is calculated to be 1230 W m^{-2} K, 880 W m^{-2} K and 720 W m^{-2} K, at q_s = 11.3 kW m^{-2}, 18 kW m^{-2} and 27 kW m^{-2} respectively, which is comparable to the single-phase microchannel heat sink (~ 1000 W m^{-2} K^{-1} [379]). Figure 8-20D shows the cyclic operation of the FET with alternating on-/off-peak hours every 3 h with q_s = 11.3 kW m^{-2} on peak and q_s = 0 kW m^{-2} off-peak at T_a = 22 ℃ and RH = 70% under natural convection. The hydrogel was regenerated by moisture adsorption during the off-peak hours. It can be seen that T_{chip} with MTB stabilizes around 37-40 ℃ in the six cycles and is consistently 6~7 ℃ lower than that cooled by the

solid heat sink, indicating the stable operation of the MTB. We calculated the equivalent thermal capacity (Q_t) by the product of heat flux and stable operational time (t_c), e.g., the MTB can stably operate for 18 h at q_s = 11.3 kW m^{-2}, and thus the thermal capacity is 203 kWh m^{-2} in the six-cycle test.

We compare the effective HTC and thermal capacity of the MTB to other sorption-based evaporative cooling devices[328-331,341,343-345,347-351] as shown in Figure 8-20E. In general, the previous sorption-based devices are limited with low HTC and capacity (i.e., h_t < 100 W m^{-2} K^{-1} and Q_t < 10 kWh m^{-2} due to the thick hydrogel layer and small effective surface area. Our design improves the state-of-the-art h_t and Q_t by an order of magnitude to h_t ~ 1000 W m^{-2} K^{-1} and Q_t ~ 200 kWh m^{-2}) via scale structural engineering. The MTB is scalable because the raw materials (SA and Alg, etc.) and substrate (Al heat sink) are inexpensive. The hydrogel layer was synthesized by scalable facile dip-coating and thermally driven processes. The cost of MTB is estimated to be as low as ~ 12 USD (Table 8-4). The hydrogel materials only cost ~ 2 USD. The autonomous operation with high cooling performance makes the MTB a suitable candidate for thermal management of high-power electronics, e.g., 5G chips (q_s ~ 60 kW m^{-2} and Q_t ~ 400 kWh m^{-2} [378]), power battery (q_s ~ 1 kW m^{-2} [380,381] and Q_t ~ 10 kWh m^{-2}), server/data center (q_s ~ 100 kW m^{-2} for CPU and 1-10 kW m^{-2} for racks[382]) and optoelectronics (q_s ~ 10 kW m^{-2} for diode laser[383]), etc.

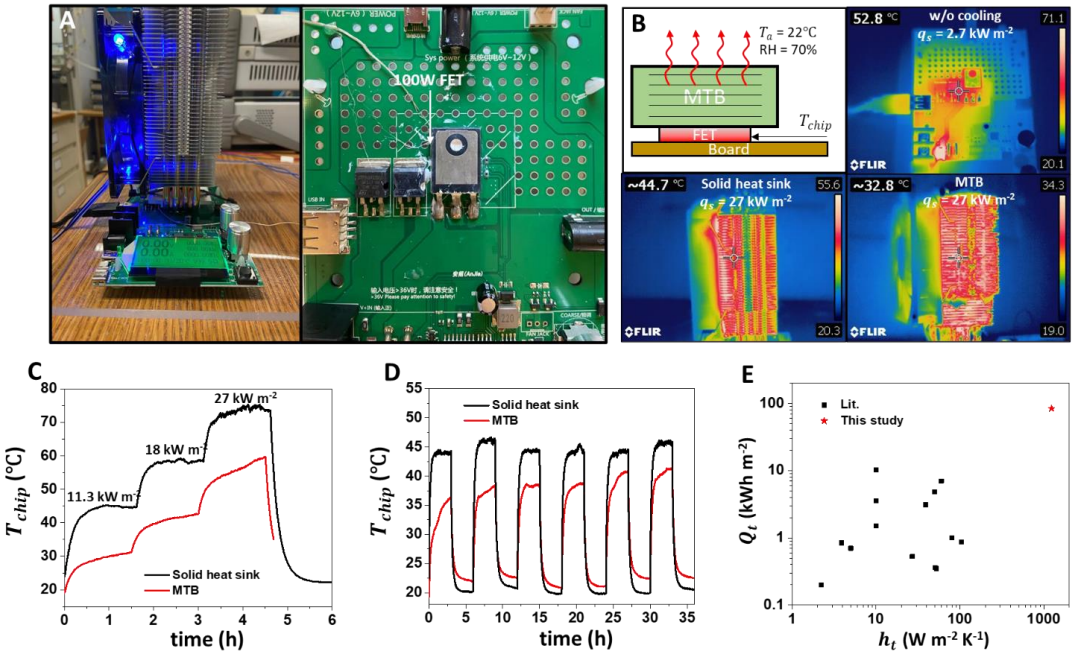

Figure 8-20. Thermal management of high-power (100 Watt) field effect transistor (FET). The experiments are conducted under the condition of T_a = 22 ℃ and RH = 70%. (A) Photograph of the FET board cooled by the MTB. The FET is connected on an electronic load board with 85% of input power dissipated by the FET as heat. The operating power of the FET is monitored *in-situ* by the board and the temperature of the FET is recorded using a thermocouple. (B) Schematic of the testing setup (upper left). Infrared images of the FET and cooling device. FET temperature without heat sink at q_s = 2.7 kW m^{-2} (upper right), with solid heat sink at q_s = 18 kW m^{-2} (bottom left) and with MTB at q_s = 18 kW m^{-2} (bottom right). (C) FET chip temperature (T_{chip}) at different operation power when cooled by the solid heat sink and MTB. (D) Cyclic operation of the FET with alternating peak hour (q_s = 11.3 kW m^{-2}) and off-peak hour (q_s = 0 kW m^{-2}) by every 3 h. The MTB adsorbs moisture during the off-peak hour for evaporative cooling in the subsequent heating cycle in the peak hour. (E) Comparison of effective HTC and thermal capacity of the MTB in this study to other sorption-based cooling devices in the literature [328-331,341,343-345,347-351].

Thermal Management of CPU for Workstation

The annual energy consumption of data center worldwide is estimated to be ~ 200 TWh, corresponding to about 1.4% of worldwide electricity consumption[384]. About 40% of the energy flow in the data center is dissipated as heat[385]. In this section, we demonstrated the passive the thermal management of an 80 W-rated CPU for workstation using MTB. As shown in Figure 8-21A. The MTB was placed on top of the CPU and the

setup was kept under the ambient condition of T_a = 22 ℃ and RH = 70% under natural convection. The same HSHP-based MTB demonstrated for the FET was used. As shown in Figure 8-21B, we first characterized the transient performance of the CPU with fluctuating power from 0 - 50 W for 30 mins, corresponding to q_s = 0 - 41 kW m^{-2}. The core temperature of CPU (T_{core}) was monitored. As shown in Figure 8-21C, due to the fluctuating power, T_{core} also fluctuates during the 30-min stress-test. T_{core} with MTB is consistently 10-15 ℃ lower than that with solid heat sink.

To demonstrate the passive regeneration, we run the CPU with alternating high- and low utilization (i.e., high and low power) for 48 h. As shown in Figure 8-21D, the CPU was run on and off randomly during the test, with maximum duration of peak-hour of 5 h and the minimum off-peak hour of 3 h between two peak-hours. The peak power was ~ 23 W (i.e., q_s ~ 18.8 kW m^{-2}) and the off-peak power was ~ 3 W (i.e., q_s ~ 2.4 kW m^{-2}). While the operational time was random, the total CPU energy consumption was kept the same at ~ 400 Wh in 48 hours for both the MTB and solid heat sink cooling. Figure 8-21E shows the CPU core temperature in the 48-h test. T_{core} with MTB is consistently lower than that with the solid heat sink by about ~ 10 ℃ throughout the test, confirming the effective and autonomous cooling of MTB.

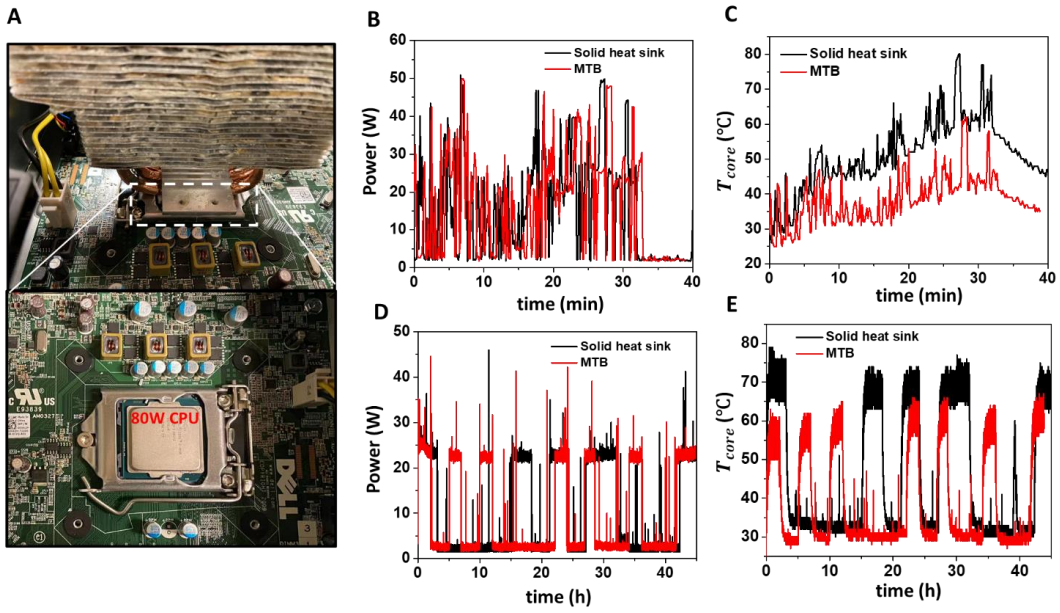

Figure 8-21. Thermal management of an 80W CPU (Intel i5-4570) for workstation. (A) Photograph of the workstation with an MTB on top of the CPU for thermal management. The setup is placed in the benchtop environment of T_a = 22 ℃ and RH = 70% under natural convection. The CPU temperature and power are monitored by the embedded thermometer and power meter in the CPU. (B) Transient CPU power and (C) CPU temperature with and without the MTB for a 30-min test when operating a benchmark program (3D Mark). (D) CPU power and (E) CPU temperature with and without the MTB with periodic on-/off- peak CPU power by running a numerical simulation program for two consecutive days. The peak power is ~ 23 W and the off-peak power is ~ 3 W. The total energy consumption by the CPU is identical (~ 400 Wh) for both cases while the operational time is randomly chosen. The maximum duration of peak-hour is 5 h and the minimum off-peak duration is 3 h.

8.4. Conclusions

Passive thermal management of high-power electronics has been challenging due to the fluctuating power between on-/off-peak hours, which requires active power supply and cooling capacity. In this study, we developed a scalable moisture thermal battery for passive thermal management of power electronics with capability of adaptive thermal energy storage and release to mitigate the temperature fluctuation. The MTB dissipates heat flux from electronics by evaporative cooling on-peak and regenerate off-peak. The MTB was made by coating thin P(SA) hydrogel layer on the external surface of an

aluminum substrate with 10-760-fold enhanced effective surface area. The hydrogel layer absorbed moisture from air during the off-peak hour which evaporated during the peak-hour to carry away a large amount of heat from electronics by the evaporative latent heat of water. The performance of MTB depended on the effective surface area of the substrate and the hydrogel layer thickness, which should be carefully designed at the tradeoff of thermal conductance, thermal capacity and regeneration time. The effect of operational conditions, including convection effect, initial water loading, heat flux and regeneration time were systematically analyzed. We demonstrated the passive thermal management of high-power field effect transistor and CPU using MTB with an effective surface area of ~ 760-fold compared to the base area and achieved ultra-high thermal conductance (~ 1000 W m^{-2} K^{-1}) and thermal capacity (~ 200 kWh m^{-2}) which have not been attained before. The metrics of MTB meet the requirement of thermal management for 5G chips, power battery, server/data center, and optoelectronics, etc. The MTB was made of cheap materials (e.g., sodium acrylate and commercial aluminum heat sink) by facile dip-coating methods. The cost of the MTB is estimated to be ~ 12 USD, which is favorable for large-scale production.

Chapter 8, in full, is being prepared for publication by Jian Zeng, Xintong Zhang, Ka Man Chung, Ravi Prasher and Renkun Chen. The dissertation author was the primary investigator and first author of this paper.

9. Chapter 9: Summary and future work

9.1. Summary

90% of today's energy budget centres around thermal energy. In face of the increasing severe energy crisis and water-energy nexus, efficient harnessing and effective management of thermal energy have been considered critical steps towards the ambitious goal peak the carbon emission by 2030 and neutralize carbon emission by 2050.

Concentrating solar power (CSP) shows the potential to convert solar energy into high-grade thermal energy for on-demand electricity generation due to its storage capability and high thermal efficiency at high operation temperature. However, the development of CSP has been hindered by lack of knowledge of thermal transport mechanism in high-temperature media, such as in the solar absorbing coating, containment materials, granular flow and molten salt flow, etc. To solve this bottleneck, a non-contact laser-based modulated photothermal radiometry (MPR) system was developed to measure the thermophysical properties of a variety of high-temperature components in CSP up to 700℃. The MPR system showed high compatibility with thermal conductivity measurement under extreme conditions due to the high signal-to-noise ratio at high temperature and robustness of the thermal emission from black coating surface. We first demonstrated that the MPR system could measure the thermal conductivity of solar absorbing coatings and high-temperature bulk alloys with error less than 10%. Subsequently, it was modified to measure the intrinsic thermal conductivity and convection heat transfer coefficient of flowing fluid in a channel. The critical

criteria for intrinsic property measurement was rigorously derived, which provided a strong *in-operando* diagnostic tool of flowing molten salt in the CSP plant. Afterwards, the MPR system was applied for the measurement of moving particle bed for CSP. The system was modified to measure the effective thermal conductivity of moving particle with variation in the flowing velocity, temperature, particle size, and particle morphology. It was found that the effective thermal conductivity decreased with increasing flowing velocity, which became more prominent for larger and more irregular particles. We conducted a discrete element modelling (DEM) to extract the packing structure of moving particle bed and found that the near-wall thermal resistance was the major reason for the degraded performance of particle heat exchanger at high velocity. The near-wall thermal resistance was induced by the near-wall airgap layer, where the particles diffused away from wall at high velocity. This was the first experimental and theoretical evidence of the mechanistic origin of near-wall thermal resistance in granular flow while it has been known to exist since 1970s.

Low-grade thermal energy is universal from industrial waste-heat, power electronics, and distributed sunlight, etc. They are more ready to be explored for mitigate the water-energy in the less-developed area because of the easy-access and cheap infrastructures. The efficient utilization of low-grade thermal energy from power devices has the potential to save 8-21% of the annual electricity consumption, which otherwise has to be actively cooled. To explore this energy source for water-energy nexus, we developed a new class of thermoresponsive hydrogel for forward-osmosis desalination where the hydrogel draws water

molecules across the membrane from seawater due to its high ionic strength. This new class of draw agent processed the unique LCST phase transition to release water in liquid phase at 35℃ to avoid the latent heat penalty in conventional FO desalination. Subsequently, we applied polyelectrolyte hydrogel for continuous solar-drive evaporative desalination, where solar energy was directly converted to heat to evaporate the seawater. To avoid the intrinsic geometric limit and salt crystallization problem in conventional capillary wick, we used the high osmotic pressure in polyelectrolyte hydrogel to pump seawater to the evaporative surface. Due to the high ionic strength of hydrogel, we avoid the salt crystallization problem. Lastly, we demonstrated that the hydrogel materials can also be applied for water harvesting from the moisture in air by adsorption-desorption process. The generic idea was to coat a thin hydrogel layer on a metallic scaffold with 100-1000-fold enhanced effective surface. Due to the thin hydrogel thickness and large surface area, the daily water yield from our design was much higher than the state-of-the-art techniques. Due to the evaporative latent heat in the desorption process, we found that the water harvesting device also manifested itself a superior heat sink for power electronic thermal management. Based on the same design, we developed a moisture thermal battery (MTB) and demonstrate the passive thermal management of 5G device and CPU using the MTB.

9.2. Future work

In the MPR measurement of moving particle, we have experimentally quantified the near-wall airgap thickness and identified the diffusive behaviour of particle motion as the mechanistic origin of the near-wall airgap. However, our

measurement has been limited the fully developed region. It is still not well understood how the near-wall thermal resistance develops along the channel. Besides, the operational conditions were limited, e.g., we only measured particle sizes from 150 to 400 μm and the flowing velocity was limited to 60 mm s^{-1}. It has been recognized the trade-off between the convective heat transfer and near-wall thermal resistance as the velocity increased. It is intuitive that the particle flow would become fluid-like as the particle size decrease where the near-wall thermal resistance might diminish. Therefore, it is of interest to extend the operational condition to further investigate the critical condition where the near-wall airgap become prominent. In addition, the MPR shows great potential for *in-operando* measurement at industrial-level. It will be of great excitement to work with our collaborators from the industry to integrate this technique with the MW level CSP system for *in-situ* diagnostic.

In the water harvesting from air project, we have demonstrated that ultrahigh water yield could be obtained from fast adsorption-desorption cycle by improving the kinetics. However, up to now, we only presented the water yield in the form of mass change in the hydrogel layer. Due to the small sample used, it is difficult to collect the released liquid water. Therefore, in the next step, we will make larger samples and use centrifugal method to collect the liquid-phase water. Besides, the high osmotic pressure of the polyelectrolyte hydrogel could be used to pump liquid flow in two-phase heat transfer devices, e.g., to replace the capillary wick in heat pipe. The osmotic pressure in hydrogel is a few order of magnitude

higher than the capillary pressure in microporous media, implying the potential of higher critical heat flux when using the osmotic pumping mechanism.

Appendix

Appendix I.

The temperature distribution along the fin can be modeled considering both the convection and evaporation heat losses as follows:

$$k_s A_c \frac{d^2T}{dx^2} - h_c P(T - T_a) - \Delta H_{fg} P\dot{m} = 0 \quad \text{(S1)}$$

$$-k_s \frac{dT}{dx}|_{x=0} = q_t$$

$$\frac{dT}{dx}|_{x=L} = 0$$

where k_s is the solid thermal conductivity of heat sink made of aluminum (~ 100 W m^{-1} K^{-1}); A_c, P and L are the cross-sectional area, perimeter and length of the fin; T_a is the ambient temperature kept at ~ 22 ℃ and ΔH_{fg} is the evaporative latent heat of water ~ 2300 kJ kg^{-1}. q_t is the heat flux through the fin and is related to the heat flux based on the based area q_s by $q_t = q_s(\frac{4P_f^2}{\pi D_f^2})$. $\dot{m}$ is the local evaporative mass flux and is an exponential function of the local temperature $T(x)$ and ambient relative humidity RH (~ 60%) as follows:

$$m^{\cdot} = \phi(x_s - x) \quad \text{(S2)}$$

where $\dot{m}$ is the evaporative flux (kg m^{-2} h^{-1}); ϕ is the evaporation coefficient and is estimated by:

$$\phi = 25 + 19v \quad \text{(S3)}$$

where v is the air speed. For natural convection, v = 0 m s^{-1}. For forced convection, it is determined by the anemometer. It is noted that the unit of ϕ does not match the unit on the left-hand side of the equation because this is an empirical correlation. x_s is the maximum humidity ratio of saturated air at the surface temperature $T(x)$ and for ideal gas, it is given as:

$$x_s = \frac{0.622P_{ws}}{P_a - P_{ws}} \quad \text{(S4)}$$

where P_{ws} is the saturation pressure of water vapor at $T(x)$ and P_a is the atmospheric pressure of moist air ($1.01 \times 10^5\ Pa$). The saturation pressure of water is given by:

$$P_{ws} = \frac{\exp\left(77.345 + 0.0057T_s - \frac{7235}{T_s}\right)}{T_s^{8.2}}) \quad \text{(S5)}$$

x is the humidity ratio:

$$x = \frac{0.622 P_w}{P_a - P_w} \tag{S6}$$

where P_w is the partial pressure of water vapor in the moist air at T_a and is given by:

$$P_w = RH \times P_{ws}^a \tag{S7}$$

where P_{ws}^a is P_{ws} estimated at T_a.

It can be clearly seen that $\dot{m}$ is a highly nonlinear function of $T(x)$ as shown in Figure 8-11A, making Equation S1 difficult to solve analytically. To simplify the model, we linearize $\dot{m}(T)$ by fitting the $\dot{m}(T)$ within a specific temperature range, e.g., from 300 K to 325 K as shown in Figure 8-11B where the linear fitting has high $R^2 > 0.967$. In this case, $\dot{m}(T)$ (in the unit of kg m^{-2} s^{-1}) can be expressed as:

$$\dot{m} = aT + b \tag{S8}$$

where a = 0.0617/3600 kg m^{-2} s^{-1} K^{-1} and b = -18.264/3600 kg m^{-2} s^{-1}. As a result, Equation S1 can be simplified as:

$$k_s A_c \frac{d^2T}{dx^2} - h_c P(T - T_a) - \Delta H_{fg} P(aT + b) = 0 \tag{S9}$$

$$-k_s \frac{dT}{dx}|_{x=0} = q_t$$

$$\frac{dT}{dx}|_{x=L} = 0$$

The dimension of the pin heat sink (i.e., A_c and P) and thermal conductivity of heat sink (k_s = 100 W m^{-1} K^{-1}) are known. The convection heat transfer coefficient for natural convection (i.e., v = 0 m s^{-1}) is given by:

$$h_c = 1.43 \left(\frac{\Delta T}{L}\right)^{1/4} \tag{S10}$$

where L is the length of fin and $\Delta T = T_b - T_a$. For forced convection it is given by:

$$h_c = 0.664 Re_L^{1/2} Pr^{1/3} \tag{S11}$$

where Re_L is the Reynolds number $Re_L = \frac{vL}{v_a}$, v_a is the kinematic viscosity of air at the characteristic temperature $T_c = \frac{T_a + T_b}{2}$, respectively; Pr is the Prandtl number of air, $Pr = \frac{v_a}{\alpha}$ where α is thermal diffusivity of air at T_c. Equation S9 can thus be analytically solved and the temperature distribution along the fin can be obtained:

$$T(x) = \frac{q_t}{k_s\sqrt{A}}\left(\frac{\cosh(\sqrt{A}x)}{\tanh(\sqrt{A}L)} - \sinh(\sqrt{A}x)\right) - \frac{B}{A} \quad \text{(S12)}$$

where $A = \frac{h_c P + a\Delta H_{fg} P}{k_s A_c}$ and $B = \frac{\Delta H_{fg} P b - h_c P T_a}{k_s A_c}$.

Since the h_c is dependent on the base temperature T_b and the $\dot{m}$ is linearized within a certain temperature range (e.g., 300-325 K as shown above), it is necessary to check the following points after simulation:

a. Assumed h_c (based on an assumed T_b) is close to the one calculated on based on the modelled T_b;
b. Calculated T_b is within the presumed temperature range for linearization of $\dot{m}$.

Iteration is conducted until the above criteria are fulfilled.

References

1. https://flowcharts.llnl.gov/.

2. Ho, C.K., and Iverson, B.D. (2014). Review of high-temperature central receiver designs for concentrating solar power. Renewable and Sustainable Energy Reviews *29*, 835-846.

3. Palacios, A., Barreneche, C., Navarro, M., and Ding, Y. (2020). Thermal energy storage technologies for concentrated solar power–A review from a materials perspective. Renewable Energy *156*, 1244-1265.

4. Vignarooban, K., Xu, X., Arvay, A., Hsu, K., and Kannan, A.M. (2015). Heat transfer fluids for concentrating solar power systems–a review. Applied Energy *146*, 383-396.

5. Turchi, C.S., Vidal, J., and Bauer, M. (2018). Molten salt power towers operating at 600–650 C: Salt selection and cost benefits. Solar Energy *164*, 38-46.

6. Chochliouros, I.P., Kourtis, M.-A., Spiliopoulou, A.S., Lazaridis, P., Zaharis, Z., Zarakovitis, C., and Kourtis, A. (2021). Energy efficiency concerns and trends in future 5G network infrastructures. Energies *14*, 5392.

7. Outlook, A.E. (2010). Energy information administration. Department of Energy *92010*, 1-15.

8. Lemar, P., and De Fontaine, A. (2017). Energy data management manual for the wastewater treatment sector. Oak Ridge National Lab.(ORNL), Oak Ridge, TN (United States).

9. Forman, C., Muritala, I.K., Pardemann, R., and Meyer, B. (2016). Estimating the global waste heat potential. Renewable and Sustainable Energy Reviews *57*, 1568-1579.

10. Zeng, J., Cui, S., Wang, Q., and Chen, R. (2019). Multi-layer temperature-responsive hydrogel for forward-osmosis desalination with high permeable flux and fast water release. Desalination *459*, 105-113.

11. Zeng, J., Wang, Q., Shi, Y., Liu, P., and Chen, R. (2019). Osmotic pumping and salt rejection by polyelectrolyte hydrogel for continuous solar desalination. Advanced Energy Materials *9*, 1900552.

12. Ren, H., Tang, M., Guan, B., Wang, K., Yang, J., Wang, F., Wang, M., Shan, J., Chen, Z., and Wei, D. (2017). Hierarchical graphene foam for efficient omnidirectional solar–thermal energy conversion. Advanced Materials *29*, 1702590.

13. Yang, Y., Zhao, R., Zhang, T., Zhao, K., Xiao, P., Ma, Y., Ajayan, P.M., Shi, G., and Chen, Y. (2018). Graphene-Based Standalone Solar Energy Converter for Water Desalination and Purification. ACS nano *12*, 829-835.

14. Zhao, F., Zhou, X., Liu, Y., Shi, Y., Dai, Y., and Yu, G. (2019). Super moisture‐absorbent gels for all‐weather atmospheric water harvesting. Advanced Materials *31*, 1806446.

15. Kim, H., Rao, S.R., Kapustin, E.A., Zhao, L., Yang, S., Yaghi, O.M., and Wang, E.N. (2018). Adsorption-based atmospheric water harvesting device for arid climates. Nature communications *9*, 1-8.

16. Yao, H., Zhang, P., Huang, Y., Cheng, H., Li, C., and Qu, L. (2020). Highly efficient clean water production from contaminated air with a wide humidity range. Advanced Materials *32*, 1905875.

17. Yang, L., Nandakumar, D.K., Miao, L., Suresh, L., Zhang, D., Xiong, T., Vaghasiya, J.V., Kwon, K.C., and Tan, S.C. (2020). Energy harvesting from atmospheric humidity by a hydrogel-integrated ferroelectric-semiconductor system. Joule *4*, 176-188.

18. Nandakumar, D.K., Ravi, S.K., Zhang, Y., Guo, N., Zhang, C., and Tan, S.C. (2018). A super hygroscopic hydrogel for harnessing ambient humidity for energy conservation and harvesting. Energy & Environmental Science *11*, 2179-2187.

19. Schroeder, N., and Albrecht, K. (2021). Assessment of Particle Candidates for Falling Particle Receiver Applications Through Irradiance and Thermal Cycling. (American Society of Mechanical Engineers), pp. V001T002A003.

20. https://www.energy.gov/eere/solar/csp-component-research-and-development.

21. Coventry, J., and Burge, P. (2017). Optical Properties of Pyromark 2500 Coatings of Variable Thicknesses on a Range of Materials for Concentrating Solar Thermal Applications. AIP Conference Proceedings *1850*, 030012. 10.1063/1.4984355.

22. Song, X., Huan, K., Dong, W., Wang, J., Zang, Y., and Shi, X. (2014). Research on infrared radiation characteristics of Pyromark1200 high-temperature coating. Proc. of SPIE *9300*, 93001S. 10.1117/12.2072577.

23. Rubin, E.B., Chen, Y.M., and Chen, R.K. (2019). Optical properties and thermal stability of Cu spinel oxide nanoparticle solar absorber coatings. Sol Energ Mat Sol C *195*, 81-88. 10.1016/j.solmat.2019.02.032.

24. An, X.H., Cheng, J.H., Yin, H.Q., Xie, L.D., and Zhang, P. (2015). Thermal conductivity of high temperature fluoride molten salt determined by laser flash technique. Int J Heat Mass Tran *90*, 872-877. 10.1016/j.ijheatmasstransfer.2015.07.042.

25. Hahn, O., Raether, F., ArduiniSchuster, M.C., and Fricke, J. (1997). Transient coupled conductive/radiative heat transfer in absorbing, emitting and scattering media: Application to laser-flash measurements on ceramic materials. Int J Heat Mass Tran *40*, 689-698. 10.1016/0017-9310(96)00137-8.

26. Nagasaka, Y., and Nagashima, A. (1981). Simultaneous Measurement of the Thermal-Conductivity and the Thermal-Diffusivity of Liquids by the Transient Hot-Wire Method. Rev Sci Instrum *52*, 229-232. 10.1063/1.1136577.

27. Gustafsson, S.E. (1991). Transient Plane Source Techniques for Thermal-Conductivity and Thermal-Diffusivity Measurements of Solid Materials. Rev Sci Instrum *62*, 797-804. 10.1063/1.1142087.

28. Zheng, Q.Y., Kaur, S., Dames, C., and Prasher, R.S. (2020). Analysis and improvement of the hot disk transient plane source method for low thermal conductivity materials. Int J Heat Mass Tran *151*, 119331, 119331. 10.1016/j.ijheatmasstransfer.2020.119331.

29. Cahill, D.G. (1990). Thermal-Conductivity Measurement from 30-K to 750-K: the 3-Omega Method. Rev Sci Instrum *61*, 802-808. 10.1063/1.1141498.

30. Wang, H., and Sen, M. (2009). Analysis of the 3-omega method for thermal conductivity measurement. Int J Heat Mass Tran *52*, 2102-2109. 10.1016/j.ijheatmasstransfer.2008.10.020.

31. Dames, C. (2013). Measuring the thermal conductivity of thin films: 3 omega and related electrothermal methods. In Annual Review of Heat Transfer, pp. 7-49. 10.1615/AnnualRevHeatTransfer.v16.20.

32. Regner, K.T., Sellan, D.P., Su, Z.H., Amon, C.H., McGaughey, A.J.H., and Malen, J.A. (2013). Broadband phonon mean free path contributions to thermal conductivity measured using frequency domain thermoreflectance. Nat Commun *4*, 1640, 1640. 10.1038/ncomms2630.

33. Malen, J.A., Baheti, K., Tong, T., Zhao, Y., Hudgings, J.A., and Majumdar, A. (2011). Optical Measurement of Thermal Conductivity Using Fiber Aligned Frequency Domain Thermoreflectance. J Heat Trans-T Asme *133*, 081601. 10.1115/1.4003545.

34. Cahill, D.G. (2004). Analysis of heat flow in layered structures for time-domain thermoreflectance. Rev Sci Instrum *75*, 5119-5122. 10.1063/1.1819431.

35. Alwi, H.A., Kim, Y.Y., Awang, R., Rahman, S.A., and Krishnaswamy, S. (2013). Measurement of thermophysical properties of hydrogenated amorphous carbon thin films using picosecond thermoreflectance technique. Int J Heat Mass Tran *63*, 199-203. 10.1016/j.ijheatmasstransfer.2013.03.062.

36. Albrecht, K.J., and Ho, C.K. (2019). Heat transfer models of moving packed-bed particle-to-sCO2 heat exchangers. Journal of Solar Energy Engineering *141*, 031006.

37. Fuente, R., Apinaniz, E., and Mendioroz, E. (2011). Simultaneous measurement of thermal diffusivity and optical absorption coefficient using photothermal radiometry. J Appl Phys *110*, 033515. 10.1063/1.3614524.

38. Salazar, A., Fuente, R., Apinaniz, E., Mendioroz, A., and Celorrio, R. (2011). Simultaneous measurement of thermal diffusivity and optical absorption coefficient using photothermal radiometry. II Multilayered solids,. J Appl Phys *110*, 033516. 10.1063/1.3614525.

39. Li, X., Li, J., Lu, J., Xu, N., Chen, C., Min, X., Zhu, B., Li, H., Zhou, L., and Zhu, S. (2018). Enhancement of interfacial solar vapor generation by environmental energy. Joule *2*, 1331-1338.

40. Igor, S. (1993). World fresh water resources. Water in crisis: a guide to the world's. Oxford University Press, Inc, Oxford.

41. Bhushan, B. (2016). Biomimetics: bioinspired hierarchical-structured surfaces for green science and technology (Springer).

42. Shin, S., Wang, Q.Y., Luo, J., and Chen, R.K. (2020). Advanced Materials for High-Temperature Thermal Transport. Adv Funct Mater *30*, 1904815. 10.1002/adfm.201904815.

43. Turchi, C.S., Vidal, J., and Bauer, M. (2018). Molten salt power towers operating at 600-650 degrees C: Salt selection and cost benefits. Sol Energy *164*, 38-46. 10.1016/j.solener.2018.01.063.

44. Marti, J., Haselbacher, A., and Steinfeld, A. (2015). A numerical investigation of gas-particle suspensions as heat transfer media for high-temperature concentrated solar power. Int J Heat Mass Tran *90*, 1056-1070. 10.1016/j.ijheatmasstransfer.2015.07.033.

45. Carrillo, A.J., Gonzalez-Aguilar, J., Romero, M., and Coronado, J.M. (2019). Solar Energy on Demand: A Review on High Temperature Thermochemical Heat Storage Systems and Materials. Chem Rev *119*, 4777-4816. 10.1021/acs.chemrev.8b00315.

46. Clarke, D.R., Oechsner, M., and Padture, N.P. (2012). Thermal-barrier coatings for more efficient gas-turbine engines. M.R.S. Bulletin *37*, 891-902. 10.1557/mrs.2012.232.

47. Curry, N., VanEvery, K., Snyder, T., and Markocsan, N. (2014). Thermal conductivity analysis and lifetime testing of suspension plasma-sprayed thermal barrier coatings. Coatings *4*, 630. 10.3390/coatings4030630.

48. Macias, J.D., Herrera-Zamora, D.M., Lizama-Tzec, F.I., Bante-Guerra, J., Arés-Muzio, O.E., Oskam, G., Rubio, H.R.-P., Alvarado-Gil, J.J., Arancibia-Bulnes, C., Ramos-Sánchez, V., and Villafán-Vidales, H.I. (2017). Optical and thermal properties of selective absorber coatings under CSP conditions. AIP Conference Proceedings *1850*, 120001. 10.1063/1.4984492.

49. Wang, H., and Dinwiddie, R.B. (2000). Reliability of laser flash thermal diffusivity measurements of the thermal barrier coatings. J Therm Spray Techn *9*, 210-214. 10.1361/105996300770349944.

50. Zhao, D., Qian, X., Gu, X., Jajja, S.A., and Yang, R.G. Measurement techniques for thermal conductivity and interfacial thermal conductance of bulk and thin film materials. Journal of Electronic Packaging, *138*, 040802. 10.1115/1.4034605.

51. Zhou, A.J., Wang, W.H., Yang, B., Li, J.Z., and Zhao, Q.W. (2016). Thermal conductivity study of micrometer-thick thermoelectric films by using three-omega methods. Applied Thermal Engineering *98*, 683-689. 10.1016/j.applthermaleng.2015.12.145.

52. Kim, J.H., Feldman, A., and Novotny, D. (1999). Application of the three omega thermal conductivity measurement method to a film on a substrate of finite thickness. Journal of applied physics *86*, 3959-3963.

53. Kaul, P.B., Day, K.A., and Abramson, A.R. (2007). Application of the three omega method for the thermal conductivity measurement of polyaniline. J Appl Phys *101*, 083507. 10.1063/1.2714650.

54. Jiang, P.Q., Qian, X., and Yang, R.G. (2018). Tutorial: Time-domain thermoreflectance (TDTR) for thermal property characterization of bulk and thin film materials. J Appl Phys *124*, 161103. 10.1063/1.5046944.

55. Wang, Y.X., Park, J.Y., Koh, Y.K., and Cahill, D.G. (2010). Thermoreflectance of metal transducers for time-domain thermoreflectance. J Appl Phys *108*, 043507. 10.1063/1.3457151.

56. Wei, L.C., Ehrlich, L.E., Powell-Palm, M.J., Montgomery, C., Beuth, J., and Malen, J.A. (2018). Thermal conductivity of metal powders for powder bed additive manufacturing. Additive Manufacturing *21*, 201-208.

57. Depriester, M., Hus, P., Delenclos, S., and Sahraoui, A.H. (2005). New methodology for thermal parameter measurements in solids using photothermal radiometry. Rev Sci Instrum *76*, 074902. 10.1063/1.1942532.

58. Aissa, K.A., Semmar, N., Meneses, D.D.S., Le Brizoual, L., Gaillard, M., Petit, A., Jouan, P., Boulmer-Leborgne, C., and Djouadi, M.A. (2012). Thermal conductivity measurement of AlN films by fast photothermal method. Journal of Physics: Conference Series *395*, 012089. 10.1088/1742-6596/395/1/012089.

59. Martan, J., Semmar, N., Boulmer-Leborgne, C., Plantin, P., and Le Menn, E. (2006). Thermal characterization of tungsten thin films by pulsed photothermal radiometry. Nanoscale and Microscale Thermophysical Engineering *10*, 333-344. 10.1080/15567260601009189.

60. Martan, J., Semmar, N., Leborgne, C., Le Menn, E., and Mathias, J. (2005). Thermal properties characterization of conductive thin films and surfaces by pulsed lasers. Applied Surface Science *247*, 57-63. 10.1016/j.apsusc.2005.01.062.

61. Pawlak, M., Jukam, N., Kruck, T., Dziczek, D., Ludwig, A., and Wieck, A. (2020). Measurement of thermal transport properties of selected superlattice and thin films using frequency-domain photothermal infrared radiometry. Measurement *166*, 108226.

62. Horny, N., Chirtoc, M., Fleming, A., Hamaoui, G., and Ban, H. (2016). Kapitza thermal resistance studied by high-frequency photothermal radiometry. Applied Physics Letters *109*, 033103.

63. Zambrano-Arjona, M., Medina-Esquivel, R., and Alvarado-Gil, J.J. (2007). Photothermal radiometry monitoring of light curing in resins. J Phys D Appl Phys *40*, 6098. 10.1088/0022-3727/40/19/050.

64. Martan, J., Čapek, J., and Chalhoub, E.A. (2010). Measurement of thermal properties of thin films up to high temperatures—Pulsed photothermal radiometry system and Si–B–C–N films. Rev Sci Instrum *81*, 124902. 10.1063/1.3506638.

65. Assael, M.J., Botsios, S., Gialou, K., and Metaxa, I.N. (2005). Thermal conductivity of polymethyl methacrylate (PMMA) and borosilicate crown glass BK7. Int J Thermophys *26*, 1595-1605. 10.1007/s10765-005-8106-5.

66. Assael, M.J., Gialou, K., Kakosimos, K., and Metaxa, I. (2004). Thermal conductivity of reference solid materials. Int J Thermophys *25*, 397-408. 10.1023/B:IJOT.0000028477.74595.d5.

67. Salmon, D.R., Brandt, R., and Tye, R.P. (2010). Pyroceram 9606, A Certified Ceramic Reference Material For High-Temperature Thermal Transport Properties: Part 2-Certification Measurements. Int J Thermophys *31*, 355-373. 10.1007/s10765-010-0710-3.

68. Salmon, D.R., and Tye, R.P. (2010). Pyroceram 9606, A Certified Ceramic Reference Material for High-Temperature Thermal Transport Properties: Part 1-Material Selection and Characterization. Int J Thermophys *31*, 338-354. 10.1007/s10765-010-0709-9.

69. Wright, A.J., Wang, Q.Y., Huang, C.Y., Nieto, A., Chen, R.K., and Luo, J. (2020). From high-entropy ceramics to compositionally-complex ceramics: A case study of fluorite oxides. J Eur Ceram Soc *40*, 2120-2129. 10.1016/j.jeurceramsoc.2020.01.015.

70. Sweet, J.N., Roth, E.P., and Moss, M. (1987). Thermal-Conductivity of Inconel-718 and 304 Stainless-Steel. Int J Thermophys *8*, 593-606. 10.1007/Bf00503645.

71. Schmidt, A., Chiesa, M., Chen, X.Y., and Chen, G. (2008). An optical pump-probe technique for measuring the thermal conductivity of liquids. Rev Sci Instrum *79*. 10.1063/1.2937458.

72. Salmon, D., Brandt, R., and Tye, R. (2010). Pyroceram 9606, A certified ceramic reference material for high-temperature thermal transport properties: part 2—certification measurements. International Journal of Thermophysics *31*, 355-373.

73. Kim, T.K., VanSaders, B., Caldwell, E., Shin, S., Liu, Z.W., Jin, S.H., and Chen, R.K. (2016). Copper-alloyed spinel black oxides and tandem-structured solar absorbing layers for high-temperature concentrating solar power systems. Sol Energy *132*, 257-266. 10.1016/j.solener.2016.03.007.

74. Rubin, E.B., Chen, Y., and Chen, R. (2019). Optical properties and thermal stability of Cu spinel oxide nanoparticle solar absorber coatings. Solar Energy Materials and Solar Cells *195*, 81-88.

75. Kim, T.K., VanSaders, B., Caldwell, E., Shin, S., Liu, Z., Jin, S., and Chen, R. (2016). Copper-alloyed spinel black oxides and tandem-structured solar absorbing layers for high-temperature concentrating solar power systems. Solar Energy *132*, 257-266.

76. Richet, P., Bouhifd, M.A., Courtial, P., and Tequi, C. (1997). Configurational heat capacity and entropy of borosilicate melts. J Non-Cryst Solids *211*, 271-280. 10.1016/S0022-3093(96)00646-1.

77. Pacheco, J.E., Bradshaw, R.W., Dawson, D.B., De la Rosa, W., Gilbert, R., and Goods, S.H. (2002). Final test and evaluation results from the solar two project. SAND2002-0120.

78. Ho, C.K., Mahoney, A.R., Ambrosini, A., Bencomo, M., Hall, A., and Lambert, T.N. (2012). Characterization of Pyromark 2500 for high-temperature solar receivers. (American Society of Mechanical Engineers Digital Collection), pp. 509-518.

79. Mehos, M., Turchi, C., Vidal, J., Wagner, M., Ma, Z., Ho, C., Kolb, W., Andraka, C., and Kruizenga, A. (2017). Concentrating solar power Gen3 demonstration roadmap. National Renewable Energy Lab.(NREL), Golden, CO (United States).

80. Li, P., Molina, E., Wang, K., Xu, X., Dehghani, G., Kohli, A., Hao, Q., Kassaee, M.H., Jeter, S.M., and Teja, A.S. (2016). Thermal and transport properties of NaCl–KCl–ZnCl2 eutectic salts for new generation high-temperature heat-transfer fluids. Journal of Solar Energy Engineering *138*.

81. Van der Meer, J., and Konings, R. (2007). Thermal and physical properties of molten fluorides for nuclear applications. Journal of nuclear materials *360*, 16-24.

82. Holcomb, D.E., Flanagan, G.F., Mays, G.T., Pointer, W.D., Robb, K.R., and Yoder Jr, G.L. (2013). Fluoride salt-cooled high-temperature reactor technology development and demonstration roadmap. ORNL/TM-2013/401, ORNL, Oak Ridge, TN.

83. Alva, G., Lin, Y., and Fang, G. (2018). An overview of thermal energy storage systems. Energy *144*, 341-378.

84. Hodges, W., and Dames, C. (2019). A multi-frequency 3 ω method for tracking moving phase boundaries. Review of Scientific Instruments *90*, 094903.

85. Clausen, C., Pedersen, T., and Bentien, A. (2017). The 3-omega method for the measurement of fouling thickness, the liquid flow rate, and surface contact. Sensors *17*, 552.

86. Lee, S., Choi, S.-S., Li, S., and, and Eastman, J. (1999). Measuring thermal conductivity of fluids containing oxide nanoparticles.

87. Perkins, R., Roder, H., and de Castro, C.N. (1991). A high-temperature transient hot-wire thermal conductivity apparatus for fluids. Journal of research of the National Institute of Standards and Technology *96*, 247.

88. Sklyarchuk, V., and Plevachuk, Y. (2005). A modified steady state apparatus for thermal conductivity measurements of liquid metals and semiconductors. Measurement Science and Technology *16*, 467.

89. Li, C.H., Williams, W., Buongiorno, J., Hu, L.-W., and Peterson, G. (2008). Transient and steady-state experimental comparison study of effective thermal conductivity of Al2O3/water nanofluids. Journal of heat Transfer *130*.

90. Hepp, C.J., Krogmann, F.T., and Urban, G.A. (2017). Flow rate independent sensing of thermal conductivity in a gas stream by a thermal MEMS-sensor–simulation and experiments. Sensors and Actuators A: Physical *253*, 136-145.

91. Stankus, S., and Savchenko, I. (2009). Laser flash method for measurement of liquid metals heat transfer coefficients. Thermophysics and Aeromechanics *16*, 585-592.

92. Ohta, H., Ogura, G., Waseda, Y., and Suzuki, M. (1990). Thermal diffusivity measurements of molten salts using a three‐layered cell by the laser flash method. Review of scientific instruments *61*, 2645-2649.

93. Hong, J., and Kim, D. (2012). Measuring the thermal conductivity of flowing liquid samples using the three omega method. Journal of heat transfer *134*.

94. Roy-Panzer, S., Kodama, T., Lingamneni, S., Panzer, M.A., Asheghi, M., and Goodson, K.E. (2015). Thermal characterization and analysis of microliter liquid volumes using the three-omega method. Review of Scientific Instruments *86*, 024901.

95. Schmidt, A., Chiesa, M., Chen, X., and Chen, G. (2008). An optical pump-probe technique for measuring the thermal conductivity of liquids. Review of Scientific Instruments *79*, 064902.

96. Reyes-Romero, D., Cubukcu, A.S., and Urban, G. (2014). Determination of thermal properties of gases under flow conditions. (IEEE), pp. 1644-1647.

97. Mehrvand, M., and Putnam, S.A. (2017). Probing the local heat transfer coefficient of water-cooled microchannels using time-domain thermoreflectance. Journal of Heat Transfer *139*.

98. Guo, S., Zhang, J., Wu, W., and Zhou, W. (2018). Corrosion in the molten fluoride and chloride salts and materials development for nuclear applications. Progress in Materials Science *97*, 448-487.

99. Bonk, A., Sau, S., Uranga, N., Hernaiz, M., and Bauer, T. (2018). Advanced heat transfer fluids for direct molten salt line-focusing CSP plants. Progress in Energy and Combustion Science *67*, 69-87.

100. Wingert, M., Zhao, A., Kodera, Y., Obrey, S., and Garay, J. (2020). Frequency-domain hot-wire sensor and 3D model for thermal conductivity measurements of reactive and corrosive materials at high temperatures. Review of Scientific Instruments *91*, 054904.

101. Zeng, J., Chung, K.M., Wang, Q., Wang, X., Pei, Y., Li, P., and Chen, R. (2021). Measurement of High-temperature Thermophysical Properties of Bulk and Coatings Using Modulated Photothermal Radiometry. International Journal of Heat and Mass Transfer *170*, 120989.

102. Wang, C., Mandelis, A., and Liu, Y. (2004). Photothermal radiometry with solid cylindrical samples. Journal of applied physics *96*, 3756-3762.

103. Zhao, D., Qian, X., Gu, X., Jajja, S.A., and Yang, R. (2016). Measurement techniques for thermal conductivity and interfacial thermal conductance of bulk and thin film materials. Journal of Electronic Packaging *138*.

104. Kato, R., and Hatta, I. (2005). Thermal conductivity measurement of thermally-oxidized SiO 2 films on a silicon wafer using a thermo-reflectance technique. International Journal of Thermophysics *26*, 179-190.

105. Hiller, W., Kowalewski, T., and Stella, F. (1993). Onset of natural convection in a cube. International journal of heat and mass transfer *36*, 3251-3263.

106. Parsons Jr, J., and Mulligan, J. (1980). Onset of natural convection from a suddenly heated horizontal cylinder.

107. Davenport, I.F. (1974). The onset of natural convection from time-dependent profiles. International Journal of Heat and Mass Transfer *17*, 69-76.

108. Malen, J.A., Baheti, K., Tong, T., Zhao, Y., Hudgings, J.A., and Majumdar, A. (2011). Optical measurement of thermal conductivity using fiber aligned frequency domain thermoreflectance. Journal of Heat Transfer *133*.

109. Vargaftik, N.B. (1975). Handbook of physical properties of liquids and gases-pure substances and mixtures.

110. Dinçer, İ., and Zamfirescu, C. (2016). Drying phenomena: theory and applications (John Wiley & Sons).

111. https://www.radcoind.com/media/600-EP.pdf.

112. Lerou, J.J., and Froment, G.F. (1977). Velocity, Temperature and Conversion Profiles in Fixed-Bed Catalytic Reactors. Chem Eng Sci *32*, 853-861.

113. You, E.S., Sun, X.M., Chen, F.B., Shi, L., and Zhang, Z.Y. (2017). An improved prediction model for the effective thermal conductivity of compact pebble bed reactors. Nucl Eng Des *323*, 95-102.

114. Liu, S.L., Pu, Y., Cheng, X.M., Li, J., Peng, C.H., Ma, X.B., and Chen, L. (2014). Conceptual design of a water cooled breeder blanket for CFETR. Fusion Eng Des *89*, 1380-1385.

115. Albrecht, K.J., and Ho, C.K. (2019). Design and operating considerations for a shell-and-plate, moving packed bed, particle-to-sCO(2) heat exchanger. Sol Energy *178*, 331-340.

116. Baumann, T., and Zunft, S. (2015). Properties of granular materials as heat transfer and storage medium in CSP application. Sol Energ Mat Sol C *143*, 38-47.

117. Schrader, A.J., Schieber, G.L., Ambrosini, A., and Loutzenhiser, P.G. (2020). Experimental demonstration of a 5 kW(th) granular-flow reactor for solar thermochemical energy storage with aluminum-doped calcium manganite particles. Appl Therm Eng *173*.

118. Prasher, R. (2006). Ultralow thermal conductivity of a packed bed of crystalline nanoparticles: A theoretical study. Phys Rev B *74*.

119. Wang, H., Qu, Z.G., Yin, Y., Bai, J.Q., and He, C. (2021). Prediction of the effective thermal conductivity of an adsorption bed packed with 5A zeolite particles under working conditions. Int J Therm Sci *159*.

120. Zhou, J., Yu, A., and Zhang, Y. (2007). A boundary element method for evaluation of the effective thermal conductivity of packed beds.

121. Van Antwerpen, W., Du Toit, C., and Rousseau, P.G. (2010). A review of correlations to model the packing structure and effective thermal conductivity in packed beds of mono-sized spherical particles. Nuclear Engineering and design *240*, 1803-1818.

122. Cerecedo, L.O.L., Pitalua-Diaz, N., Transito, I.S., Contreras, L.E.V., and Bulnes, C.A. (2013). Optical performance modeling of a solar tower heliostat field and estimation of receiver temperature. (IEEE), pp. 1-6.

123. Albrecht, K.J., and Ho, C.K. (2019). Design and operating considerations for a shell-and-plate, moving packed-bed, particle-to-sCO2 heat exchanger. Solar Energy *178*, 331-340.

124. Sullivan, W.N., and Sabersky, R. (1975). Heat transfer to flowing granular media. International Journal of Heat and Mass Transfer *18*, 97-107.

125. Bird, R.B., Stewart, W.E., and Lightfoot, E.N. (2006). Transport phenomena (John Wiley & Sons).

126. Botterill, J., Salway, A., and Teoman, Y. (1989). The effective thermal conductivity of high temperature particulate beds—II. Model predictions and the implication of the experimental values. International journal of heat and mass transfer *32*, 595-609.

127. Woodside, W., and Messmer, J. (1961). Thermal conductivity of porous media. I. Unconsolidated sands. Journal of applied physics *32*, 1688-1699.

128. Yagi, S., and Kunii, D. (1957). Studies on effective thermal conductivities in packed beds. AIChE Journal *3*, 373-381.

129. Kunii, D., and Smith, J. (1960). Heat transfer characteristics of porous rocks. AIChE Journal *6*, 71-78.

130. Masamune, S., and Smith, J. (1963). Thermal conductivity of beds of spherical particles. Industrial & Engineering Chemistry Fundamentals *2*, 136-143.

131. Godbee, H.W., and Ziegler, W.T. (1966). Thermal conductivities of MgO, Al2O3, and ZrO2 powders to 850 C. II. Theoretical. Journal of Applied Physics *37*, 56-65.

132. Beveridge, G., and Haughey, D. (1971). Axial heat transfer in packed beds. Stagnant beds between 20 and 750 C. International Journal of Heat and Mass Transfer *14*, 1093-1113.

133. Eder, C., Hofer, G., and Pröll, T. (2021). Wall-to-Bed Heat Transfer in Bubbling Fluidized Bed Reactors with an Immersed Heat Exchanger and Continuous Particle Exchange. Industrial & Engineering Chemistry Research *60*, 7417-7428.

134. Ma, Z., Glatzmaier, G., and Mehos, M. (2014). Fluidized bed technology for concentrating solar power with thermal energy storage. Journal of solar energy engineering *136*.

135. Hall, R., and Martin, D. (1981). The thermal conductivity of powder beds. A model, some measurements on UO2 vibro-compacted microspheres, and their correlation. Journal of Nuclear Materials *101*, 172-183.

136. van Antwerpen, W.d., Du Toit, C., and Rousseau, P. (2010). A review of correlations to model the packing structure and effective thermal conductivity in packed beds of mono-sized spherical particles. Nuclear Engineering and design *240*, 1803-1818.

137. Moscardini, M., Gan, Y., Pupeschi, S., and Kamlah, M. (2018). Discrete element method for effective thermal conductivity of packed pebbles accounting for the Smoluchowski effect. Fusion Engineering and Design *127*, 192-201.

138. Chen, L., Wang, C., Moscardini, M., Kamlah, M., and Liu, S. (2019). A DEM-based heat transfer model for the evaluation of effective thermal conductivity of packed beds filled with stagnant fluid: Thermal contact theory and numerical simulation. International Journal of Heat and Mass Transfer *132*, 331-346.

139. Dai, W., Hanaor, D., and Gan, Y. (2019). The effects of packing structure on the effective thermal conductivity of granular media: A grain scale investigation. International Journal of Thermal Sciences *142*, 266-279.

140. Wang, C., Chen, L., and Liu, S. (2019). A DEM-CFD numerical model for the prediction of the effective thermal conductivity of pebble beds with contact conduction. Fusion Engineering and Design *147*, 111257.

141. Desu, R.K., Peeketi, A.R., and Annabattula, R.K. (2020). Influence of bed conditions on the effective thermal conductivity of ceramic breeder pebble beds using thermal DEM (TDEM). Fusion Engineering and Design *159*, 111767.

142. Chung, K.M., Zeng, J., Adapa, S.R., Feng, T., Bagepalli, M.V., Loutzenhiser, P.G., Albrecht, K.J., Ho, C.K., and Chen, R. (2021). Measurement and Analysis of Thermal Conductivity of Ceramic Particle Beds for Solar Thermal Energy Storage. arXiv: 2105.02366.

143. Sakatani, N., Ogawa, K., Iijima, Y., Arakawa, M., Honda, R., and Tanaka, S. (2017). Thermal conductivity model for powdered materials under vacuum based on experimental studies. Aip Adv *7*. Artn 015310
10.1063/1.4975153.

144. Sakatani, N., Ogawa, K., Iijima, Y.-i., Arakawa, M., Honda, R., and Tanaka, S. (2017). Thermal conductivity model for powdered materials under vacuum based on experimental studies. AIP Advances *7*, 015310.

145. Bu, S., Li, Z., Ma, Z., Sun, W., Zhang, L., and Chen, D. (2020). Numerical study of natural convection effects on effective thermal conductivity in a pebble bed. Annals of Nuclear Energy *144*, 107524.

146. Prasher, R. (2006). Ultralow thermal conductivity of a packed bed of crystalline nanoparticles: A theoretical study. Physical Review B *74*, 165413.

147. Hu, X.J., Prasher, R., and Lofgreen, K. (2007). Ultralow thermal conductivity of nanoparticle packed bed. Applied Physics Letters *91*, 203113.

148. Zhang, S., Lane, B., Whiting, J., and Chou, K. (2018). An investigation into metallic powder thermal conductivity in laser powder bed fusion additive manufacturing. (University of Texas at Austin).

149. Merckx, B., Dudoignon, P., Garnier, J., and Marchand, D. (2012). Simplified transient hot-wire method for effective thermal conductivity measurement in geo materials: microstructure and saturation effect. Advances in Civil Engineering *2012*.

150. Zheng, Q., Kaur, S., Dames, C., and Prasher, R.S. (2020). Analysis and improvement of the hot disk transient plane source method for low thermal conductivity materials. International Journal of Heat and Mass Transfer *151*, 119331.

151. Zheng, X., Qiu, L., Su, G., Tang, D., Liao, Y., and Chen, Y. (2011). Thermal conductivity and thermal diffusivity of SiO 2 nanopowder. Journal of Nanoparticle Research *13*, 6887-6893.

152. Goni, M., Patelka, M., Ikeda, S., Sato, T., and Schmidt, A.J. (2018). Frequency domain thermoreflectance technique for measuring the thermal conductivity of individual micro-particles. Review of Scientific Instruments *89*, 074901.

153. Andersson, P., and Bäckström, G. (1976). Thermal conductivity of solids under pressure by the transient hot wire method. Review of Scientific Instruments *47*, 205-209.

154. Millat, J., Vesovic, V., and Wakeham, W. (1996). Transport properties of dilute gases and gaseous mixtures. Transport properties of fluids, 29-65.

155. Nagasaka, Y., and Nagashima, A. (1981). Absolute measurement of the thermal conductivity of electrically conducting liquids by the transient hot-wire method. Journal of Physics E: Scientific Instruments *14*, 1435.

156. Kang, C., Park, Y.-H., Van Lew, J.T., Ying, A., Abdou, M., and Cho, S. (2017). Transient hot-wire experimental system for measuring the effective thermal conductivity of a ceramic breeder pebble bed. Fusion Science and Technology *72*, 263-270.

157. Haarman, J. (1971). A contribution to the theory of the transient hot-wire method. Physica *52*, 605-619.

158. Healy, J., De Groot, J., and Kestin, J. (1976). The theory of the transient hot-wire method for measuring thermal conductivity. Physica B+ c *82*, 392-408.

159. Vozár, L. (1996). A computer-controlled apparatus for thermal conductivity measurement by the transient hot wire method. Journal of thermal analysis *46*, 495-505.

160. Arblaster, J.W. (2015). Selected electrical resistivity values for the platinum group of metals Part I: palladium and platinum. Johnson Matthey Technology Review *59*, 174-181.

161. Siegel, N., Gross, M., Ho, C., Phan, T., and Yuan, J. (2014). Physical properties of solid particle thermal energy storage media for concentrating solar power applications. Energy Procedia *49*, 1015-1023.

162. Siegel, N.P., Gross, M.D., and Coury, R. (2015). The development of direct absorption and storage media for falling particle solar central receivers. Journal of Solar Energy Engineering *137*.

163. Chase Jr, M.W. (1998). NIST-JANAF thermochemical tables. J. Phys. Chem. Ref. Data, Monograph *9*.

164. Broeke, J., Pérez, J.M.M., and Pascau, J. (2015). Image processing with ImageJ (Packt Publishing Ltd).

165. Kumari, R., and Rana, N. (2015). Particle size and shape analysis using Imagej with customized tools for segmentation of particles. Int. J. Eng. Res *4*, 23-28.

166. Igathinathane, C., Pordesimo, L., Columbus, E., Batchelor, W., and Methuku, S. (2008). Shape identification and particles size distribution from basic shape parameters using ImageJ. Computers and electronics in agriculture *63*, 168-182.

167. Siegel, N., Kolb, G., Kim, K., Rangaswamy, V., and Moujaes, S. (2007). Solid Particle Receiver Flow Characerization Studies. pp. 877-883.

168. Siegel, N.P., Ho, C.K., Khalsa, S.S., and Kolb, G.J. (2010). Development and evaluation of a prototype solid particle receiver: on-sun testing and model validation. Journal of solar energy engineering *132*.

169. Albrecht, K.J., and Ho, C.K. (2018). High-temperature flow testing and heat transfer for a moving packed-bed particle/sCO2 heat exchanger. In 1. (AIP Publishing LLC), pp. 040003.

170. Gupta, M., Yang, J., and Roy, C. (2002). Modelling the effective thermal conductivity in polydispersed bed systems: a unified approach using the linear packing theory and unit cell model. The Canadian Journal of Chemical Engineering *80*, 830-839.

171. Xu, M., Abdou, M.A., and Raffray, A.R. (1995). Thermal conductivity of a beryllium gas packed bed. Fusion engineering and design *27*, 240-246.

172. Cahill, D.G. (1990). Thermal conductivity measurement from 30 to 750 K: the 3ω method. Review of scientific instruments *61*, 802-808.

173. Kloss, C., Goniva, C., Hager, A., Amberger, S., and Pirker, S. (2012). Models, algorithms and validation for opensource DEM and CFD–DEM. Progress in Computational Fluid Dynamics, an International Journal *12*, 140-152.

174. Du Toit, C.G. (2008). Radial variation in porosity in annular packed beds. Nuclear engineering and design *238*, 3073-3079.

175. Martin, H. (1978). Low Peclet number particle-to-fluid heat and mass transfer in packed beds. Chemical Engineering Science *33*, 913-919.

176. De Klerk, A. (2003). Voidage variation in packed beds at small column to particle diameter ratio. AIChE journal *49*, 2022-2029.

177. Yarrington, J.D., Bagepalli, M.V., Pathikonda, G., Schrader, A.J., Zhang, Z.M., Ranjan, D., and Loutzenhiser, P.G. (2021). Numerical analyses of high temperature dense, granular flows coupled to high temperature flow property measurements for solar thermal energy storage. Solar Energy *213*, 350-360.

178. Schonhorn, H. (1965). Theoretical relationship between surface tension and cohesive energy density. The Journal of Chemical Physics *43*, 2041-2043.

179. Becher, P. (1972). The calculation of cohesive energy density from the surface tension of liquids. Journal of Colloid and Interface Science *38*, 291-293.

180. Sasaki, S., Kou, H., Masuda, H., and Kiyohashi, H. (2004). Total hemispherical emissivity of glass sheets with different thicknesses measured by a transient calorimetric.

181. Johnson, K.L., Kendall, K., and Roberts, a. (1971). Surface energy and the contact of elastic solids. Proceedings of the royal society of London. A. mathematical and physical sciences *324*, 301-313.

182. Morris, A., Pannala, S., Ma, Z., and Hrenya, C. (2015). A conductive heat transfer model for particle flows over immersed surfaces. International Journal of Heat and Mass Transfer *89*, 1277-1289.

183. Presley, M.A., and Christensen, P.R. (1997). Thermal conductivity measurements of particulate materials 2. Results. Journal of Geophysical Research: Planets *102*, 6551-6566.

184. Spelt, J., Brennen, C., and Sabersky, R. (1982). Heat transfer to flowing granular material. International Journal of Heat and Mass Transfer *25*, 791-796.

185. Denloye, A., and Botterill, J. (1977). Heat transfer in flowing packed beds. Chemical Engineering Science *32*, 461-465.

186. Botterill, J., and Denloye, A. (1978). A theoretical model of heat transfer to a packed or quiescent fluidized bed. Chemical Engineering Science *33*, 509-515.

187. Kubie, J., and Broughton, J. (1975). A model of heat transfer in gas fluidized beds. International Journal of Heat and Mass Transfer *18*, 289-299.

188. Watkins, M.F., Chilamkurti, Y.N., and Gould, R.D. (2020). Analytic Modeling of Heat Transfer to Vertical Dense Granular Flows. Journal of Heat Transfer *142*, 022103.

189. Watkins, M.F., Chilamkurti, Y.N., and Gould, R.D. (2018). Effective Thermal Conductivity of Wall-Adjacent Layer in Gravity-Driven Vertical Dense Granular Flows. (American Society of Mechanical Engineers), pp. V001T011A005.

190. Fang, W., Chen, S., Xu, J., and Zeng, K. (2021). Predicting heat transfer coefficient of a shell-and-plate, moving packed-bed particle-to-sCO2 heat exchanger for concentrating solar power. Energy *217*, 119389.

191. Yu, Y., Nie, F., Bai, F., and Wang, Z. (2021). Theoretical and experimental investigation on heating moving packed beds in a single tube with constant wall temperature. International Journal of Heat and Mass Transfer *180*, 121725.

192. Zou, R., and Yu, A. (1995). The packing of spheres in a cylindrical container: the thickness effect. Chemical engineering science *50*, 1504-1507.

193. Benyahia, F. (2004). On the modeling of flow in packed bed systems. Particulate science and technology *22*, 367-378.

194. Saitoh, K. (2012). Kinetic Theory of Granular Gases. University of Twente.

195. Utter, B., and Behringer, R.P. (2004). Self-diffusion in dense granular shear flows. Physical Review E *69*, 031308.

196. Hsiau, S.-S., and Shieh, Y.-M. (1999). Fluctuations and self-diffusion of sheared granular material flows. Journal of Rheology *43*, 1049-1066.

197. Carnahan, N.F., and Starling, K.E. (1969). Equation of state for nonattracting rigid spheres. The Journal of chemical physics *51*, 635-636.

198. Natarajan, V., Hunt, M., and Taylor, E. (1995). Local measurements of velocity fluctuations and diffusion coefficients for a granular material flow. Journal of Fluid Mechanics *304*, 1-25.

199. Chapman, S., and Cowling, T.G. (1990). The mathematical theory of non-uniform gases: an account of the kinetic theory of viscosity, thermal conduction and diffusion in gases (Cambridge university press).

200. Savage, S., and Dai, R. (1993). Studies of granular shear flows wall slip velocities,'layering'and self-diffusion. Mechanics of Materials *16*, 225-238.

201. Hsiau, S., and Hunt, M. (1993). Kinetic theory analysis of flow-induced particle diffusion and thermal conduction in granular material flows.

202. Hunt, M. (1997). Discrete element simulations for granular material flows: effective thermal conductivity and self-diffusivity. International journal of heat and mass transfer *40*, 3059-3068.

203. Al-Ansary, H., El-Leathy, A., Al-Suhaibani, Z., Jeter, S., Sadowski, D., Alrished, A., and Golob, M. (2012). Experimental study of a sand–air heat exchanger for use with a high-temperature solar gas turbine system. Journal of solar energy engineering *134*.

204. Huerta, D., and Ruiz-Suárez, J. (2004). Vibration-induced granular segregation: a phenomenon driven by three mechanisms. Physical Review Letters *92*, 114301.

205. Schröter, M., Ulrich, S., Kreft, J., Swift, J.B., and Swinney, H.L. (2006). Mechanisms in the size segregation of a binary granular mixture. Physical review E *74*, 011307.

206. Sun, J., Battaglia, F., and Subramaniam, S. (2006). Dynamics and structures of segregation in a dense, vibrating granular bed. Physical Review E *74*, 061307.

207. Albrecht, K.J., and Ho, C.K. (2017). Heat Transfer Models of Moving Packed-Bed Particle-to-SCO2 Heat Exchangers. (American Society of Mechanical Engineers Digital Collection).

208. Chung, K.M., Zeng, J., Adapa, S.R., Feng, T., Bagepalli, M.V., Loutzenhiser, P.G., Albrecht, K.J., Ho, C.K., and Chen, R. (2021). Measurement and Analysis of Thermal Conductivity of Ceramic Particle Beds for Solar Thermal Energy Storage. arXiv preprint arXiv:2105.02366.

209. Özisik, M.N., and Orlande, H.R. (2021). Inverse heat transfer: fundamentals and applications (CRC press).

210. Cath, T.Y., Childress, A.E., and Elimelech, M. (2006). Forward osmosis: principles, applications, and recent developments. Journal of membrane science *281*, 70-87.

211. Chung, T.-S., Zhang, S., Wang, K.Y., Su, J., and Ling, M.M. (2012). Forward osmosis processes: yesterday, today and tomorrow. Desalination *287*, 78-81.

212. Elimelech, M., and Phillip, W.A. (2011). The future of seawater desalination: energy, technology, and the environment. science *333*, 712-717.

213. Hoover, L.A., Phillip, W.A., Tiraferri, A., Yip, N.Y., and Elimelech, M. (2011). Forward with osmosis: emerging applications for greater sustainability. Environmental science & technology *45*, 9824-9830.

214. McGinnis, R.L., and Elimelech, M. (2008). Global challenges in energy and water supply: the promise of engineered osmosis. Environmental science & technology *42*, 8625-8629.

215. Zhao, S., Zou, L., Tang, C.Y., and Mulcahy, D. (2012). Recent developments in forward osmosis: opportunities and challenges. Journal of membrane science *396*, 1-21.

216. Su, J., Zhang, S., Ling, M.M., and Chung, T.-S. (2012). Forward osmosis: an emerging technology for sustainable supply of clean water. Clean Technologies and Environmental Policy *14*, 507-511.

217. Luo, H., Wang, Q., Tao, T., Zhang, T.C., and Zhou, A. (2014). Performance of strong ionic hydrogels based on 2-acrylamido-2-methylpropane sulfonate as draw agents for forward osmosis. Journal of Environmental Engineering *140*, 04014044.

218. Ge, Q., Ling, M., and Chung, T.-S. (2013). Draw solutions for forward osmosis processes: developments, challenges, and prospects for the future. Journal of membrane science *442*, 225-237.

219. Achilli, A., Cath, T.Y., and Childress, A.E. (2010). Selection of inorganic-based draw solutions for forward osmosis applications. Journal of membrane science *364*, 233-241.

220. Johnson, D.J., Suwaileh, W.A., Mohammed, A.W., and Hilal, N. (2017). Osmotic's potential: An overview of draw solutes for forward osmosis. Desalination.

221. Al-Karaghouli, A., and Kazmerski, L.L. (2013). Energy consumption and water production cost of conventional and renewable-energy-powered desalination processes. Renewable and Sustainable Energy Reviews *24*, 343-356.

222. Al-Obaidani, S., Curcio, E., Macedonio, F., Di Profio, G., Al-Hinai, H., and Drioli, E. (2008). Potential of membrane distillation in seawater desalination: thermal efficiency, sensitivity study and cost estimation. Journal of Membrane Science *323*, 85-98.

223. Phillip, W.A., Yong, J.S., and Elimelech, M. (2010). Reverse draw solute permeation in forward osmosis: modeling and experiments. Environmental science & technology *44*, 5170-5176.

224. Luo, H., Wang, Q., Zhang, T.C., Tao, T., Zhou, A., Chen, L., and Bie, X. (2014). A review on the recovery methods of draw solutes in forward osmosis. Journal of Water Process Engineering *4*, 212-223.

225. Lu, Y., Chen, T., Mei, A., Chen, T., Ding, Y., Zhang, X., Xu, J., Fan, Z., and Du, B. (2013). Solution behaviors and microstructures of PNIPAm-P123-PNIPAm pentablock terpolymers in dilute and concentrated aqueous solutions. Physical Chemistry Chemical Physics *15*, 8276-8286.

226. Grinberg, V.Y., Dubovik, A.S., Kuznetsov, D.V., Grinberg, N.V., Grosberg, A.Y., and Tanaka, T. (2000). Studies of the thermal volume transition of poly (N-isopropylacrylamide) hydrogels by high-sensitivity differential scanning microcalorimetry. 2. Thermodynamic functions. Macromolecules *33*, 8685-8692.

227. Cho, E.C., Lee, J., and Cho, K. (2003). Role of bound water and hydrophobic interaction in phase transition of poly (N-isopropylacrylamide) aqueous solution. Macromolecules *36*, 9929-9934.

228. Zhang, K., Wu, W., Guo, K., Chen, J., and Zhang, P. (2010). Synthesis of temperature-responsive poly (N-isopropyl acrylamide)/poly (methyl methacrylate)/silica hybrid capsules from inverse pickering emulsion polymerization and their application in controlled drug release. Langmuir : the ACS journal of surfaces and colloids *26*, 7971-7980.

229. Chen, L.B., Zhang, F., and Wang, C.C. (2009). Rational synthesis of magnetic thermosensitive microcontainers as targeting drug carriers. Small *5*, 621-628.

230. Huang, G., Gao, J., Hu, Z., John, J.V.S., Ponder, B.C., and Moro, D. (2004). Controlled drug release from hydrogel nanoparticle networks. Journal of Controlled Release *94*, 303-311.

231. Okano, T., Bae, Y., Jacobs, H., and Kim, S. (1990). Thermally on-off switching polymers for drug permeation and release. Journal of Controlled Release *11*, 255-265.

232. Maurdev, G., and Millington, K.R. (2009). Potential for desalination using lower critical solution temperature polymers: Concentration of salt solutions by pluronic PE6200. Journal of applied polymer science *113*, 2346-2352.

233. Li, D., Zhang, X., Simon, G.P., and Wang, H. (2013). Forward osmosis desalination using polymer hydrogels as a draw agent: Influence of draw agent, feed solution and membrane on process performance. Water research *47*, 209-215.

234. Tamai, Y., Tanaka, H., and Nakanishi, K. (1996). Molecular dynamics study of polymer− water interaction in hydrogels. 1. Hydrogen-bond structure. Macromolecules *29*, 6750-6760.

235. Razmjou, A., Liu, Q., Simon, G.P., and Wang, H. (2013). Bifunctional polymer hydrogel layers as forward osmosis draw agents for continuous production of fresh water using solar energy. Environmental science & technology *47*, 13160-13166.

236. Ou, R., Wang, Y., Wang, H., and Xu, T. (2013). Thermo-sensitive polyelectrolytes as draw solutions in forward osmosis process. Desalination *318*, 48-55.

237. Li, D., Zhang, X., Yao, J., Zeng, Y., Simon, G.P., and Wang, H. (2011). Composite polymer hydrogels as draw agents in forward osmosis and solar dewatering. Soft Matter *7*, 10048-10056.

238. Zeng, Y., Qiu, L., Wang, K., Yao, J., Li, D., Simon, G.P., Wang, R., and Wang, H. (2013). Significantly enhanced water flux in forward osmosis desalination with polymer-graphene composite hydrogels as a draw agent. Rsc Advances *3*, 887-894.

239. McGovern, R.K. (2014). On the potential of forward osmosis to energetically outperform reverse osmosis desalination. Journal of Membrane Science *469*, 245-250.

240. Cai, Y., Shen, W., Loo, S.L., Krantz, W.B., Wang, R., Fane, A.G., and Hu, X. (2013). Towards temperature driven forward osmosis desalination using Semi-IPN hydrogels as reversible draw agents. Water research *47*, 3773-3781.

241. Hartanto, Y., Yun, S., Jin, B., and Dai, S. (2015). Functionalized thermo-responsive microgels for high performance forward osmosis desalination. Water research *70*, 385-393.

242. Zhao, D., Wang, P., Zhao, Q., Chen, N., and Lu, X. (2014). Thermoresponsive copolymer-based draw solution for seawater desalination in a combined process of forward osmosis and membrane distillation. Desalination *348*, 26-32.

243. Hirotsu, S., Hirokawa, Y., and Tanaka, T. (1987). Volume‐phase transitions of ionized N‐isopropylacrylamide gels. The Journal of chemical physics *87*, 1392-1395.

244. Sato Matsuo, E., and Tanaka, T. (1988). Kinetics of discontinuous volume–phase transition of gels. The Journal of chemical physics *89*, 1695-1703.

245. Wang, L., Shelton, R., Cooper, P., Lawson, M., Triffitt, J., and Barralet, J. (2003). Evaluation of sodium alginate for bone marrow cell tissue engineering. Biomaterials *24*, 3475-3481.

246. Naghieh, S., Karamooz-Ravari, M.R., Sarker, M., Karki, E., and Chen, X. (2018). Influence of crosslinking on the mechanical behavior of 3D printed alginate scaffolds: Experimental and numerical approaches. Journal of the Mechanical Behavior of Biomedical Materials.

247. Cheng, H., Liu, G., Wang, C., Zhang, G., and Wu, C. (2006). Collapse and swelling of poly (N‐isopropylacrylamide‐co‐sodium acrylate) copolymer brushes grafted on a flat SiO2 surface. Journal of Polymer Science Part B: Polymer Physics *44*, 770-778.

248. Maeda, Y., Yamamoto, H., and Ikeda, I. (2004). Effects of ionization on the phase behavior of poly (N-isopropylacrylamide-co-acrylic acid) and poly (N, N-diethylacrylamide-co-acrylic acid) in water. Colloid and Polymer Science *282*, 1268-1273.

249. Maeda, Y., Higuchi, T., and Ikeda, I. (2001). FTIR spectroscopic and calorimetric studies of the phase transitions of N-isopropylacrylamide copolymers in water. Langmuir : the ACS journal of surfaces and colloids *17*, 7535-7539.

250. Maeda, Y., Higuchi, T., and Ikeda, I. (2000). Change in hydration state during the coil− globule transition of aqueous solutions of poly (N-isopropylacrylamide) as evidenced by FTIR spectroscopy. Langmuir : the ACS journal of surfaces and colloids *16*, 7503-7509.

251. Mohan, Y., Premkumar, T., Joseph, D., and Geckeler, K. (2007). Stimuli-responsive poly (N-isopropylacrylamide-co-sodium acrylate) hydrogels: A swelling study in surfactant and polymer solutions. Reactive and Functional Polymers *67*, 844-858.

252. Li, D., Zhang, X., Yao, J., Simon, G.P., and Wang, H. (2011). Stimuli-responsive polymer hydrogels as a new class of draw agent for forward osmosis desalination. Chemical Communications *47*, 1710-1712.

253. Razmjou, A., Barati, M.R., Simon, G.P., Suzuki, K., and Wang, H. (2013). Fast deswelling of nanocomposite polymer hydrogels via magnetic field-induced

heating for emerging FO desalination. Environmental science & technology *47*, 6297-6305.

254. Hartanto, Y., Zargar, M., Cui, X., Shen, Y., Jin, B., and Dai, S. (2016). Thermoresponsive cationic copolymer microgels as high performance draw agents in forward osmosis desalination. Journal of Membrane Science *518*, 273-281.

255. Holman, J.P., and Gajda, W.J. (2001). Experimental methods for engineers (McGraw-Hill New York).

256. Li, Z., Xiong, D.a., Xu, B., Wu, C., An, Y., Ma, R., and Shi, L. (2009). Fabrication of an asymmetric hollow particle with a thermo-sensitive PNIPAM inside corona. Polymer *50*, 825-831.

257. Jones, C.D., and Lyon, L.A. (2003). Shell-restricted swelling and core compression in poly (N-isopropylacrylamide) core− shell microgels. Macromolecules *36*, 1988-1993.

258. Fan, X., Liu, H., Gao, Y., Zou, Z., Craig, V.S., Zhang, G., and Liu, G. (2016). Forward‐Osmosis Desalination with Poly (Ionic Liquid) Hydrogels as Smart Draw Agents. Advanced Materials *28*, 4156-4161.

259. Zhang, H., Li, J., Cui, H., Li, H., and Yang, F. (2015). Forward osmosis using electric-responsive polymer hydrogels as draw agents: influence of freezing–thawing cycles, voltage, feed solutions on process performance. Chemical Engineering Journal *259*, 814-819.

260. Ge, Q., Su, J., Amy, G.L., and Chung, T.-S. (2012). Exploration of polyelectrolytes as draw solutes in forward osmosis processes. Water research *46*, 1318-1326.

261. Koschikowski, J., Wieghaus, M., and Rommel, M. (2003). Solar thermal-driven desalination plants based on membrane distillation. Desalination *156*, 295-304.

262. Banat, F., Jwaied, N., Rommel, M., Koschikowski, J., and Wieghaus, M. (2007). Desalination by a "compact SMADES" autonomous solarpowered membrane distillation unit. Desalination *217*, 29-37.

263. Banat, F., Jwaied, N., Rommel, M., Koschikowski, J., and Wieghaus, M. (2007). Performance evaluation of the "large SMADES" autonomous desalination solar-driven membrane distillation plant in Aqaba, Jordan. Desalination *217*, 17-28.

264. Winter, D., Koschikowski, J., and Wieghaus, M. (2011). Desalination using membrane distillation: Experimental studies on full scale spiral wound modules. Journal of Membrane Science *375*, 104-112.

265. De Andres, M., Doria, J., Khayet, M., Pena, L., and Mengual, J. (1998). Coupling of a membrane distillation module to a multieffect distiller for pure water production. Desalination *115*, 71-81.

266. Raluy, R.G., Schwantes, R., Subiela, V.J., Peñate, B., Melián, G., and Betancort, J.R. (2012). Operational experience of a solar membrane distillation demonstration plant in Pozo Izquierdo-Gran Canaria Island (Spain). Desalination *290*, 1-13.

267. Meindersma, G., Guijt, C., and De Haan, A. (2006). Desalination and water recycling by air gap membrane distillation. Desalination *187*, 291-301.

268. Yoo, M.K., Sung, Y.K., Chong, S.C., and Young, M.L. (1997). Effect of polymer complex formation on the cloud-point of poly (N-isopropyl acrylamide)(PNIPAAm) in the poly (NIPAAm-co-acrylic acid): polyelectrolyte complex between poly (acrylic acid) and poly (allylamine). Polymer *38*, 2759-2765.

269. Jain, K., Vedarajan, R., Watanabe, M., Ishikiriyama, M., and Matsumi, N. (2015). Tunable LCST behavior of poly (N-isopropylacrylamide/ionic liquid) copolymers. Polymer Chemistry *6*, 6819-6825.

270. Lee, H., He, F., Song, L., Gilron, J., and Sirkar, K.K. (2011). Desalination with a cascade of cross‐flow hollow fiber membrane distillation devices integrated with a heat exchanger. AIChE Journal *57*, 1780-1795.

271. Song, L., Li, B., Sirkar, K.K., and Gilron, J.L. (2007). Direct contact membrane distillation-based desalination: novel membranes, devices, larger-scale studies, and a model. Industrial & engineering chemistry research *46*, 2307-2323.

272. Moustafa, S., Jarrar, D., and El-Mansy, H. (1985). Performance of a self-regulating solar multistage flash desalination system. Solar Energy *35*, 333-340.

273. Tzen, E., Theofilloyianakos, D., and Kologios, Z. (2008). Autonomous reverse osmosis units driven by RE sources experiences and lessons learned. Desalination *221*, 29-36.

274. Mohamed, E.S., and Papadakis, G. (2004). A stand alone sea water reverse osmosis desalination unit powered by hybrid wind-photovoltaic system for rural development and small villages.

275. Li, D., and Wang, H. (2013). Smart draw agents for emerging forward osmosis application. Journal of Materials Chemistry A *1*, 14049-14060.

276. Gupta, M., and Kaushik, S. (2010). Exergy analysis and investigation for various feed water heaters of direct steam generation solar–thermal power plant. Renewable Energy *35*, 1228-1235.

277. Neumann, O., Feronti, C., Neumann, A.D., Dong, A., Schell, K., Lu, B., Kim, E., Quinn, M., Thompson, S., and Grady, N. (2013). Compact solar autoclave based on steam generation using broadband light-harvesting nanoparticles. Proceedings of the National Academy of Sciences *110*, 11677-11681.

278. Zhao, F., Zhou, X., Shi, Y., Qian, X., Alexander, M., Zhao, X., Mendez, S., Yang, R., Qu, L., and Yu, G. (2018). Highly efficient solar vapour generation via hierarchically nanostructured gels. Nature nanotechnology *13*, 489.

279. Cavusoglu, A.-H., Chen, X., Gentine, P., and Sahin, O. (2017). Potential for natural evaporation as a reliable renewable energy resource. Nature communications *8*, 617.

280. Hu, X., Xu, W., Zhou, L., Tan, Y., Wang, Y., Zhu, S., and Zhu, J. (2017). Tailoring Graphene Oxide‐Based Aerogels for Efficient Solar Steam Generation under One Sun. Advanced materials *29*, 1604031.

281. Ito, Y., Tanabe, Y., Han, J., Fujita, T., Tanigaki, K., and Chen, M. (2015). Multifunctional Porous Graphene for High‐Efficiency Steam Generation by Heat Localization. Advanced materials *27*, 4302-4307.

282. Li, Y., Alibakhshi, M.A., Zhao, Y., and Duan, C. (2017). Exploring ultimate water capillary evaporation in nanoscale conduits. Nano letters *17*, 4813-4819.

283. Ni, G., Li, G., Boriskina, S.V., Li, H., Yang, W., Zhang, T., and Chen, G. (2016). Steam generation under one sun enabled by a floating structure with thermal concentration. Nature Energy *1*, nenergy2016126.

284. Chang, C., Yang, C., Liu, Y., Tao, P., Song, C., Shang, W., Wu, J., and Deng, T. (2016). Efficient solar-thermal energy harvest driven by interfacial plasmonic heating-assisted evaporation. ACS applied materials & interfaces *8*, 23412-23418.

285. Chen, C., Li, Y., Song, J., Yang, Z., Kuang, Y., Hitz, E., Jia, C., Gong, A., Jiang, F., and Zhu, J. (2017). Highly flexible and efficient solar steam generation device. Advanced materials *29*, 1701756.

286. Zhang, Y., Ravi, S.K., Vaghasiya, J.V., and Tan, S.C. (2018). A Barbeque-Analog Route to Carbonize Moldy Bread for Efficient Steam Generation. iScience *3*, 31-39.

287. Ghasemi, H., Ni, G., Marconnet, A.M., Loomis, J., Yerci, S., Miljkovic, N., and Chen, G. (2014). Solar steam generation by heat localization. Nature communications *5*, ncomms5449.

288. Zhang, X., Kan, W., Jiang, H., Chen, Y., Cheng, T., Jiang, H., and Hu, X. (2017). Capillary-driven low grade heat desalination. Desalination *410*, 10-18.

289. Finnerty, C., Zhang, L., Sedlak, D.L., Nelson, K.L., and Mi, B. (2017). Synthetic graphene oxide leaf for solar desalination with zero liquid discharge. Environmental science & technology *51*, 11701-11709.

290. Bacchin, P., Derekx, Q., Veyret, D., Glucina, K., and Moulin, P. (2014). Clogging of microporous channels networks: role of connectivity and tortuosity. Microfluidics and nanofluidics *17*, 85-96.

291. Shi, L., Shi, Y., Li, R., Chang, J., Zaouri, N., Ahmed, E., Jin, Y., Zhang, C., Zhuo, S., and Wang, P. (2018). SiC–C Composite as a Highly Stable and Easily Regenerable Photothermal Material for Practical Water Evaporation. ACS Sustainable Chemistry & Engineering *6*, 8192-8200.

292. Ni, G., Zandavi, S.H., Javid, S.M., Boriskina, S.V., Cooper, T.A., and Chen, G. (2018). A salt-rejecting floating solar still for low-cost desalination. Energy & Environmental Science *11*, 1510-1519.

293. Xu, W., Hu, X., Zhuang, S., Wang, Y., Li, X., Zhou, L., Zhu, S., and Zhu, J. (2018). Flexible and salt resistant Janus absorbers by electrospinning for stable and efficient solar desalination. Advanced Energy Materials *8*, 1702884.

294. Chen, C., Kuang, Y., and Hu, L. (2019). Challenges and Opportunities for Solar Evaporation. Joule.

295. Li, J., Suo, Z., and Vlassak, J.J. (2014). A model of ideal elastomeric gels for polyelectrolyte gels. Soft matter *10*, 2582-2590.

296. Nandakumar, D.K., Zhang, Y., Ravi, S.K., Guo, N., Zhang, C., and Tan, S.C. (2019). Solar Energy Triggered Clean Water Harvesting from Humid Air Existing above Sea Surface Enabled by a Hydrogel with Ultrahigh Hygroscopicity. Advanced materials *31*, 1806730.

297. Höpfner, J., Klein, C., and Wilhelm, M. (2010). A novel approach for the desalination of seawater by means of reusable poly (acrylic acid) hydrogels and mechanical force. Macromolecular rapid communications *31*, 1337-1342.

298. Ali, W., Gebert, B., Hennecke, T., Graf, K., Ulbricht, M., and Gutmann, J.S. (2015). Design of thermally responsive polymeric hydrogels for brackish water desalination: effect of architecture on swelling, deswelling, and salt rejection. ACS applied materials & interfaces *7*, 15696-15706.

299. Yasuda, H., Lamaze, C., and Peterlin, A. (1971). Diffusive and hydraulic permeabilities of water in water‐swollen polymer membranes. Journal of Polymer Science Part A‐2: Polymer Physics *9*, 1117-1131.

300. Sagle, A.C., Ju, H., Freeman, B.D., and Sharma, M.M. (2009). PEG-based hydrogel membrane coatings. Polymer *50*, 756-766.

301. Nagai, K., Tanaka, S., Hirata, Y., Nakagawa, T., Arnold, M.E., Freeman, B.D., Leroux, D., Betts, D.E., DeSimone, J.M., and DiGiano, F.A. (2001). Solubility and diffusivity of sodium chloride in phase-separated block copolymers of poly (2-dimethylaminoethyl methacrylate), poly (1, 1′ -dihydroperfluorooctyl methacrylate) and poly (1, 1, 2, 2-tetrahydroperfluorooctyl acrylate). Polymer *42*, 09941-09948.

302. Crank, J. (1979). The mathematics of diffusion (Oxford university press).

303. Ju, H., Sagle, A.C., Freeman, B.D., Mardel, J.I., and Hill, A.J. (2010). Characterization of sodium chloride and water transport in crosslinked poly (ethylene oxide) hydrogels. Journal of Membrane Science *358*, 131-141.

304. Wang, J.H. (1965). Self-diffusion coefficients of water. The Journal of Physical Chemistry *69*, 4412-4412.

305. https://power.larc.nasa.gov/data-access-viewer/.

306. Wang, X., He, Y., Liu, X., Cheng, G., and Zhu, J. (2017). Solar steam generation through bio-inspired interface heating of broadband-absorbing plasmonic membranes. Applied energy *195*, 414-425.

307. Ni, G., Miljkovic, N., Ghasemi, H., Huang, X., Boriskina, S.V., Lin, C.-T., Wang, J., Xu, Y., Rahman, M.M., and Zhang, T. (2015). Volumetric solar heating of nanofluids for direct vapor generation. Nano Energy *17*, 290-301.

308. Wang, Z., Liu, Y., Tao, P., Shen, Q., Yi, N., Zhang, F., Liu, Q., Song, C., Zhang, D., and Shang, W. (2014). Bio‐Inspired Evaporation Through Plasmonic Film of Nanoparticles at the Air‐Water Interface. Small *10*, 3234-3239.

309. Liu, Y., Yu, S., Feng, R., Bernard, A., Liu, Y., Zhang, Y., Duan, H., Shang, W., Tao, P., and Song, C. (2015). A bioinspired, reusable, paper‐based system for high‐performance large‐scale evaporation. Advanced materials *27*, 2768-2774.

310. Bae, K., Kang, G., Cho, S.K., Park, W., Kim, K., and Padilla, W.J. (2015). Flexible thin-film black gold membranes with ultrabroadband plasmonic nanofocusing for efficient solar vapour generation. Nature communications *6*, 10103.

311. Zeng, Y., Yao, J., Horri, B.A., Wang, K., Wu, Y., Li, D., and Wang, H. (2011). Solar evaporation enhancement using floating light-absorbing magnetic particles. Energy & Environmental Science *4*, 4074-4078.

312. Yang, J., Pang, Y., Huang, W., Shaw, S.K., Schiffbauer, J., Pillers, M.A., Mu, X., Luo, S., Zhang, T., and Huang, Y. (2017). Functionalized graphene enables highly efficient solar thermal steam generation. ACS nano *11*, 5510-5518.

313. Li, X., Xu, W., Tang, M., Zhou, L., Zhu, B., Zhu, S., and Zhu, J. (2016). Graphene oxide-based efficient and scalable solar desalination under one sun with a confined 2D water path. Proceedings of the National Academy of Sciences *113*, 13953-13958.

314. Zhou, L., Tan, Y., Wang, J., Xu, W., Yuan, Y., Cai, W., Zhu, S., and Zhu, J. (2016). 3D self-assembly of aluminium nanoparticles for plasmon-enhanced solar desalination. Nature Photonics *10*, 393.

315. Jiang, Q., Tian, L., Liu, K.K., Tadepalli, S., Raliya, R., Biswas, P., Naik, R.R., and Singamaneni, S. (2016). Bilayered biofoam for highly efficient solar steam generation. Advanced materials *28*, 9400-9407.

316. Zhou, L., Tan, Y., Ji, D., Zhu, B., Zhang, P., Xu, J., Gan, Q., Yu, Z., and Zhu, J. (2016). Self-assembly of highly efficient, broadband plasmonic absorbers for solar steam generation. Science Advances *2*, e1501227.

317. Zhang, P., Li, J., Lv, L., Zhao, Y., and Qu, L. (2017). Vertically aligned graphene sheets membrane for highly efficient solar thermal generation of clean water. ACS nano *11*, 5087-5093.

318. Politano, A., Argurio, P., Di Profio, G., Sanna, V., Cupolillo, A., Chakraborty, S., Arafat, H.A., and Curcio, E. (2017). Photothermal membrane distillation for seawater desalination. Advanced materials *29*, 1603504.

319. Zhang, L., Tang, B., Wu, J., Li, R., and Wang, P. (2015). Hydrophobic Light‐to‐Heat Conversion Membranes with Self‐Healing Ability for Interfacial Solar Heating. Advanced materials *27*, 4889-4894.

320. Zeng, Y., Wang, K., Yao, J., and Wang, H. (2014). Hollow carbon beads for significant water evaporation enhancement. Chemical Engineering Science *116*, 704-709.

321. Cui, L., Zhang, P., Xiao, Y., Liang, Y., Liang, H., Cheng, Z., and Qu, L. (2018). High Rate Production of Clean Water Based on the Combined Photo‐Electro‐Thermal Effect of Graphene Architecture. Advanced materials *30*, 1706805.

322. Zhuang, S., Zhou, L., Xu, W., Xu, N., Hu, X., Li, X., Lv, G., Zheng, Q., Zhu, S., and Wang, Z. (2018). Tuning Transpiration by Interfacial Solar Absorber‐Leaf Engineering. Advanced Science *5*, 1700497.

323. Li, X., Lin, R., Ni, G., Xu, N., Hu, X., Zhu, B., Lv, G., Li, J., Zhu, S., and Zhu, J. (2017). Three-dimensional artificial transpiration for efficient solar waste-water treatment. National Science Review *5*, 70-77.

324. Aslan, Y., Puskely, J., Janssen, J., Geurts, M., Roederer, A., and Yarovoy, A. (2018). Thermal-aware synthesis of 5G base station antenna arrays: an overview and a sparsity-based approach. IEEE Access *6*, 58868-58882.

325. Aslan, Y., Puskely, J., Roederer, A., and Yarovoy, A. (2019). Multiple beam synthesis of passively cooled 5G planar arrays using convex optimization. IEEE Transactions on Antennas and Propagation *68*, 3557-3566.

326. Liu, X., Ren, D., Hsu, H., Feng, X., Xu, G.-L., Zhuang, M., Gao, H., Lu, L., Han, X., and Chu, Z. (2018). Thermal runaway of lithium-ion batteries without internal short circuit. Joule *2*, 2047-2064.

327. Hao, M., Li, J., Park, S., Moura, S., and Dames, C. (2018). Efficient thermal management of Li-ion batteries with a passive interfacial thermal regulator based on a shape memory alloy. Nature Energy *3*, 899-906.

328. Pu, S., Su, J., Li, L., Wang, H., Chen, C., and Hu, X. (2019). Bioinspired sweating with temperature sensitive hydrogel to passively dissipate heat from high-end wearable electronics. Energy Conversion and Management *180*, 747-756.

329. Wang, C., Hua, L., Yan, H., Li, B., Tu, Y., and Wang, R. (2020). A thermal management strategy for electronic devices based on moisture sorption-desorption processes. Joule *4*, 435-447.

330. Li, R., Shi, Y., Wu, M., Hong, S., and Wang, P. (2020). Photovoltaic panel cooling by atmospheric water sorption–evaporation cycle. Nature Sustainability *3*, 636-643.

331. Pu, S., Liao, Y., Chen, K., Fu, J., Zhang, S., Ge, L., Conta, G., Bouzarif, S., Cheng, T., and Hu, X. (2020). Thermogalvanic hydrogel for synchronous evaporative cooling and low-grade heat energy harvesting. Nano letters *20*, 3791-3797.

332. Andresen, M., and Liserre, M. (2014). Impact of active thermal management on power electronics design. Microelectronics Reliability *54*, 1935-1939.

333. Wang, X., Zhou, Z., Xiao, F., Xing, K., Yang, Z., Liu, Y., and Peng, C. (2018). Spatio-temporal analysis and prediction of cellular traffic in metropolis. IEEE Transactions on Mobile Computing *18*, 2190-2202.

334. Zhao, D., Aili, A., Zhai, Y., Lu, J., Kidd, D., Tan, G., Yin, X., and Yang, R. (2019). Subambient cooling of water: Toward real-world applications of daytime radiative cooling. Joule *3*, 111-123.

335. Zhao, B., Hu, M., Ao, X., Chen, N., and Pei, G. (2019). Radiative cooling: A review of fundamentals, materials, applications, and prospects. Applied energy *236*, 489-513.

336. Bhatia, B., Leroy, A., Shen, Y., Zhao, L., Gianello, M., Li, D., Gu, T., Hu, J., Soljačić, M., and Wang, E.N. (2018). Passive directional sub-ambient daytime radiative cooling. Nature communications *9*, 1-8.

337. Ferreira, J., and Kaviany, M. (2020). Geometric-confinement suppression of flow-boiling instability using perforated wick: Part I CHF and conductance enhancement. International Journal of Heat and Mass Transfer *159*, 120080.

338. Ong, C., and Thome, J. (2011). Macro-to-microchannel transition in two-phase flow: Part 2–Flow boiling heat transfer and critical heat flux. Experimental thermal and fluid science *35*, 873-886.

339. Hyun, D.C., Levinson, N.S., Jeong, U., and Xia, Y. (2014). Emerging applications of phase‐change materials (PCMs): teaching an old dog new tricks. Angewandte Chemie International Edition *53*, 3780-3795.

340. Aftab, W., Huang, X., Wu, W., Liang, Z., Mahmood, A., and Zou, R. (2018). Nanoconfined phase change materials for thermal energy applications. Energy & Environmental Science *11*, 1392-1424.

341. Cui, S., Ahn, C., Wingert, M.C., Leung, D., Cai, S., and Chen, R. (2016). Bio-inspired effective and regenerable building cooling using tough hydrogels. Applied Energy *168*, 332-339.

342. Zeng, Z., Zhao, B., and Wang, R. (2021). Passive day and night heating for zero energy buildings with solar-based adsorption thermal battery. Cell Reports Physical Science *2*, 100578.

343. Zhao, R., Zhang, S., Gu, J., Liu, J., Carkner, S., and Lanoue, E. (2014). An experimental study of lithium ion battery thermal management using flexible hydrogel films. Journal of Power Sources *255*, 29-36.

344. Feng, C., Yang, P., Liu, H., Mao, M., Liu, Y., Xue, T., Fu, J., Cheng, T., Hu, X., and Fan, H.J. (2021). Bilayer porous polymer for efficient passive building cooling. Nano Energy *85*, 105971.

345. Lv, T., Sun, L., Yang, Y., and Huang, J. (2021). Bio-inspired hydrogel with all-weather adhesion, cooling and reusability functions for photovoltaic panels. Solar Energy *216*, 358-364.

346. Zamengo, M., and Morikawa, J. (2019). Evaluation of cooling ability for a novel heat sink made of polyvinyl alcohol hydrogel. International Journal of Heat and Mass Transfer *143*, 118523.

347. Arslan Bin Riaz, M., Nasir, M.A., Nauman, S., Amin, S., Mehmood, F., Anwar, O.B., Hafeez, O., and Abid, T. (2021). Passive cooling performance of polyacrylamide hydrogel on wooden and brick houses and effect of nanoparticle integration on its mechanical strength. Plastics, Rubber and Composites, 1-11.

348. Lu, Z., Strobach, E., Chen, N., Ferralis, N., and Grossman, J.C. (2020). Passive Sub-Ambient Cooling from a Transparent Evaporation-Insulation Bilayer. Joule *4*, 2693-2701.

349. Pu, S., Fu, J., Liao, Y., Ge, L., Zhou, Y., Zhang, S., Zhao, S., Liu, X., Hu, X., and Liu, K. (2020). Promoting energy efficiency via a self‐adaptive evaporative cooling hydrogel. Advanced Materials *32*, 1907307.

350. Li, X., Xuan, Y., and Li, Q. (2021). Self-adaptive chip cooling with template-fabricated nanocomposite P (MEO2MA-co-OEGMA) hydrogel. International Journal of Heat and Mass Transfer *166*, 120790.

351. Xu, J., Chao, J., Li, T., Yan, T., Wu, S., Wu, M., Zhao, B., and Wang, R. (2020). Near-zero-energy smart battery thermal management enabled by sorption energy harvesting from air. ACS central science *6*, 1542-1554.

352. Yuk, H., Zhang, T., Lin, S., Parada, G.A., and Zhao, X. (2016). Tough bonding of hydrogels to diverse non-porous surfaces. Nature materials *15*, 190-196.

353. Sun, J.-Y., Zhao, X., Illeperuma, W.R., Chaudhuri, O., Oh, K.H., Mooney, D.J., Vlassak, J.J., and Suo, Z. (2012). Highly stretchable and tough hydrogels. Nature *489*, 133-136.

354. Zhang, S., Zhao, R., Liu, J., and Gu, J. (2014). Investigation on a hydrogel based passive thermal management system for lithium ion batteries. Energy *68*, 854-861.

355. Zhou, X., Zhang, P., Zhao, F., and Yu, G. (2020). Super moisture absorbent gels for sustainable agriculture via atmospheric water irrigation. ACS Materials Letters *2*, 1419-1422.

356. Karmakar, A., Mileo, P.G., Bok, I., Peh, S.B., Zhang, J., Yuan, H., Maurin, G., and Zhao, D. (2020). Thermo‐Responsive MOF/Polymer Composites for Temperature‐Mediated Water Capture and Release. Angewandte Chemie International Edition *59*, 11003-11009.

357. Li, R., Shi, Y., Wu, M., Hong, S., and Wang, P. (2020). Improving atmospheric water production yield: Enabling multiple water harvesting cycles with nano sorbent. Nano Energy *67*, 104255.

358. Entezari, A., Ejeian, M., and Wang, R. (2020). Super atmospheric water harvesting hydrogel with alginate chains modified with binary salts. ACS Materials Letters *2*, 471-477.

359. Fathieh, F., Kalmutzki, M.J., Kapustin, E.A., Waller, P.J., Yang, J., and Yaghi, O.M. (2018). Practical water production from desert air. Science advances *4*, eaat3198.

360. Xu, J., Li, T., Chao, J., Wu, S., Yan, T., Li, W., Cao, B., and Wang, R. (2020). Efficient Solar‐Driven Water Harvesting from Arid Air with Metal‐Organic Frameworks Modified by Hygroscopic Salt. Angewandte Chemie International Edition *59*, 5202-5210.

361. Entezari, A., Ejeian, M., and Wang, R. (2019). Modifying water sorption properties with polymer additives for atmospheric water harvesting applications. Applied Thermal Engineering *161*, 114109.

362. Qi, H., Wei, T., Zhao, W., Zhu, B., Liu, G., Wang, P., Lin, Z., Wang, X., Li, X., and Zhang, X. (2019). An Interfacial Solar‐Driven Atmospheric Water Generator Based on a Liquid Sorbent with Simultaneous Adsorption‐Desorption. Advanced Materials *31*, 1903378.

363. Burtch, N.C., Jasuja, H., and Walton, K.S. (2014). Water stability and adsorption in metal–organic frameworks. Chemical reviews *114*, 10575-10612.

364. Lee, J., and Lee, D.-Y. (2012). Sorption characteristics of a novel polymeric desiccant. International journal of refrigeration *35*, 1940-1949.

365. Yang, Y., Rana, D., and Lan, C.Q. (2015). Development of solid super desiccants based on a polymeric superabsorbent hydrogel composite. RSC Advances *5*, 59583-59590.

366. Yang, H., Zhu, H., Hendrix, M.M., Lousberg, N.J., de With, G., Esteves, A.C.C., and Xin, J.H. (2013). Temperature‐Triggered Collection and Release of Water from Fogs by a Sponge‐Like Cotton Fabric. Adv. Mater. *25*, 1150-1154.

367. Ghatikar, G., Piette, M.A., Fujita, S., McKane, A., Dudley, J.H., Radspieler, A., Mares, K., and Shroyer, D. (2009). Demand response and open automated demand response opportunities for data centers. Lawrence Berkeley National Lab.(LBNL), Berkeley, CA (United States).

368. https://www.alibaba.com/product-detail/Sodium-Acrylate-16-Years-Service-Life_1600353164535.html?spm=a2700.galleryofferlist.normal_offer.d_title.3b9d108aQKKocV&s=p.

369. https://www.alibaba.com/product-detail/Sodium-Alginate-Sodium-Alginate-Sodium-Alginate_60465002652.html?spm=a2700.galleryofferlist.normal_offer.d_title.2c9e65f0DZxEFN&s=p.

370. https://www.alibaba.com/product-detail/N-Factory-Supply-N-N-Methylenebisacrylamide_1600303416236.html?spm=a2700.galleryofferlist.normal_offer.d_title.41ac3381pjMADf&s=p.

371. https://www.alibaba.com/product-detail/99-Purity-Ammonium-persulfate-with-low_1600239908238.html?spm=a2700.galleryofferlist.normal_offer.d_title.1bb52c41SFIWQH.

372. https://www.alibaba.com/product-detail/Coupling-agent-3-Trimethoxysilyl-propyl-methacrylate_1600364929863.html?spm=a2700.galleryofferlist.normal_offer.d_title.18d71c7aEoIMn7.

373. https://www.alibaba.com/product-detail/Customized-Aluminum-High-efficient-Copper-Pipe_60541617193.html?spm=a2700.galleryofferlist.normal_offer.d_title.698075daBk2BiJ.

374. https://www.alibaba.com/product-detail/Pipe-Heat-Sink-6pipe-Refrigerator-Aluminum_62422889225.html?spm=a2700.galleryofferlist.topad_creative.d_title.698075daBk2BiJ.

375. https://www.alibaba.com/product-detail/Heat-Sink-Pipe-Photography-Light-Heat_1600175202768.html?spm=a2700.galleryofferlist.normal_offer.d_image.698075daBk2BiJ&s=p.

376. https://www.alibaba.com/product-detail/Heat-Pipe-Sink-High-Bay-Large_62415916830.html?spm=a2700.7735675.normal_offer.d_title.47101f76kSQZdT&s=p.

377. Peniche‐Covas, C., Argüelles‐Monal, W., and San Román, J. (1995). Sorption and desorption of water vapour by membranes of the polyelectrolyte complex of chitosan and carboxymethyl cellulose. Polym. Int. *38*, 45-52.

378. Aslan, Y., Kiper, C.E., van den Biggelaar, A.J., Johannsen, U., and Yarovoy, A. (2019). Passive cooling of mm-wave active integrated 5G base station antennas using CPU heatsinks. (IEEE), pp. 121-124.

379. Ma, L., Zhao, X., Sun, H., Wu, Q., and Liu, W. (2016). Experimental study of single phase flow in a closed-loop cooling system with integrated mini-channel heat sink. Entropy *18*, 128.

380. Xie, Y., Shi, S., Tang, J., Wu, H., and Yu, J. (2018). Experimental and analytical study on heat generation characteristics of a lithium-ion power battery. International Journal of Heat and Mass Transfer *122*, 884-894.

381. Christen, R., Rizzo, G., Gadola, A., and Stöck, M. (2017). Test method for thermal characterization of Li-ion cells and verification of cooling concepts. Batteries *3*, 3.

382. Ebrahimi, K., Jones, G.F., and Fleischer, A.S. (2014). A review of data center cooling technology, operating conditions and the corresponding low-grade waste

heat recovery opportunities. Renewable and Sustainable Energy Reviews *31*, 622-638.

383. Zhang, W., Shen, L., Yang, Y., and Chen, H. (2015). Thermal management for a micro semiconductor laser based on thermoelectric cooling. Applied Thermal Engineering *90*, 664-673.

384. Masanet, E., Shehabi, A., Lei, N., Smith, S., and Koomey, J. (2020). Recalibrating global data center energy-use estimates. Science *367*, 984-986.

385. Shehabi, A., Smith, S., Sartor, D., Brown, R., Herrlin, M., Koomey, J., Masanet, E., Horner, N., Azevedo, I., and Lintner, W. (2016). United states data center energy usage report.